Multiparticle production in proton-proton collisions at the LHC energies

By

SHREYASI ACHARYA

Enrolment No.: PHYS04201504012

Variable Energy Cyclotron Centre, Kolkata

A thesis submitted to

The Board of Studies in Physical Sciences

In partial fulfillment of requirements

For the Degree of

DOCTOR OF PHILOSOPHY

of

HOMI BHABHA NATIONAL INSTITUTE

July, 2021

Homi Bhabha National Institute[1]

Recommendations of the Viva Voce Committee

As members of the Viva Voce Committee, we certify that we have read the dissertation prepared by **Shreyasi Acharya** entitled "**Multiparticle production in proton-proton collisions at the LHC energies**" and recommend that it may be accepted as fulfilling the thesis requirement for the award of Degree of Doctor of Philosophy.

Chairman - Dr. Jane Alam		**Date:** 22/10/2021
Guide / Convener - Dr. Subhasis Chattopadhyay		**Date:** 22/10/2021
Examiner - Dr. Seema Sharma		**Date:** 22-10-2021
Member 1- Dr. Anand Kumar Dubey		**Date:** 22.10.2021
Member 2 - Dr. Sourav Sarkar		**Date:** 22-10-2021
Member 3 - Dr. Sidharth Kumar Prasad		**Date:** 22-10-2021

Final approval and acceptance of this thesis is contingent upon the candidate's submission of the final copies of the thesis to HBNI.

I/~~We~~ hereby certify that I/~~we~~ have read this thesis prepared under my/~~our~~ direction and recommend that it may be accepted as fulfilling the thesis requirement.

Date: 22/10/21

Place: KOLKATA

Signature
Guide 22/10/21

[1] This page is to be included only for final submission after successful completion of viva voce.

STATEMENT BY AUTHOR

This dissertation has been submitted in partial fulfilment of requirements for an advanced degree at Homi Bhabha National Institute (HBNI) and is deposited in the Library to be made available to borrowers under rules of the HBNI. Brief quotations from this dissertation are allowable without special permission, provided that accurate acknowledgement of source is made. Requests for permission for extended quotation from or reproduction of this manuscript in whole or in part may be granted by the competent authority of HBNI when in his or her judgement the proposed use of the material is in the interest of scholarship. In all other instances, however, permission must be obtained from the author.

Shreyasi Acharya

DECLARATION

I, hereby declare that the investigation presented in the thesis has been carried out by me. The work is original and has not been submitted earlier as a whole or in part for a degree / diploma at this or any other Institution / University.

Shreyasi Acharya

List of Publications arising from the thesis

Journal publication

1. "Estimation of initial-state structures in high-energy heavy-ion collisions using principal component analysis",
   – Shreyasi Acharya and Subhasis Chattopadhyay
   Phys. Rev. C 103, 034909 (2021)

ALICE paper in the final stage before submission

1. "Inclusive and multiplicity dependent production of electrons from heavy-flavour hadron decays in pp and p–Pb collisions",
   – Shreyasi Acharya as one of the principal authors
   Paper in Internal Review Committee (IRC) round of ALICE, final stage before submission
   `https://alice-publications.web.cern.ch/node/6090`

Proceedings of conferences

1. "Heavy-flavour production in small systems and evolution with multiplicity with ALICE",
   Oral presentation at Strangeness in Quark Matter (SQM 2021, online) conference
   – Shreyasi Acharya for the ALICE collaboration,
   Proceeding submitted to EPJ Web of Conference: Accepted

2. "Event-multiplicity and event-shape dependence of open heavy flavour production in pp collisions with ALICE at the LHC"
   – Shreyasi Acharya for the ALICE collaboration,
   Proceedings at PoS HardProbes2018 (2019) 153
   Oral presentation at Hard Probes 2018, Aix-Les-Bains, France

3. "Production of electrons from heavy-flavour hadron decays in pp collisions at $\sqrt{s}$ = 13 TeV as a function of charged-particle multiplicity with ALICE"

– Shreyasi Acharya for the ALICE collaboration,
Proceedings at PoS LHCP2018 (2018) 044
Poster presentation at LHCP conference 2018, Bologna, Italy

4. "Heavy flavour decay electron yield in pp collisions at $\sqrt{s} = 13$ TeV with ALICE at the LHC"
   – Shreyasi Acharya for the ALICE collaboration,
   Proceedings of the DAE-BRNS Symp. on Nucl. Phys. 62 (2017) 818-819
   Oral presentation at DAE-BRNS Symposium on Nuclear Physics 2017, India

Contributions to other conferences

1. "Production of electrons from heavy-flavour hadron decays in pp collisions at $\sqrt{s} = 13$ TeV as a function of charged-particle multiplicity with ALICE"
   Poster presentation at Quark Matter 2018 conference, Venice, Italy

ALICE Analysis Notes

1. p_{T}-differential cross section of electrons from heavy-flavour hadron decays and yield as a function of charged-particle multiplicity in pp collisions at $\sqrt{s} = 13$ TeV
   `https://alice-notes.web.cern.ch/node/1180`

2. Production of heavy-flavour hadron decay electrons in pp collisions at $\sqrt{s} = 13$ TeV using TPC+TOF as a function of charged-particle multiplicity
   `https://alice-notes.web.cern.ch/node/781`

Shreyasi Acharya

Shreyasi Acharya

ACKNOWLEDGMENTS

First and foremost, I would like to express my sincere and deepest gratitude and respect to my supervisor Dr. Subhasis Chattopadhyay. He has provided me constant guidance on the work in this thesis, especially during this difficult pandemic situation. I have confided in him with my silliest queries and problems. He is an amazing teacher and I have learned a lot from him. Without Sir as my supervisor, I may not have reached this position where I complete this thesis and acknowledge those who have supported me through this journey. Only a few words may not suffice, but I would thank him with my utmost regards and gratitude.

I would like to express my profound and heartfelt gratitude to Dr. Deepa Thomas (UT, Austin, US). I am very fortunate that I got to work under her guidance on the ALICE data analysis. Working remotely in the data analysis could have been arduous and daunting task without her help. She has been a constant source of enthusiasm, motivation and a zealous support system through out these years.

I would like to convey my earnest and wholehearted thanks to Dr. Andrea Dubla (GSI, Germany) for his tremendous support and ceaseless help. His passionate guidance and helpful suggestions on the ALICE data analysis and beyond has motivated me to perform better and has helped me immensely through out this journey.

I would like to convey special thanks to my ALICE collaborators (also seniors) Dr. Alessandro Grelli, Dr. Andrea Rossi, Dr. Cristina Terevolli, Dr. Shingo Sakai, Dr. Jurgen Schukraft for their compassionate help, suggestions and discussions. I would also like to sincerely thank Dr. Tapan Nayak for always being supportive in my endeavours.

I sincerely thank the members of my Doctoral Committee: Dr. Jane Alam, Dr. Anand Kumar Dubey, Dr. Sourav Sarkar and Dr. Sidharth Kumar Prasad. I have learned a lot from them. It has always been a pleasure to attend Jane Sir's classes. I would like to thank all members of my doctoral committee for their support in providing a healthy research environment.

I would like to thank Dr. Paramita Mukherjee for her unwavering and rock-solid support, specially during the unfavorable times of my PhD tenure. Having ma'am by my side has given me tremendous strength to get me through the trying times. Her well wishes and encouragement has always been a source of moral boost and positivity for me. I would like to express my earnest and wholehearted gratitude and regards towards her.

I would like to heartily acknowledge the help from Dr. Sumit Som (Director) and Dr. Parnika Das (Dean) and thank them for providing a spirited working atmosphere.

I would also like to thank Dr. Tilak Kumar Ghosh for his support and help, from the tiniest of matters to greater academic and administrative issues. I also thank Dr. Gayathri N. Banerjee and Dr. Vaishali Naik for always looking out for me and for their well wishes.

I would like to extend my special thanks to Mr. Prasun Singha Roy and the entire VECC grid computing team. The VECC grid computing has always been there for all sort of technical support at an instant, from detecting hardware problems to solving software issues. I also thank them for constantly maintaining the active grid facility.

I would also like to acknowledge the support of the entire VECC Guest House staff. Their welcoming and kind nature has helped in creating a positive and pleasant working environment.

I would like to acknowledge the support of my positive minded classmates and friends at VECC (in alphabetical order): Abhishek, Mahfuzur, Mitali, Sanchari, Santanu, Shuvo, Sinjini, Soumen, Sumit, Tanay; and seniors/colleagues: Ajit da, Apar, Arghya da, Ashik da, Debojit da, Deekshit, Dipen, Ekata di, Nachiketa da, Noor da, Rajendra da, Rajesh da, Rajkumar, Shabir, Somnath da, Vivek. I have a lot of fun and nice memories with them during my stay at VECC. I would also like to thank my collaborators and friends Preeti Dhankher (IIT Bombay) and Sudhir Rode (IIT Indore). I would also like to extend my thanks to my friends Meera and Lisa who have been a constant positive presence in my life. I also specially thank the members of NextLevelMMA, especially Shiba da, Joy and Prem who have always supported and encouraged me to perform better in all walks of life.

Finally, I would like to thank my family. I would especially like to thank Mrs. Krishna Acharya Saha (pisi), Mr. Sanjukt Saha (piso) and Damayanti (bon). Pisi has been the guardian, mentor and friend, without whom I would not have made it this far. I also feel lucky to have a very supportive joint family, especially my cousins. I would like to specially thank Mr. Amal & Mrs. Sangeeta Acharya (kaku, kakima), Mr. Chinmoy Goswami (mama), Mr. Kamal & Mrs. Sukla Acharya (kaku, kakima), Mr. Manoj Goswami (dada) and Siddhartha (bhai) for being a constant supportive presence, especially during the difficult pandemic times. Special thanks to Apabrita (bon) for her heartening exotic home made food, Aparupa (bon) for creating a jolly environment and Saswata (bhai) for his well wishes.

Lastly, this goes without saying explicitly, I thank my beloved and wonderful parents (Mr. Parimal Acharya and Mrs. Mamata Acharya), to whom I owe everything in my life.

Shreyasi Acharya

Shreyasi Acharya

Contents

Homi Bhabha National Institute

Synopsis of PhD Thesis

1. Name of the Student: SHREYASI ACHARYA

2. Name of the Constituent Institution: Variable Energy Cyclotron Centre, Kolkata

3. Enrolment No. : PHYS04201504012

4. Title of the Thesis: Multiparticle production in proton-proton collisions at the LHC energies

5. Board of Studies: Physical Sciences

Nuclear matter, such as the proton, neutron, pion and other composite hadrons, are made up of quarks and gluons. Quarks and gluons form the fundamental building blocks of matter and, under normal nuclear density and temperature they cannot be isolated, as quarks remain confined inside hadrons via gluons. This phenomena of confinement of color-charged particles into composite hadrons is governed by the two main properties of QCD, the theory of strong interactions, known as color confinement and asymptotic freedom of quarks [1]. The concept of asymptotic freedom states that at very short distance, $\lesssim$ size of the nucleon, quarks and gluons appear to be quasi-free as the effective coupling strength between quarks decreases and becomes very small. However, at sufficiently high energy density and/or net baryo-chemical potential, a phase transition is expected to occur from a state of nucleons to a state of deconfined quarks and gluons (from their individual nucleons) covering the entire volume of nuclear matter or a volume with many units of the characteristics length scale. This state is expected to be in local thermal and chemical equilibrium and is known as Quark-Gluon Plasma (QGP) [2].

The universe is believed to have started from an infinitely hot and dense singularity, in-

flating and cooling over the billion years to form the cosmos as we know it today. The early universe, a few microseconds after the Big Bang, is believed to have been in a state of such deconfined quark and gluon at high temperatures and zero baryo-chemical potential [3]. The study of the formation of the quark-gluon plasma can provide an in-depth understanding and knowledge about nuclear matter under extreme conditions. Nuclear matter under extreme conditions is studied by colliding ions of heavy nuclei (e.g AuAu, PbPb) at relativistic energies in laboratories such as the Large Hadron Collider Experiment (LHC) at CERN. Such relativistic heavy ion collisions recreates droplets of the quark-gluon plasma [4], similar to those of the early universe [5]. As the lifetime of the QGP state is of the orders of few fm/c, and cannot be detected directly, several experimental observables involving the produced particles are used to characterize the formation the QGP in such heavy ion collisions. Some of the key signatures include nuclear modification factor of high p_{T} particles [6] and/or jet quenching [7] (hard signatures) and anisotropic flow [8], strangeness enhancement [9] (soft signatures) etc.

In addition to heavy-ion collisions, the LHC experiments also take data using proton beams. These proton-proton (pp) collisions act as no-QGP reference for studying the QGP related signals in heavy-ion collisions. Due to the very small dimensions of proton compared to Au or Pb ions, the formation of a QGP medium was not expected in such small collisional systems. Contradicting our traditional wisdom, results at LHC over the last decade, have revealed certain soft signatures of QGP medium in high multiplicity small system collisions (pp and p–Pb), such as the collective flow [10] and strange baryon enhancement [11]. Hence, multiplicity dependent studies of particle production in high energy pp collisions has become of particular relevance in understanding the particle production mechanism in such systems.

In this thesis, using the ALICE experimental data at the LHC energies, the p_{T}-differential cross section of electrons decayed from open heavy flavour hadrons in pp collisions at $\sqrt{s}$ = 13 TeV and its multiplicity dependent yield has been measured. Heavy quarks (charm and beauty) are produced at the very early stages of collision through the hard scatterings and their production cross sections can be calculated through the framework of perturbative QCD down to very low p_{T}. Hence, heavy flavour particles act as efficient probes for the QGP medium formed in heavy ion collisions, as the heavy quarks being produced well before the

formation of QGP, traverse through the medium during its entire evolution. Measurements of heavy flavour hadron production in proton-proton collision act as baseline for the study of heavy flavour particles in heavy-ion collisions and could also provide new insights into the production and hadronization mechanisms in pp collisions through their multiplicity dependent studies.

Heavy flavour particles are studied through the decayed final state particles as they have a very short life time. The decays of heavy flavour particles can be classified into the hadronic decay channel and semi-leptonic decay channel. In the hadronic channel, the heavy flavour particle decays into two or more hadrons, and full reconstruction of the decayed particles via the invariant mass analysis is performed to identify the parent heavy flavour particle. In the semi-leptonic decay channel, the heavy flavour hadron decays into a lepton (electron or muon), a corresponding neutrino and hadron(s) ($\mathrm{B, D} \rightarrow \mathrm{e} + \nu_{\mathrm{e}} + \mathrm{X}$). Unlike the hadronic channel, full reconstruction of the parent hadron is not possible due to the missing neutrinos. The yield of electrons decayed from the heavy flavour hadrons are obtained by subtracting the background non-heavy-flavour electrons from the inclusive electrons yield. Since, electrons primarily interact electromagnetically, they provide cleaner signals. This thesis pertains to the semi-electronic channel.

The analysis was performed combining two different strategies with different detector combinations to identify the electrons decayed in a wide range of p_{T} (0.5 GeV/c $< p_{\mathrm{T}} <$ 35 GeV/c). The electron identification at low and intermediate p_{T} (0.5 GeV/c $< p_{\mathrm{T}} <$ 4 GeV/c) is ensured by the Time Projection Chamber (TPC) and Time-Of-Flight (TOF) detectors and at high transverse momentum (3 GeV/c $< p_{\mathrm{T}} <$ 35 GeV/c) by the TPC and Electromagnetic Calorimeter system (EMCal). The Inner Tracking System (ITS) is used for vertex determination and together with the TPC for tracking in the mid rapidity region. Events used in this analysis are obtained using the minimum bias (MB) trigger and with two different energy thresholds ($\mathrm{E_{th}}$) of the EMCal trigger, namely the EG2 ($\mathrm{E_{th}} \sim$ 4.5 GeV) and EG1 ($\mathrm{E_{th}} \sim$ 10 GeV) triggers. The EG2 and EG1 triggers help to provide adequate statistics which allows the analysis to extent to such high p_{T} ranges. Additional event selection criteria are applied to reject pile up events. Reconstructed tracks are selected based on the several criteria to select high purity electron samples by rejecting fake and uncorrelated tracks which produce signals

in the detector. The charged particle identification (PID) in the TPC is based on the specific energy loss measurement (dE/dx) of a particle in the gas detector. At low $p_{\rm T}$, in addition to the TPC, particle identification from TOF is required to reduce the background from kaons and protons. TOF detector uses the time of flight of the charged particle for particle identification. For the low and intermediate $p_{\rm T}$ range, the electron sample is selected within the optimized TOF PID selection interval $|n\sigma_e^{\rm TOF}| < 3$ where $n\sigma$ is the difference of the measured signal in the detector from the expected value for electrons in terms of the detector resolution. To remove the hadron contamination from the sample, the TPC nσ_e (dE/dx - $\langle$dE/d$x\rangle$ in terms of dE/dx resolution) is evaluated in several momentum slices and the resulting plots are fitted with Gaussian functions for electrons and protons, kaons and a convolution of Landau and exponential function for pions. The electron sample is selected within the TPC PID selection interval -1 $< n\sigma_e^{\rm TPC} <$ 3. The hadron contamination is obtained by measuring the fraction of pions, protons and kaons in the interval -1 $< n\sigma_e^{\rm TPC} <$ 3 and is found to be negligible at 0.5 GeV/c and increases to $\sim$ 5% at 4 GeV/c. For the intermediate and high $p_{\rm T}$ range, the electron identification capabilities of the electromagnetic calorimeter is employed. Electrons (and photons) tend to deposit all of their energy in the EMCal in the form of clusters through electromagnetic showers. Hence, the total energy deposited by the electrons in the EMCal (E) should be equal to its momentum (p), which is obtained from the TPC, i.e., E/$p \approx$ 1. The hadrons, however, do not deposit their entire energy in the EMCal as they interact mainly via the strong nuclear force. For hadrons the E/p should be less than 1. Electrons are separated from photons by matching EMCal clusters to the tracks from TPC as photons do not give signal in the TPC. Electron candidates are selected using the optimized values of -1 $< n\sigma_e^{\rm TPC} <$ 3. A $p_{\rm T}$ dependent shower shape selection criteria was applied to reduce hadron contamination at higher $p_{\rm T}$ while not affecting the electron selection efficiency significantly. A lower threshold of the shower shape was chosen to remove contamination caused by neutrons hitting the electronics. To remove the residual contribution from hadrons, the E/p distribution of hadrons (obtained using $n\sigma_e^{\rm TPC} <$ - 3.5) was scaled to match the electron candidates within E/$p <$ 0.7 and subtracted from the electron candidate E/p spectrum. The electron yield was obtained by integrating the scaled hadron subtracted electron distribution within 0.85 $<$ E/$p <$ 1.2. This procedure was iterated for each $p_{\rm T}$ interval. The hadron contamination was measured to be

negligible at 3 GeV/c, increasing to $\sim$ 23% at 35 GeV/c. To obtain the yield of electrons from the heavy-flavour decays, the non-heavy flavour background sources are subtracted from the inclusive electron spectra. The dominant source of background electrons come from the Dalitz decay of light neutral mesons (π^0 and η) and γ conversions in the detector material. These are known as the photonic electrons. To identify electrons from photonic sources, opposite signed partners (e^- e^+) are paired in an invariant mass spectrum. While the unlike sign (ULS, e^- e^+) pairs give both the correlated signals from the actual decay (π^0 and η), γ conversions and uncorrelated combinatorial background, the like sign (LS, e^- e^- and e^+ e^+) pairs are used to estimate and subtract the random combinatorial background. An invariant mass cut of 0.14 GeV/c^2 is used to select the photonic electrons. The raw photonic spectra from data is corrected for the loss of signal due to detector acceptances and selection criteria by the tagging efficiency ($\epsilon_{\rm tag}$). The tagging efficiency, defined as the efficiency of finding the partner electron, is estimated using the Monte-Carlo (MC) simulations. The non-heavy flavour contribution is subtracted from inclusive electron sample and is corrected by the reconstruction efficiency, using the Monte-Carlo (MC) simulations for signal losses due to detector the inefficiencies, limited acceptance, track $\&$ particle selection criteria. Electrons from W and Z boson decays form a significant background for $p_{\rm T} >$ 20 GeV/c. Their contribution is calculated using the PYTHIA+POWHEG event generator and is subtracted from the reconstruction efficiency corrected cross section. The contribution is negligible for $p_{\rm T} <$ 5 GeV/c and increases to $\sim$ 25% at 35 GeV/c with respect to the heavy flavour decay electron spectra before the subtraction of the W, Z decay electron contribution. Systematic uncertainties on the invariant yield are measured by identifying the different sources and varying the various selection criteria applied on the measurement. Contributions from different sources are summed in quadrature as they are considered to be uncorrelated. Uncertainty from the correlated sources are summed linearly. Figure 1 (left) presents the cross section of electrons from heavy-flavour hadron decays in pp collisions at $\sqrt{s}$ = 13 TeV, from different measurements. A cross check with the cross section obtained from another analysis with low B (B = 0.2 T) data has been done. Comparison of the measured cross sections is performed in the overlapping $p_{\rm T}$ intervals. The different measurements are is very good agreement within the statistical and systematic uncertainty. The final spectra of the cross section of electrons from heavy flavour decays is shown in the right

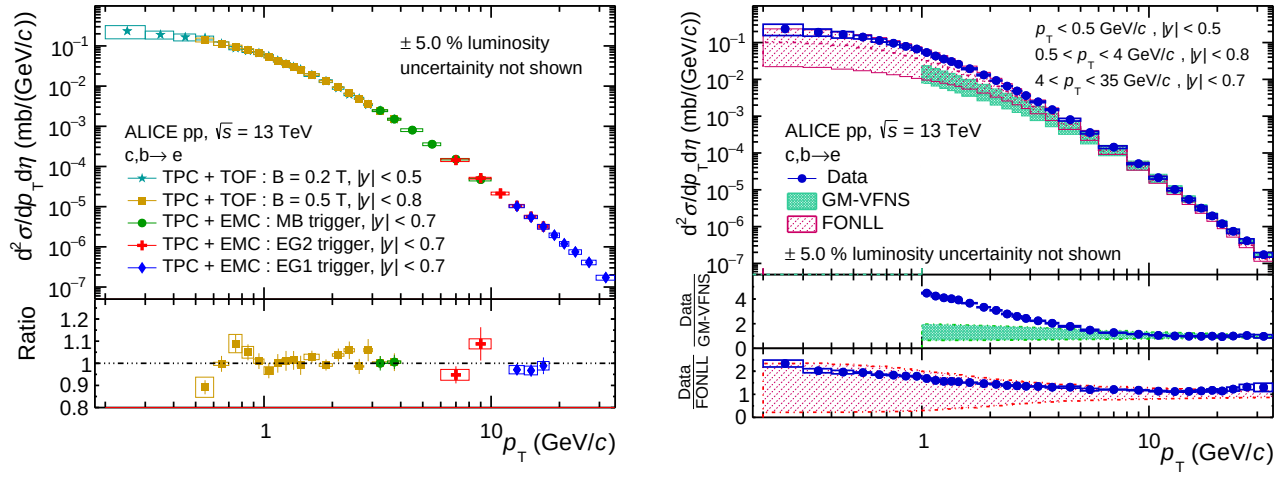

Figure 1: The p_{T}-differential cross section of electrons from heavy-flavour hadron decays in pp collisions at $\sqrt{s}$= 13 TeV. Left: From different measurements, Right: Compared with FONLL and GM-VFNS predictions

panel of figure 1. For the total cross section, the following p_{T} intervals from this analysis are chosen such that the statistical and systematic uncertainty are minimized: 0.5 GeV/c < p_{T} <4 GeV/c from the TPC–TOF analysis (nominal B); 4 GeV/c < p_{T} < 6 GeV/c, 6 GeV/c < p_{T} < 12, 12 GeV/c < p_{T} < 35 GeV/c from the MB, EG2, EG1 triggers from the TPC–EMCal analysis respectively. The spectra from 0.2 GeV/c < p_{T} < 0.5 GeV/c is taken from the TPC–TOF analysis low-B analysis. In figure 1 (right) the p_{T}-differential cross section of heavy lavour decay electrons has been compared with the Fixed-Order-Next-to-Leading-Log (FONLL) and General-Mass-Variable-Flavour-Number-Scheme (GM-VFNS) pQCD calculations. The FONLL calculation describes the measurements within the statistical and systematic uncertainties and the data points are found be close to the upper edge of the theoretical predictions. The GM-VFNS model largely underpredicts the data in low and mid p_{T}, while data the lies within the uncertainty in the high p_{T} range (p_{T} > 5 GeV/c).

The multiplicity dependent analysis of the electron yield from the heavy flavour decays has also been presented in terms of the self-normalized yield of electrons (yield of heavy flavour decayed electrons in multplicity classes normalised by the yield at minimum bias collision) as a function of the self normalised charged-particle pseudorapidity density. The charged-particle pseudorapidity density ($\mathrm{d}N_{\mathrm{ch}}/\mathrm{d}\eta$) is measured using the number of tracklets from the Silicon Pixel Detector (SPD). The raw number tracklets (N_{tr}) as a function of z_{vtx} is corrected for the detector inefficiencies and dead modules along the Z vertex and over time, to

obtained the corrected number of tracklets ($N_{\rm tr}^{\rm corr}$), following the procedure discussed in [12]. However, this correction does not account for the global loss of the particles. The true number of charged particles produced in an event ($N_{\rm ch}$) is obtained from $N_{\rm tr}^{\rm corr}$using MC simulations. Events are sliced in $N_{\rm tr}^{\rm corr}$ intervals, and the corresponding $\mathrm{d}N_{\rm ch}/\mathrm{d}\eta$ is obtained using MC and is corrected by trigger and vertex finding efficiencies, which are close to unity for all multiplicity classes expect for the lowest multiplicity interval. The $\langle \mathrm{d}N_{\rm ch}/\mathrm{d}\eta \rangle$ from this analysis is found to be 6.77 $\pm$ 0.34 which is within a good agreement (within 4%) with previous published ALICE measurements [13]. Figure 2 (left) shows the self-normalized yield of electrons

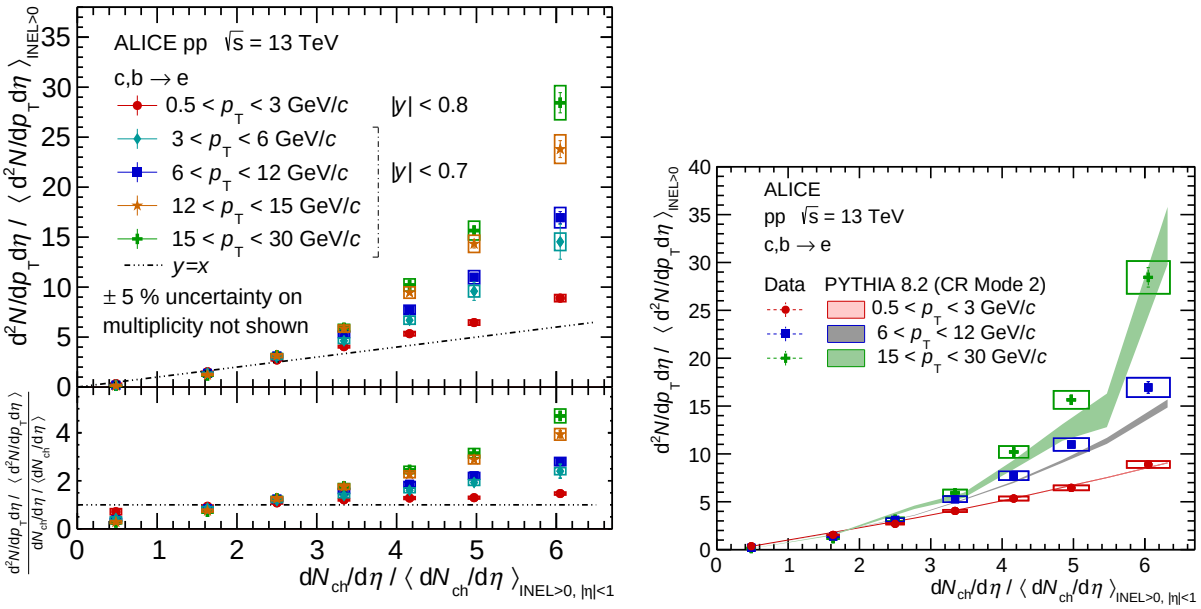

Figure 2: Self-normalised yield of electrons decayed from heavy flavour hadrons as a function of normalised charged-particle pseudorapidity density at mid rapidity. Left: In different $p_{\rm T}$ intervals, Right: Comparison with PYTHIA CR mode 2 tune

decayed from heavy flavour hadrons ($\mathrm{d}^2N/\mathrm{d}p_{\rm T}\mathrm{d}\eta/\ \langle \mathrm{d}^2N/\mathrm{d}p_{\rm T}\mathrm{d}\eta \rangle$) as a function of the normalised charged-particle pseudorapidity density ($\mathrm{d}N_{\rm ch}/\mathrm{d}\eta/\ \langle \mathrm{d}N_{\rm ch}/\mathrm{d}\eta \rangle$) at mid rapidity ($|\eta| <$ 1.0) in five $p_{\rm T}$ intervals from 0.5 GeV/c $< p_{\rm T} <$ 30 GeV/c. The normalised yield shows a faster than linear increasing trend with respect to the normalised charged-particle density and the results at higher $p_{\rm T}$ intervals show a tendency of steeper increase. The increase in the electron yield is approximately a factor of $\sim$ 9 for the lowest measured $p_{\rm T}$ (0.5 GeV/c $< p_{\rm T} <$ 3 GeV/c) and a factor of $\sim$ 28 for the highest measured $p_{\rm T}$ (15 GeV/c $< p_{\rm T} <$ 30 GeV/c) for increase in multiplicities of 6 times the average multiplicity. A comparison of the yield with predictions from PYTHIA 8.2 Monash tune (default) and an improved color reconnection (CR) Mode-2

tune has been done. The right panel of figure 2 shows the comparison with the predictions for the PYTHIA CR mode-2 tune. Although, PYTHIA 8.2 Monash tune describes the trend in data, slope is overestimated at higher p_{T}. PYTHIA 8.2 with CR Mode-2 however tends to reproduce the slope at all p_{T} intervals fairly well and describes the normalised yield better than that by the Monash tune. This study forms the largest part of the publication in preparation with the ALICE collaboration [14] and is currently in the internal review committee (IRC) rounds of ALICE. A comparison of the self normalised yields of heavy flavour decay electrons have been done with the normalised yields of other heavy and light flavour hadrons (all charged particles, J/ψ, D-mesons, kaon, π, proton, K^0_s, Λ, Ξ). To perform an in-depth p_{T} dependent comparison, the double ratio of the self-normalized yields (bottom panel figure 2, left) in different p_{T} intervals have been fitted with a linear function. The $\langle p_{\mathrm{T}} \rangle$ vs. slope of linear fit of the various particles have been compared (not shown here). Comparison has been done in two multiplicity selection scenarios, i.e., where events are divided using SPD tracklet multiplicity estimator at mid rapidity and using V0 estimator in forward rapidity. A baryon vs. meson trend is observed for both the multiplicity selction scenarios. For measurements where multiplicity estimator is SPD tracklet, no saturation with increasing $\langle p_{\mathrm{T}} \rangle$ is seen. Mesons (heavy flavour decay electrons, D-mesons, J/ψ, K^0_s and all charged particles which is mostly π) tend to follow a similar trend. Baryons (Ξ and Λ) follows a different trend. For measurements using V0 multiplicity estimator, the baryon trend saturates at $p_{\mathrm{T}} \gtrsim 4$ GeV/c. This trend could indicate common physical origin independent of particle species.

In this thesis, a study on the structures in the initial collision zone and how they effect the final state particles using PbPb collisions from AMPT event generator at $\sqrt{s_{\mathrm{NN}}}$ = 200 GeV using the principal component analysis (PCA) method has also been presented. The particle production mechanisms and initial state and geometry of the system are highly entangled and structures in the initial collision zone is a matter of intense investigation, both from theory and experimental points of views, in high-energy heavy-ion collisions. The main scope of the study in this thesis is to probe the initial conditions by using the method of Principal Component Analysis, a simple method of unsupervised learning algorithm often used for reducing dimensions and for de-correlating multivariate data. A formalism to implement clusters at the partonic level in the string melting version of the AMPT model for PbPb collisions at $\sqrt{s_{\mathrm{NN}}}$

= 200 GeV has been presented which are then propagated through the AMPT hadronization scheme. The clusters are formed in two steps, first by bringing partons closer in positions to an extent defined by two parameters i.e., the radius of the partonic zone (R) and the scaling factor on the inter-partonic distance (df). In this study, the following values have been used as R = 2 fm, 5 fm and df = 0.05 and 0.1. Figure 3 shows the X-Y distribution of the partons before (left) and after (right) clustering. A thermal distribution to the cluster partons by tuning the

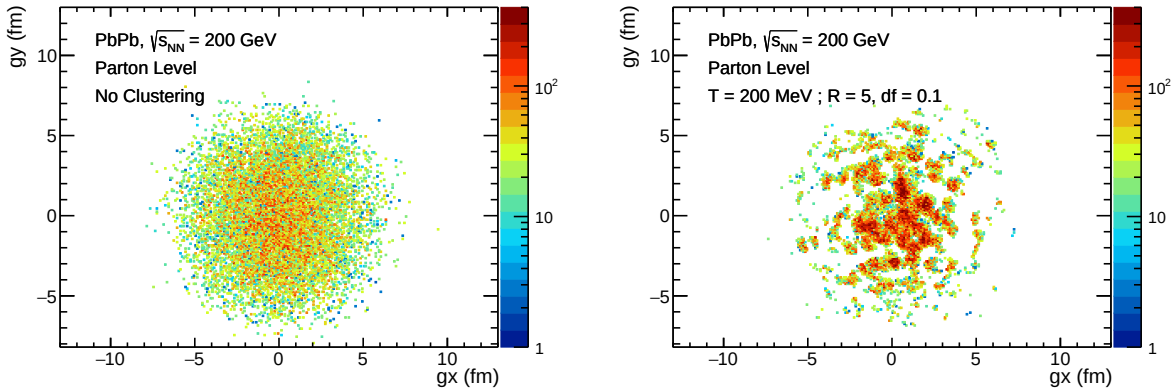

Figure 3: X-Y distribution of the partons before (left) and after (right) clustering

temperature parameters has been introduced, using two temperature values i.e., T = 200 MeV and T = 400 MeV. PCA method has been used on η, ϕ and p_{T} distributions of the produced charged particles before and after clustering. It is has been found that the first few prominent eigenvalues are sensitive to the inclusion of clustering for all the three distributions, however different sensitivity of the the eigenvalues to position and temperature clustering has been found. The centrality dependence of the first two eigenvalues has also been reported. This study has been recently published in [15].

References

[1] J. Greensite, An introduction to the confinement problem, vol. 821. 2011.

[2] L. C. P. Van Hove, "Theoretical prediction of a new state of matter, the 'quark-gluon plasma' (also called 'quark matter'),". `https://cds.cern.ch/record/183417`.

[3] K. Yagi, T. Hatsuda, and Y. Miake, Quark-gluon plasma: From big bang to little bang, vol. 23. 2005

[4] BRAHMS Collaboration, Nucl. Phys. A 757 (2005) 1-27; PHOBOS Collaboration, Nucl. Phys. A 757 (2005) 28-101; STAR Collaboration, Nucl. Phys. A 757 (2005) 102-183; PHENIX Collaboration, Nucl. Phys. A 757 (2005) 184-283

[5] "The Latest from the LHC : Last period of proton running for 2010. ? CERN Bulletin" Cdsweb.cern.ch. 1 November 2010. Retrieved 17 August 2011.

[6] ALICE Collaboration, Eur. Phys. J. C 74 no. 9, (2014) 3054; ALICE Collaboration, Phys. Lett. B 804 (2020) 135377.

[7] STAR Collaboration, Nucl. Phys. A 757 (2005) 102-183

[8] ALICE Collaboration, 40th International Conference on High Energy Physics. 11, 2020, arXiv:2011.06291 [nucl-ex].

[9] ALICE Collaboration, Phys. Lett. B 728 (2014) 216-227 [Erratum: Phys.Lett.B 734, 409?410 (2014)]

[10] CMS Collaboration, JHEP 09 (2010) 091; CMS Collaboration Phys. Lett. B 765 (2017) 193–220

[11] ALICE Collaboration, Nature Phys. 13 (2017) 535–539

[12] ALICE Collaboration, JHEP 09 (2015) 148; ALICE Collaboration, Eur. Phys. J. C79 no. 10, (2019) 857

[13] ALICE Collaboration, Phys. Lett. B 810 (2020) 135758; ALICE Collaboration, Phys. Lett. B 753 (2016) 319-329

[14] ALICE paper in preparation : "Inclusive and multiplicity dependent production of heavy-flavour hadron decay electrons in pp and p-Pb collisions" https://alice-publications.web.cern.ch/node/6090

[15] S. Acharya, S. Chattopadhyay, Phys. Rev. C 103, 034909 (2021)

Doctoral Committee:

S. No	Name	Designation	Signature	Date
1.	Dr. Jane Alam	Chairman		7/7/2021
2.	Dr. Subhasis Chattopadhyay	Guide/Convener		7/7/21
3.	Dr. Anand Kumar Dubey	Member		07/07/21
4.	Dr. Sourav Sarkar	Member		07/07/2021
5.	Dr. Sidharth Prasad	Member		07/07/2021

Chapter 1

Introduction

1.1 Motivation

High-energy physics deals with the physics of basic constituents of matter and the interactions between them, and is studied experimentally through collisions of highly energetic particles (leptons, hadrons, nuclei). While on one hand, higher collision energy explores the formation of particles and aims to study their properties, including the structure, on the other hand, nuclear collisions at higher energies helps to explore the nuclear matter under extreme conditions of temperature and density. Nuclear matter under extreme conditions is studied by colliding ions of heavy nuclei (e.g Au–Au, Pb–Pb) at relativistic energies. The mathematical construct that explains so far the particle physics is known as the Standard Model[1], which consists of the following elementary particles: 6 leptons (e, μ, τ, ν_e, ν_μ, ν_τ), 6 quarks (u, d, c, s, b, t), 4 gauge bosons (g, γ, Z, $W^{\pm}$) and one scalar boson (Higgs). They interact among themselves through three interactions (strong, weak and electromagnetic forces). The mathematical formulation of the Standard Model is a combination of the electroweak theory and the quantum chromodynamics (QCD). While the electroweak theory is a generalization of the quantum electrodynamics (QED), the theory of electromagnetic

[1] A recent landmark measurement confirming a difference with the standard model has been announced by Fermilab's Muon g-2 experiment [1].

interactions, unifying it with the weak nuclear force, the Quantum chromodynamics is used to describe the strong nuclear forces between quarks and gluons. These quarks and gluons are fundamental strongly interacting particles that make up composite hadrons such as the proton, neutron, pion and other hadrons. QCD exhibits two main properties through which quarks are gluons are confined together to make the hadrons, which are as follows [2].

- Color Confinement : Color-charged particles, such as quarks cannot be detected individually and are confined with other quarks via gluons, the strong force mediator, to form composite particles known as hadrons.

- Asymptotic Freedom : The potential between a quark and an anti-quark incorporates both the Coulomb force and a linear force [3]. It has the following form:

$$V \approx \frac{-\alpha_s(r)}{r} + kr$$

  where k is the colour string tension and α_s is the strong interaction coupling constant. The value of α_s is however not a constant and it is considered an effective or running QCD coupling constant. As the distance between the quark and anti-quark pair increases, the interaction strength between them increases. If the energy imparted to separate the quarks increases sufficiently to form a new "quarks anti-quark" pair, a new colourless hadron is formed. At very short distance (less than the size of the nucleon), the effective coupling strength between quarks decreases logarithmically and becomes very small. Under such conditions, quarks and gluons appear to be quasi-free. This phenomenon is known as the asymptotic freedom.

However, it is predicted that, in nuclear matter, this phenomenon of colour confinement is valid only up to a certain nuclear density and temperature [2]. At sufficiently high energy density and/or baryo-chemical potential, a transition is expected from a confined state of nucleons containing valence quarks and gluons to a state of deconfined quarks and gluons (from their individual nucleons) covering the entire volume of nuclear matter or a volume

with many units of the characteristics length scale (λ_{QCD}). This state, known as the Quark-Gluon Plasma (QGP) [4], is expected to be in local thermal and chemical equilibrium. The basic properties of QGP are (i) local equilibrium of matter and (ii) deconfinement of color over the nuclear volume, making quarks and gluons as the effective degrees of freedom in place of nucleons.

In nature, the QCD matter is presumed to be deconfined into the state of QGP under two scenarios of extreme conditions i.e. high temperature (via heating) or high net-baryon density (via compression). The early universe, a few microseconds after the Big Bang, is believed to have been in a state of such deconfined quark and gluon at high temperatures and zero baryo-chemical potential [5,6]. The QGP matter at high net-baryon density formed due to compression of nuclear matter might be present inside the cores of neutron stars [7].

Such systems of extreme temperatures resembling that of the early universe have been created in the laboratories such as the Large Hadron Collider Experiment (LHC) at CERN, Relativistic Heavy Ion Collider (RHIC) at BNL by colliding beams of heavy-nuclei e.g, gold (Au), lead (Pb) at ultra-relativistic velocities. These collisions generate an extremely high temperature ($\sim 10^{12}$ K) and energy density (~ 3 GeV/fm^3) [8] required for the deconfinement of the QCD matter and subsequent equilibration to form the quark-gluon plasma. An indication of the new phase of matter has first been reported by the fixed target heavy-ion experiment at the Super Proton Synchrotron (SPS) at CERN in lead-lead collisions (Pb–Pb) at energy per nucleon-nucleon pair ($\sqrt{s_{\rm NN}}$) up to 17.3 GeV in the center of momentum frame [9]. The first confirmation of the formation of QGP in gold-gold (Au–Au) collisions at $\sqrt{s_{\rm NN}} = 200$ GeV has been provided by experiments at RHIC in 2005 [10–13].

The experimental studies of the formation of quark-gluon plasma in these heavy-ion collisions also provide an in-depth understanding and knowledge about the mechanism of the production of particles and their properties. Since, the heavy-ion collisions recreate droplets of the Big-Bang matter, they are commonly known as “little bangs” or “mini-bangs”. The macroscopic properties of such systems, such as the temperature, pressure, volume, entropy

are studied using the properties of the produced particles for a thermodynamically equilibrated system. For attaining equilibrium, the volume has to be reasonably large ($\gtrsim \lambda_{QCD}$). From this thermodynamical point of view, the general condition suggests that only heavy-ion collisions can provide the large volume and long scattering time, prerequisite for the formation of a QGP medium. Although there is no clear demarcation separating heavy-ions from light-ions, the term "heavy" implies nuclei or ions with large number of protons (nucleons), in $\sim$ order of 100, which have extended dimensions required for equilibration to happen. Owing to the significantly smaller dimension of a proton, the formation of any QGP-like medium is not expected in a proton-proton (pp) collision. Typically, pp collisions were used as a no-QGP reference for studying QGP related signals in heavy-ion collisions. However, recent results at LHC [14–19] have revealed certain unexpected characteristic signatures of a QGP-like medium in pp collisions, which are usually observed in relativistic heavy nucleus-nucleus collisions. These unusual results in pp collisions compel us to rethink about the scenarios of particle formation at such high energies. Details on these unexpected signatures are discussed in section 1.4 of this chapter.

1.2 Relativistic heavy-ion collisions

The first picture of the space-time evolution of the relativistic heavy-ion collisions was proposed by J. D. Bjorken in 1983 [8], using the concept of hydrodynamic at the central rapidity. For simplicity, the central collisions (i.e., zero impact parameter) of identical nuclei in their center-of-momentum frames have been considered. In a nucleon, the valence quarks, e.g., up and down quarks in a proton, are distributed such that the probability distribution of finding a parton peaks around $x \sim 0.2$ and vanishes at $x \to 0$ or 1, in which x is known as the Bjorken scaling variable determining the fraction of proton momentum carried by the quarks. The sea quarks and gluon distributions shoot up at $x \to 0$. As the nuclei travel at a momentum $\gg$ their rest mass, they are Lorentz contracted in the longitudinal direction

(parallel to the beam axis) by a factor of $\sim 2R/\gamma$, where R is the nuclear radius and γ is the Lorentz factor. As the nuclei collide and start moving in opposite directions, the high-x partons move along leaving the low-x partons behind. A large number of virtual quanta are created at the mid-rapidity region from the cloud of the low-x partons of the nuclei. These virtual quanta need a finite time to decohere and turn into real quarks and gluons. Hence, it is assumed that the nuclei interpenetrates each other, as if they are transparent, forming the central plateau region through de-confinement of color strings. As the nuclei move away from each other after the interaction, central plateau region starts expanding longitudinally. This implies a symmetry in rapidity allowing for a simpler solution to the hydrodynamical equation. It is also hypothesized that the crossing time ($\tau_{\rm cross}$) is smaller than the time scale of the strong interaction($\tau_{\rm strong} \sim 1/\Lambda_{QCD} \sim 1$ fm/c) to ensure that the partons generated from the interactions are created after the parent nuclei have crossed each other. The crossing time is defined as $\tau_{\rm cross} = 2$ R/γ. This condition of $\tau_{\rm cross} \ll \tau_{\rm strong}$ requires $\sqrt{s_{\rm NN}} > 25$ GeV and are satisfied at the RHIC and LHC energies in Au-Au and Pb-Pb collisions [20]. The Lorentz factor ($\gamma = \sqrt{s_{\rm NN}}/2m_0^2$) reaches values of ~ 100 for 200 GeV collisions and ~ 1380 for 2.76 TeV collisions at the RHIC and LHC energies respectively.

Figure 1.1 illustrates the space-time evolution (1+1 dimensions) of a heavy-ion collision described by the Bjorken picture. The abscissa and ordinate are the beam direction (z-direction) and the time axis respectively. The coordinates are chosen such that the two nuclei travel towards each other along the z-direction and collide at the origin at time t = 0. The curves are hyperbolas of constant proper time ($\tau = \sqrt{t^2 - z^2}$). The different stages of the space time evolution of the system after collision are given by the different hyperbolas and are enumerated below:

1. **Pre-equilibrium (0 $< \tau <$ 1-2 fm/c)** i.e., Semi-hard particle production and Non-equilibrium QGP :

   After the collision at $\tau = 0$, the virtual quanta formed decohere and turn into real partons. These partons start interacting amongst each other. This stage is dominated

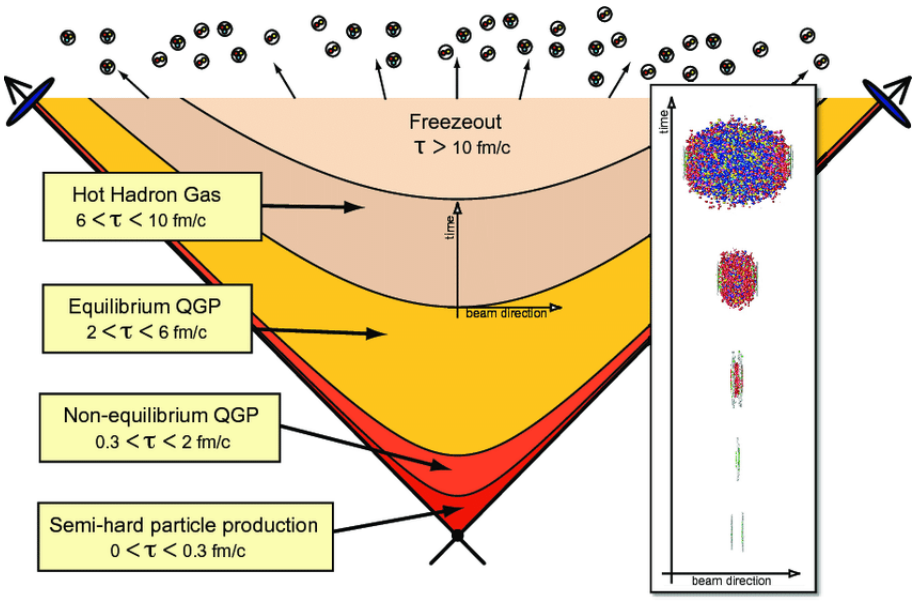

Figure 1.1: The Bjorken scenario for ultra-relativistic heavy-ion collisions, leading to the creation of strongly-interacting dense and hot deconfined matter, the so-called Quark-Gluon Plasma (QGP). Figure from [21]

by hard particle production. The earliest times after the impact are described by various models, prominent ones include the Color Glass Condensate (CGC) [22, 23] and the Glasma [24], where the nuclei before collisions are characterized as color glass condensates and the initial state formed after these condensates collide as the Glasma.

2. **Quark-Gluon plasma formation and hydrodynamic expansion (1-2 fm/c $< \tau <$ 6 fm/c)**:

   When the energy density of the system is high enough, the partons formed interact amongst themselves a multiple number of times and the system approaches local thermal equilibrium. The thermalization time is of the order of 1 fm. The system starts expanding due to the pressure gradient and consequently cools down. The system can be studied by applying viscous hydrodynamics with partonic degrees of freedom.

3. **Hadron Gas (6 fm/c $< \tau <$ 10 fm/c)**:

   The expanding system begins to cool with time. When the temperature falls below a certain critical temperature, hadronization begins. Once all the quarks and gluons

are confined to hadrons, the expanding system of hadrons is known as the hadron gas.

4. **Freeze-out ($\tau >$ 10 fm/c)**:

   The expanding system of hadrons finally "freezes out", implying that the hadrons stop interacting. Freeze-out occurs in two stages, chemical and kinetic freeze-out. At chemical freeze-out, inelastic interactions between hadrons ceases and the relative abundances of the hadrons gets fixed. After further expansion, the elastic collisions among hadrons stop and the hadrons freely stream towards the detectors.

It is evident here that, as the lifetime of the QGP state is of the orders of few fm/c ($\sim 10^{-23}$ sec), what are accessible by the detectors are information from the final state particles produced from these collisions and not directly of the deconfined quarks and gluons state. Experimentalists deduce the formation of the QGP and the initial properties of the collisions by studying these produced particles. Some of the key experimental observables used to characterize the QGP are presented in Section 1.3 of this chapter.

1.3 Experimental observables as signals of QGP in heavy-ion collisions

The evidence collected from the detector, although indirect, since it stems from the measurement of particles which have undergone significant re-interactions between the early collision stages, is currently the only way of studying the QGP formed, if any. To affirm the formation of quark-gluon plasma in such collisions, one needs to substantiate among others, that a local thermal equilibrium has been obtained. The probes of the QGP formation can be split based on the properties of the produced particles into two main groups, "hard" and "soft", depending on the stage of the collision when the particles are produced. The "hard" probes are related to the effect of the medium on the probes which are created at the initial hard parton scattering, such as heavy-flavour particles, jets, direct photons etc. Two interesting signatures based on the hard probes, among others, the *nuclear modifica-*

tion factor of high p_{T} particles and *jet quenching* are discussed below in this thesis. The observables of QGP formation based on soft probes explore the bulk properties of the system before and during hadronization, such as the energy density or the collective behaviour of the system. The soft signatures discussed in this thesis are *anisotropic flow* and *strangeness enhancement*.

1.3.1 Anisotropic Flow

The invariant cross section of the final state particles produced in relativistic collisions can be Fourier decomposed as:

$$E\frac{\mathrm{d}^3N}{\mathrm{d}^3p} = \frac{1}{p_{\mathrm{T}}}\frac{\mathrm{d}^3N}{\mathrm{d}p_{\mathrm{T}}\mathrm{d}y\mathrm{d}\phi} = \frac{\mathrm{d}^2N}{p_{\mathrm{T}}\mathrm{d}p_{\mathrm{T}}\mathrm{d}y}\Big[1 + \sum_{1}^{\infty} 2v_n\cos(n\phi)\Big] \tag{1.1}$$

$$v_n = \langle\cos(n\phi)\rangle \tag{1.2}$$

where, $p_{\mathrm{T}} = \sqrt{p_{\mathrm{x}}^2 + p_{\mathrm{y}}^2}$ is the transverse momentum, $y = \frac{1}{2}\ln\Big(\frac{E+p_{\mathrm{z}}}{E-p_{\mathrm{z}}}\Big)$ is the rapidity and ϕ $= \tan^{-1}(p_{\mathrm{y}}/p_{\mathrm{x}})$ is the azimuthal angle (with respect to the reaction plane). The x-z plane during an ion-ion collision is known as the reaction plane. The leading term in the brackets in equation 1.1 represents the azimuthally symmetric radial flow. The term v_n characterizes the azimuthal anisotropy and can be studied as a function of p_{T} and y. v_1 is known as the coefficient for directed flow, v_2 for elliptic flow, v_3 for triangular flow and so on. When a non-central collision (non-zero impact parameter) between two nuclei of finite size occurs, the resulting overlapping region forms an almond-shaped area. As a consequence, a spatial anisotropy is formed in the azimuthal plane at the initial stage of the collision. The spatial anisotropy contributes to a pressure gradient along the transverse plane. The transverse momentum of the newly formed particles is distributed isotropically, implying $v_n^{\mathrm{initial}} = 0$. If these particles do not interact amongst themselves, the final azimuthal distribution should be isotropic as well ($v_n^{\mathrm{final}} = 0$). If the particles interact with each other multiple times,

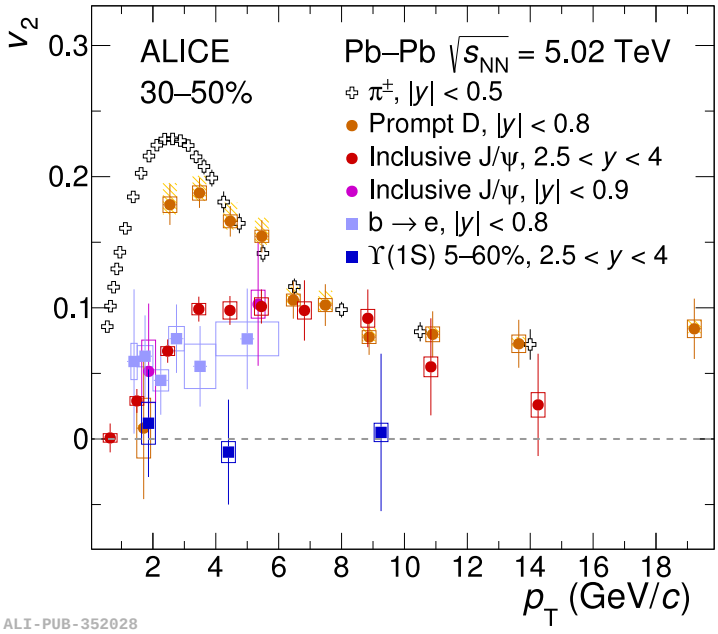

Figure 1.2: Elliptic flow coefficient (v_2) as a function of p_{T} for charged pions, non-strange D mesons, inclusive J/ψ, electrons from beauty-hadron decays, and Υ(1S) in 30-50% central Pb–Pb collisions at $\sqrt{s_{\mathrm{NN}}} = 5.02$ TeV [25]

the anisotropy in the pressure gradient of the non-uniform shaped initial state leads to a momentum anisotropy in the final state particles. More matter is pushed outwards in the direction of the steeper pressure gradient thus leading to a non-zero v_2. Ample number of re-scattering at the early stages which produces a positive v_2 also most likely ensures that a local equilibrium in the medium has been attained. This strong collective behaviour, comparable to that of fluids, is known as **collectivity** or **collective effect**. Thus, anisotropic flow is one of the signatures of collectivity in the strongly interacting thermalized medium formed during collisions.

Figure 1.2 shows the elliptic flow coefficient v_2 as a function of p_{T} for charged pions, non-strange D mesons, inclusive J/ψ, electrons from beauty-hadron decays, and Υ(1S) in 30–50% central Pb–Pb collisions at $\sqrt{s_{\mathrm{NN}}} = 5.02$ TeV [25]. Mass ordering ($v_2^{\mathrm{light-hadron}}(p_{\mathrm{T}}) > v_2^{\mathrm{heavy-hadron}}(p_{\mathrm{T}})$), due to radial flow, is visible for $p_T \lesssim 4$ GeV/c. Radial flow provides an outward kick to the emerging hadrons, thus depleting the low p_{T} region by shifting the low p_{T} hadrons to higher p_{T}. The heavier the hadron, the more momentum kick it receives.

Elliptic flow (positive values of v_2) provides the measure of degree of thermalization at low p_{T} whereas at high p_{T} it provides information of the path length dependence of the parton energy loss in the medium. v_2 builds up early in the collision when the spatial anisotropy is significant. With the expansion of the system, v_2 tends to saturate as the spatial anisotropy continues to decrease. This is unlike radial flow, which is sensitive to the evolution of the system at the early as well as the late stages after the collision and continues to grow until freeze-out. Thus, v_2 provides a signature of pressure and the measure of the degree of thermalization of the matter produced early in the collision. Higher order flow harmonics are theorized to originate due to event-by-event fluctuations in the initial distribution.

1.3.2 Nuclear Modification Factor

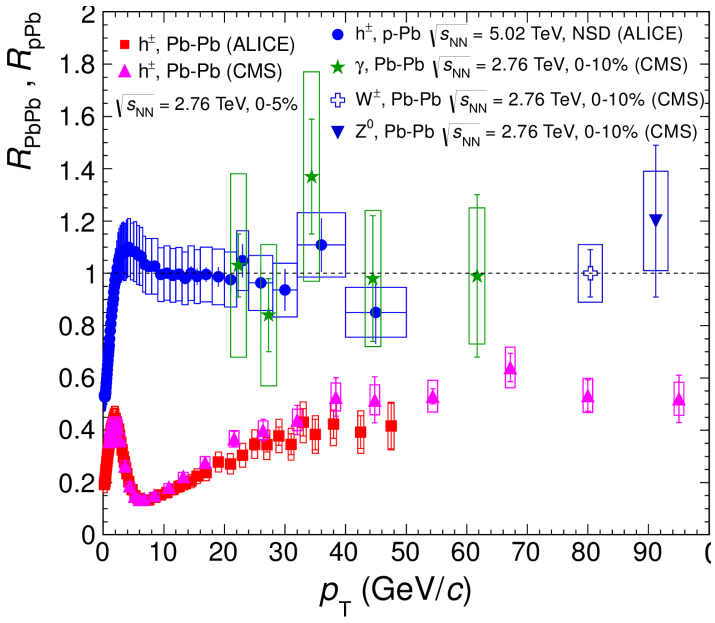

Figure 1.3: Transverse momentum dependence of nuclear modification factor of charged particles ($\mathrm{h}^{\pm}$), γ, $\mathrm{W}^{\pm}$ and Z^0 for Pb–Pb central collisions at $\sqrt{s_{\mathrm{NN}}} = 2.76$ TeV and charged particles for p-Pb at $\sqrt{s_{\mathrm{NN}}} = 5.02$ TeV [26].

The nuclear modification factor (R_{AA}) is the ratio of the p_{T}-spectra for nucleus-nucleus (AA) collisions with respect to the p_{T}-spectra for proton-proton (pp) collisions scaled with

the number of binary nucleon-nucleon collision in AA ($N_{\rm coll}$). It is defined as

$$R_{AA}(p_{\rm T}) = \frac{{\rm d}^2N/{\rm d}p_{\rm T}{\rm d}y|_{AA}}{N_{\rm coll}\ {\rm d}^2N/{\rm d}p_{\rm T}{\rm d}y|_{\rm pp}} \tag{1.3}$$

In a strongly interacting medium, particles which interact with the medium loose their energy through multiple elastic and inelastic collisions [27–29]. Hence, a suppression in the yield is expected, i.e., $R_{\rm AA}$ <1, assuming no medium is formed in pp collisions. In the absence of a QCD medium, nuclear modification factor is expected to be close to unity. Figure 1.3 shows the the nuclear modification factor ($R_{\rm PbPb}$, $R_{\rm pPb}$) as a function of $p_{\rm T}$ of charged particles ($h^{\pm}$), isolated photons and electro-weak bosons $W^{\pm}$ and Z^0 for Pb–Pb central collisions at $\sqrt{s_{\rm NN}}$ = 2.76 TeV and charged particles for p–Pb at $\sqrt{s_{\rm NN}}$ = 5.02 TeV [26]. While a suppression in the charged hadrons is seen in central Pb-Pb collisions, photons and W, Z bosons (which stem from very early phases of collision) are not suppressed as they do not carry color charges and interact via electromagnetic forces. This further

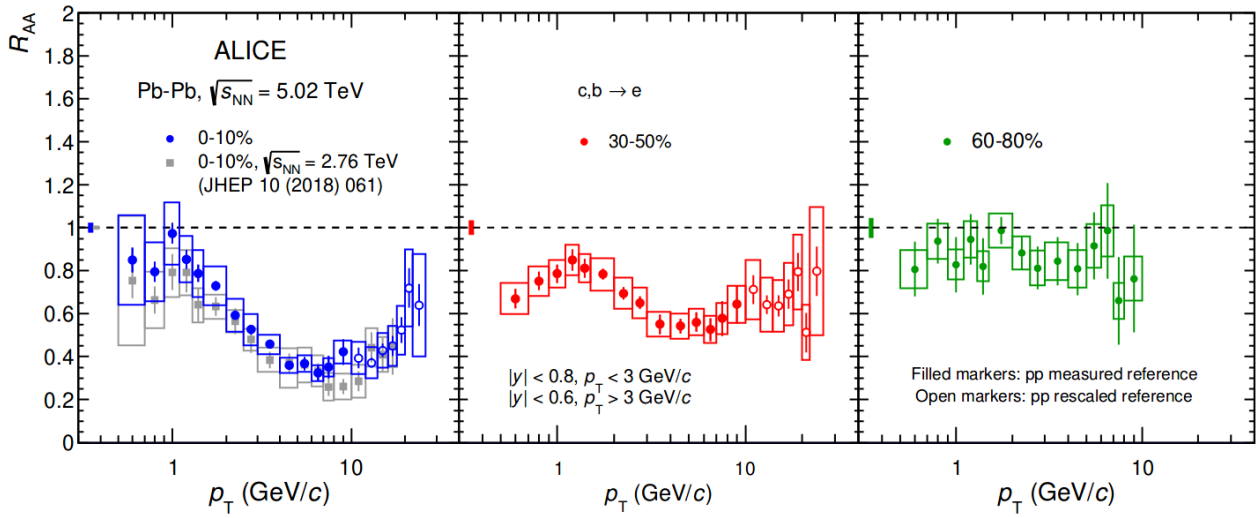

Figure 1.4: Transverse momentum dependence of nuclear modification factor of electrons decayed from heavy-flavour hadrons for Pb–Pb central collisions at $\sqrt{s_{\rm NN}}$ = 5.02 TeV in three different centrality classes [30].

solidifies the argument that a strongly interacting medium is formed in the collisions. The $R_{\rm pPb}$ measurement also shows no indication of nuclear matter modification and at high $p_{\rm T}$ is comparable with unity. Figure 1.4 shows the nuclear modification factor of electrons

from decays of heavy-flavour hadron measured in central (1-10%), semi-central (30-50%), and peripheral (60-80%) Pb–Pb collisions at $\sqrt{s_{\rm NN}} = 5.02$ TeV [30]. The study of nuclear modification factor of electrons from decays of heavy-flavour hadron provides a direct access to the in-medium energy loss of the charm and beauty quarks. The clear dependence of $R_{\rm AA}$ on centrality implies that partons lose more energy in central collisions than that in peripheral. The partonic energy loss depends on medium density, being higher for denser and bigger systems. Hence, this observation is highly in agreement with the conjecture that a larger and denser medium is formed in the most central collisions compared to that in the peripheral ones.

1.3.3 Di-hadron Azimuthal Correlation and Jet Quenching

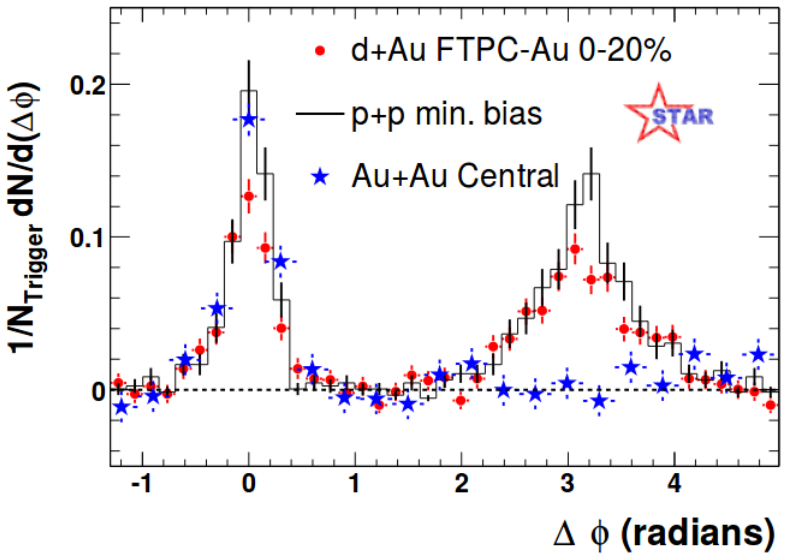

Figure 1.5: Dihadron azimuthal correlations with trigger hadron $p_{\rm T} > 4$ GeV/c and associated hadron $p_{\rm T} > 2$ GeV/c in pp, Au–Au and d–Au collisions at $\sqrt{s_{\rm NN}} = 200$ GeV with the STAR experiment [13]

Jets are the collimated sprays of particles created from the fragmentation of partons. Jets of high transverse momenta are produced at the early stages and they traverse through the entire medium through its evolution. Jets lose energy through gluon radiations and multiple collisions with the medium, and hence the process is dubbed a **jet quenching**. The di-

hadron azimuthal correlation study is used to study back-to-back high momenta jets formed near the edge of the fireball of the QCD medium. One of the jets is emitted away from the fire ball (leading jet), while the other jet emanates in the opposite direction in the transverse plane through the fireball medium. The jets measured in $\Delta\phi = \phi_{\text{trigger}} - \phi_{\text{associated}} \sim 0$, known as the near side jets, travel the shorter path in the medium. Trigger particles (used as proxy for leading particle) and associated particles are chosen within specific p_{T} ranges depending on the analysis. The away-side jet at $\Delta\phi \sim \pi$ spans through the entire medium, losing most of its energy. Figure 1.5 shows the di-hadron azimuthal correlations in pp, Au–Au and d–Au collisions at $\sqrt{s_{\text{NN}}} = 200$ GeV with the STAR experiment. Particles with $p_{\text{T}} > 4$ GeV/c have been selected as trigger and associated particles were chosen with $p_{\text{T}} > 2$ GeV/c. In Au–Au collisions, the away side jet is almost quenched while no such suppression of high p_{T} jets is observed for d–Au and pp collisions, which again corroborates the statement on medium formation and its size as discussed in the previous subsection 1.3.2. Figure 1.6

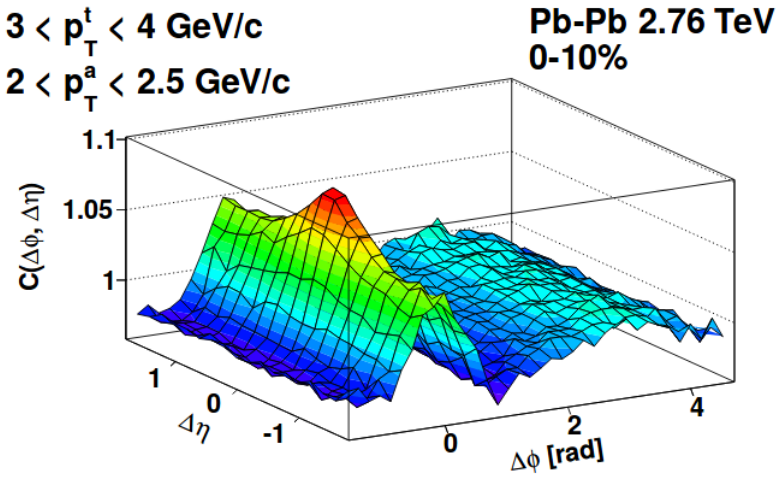

Figure 1.6: Two-particle correlations function for central Pb-Pb collisions at low to intermediate transverse momentum with the ALICE experiment[31]

shows the two-particle correlation function C($\Delta\phi$,$\Delta\eta$) for the central Pb–Pb collisions at $\sqrt{s_{\text{NN}}} = 2.76$ TeV at low to intermediate transverse momentum with the ALICE experiment [31]. The short range correlation region is characterized by $\Delta\eta = \eta_{\text{trigger}} - \eta_{\text{associated}} \sim 0$, while distributions at large $\Delta\eta$ are referred to as the long-range correlations. The anisotropy

flow coefficients (v_n) of various orders can also be calculated from the azimuthal correlation function.

1.3.4 Strangeness Enhancement

The idea of strangeness enhancement as a signature for Quark Gluon Plasma formation was first mentioned in [32] and subsequently discussed in [33, 34]. It was found that the $s\bar{s}$ is dominantly produced in QGP by the gluonic ($gg \rightarrow s\bar{s}$) channel. The strangeness enhancement in QGP is expected due to its high gluon density at RHIC and LHC energies. The mass of the strange quark ($\sim$ 150 MeV) being similar to the critical temperature (T $\sim$ 170 MeV) for the QCD phase transition, it reaches equilibrium before the change of phase of the QGP matter. Additionally, the process of Pauli blocking of the light quarks (u, d) plays a role in the enhanced formation of the strange quark pairs. All quarks being fermions follow Pauli Exclusion Principle. As more and more up and down quarks are formed in the collision, they fill up the lower Fermi energy levels, thus making the production of $s\bar{s}$ pair more favourable. Thus, the quark gluon plasma should be made of gluons, u, d as well as s quarks and an enhancement of strange hadrons compared to other light hadrons is excepted in collisions where a QGP medium is predicted to form. Experimental observation on strangeness enhancement from the ALICE experiment in Pb-Pb collisions at $\sqrt{s_{\rm NN}}$ = 2.76 TeV can be found in [35].

1.4 Novelty in pp collisions: Multiplicity dependent experimental observables

Proton-proton (pp) collision is the simplest hadronic system for investigating nuclear matter effects. Conventionally, proton-proton collisions have been used to study a diverse scope of particle physics and the Standard Model, including the landmark discovery of the Higgs boson in 2012 [36,37], for which the Noble prize for physics was awarded to physicists Peter

Higgs and François Englert for their theoretical predictions. Traditional wisdom holds that a typical proton-proton collision is too dilute to produce a fluid-like state. Formation of such a state needs a larger volume and longer thermalization time than what a pp collision can offer. However, measurements in the last decade at LHC have revealed certain signals of a QGP-like medium in high multiplicity pp collisions, few of which mentioned in this section, have prompted to a better understanding of the medium formation and particle production mechanisms in such collisions. Figure 1.7 shows a comparison of the two-

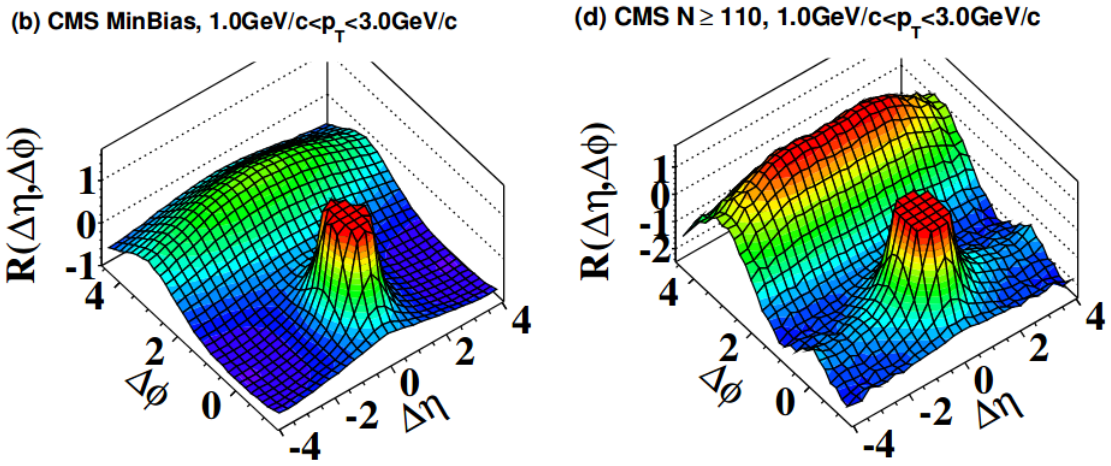

Figure 1.7: 2-D two-particle correlation functions in minimum bias (left) and high multiplicity (right) pp collisions at $\sqrt{s} = 7$ TeV with the CMS experiment [14]

particle correlation functions in minimum bias and high multiplicity pp collisions at $\sqrt{s} = 7$ TeV with the CMS experiment [14]. An enhanced structure on the near side of the $\Delta\phi$-$\Delta\eta$ correlation functions which extended over a large $\Delta\eta$ (≈ 4) was first observed in the high multiplicity pp collisions (right) while it was not present in the minimum bias sample (left). Such long range, near side structures are known as **ridges**. The ridge structure has previously been observed in heavy-ion collisions from RHIC to LHC and is also seen in figure 1.6. These long range correlation are conjectured to arise from hydrodynamic collective flow of a strongly interacting medium.

Further evidences of collectivity has been reported in pp collisions at $\sqrt{s} = 5$, 7, 13 TeV using multiplicity dependent measurements of angular correlations [15]. The second-(v_2),

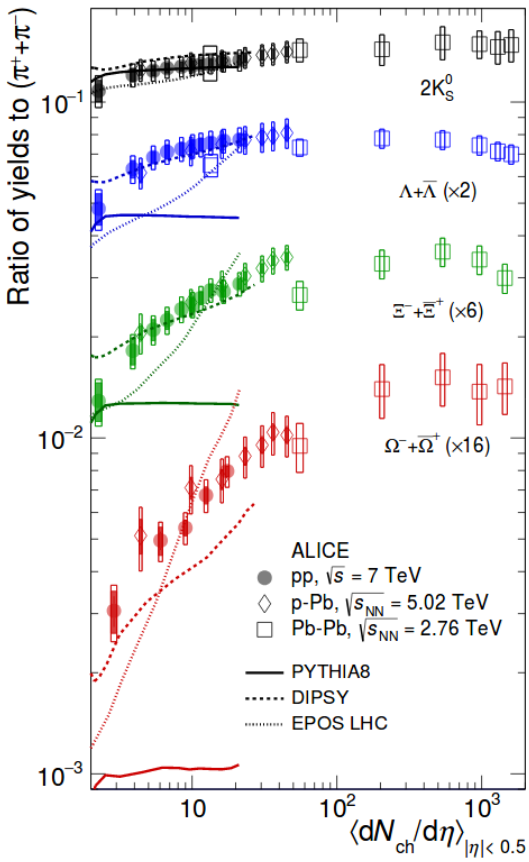

Figure 1.8: p_{T}-integrated ratio of strange hadrons to pions as a function of average charge particle multiplicity density in pp collisions at $\sqrt{s} = 13$ TeV with the ALICE experiment [16]

third-(v_3) and higher order azimuthal anisotropy harmonics of unidentified and few identified charged particles have been extracted from long-range two-particle correlations [15, 38]. A mass ordering for v_2 values has also been observed in high-multiplicity pp events.

Another important discovery is the observation of strangeness enhancement in high-multiplicity pp collisions at $\sqrt{s} = 13$ TeV [16] as shown in figure 1.8. The measurements are in wonderful agreement with p–Pb collision results and even reaches values similar to those observed in Pb–Pb collisions, thus indicating that the phenomenon is related to the final system created in the collision where a QGP is formed.

It is evident from these novel observations in pp collisions that the general understanding of the system formed after the collision and the particle production mechanism in such small system is still far from complete and multiplicity dependent studies of particle production in

high energy pp collisions is an important research topic required to further the understanding on these issues.

1.5 Heavy-flavour hadron production

A significant part of this thesis deals with the study on electrons decayed from the heavy-flavour hadrons. The spectra of electrons decayed from the heavy-flavour hadrons and its dependence on charged particle multiplicity, has been presented in this thesis. Hence, in this section, a brief motivation and introduction of heavy-flavour particles has been presented.

Open heavy-flavour hadrons, consisting of a single charm or beauty quark (and other light quarks), are one of the the key diagnostic tools available to study the dense, hot strongly interacting matter formed in relativistic collisions. The charm (c) and beauty (b) quarks known as *heavy quarks*, in contrast to the lighter u, d, s quarks, are produced at the early stages of the collision via hard scattering due to their large bare masses, $m_{\rm c} = 1.27^{+0.05}_{-0.11}$ GeV/c^2 and $m_{\rm b} = 4.29^{+0.18}_{-0.06}$ GeVc^2 [39] respectively, which exceed the QCD scale parameter $\lambda_{QCD} \sim 200$ MeV significantly. Hence, the production of a heavy quark-antiquark pair can be calculated under the perturbative QCD (pQCD) framework at all momenta, unlike the jets from light quark and gluons, which can only be treated perturbatively at high $p_{\rm T}$. The primary perturbative processes for heavy quark (Q) production are quark-anti-quark annihilation q+$\bar{\rm q}$ $\rightarrow$ Q+$\bar{\rm Q}$ and gluon-gluon fusion g+g $\rightarrow$ Q+$\bar{\rm Q}$ at the leading order, along with other higher order contributions [40]. Here, Q, $\bar{\rm Q}$ represents c, b and $\bar{\rm c}, \bar{\rm b}$ quarks respectively.

The word "perturbative" refers to a mathematical method of finding approximate solutions to a problem. If A is the full solution, $\rm A_0$ is the leading term, $\rm A_1$, $\rm A_2$, $\rm A_3$ the higher order terms, then the approximation to the full solution can be written as $A = A_0 + \beta A_1 + \beta^2 A_2 + \beta^3 A_3 + ...$ where β is a small number and for small β the higher-order terms in the series become successively smaller. The series converges iff β is sufficiently small

so that the higher order terms can be neglected. An approximate "perturbation solution" is obtained by truncating the series e.g., $A = A_0 + \beta A_1$.

In QCD, the running coupling constant α_s (which represents the constant β) is given by

$$\alpha_s(Q^2) = \frac{12\pi}{(11n_{\rm c} - 2n_{\rm f})\ \ln(Q^2/\lambda^2_{\rm QCD})}$$

where, Q^2 is the square of the momentum transferred in a hard scattering,

$\rm n_c$ is the number of colours,

$\rm n_f$ is the number of flavours,

$\lambda_{QCD} \sim 200$ MeV ~ 1 fm^{-1}

The masses of charm and beauty (and hence Q^2) being $\gg \lambda^2_{\rm QCD}$ ensures that α_s is small enough for pQCD to be applicable at all momenta. Consequently in pp collisions, measurement of heavy-flavour production provides a crucial testing ground for pQCD. More details on the estimation of yield utilizing pQCD framework, of such particles produced via hard scatterings, in pp collisions are discussed in section 1.5.1.

Additionally, measurements of open heavy-flavour in pp collisions provide a necessary reference for heavy-flavour studies in heavy-ion collisions, where the heavy quarks serve as effective probes for the produced hot and dense medium formed after collision. The production time of the heavy quarks[2]($\tau_c \sim 0.08$ fm/c, $\tau_b \sim 0.02$ fm/c) are much smaller than the QGP formation time (~ 1 fm/c). Because of their large masses, the charm and beauty quarks are mostly expected to be produced from the hard scatterings in the initial stages and their thermal production at a later stage is not significant at LHC energies. Hence, they act as cleaner probes of QGP through energy loss than light quarks, which can be generated at later during the evolution of the QGP system. After the heavy-ion collisions, as the system evolves, these heavy quarks propagate through and interact with the medium formed and a modification of the heavy-flavour yield is expected. This is the

[2]From the energy-time uncertainty principle we have $\Delta E \Delta T \geq \hbar/2$. Heavy quarks are produced in through hard scatterings in pairs of $Q\bar{Q}$. Hence, minimum energy for creation of $Q\bar{Q}$, $\Delta E \approx 2M_Q$ and $\tau = \Delta T = 1/2M_Q$

nuclear modification factor ($R_{\rm AA}$) and is discussed in section 1.3.2. Due to the energy loss of the heavy quarks, a softening of the $p_{\rm T}$ spectra with respect to pp collisions for heavy-flavour hadrons or their decay products is expected. The dominant sources of energy loss of heavy-flavour particles are radiative energy loss via medium induced gluon radiation and collisional energy loss via elastic scattering. In QCD, the energy loss through radiative process is not same for all partons. Quarks are expected to loss lesser energy than that by gluons, due to the dependence of energy loss on the colour coupling factor. Additionally, heavy quarks are expected to radiate less energy compared to that by the light quarks. The large mass of heavy quarks leads to the suppression of gluon radiation at forward angles. This is known as the dead cone effect [41] and points to the inference: $R_{\rm AA}^{u,d} < R_{\rm AA}^{c} < R_{\rm AA}^{b}$. Experimental observation of the nuclear modification of D mesons and charged particles in Pb–Pb collisions at $\sqrt{s_{\rm NN}} = 5.02$ TeV in ALICE [42] shows $R_{\rm AA}^{\rm charged-particles} < R_{\rm AA}^{\rm D-mesons}$ for all centrality classes. Measurement by the ATLAS collaboration shows that muons decayed from the charm hadrons are significantly more suppressed than those from the beauty hadrons for $p_{\rm T} \lesssim 8$ GeV/c [43]. Although, a strong conclusion at higher $p_{\rm T}$ has not been drawn due to large uncertainties of the measurement, model predictions have showed that $R_{\rm AA}$ for beauty is higher than for the charm.

1.5.1 Cross section calculation for heavy-flavour particles using the factorization theorem and pQCD

One of the primary results of this thesis is the measurement of the $p_{\rm T}$-differential production cross section of electrons decayed from the heavy-flavour hadrons. Hence, a brief overview of the steps of measurement of cross-section using perturbative QCD is presented in this section.

Proton-Proton Collision

An illustration of typically proton-proton collision is shown in figure 1.9 and the processes are listed below.

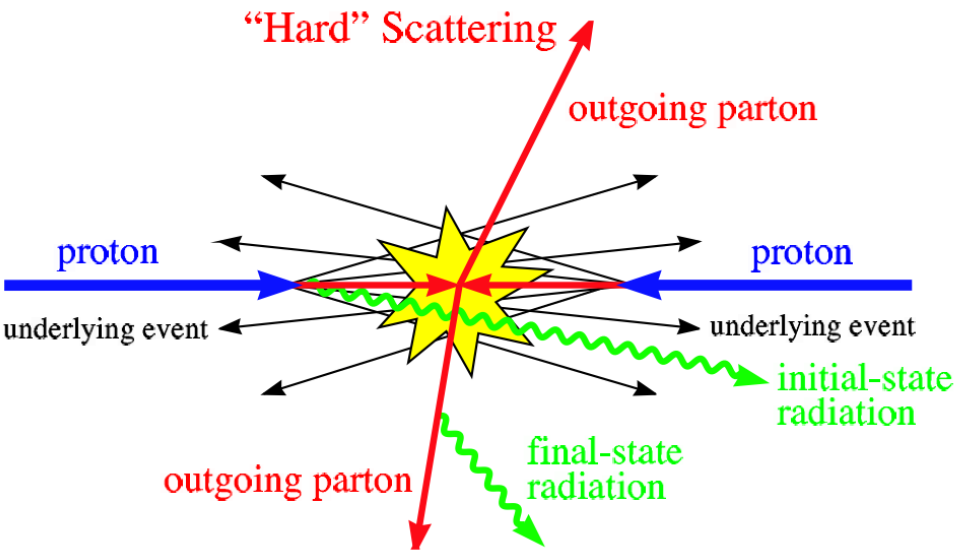

Figure 1.9: Illustration of a pp collision [44]

- **Incoming beam:** Two incoming proton-proton beams are characterized by the Parton Distribution Functions (PDFs).
- **Initial State Radiation:** The partons can emit showers e.g., q→gq or q→gg before interaction.
- **Interaction:** Hard, semi-hard or soft scattering processes occur.
- **Final State Radiation:** Branching of the outgoing partons.
- **Hadronization:** Hadronization is the process of the formation of the hadrons out of the quarks and gluons. After the collision, the outgoing quarks and gluons form colourless hadrons since they cannot exist individually due to colour confinement.

  Fragmentation: Fragmentation is a process of hadronization where high momentum quarks fragment into lower momentum partons. The fragmentation and the frag-

mentation functions are discussed in more details in this section below. Figure 1.10 illustrates a simple example where the quarks separate as the energy increases and becomes more than twice the mass of a quarks formed ($E_{string} > 2m_q$). The string (denoted by the line) breaks up into $q\bar{q}$ pairs and forms mesons.

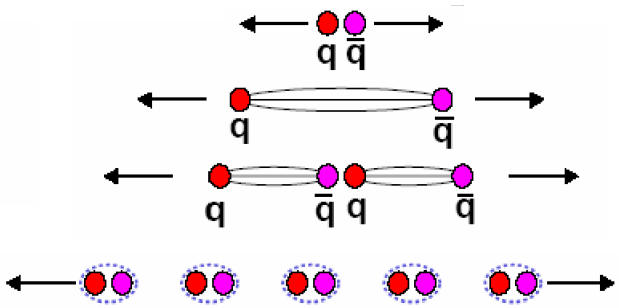

Figure 1.10: Illustration of hadronization process: String breaking up into $q\bar{q}$ pairs-fragmentation

Coalescence/Recombination: The coalescence process was introduced in [45–47] as a hadron production mechanism at intermediate p_T from the QGP formed at heavy-ion collisions. In the coalescence model, partons that are close to each other in phase space (position and momentum) are allowed to recombine into hadrons. There is no need to create a $q\bar{q}$ pairs via splitting/string breaking, unlike in the usual independent fragmentation processes.

The fragmentation and the recombination models are competing mechanisms and recombination naturally enhances baryon/meson ratios at intermediate p_T [48, 49]. Coalescence is dominant at low p_T while fragmentation seems to be dominant at high p_T. In pp collisions, the baryon over meson ratios [50] are found to be much higher than the predictions from models using the fragmentation fractions measured in e^+e^- collisions [51]. In recent predictions [52] coalescence plus fragmentation model, is found to provide a good description of the meson and baryon spectra and their ratio.

Factorization Theorem

In high-energy hadron-hadron collisions the production of hard scattered particles can be computed from the underlying parton-parton processes using the *factorization theorem*. The factorization theorem essentially states that the cross section of a hard collision is a factorisable quantity ($\sigma_{\mathrm{hard-coll}}$) and can be written as factors of parton density function (PDF), interaction cross section of the partons (σ_{int}) and fragmentation function (FF) i.e.,

$$\sigma_{\mathrm{hard-coll}} = PDF \otimes \sigma_{int} \otimes FF \tag{1.4}$$

The PDF and the FF represent the intrinsic constituents of the proton and the hadronization mechanism respectively. Since a proton has a very simple structure, protons have been used to study the PDF in experiments and has been used interchangeably with "nucleons" for the discussions in the section.

Considering a collision between two hadrons A and B which leads to the production of particle C : A + B → C + X, where X denotes all others particles formed. If `'a'` is a constituent parton of A and `'b'` a constituent parton of B, the reaction can be a result of scattering between the partons `'a'` and `'b'`. The parton-parton collision is denoted by a + b → c + X, where c is a high-p_{T} parton. This parton `c` subsequently fragments to give the final state hadron C (c → C + ...). Following the factorization theorem the cross section is given by:

$$\boxed{d\sigma^{hard}_{AB\to C} = \sum_{a,b} f_{a/A}(x_a, Q^2) \otimes f_{b/B}(x_b, Q^2) \otimes d\sigma^{hard}_{ab\to c}(x_a, x_b, Q^2) \otimes D_{c\to C}(z, Q^2)}$$

The parton distribution function (also known as the structure function) $f_{a/A}(x_a, Q^2)$, is the probability of finding a constituent parton `'a'` in particle `'A'` with momentum fraction x_a of parton `'a'` and a transverse momentum Q^2. Here, $x = \mathrm{P}_{\mathrm{parton}}$ / $\mathrm{P}_{\mathrm{nucleon}}$ is also called Bjorken-x. PDF is essentially the momentum distribution of quarks and gluons within their

proton bound state. Figure 1.11 shows the parton distribution functions for 'u' and 'd' quarks (denoted by xu_v and xd_v respectively), gluons (xg) and sea quarks (xS) [53]. The distributions of sea quarks and gluons were scaled down by a factor of 20. The peak of the

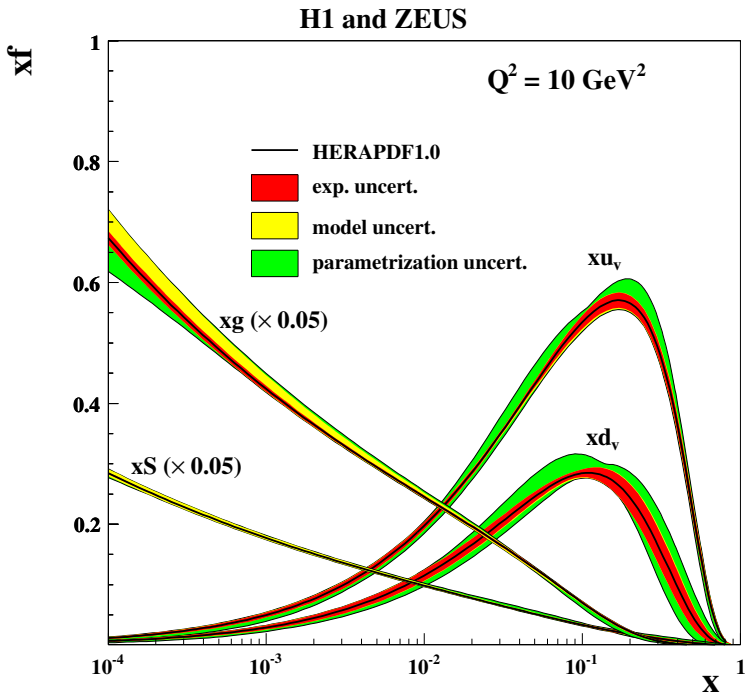

Figure 1.11: The parton distribution functions from HERAPDF1.5 NNLO [53]

valence quark distribution is approximately about x ≈ 0.2 while the probability increases of finding gluons with low fraction of momentum of the proton momentum. The fraction of the momentum carried by all quarks (valence + sea) was experimentally found by the CDHS experiment at CERN [54] to be ∼ 50 % of the proton momentum and the rest is due to the low energy gluons.

$d\sigma^{hard}_{ab\to c}$ is the interaction cross-section for the basic partonic process a + b → c + X. It is a perturbative matrix element and computable up to a given order in α_s. Few examples of QCD hard scattering subprocess are qq → qq , $q\bar{q}$ → gg, gg → gg , gg → $\gamma\gamma$ etc. The only leading order (LO) processes which contribute to heavy-flavour production are gluon fusion and quark anti-quark annihilation. For more precise calculation of the cross-section,

the next-to-leading order terms such as gluon splitting and flavour excitation are taken into consideration. Theoretical predictions for heavy-flavour cross-sections at fixed order with a next-to-leading-log re-summation (FONLL) of higher orders are available [55] and has been used for comparison with data results in chapter 3.

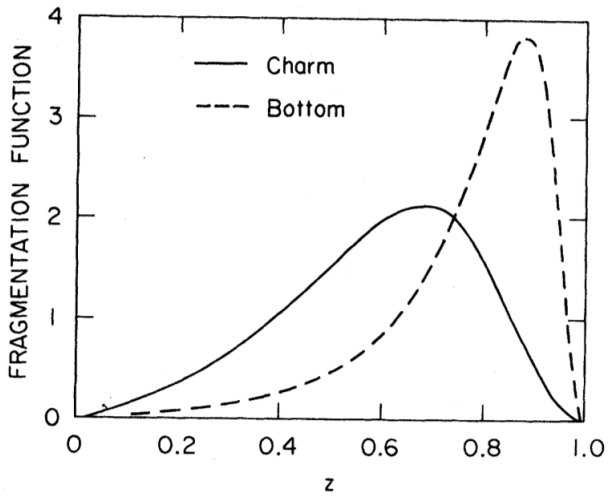

Figure 1.12: Fragmentation functions $D_c(z)$ and $D_b(z)$ using $\epsilon_c = 0.15$ and $\epsilon_b = 0.16$ [56]

$D_{c\to C}(z, Q^2)$ is the fragmentation function which indicates the probability density for finding a hadron **C** with the fraction of momentum z (P_{hadron} / P_{parton}) where **c** is the scattered parton. The Peterson fragmentation function [56] as shown in equation 1.5 is used for fragmentation of heavy quarks into hadrons containing heavy quarks by attaching a light antiquark $\bar{q}$ to a heavy quark Q for heavy meson ($Q\bar{q}$) or a di-quark qq for heavy baryon production (Qqq).

$$D_Q(z) = \frac{N}{z\left[1 - \frac{1}{z} - \frac{\epsilon_Q}{1-z}\right]^2} \tag{1.5}$$

ϵ_Q ($\sim m_q^2/m_Q^2$) is the ratio of the effective light and heavy-quark masses. N is a normalization factor and the fragmentation function follows the sum rule:

$$\sum_h \int z D_{c\to C}(z, q^2) dz = 1$$

Figure 1.12 shows the fragmentation functions $D_c(z)$ and $D_b(z)$ using the equation 1.5 and

$\epsilon_c = 0.15$ and $\epsilon_b = 0.016$. The fragmentation functions of the c-quarks and gluons into $D^\star$ mesons at the different Q^2 can be found at [57].

It may be noted here that typically only 1-2% of the produced heavy quark anti-quark pairs, instead of a pairing with other light quarks to form open heavy-flavour, form a bound quarkonium state e.g. $J/\psi(c\bar{c})$, $\Upsilon(b\bar{b})$ etc. The Dadfar fragmentation function is used for charm to J/ψ formation [58].

1.5.2 Open heavy-flavour measurements in experiments

Heavy-flavour particles have a very short life time (of the order of $\sim 10^{-12}$ s) and can not be detected directly. The only way is to study the heavy-flavour particles through the decayed final state particles. The decays of heavy-flavour particles can be classified into two main categories i.e., hadronic decay channel and semi-leptonic decay channel. In both the cases considered, the heavy-flavour hadrons decay via weak interaction into more stable non-heavy-flavour particle. In the hadronic channel, the parent hadron decays into two or more hadrons. Following are few examples of decays in the hadronic channel along with their branching ratios (BR) and decay lengths ($c\tau$) [39].

$D^0 \rightarrow K^-\pi^+$ BR $\sim 3.89\%$ $c\tau = 123 \pm 1$ μm

$D^+ \rightarrow K^-\pi^+\pi^+$ BR $\sim 8.98\%$ $c\tau = 312 \pm 2$ μm

$D_s^+ \rightarrow K^-K^+\pi^+$ BR $\sim 5.45\%$ $c\tau = 150 \pm 2$ μm

$D^{*+} \rightarrow D^0\pi^+$ BR $\sim 67.7\%$ $c\tau = (2.1 \pm 0.5) \times 10^{-5}$ μm

$\Lambda_c \rightarrow pK^-\pi^+$ BR $\sim 5\%$ $c\tau = 60 \pm 2$ μm

$B^0 \rightarrow J/\psi K_s^0$ BR $\sim 0.04\%$ $c\tau = 455 \pm 2$ μm

$B^+ \rightarrow J/\psi K^+$ BR $\sim 0.1\%$ $c\tau = 492 \pm 2$ μm

In this approach, the heavy-flavour hadrons are studied through full reconstruct of the decayed particles via invariant mass analysis. In ALICE experiment, the D-mesons and charmed baryons are studied through this channel in the mid-rapidity range. However, it is more difficult for beauty mesons due to low branching ratio. An alternate approach to

access the heavy-flavour hadron information is through the semi-leptonic decay channel, where the parent hadron decays into a lepton (electron or muon), a corresponding neutrino and hadron(s).

$$\mathrm{B, D} \rightarrow \mathrm{e} + \nu_{\mathrm{e}} + \mathrm{X} \qquad \mathrm{BR} \sim 10\%$$

For both the electron and muon channel, the branching ratio is $\sim$ 10%. In ALICE, the semi-electronic channel is studied in the mid-rapidity range, while the semi-muonic channel is studied in the forward-rapidity range. Since, this thesis pertains to the semi-electronic channel, further discussions on the semi-leptonic channel are done in terms of electrons. Unlike the hadronic channel, full reconstruction of the parent hadron is not possible due to the missing neutrino. The yield of electrons decayed from heavy-flavour hadrons are obtained by subtracting the background non-heavy-flavour electrons (e.g. $\mathrm{e^-e^+}$ from γ decays) from the inclusive electron yield. Details of the methodology are discussed in chapter 3. Since, electrons primarily interact electromagnetically, they provide cleaner signals. Another advantage of this channel is the potentiality for beauty measurement due to the high branching ratios and ALICE's excellent capability for electron identification for a wide p_{T} range.

1.6 Goal of this thesis

This thesis, titled "*Multiparticle production in pp collisions at LHC energies*", aims to shed a light on the cracks that have appeared in the picture of the particle production mechanisms in high energy pp collisions as discussed in the previous section 1.4 of the chapter. Keeping those motivations in consideration, in this thesis, using the ALICE experimental data, the p_{T}-differential cross section of electrons decayed from open heavy-flavour hadrons and its dependence on charged particle multiplicity in pp collisions at $\sqrt{s} = 13$ TeV has been presented. Heavy quarks (charm and beauty) are produced through hard scatterings, in high-energy hadronic collisions. Due to their large masses their production cross-sections can be calculated through the framework of perturbative QCD down to very low p_{T}. Moreover,

since the heavy quarks are produced at the early stages of the collision, well before the formation of QGP, heavy-flavour hadrons act as efficient probes for the QGP medium formed in heavy nucleus-nucleus collisions. Measurements of heavy-flavour hadron production in proton-proton collision acts as baseline for the study of heavy-flavour particles in heavy-ion collisions. These objectives for using heavy-flavour hadrons has been discussed at length in section 1.5 of this chapter. In this thesis, along with the p_{T}-differential spectra, the multiplicity dependent self-normalized yield of heavy-flavour hadron decayed electrons as a function of self-normalized charged particle multiplicity density has been presented in chapter. A brief review and motivation for studying the self-normalized yields have been discussed in subsection 1.6.1.

The particle production mechanisms and the initial state geometry of the system are highly entangled. In high-energy heavy-ion collisions, structures in the initial collision zone is a matter of intense investigation, both from the theory and the experimental points of views. Research in the prior decade and more so in the last quinquennial, few of which are discussed in section 1.4, put a highlight towards the similarities in sizes and properties of medium in heavy-ion collisions and high multiplicity pp collisions. This encourages us to think in the direction of commonalities between these large and small systems. Hence, we also present, in this thesis, a study on the structures in the initial collision zone and how they affect the final state particles using Pb–Pb collisions from the AMPT event generator at $\sqrt{s_{\mathrm{NN}}} = 200$ GeV using the principal component analysis (PCA), in chapter 5. A brief introduction to the principal component analysis and this study has been discussed in subsection 1.6.2.

1.6.1 Multiplicity dependent self-normalized yields in ALICE

The multiplicity dependent self-normalized yield measurements have been performed with an aim to understand the particle production mechanism in pp collisions, where the term 'self-normalized' implies that the yield in multiplicity intervals are normalized by the average multiplicity integrated yield. The first measurement of the charged-particle multiplicity

dependent self-normalized yield study in ALICE with J/ψ production in pp collisions at $\sqrt{s} = 7$ TeV was published in 2012 [59]. An approximately linearly increasing trend of J/ψ yield with charged particle multiplicity has been reported in data. However, the PYTHIA predictions do not reciprocate the trend in data. The result indicates that multi-parton interactions (MPI) affects the hard momentum scales relevant for J/ψ production or that the J/ψ production in pp is always connected to strong hadronic activity. Multiple parton interactions have substantial contribution to particle production and the total event multiplicity in pp collisions [60–63]. Hence, it was argued that if MPI mainly affects the production of light quarks and gluons, then the open heavy-flavour and J/ψ productions should be independent of the overall event multiplicity. It was also argued elsewhere [64] that MPI starts having a substantial contributions on harder scales at LHC energies, which could induce a correlation between the yield of open heavy-flavour and J/ψ production on the charged particle multiplicity of the event. More recent studies on the p_{T}-dependent self-normalized yield on the hard and soft probes has been done in ALICE with D-mesons [65] in pp collisions at $\sqrt{s} = 7$ TeV, J/ψ [66] and charged particles [67] in pp collisions at $\sqrt{s} = 13$ TeV. The charged particle multiplicity has been measured using SPD tracklets in mid rapidity ($|\eta| < 1.0$). A significant increase of particle yield with the charged-particle multiplicity, with a stronger rise for higher p_{T} ranges, is seen. To avoid biases due to auto-correlation, the D-meson measurements have been performed with multiplicity been calculated using the V0 detector. This introduces a rapidity gap in the region of the D-meson and multiplicity measurements. An increasing trend of D-meson yield with multiplicity, although smaller than that observed in the SPD selection case, has been observed. The self-normalised yield data of D-meson, J/ψ, charged particle have been compared with various model predictions, such as PYTHIA, EPOS. The J/ψ data has been additionally compared with CGC model and percolation model predictions. Although no one model predictions can describe all data quantitatively, they qualitatively reproduce the trend of the self-normalised yield. However, for conclusive and complete assessment of physics mechanisms at play, more stringent tests

on models and comparison between data are required. The behaviour of the self-normalized yield vs. the self-normalized multiplicity is an interesting topic of research as it could provide an insight to the mechanisms at the play in the microscopic levels and production processes of hard and soft particles in such high energy collisions.

1.6.2 Principal Component Analysis

The Principal Component Analysis (PCA) is a simple method of unsupervised learning algorithm used for de-correlating multivariate data. The PCA method works by reducing dimensions from a given problem by finding the most optimal basis for the problem and thus making an analysis simpler. The principle components are computed from singular value decomposition of the data matrix. They form the new basis and are ordered such that the first component contains the most informative features, the second component contains the second most informative features in data and so on.

In heavy-ion collisions, PCA has been used primarily to study various orders of flow variables and their fluctuations [68]. A particular interest is the decomposition of the azimuthal distribution in PCA in which the eigenvalues are related to the elliptic flow coefficients, as has been explained in details in [69]. It has been shown here that the flow coefficient obtained by the PCA method and conventional Fourier analysis method are nicely correlated up to v_6. The event-by-event flow coefficient has also been extracted using this method.

The main scope in this thesis is to probe the initial conditions by using the method of Principal Component Analysis. The distributions for η, p_{T}, ϕ in heavy-ion collisions at $\sqrt{s_{\mathrm{NN}}} = 200$ GeV using this method has been analysed. As a part of the result, the sensitivity of the PCA eigenvalues to the introduction of clustering at the partonic level in AMPT has been reported.

Chapter 2

The Experimental Setup

In this chapter, a brief description of the detectors and experimental setup that were used for obtaining the spectra of electrons decayed from heavy-flavour hadrons and its dependence on charged particle multiplicity, is presented. The measurements were performed using the ALICE detector system at the Large Hadron Collider (LHC) at CERN.

2.1 The Large Hadron Collider(LHC)

With new and exciting results/data emerging in the field of high energy physics since the 1970s and a need for data at higher centre-of-mass energies for collisions, the particle accelerator technology has seen tremendous progress in the last 5 decades. The Large Hadron Collider (LHC) [70] at the European Organization for Nuclear Research (CERN), which started its operation in 2009, is presently the largest and highest-energy hadron collider in the world. The LHC was installed in a 26.7 km tunnel constructed between 1984 and 1989, at a depth of 45-170 m from the surface of the earth at Swiss-French border near Geneva, Switzerland. It is designed to collide two beams of particles rotating in opposite directions. The LHC has recorded data for lead ions (Pb–Pb) at $\sqrt{s_{\rm NN}} = 2.76$ TeV and 5.02 TeV. It has also collided opposite beams of proton-proton (pp) collisions at centre-of-mass energies 0.9, 2.36, 2.76, 5, 7, 8, 13 TeV; proton-lead (p–Pb) at 5 TeV and 8.16 TeV and Xenon-Xenon

(Xe–Xe) collisions at 5.44 TeV (per nucleon). The collider has been in shutdown since December 2018 for upgrades and data taking in its Run-3 is set to commence from 2022.

There are seven experimental setups at the four interaction points of the collider, namely, ALICE [71], ATLAS [72], CMS [73], LHCb [74], LHCf [75], TOTEM [76] and MoEDAL each built with an aim to explore a varied ranges of physics interests. The TOTEM (Total, elastic and diffractive cross-section measurement) and LHCf (LHC forward) are the smallest experiments on the LHC which focus on the specialized research in the forward region. The LHCb (Large Hadron Collider beauty) is located at one of the four interaction points and specializes in b-physics experiment. MoEDAL is a small detector system which uses detectors near LHCb in the cavern. The ATLAS (A Torroidal LHC Apparatus) and the CMS (Compact Muon Solenoid) are the bigger experimental setups at two interaction points of the LHC. They are general-purpose experiments to investigate a large range of physics mainly focusing on the realm of particle physics. They look for new and heavier elementary particles and aim to study the properties, including the structure, if any, of particles with increasing energy of the colliding particles. The ALICE (A Large Ion Collider Experiment) detector system, conversely, mainly aims to study the physics of strongly interacting matter at extreme energy densities and temperatures through heavy as well as light ion (Pb–Pb, Xe–Xe, p–Pb, pp) collisions.

2.2 A Large Ion Collider Experiment (ALICE)

A Large Ion Collider Experiment (ALICE) [71], one of the four main detector systems at the Large Hadron Collider, is located at Point-2 of the LHC accelerator tunnel in St. Genis-Pouilly commune, near the Swiss-France border. It aims to address the physics of the nuclear matter under extreme conditions of high temperature and energy density. ALICE has participated in the data-taking program from heavy and light ion collisions in the LHC since its commencement. Data collected from these collisions at various energies allows an

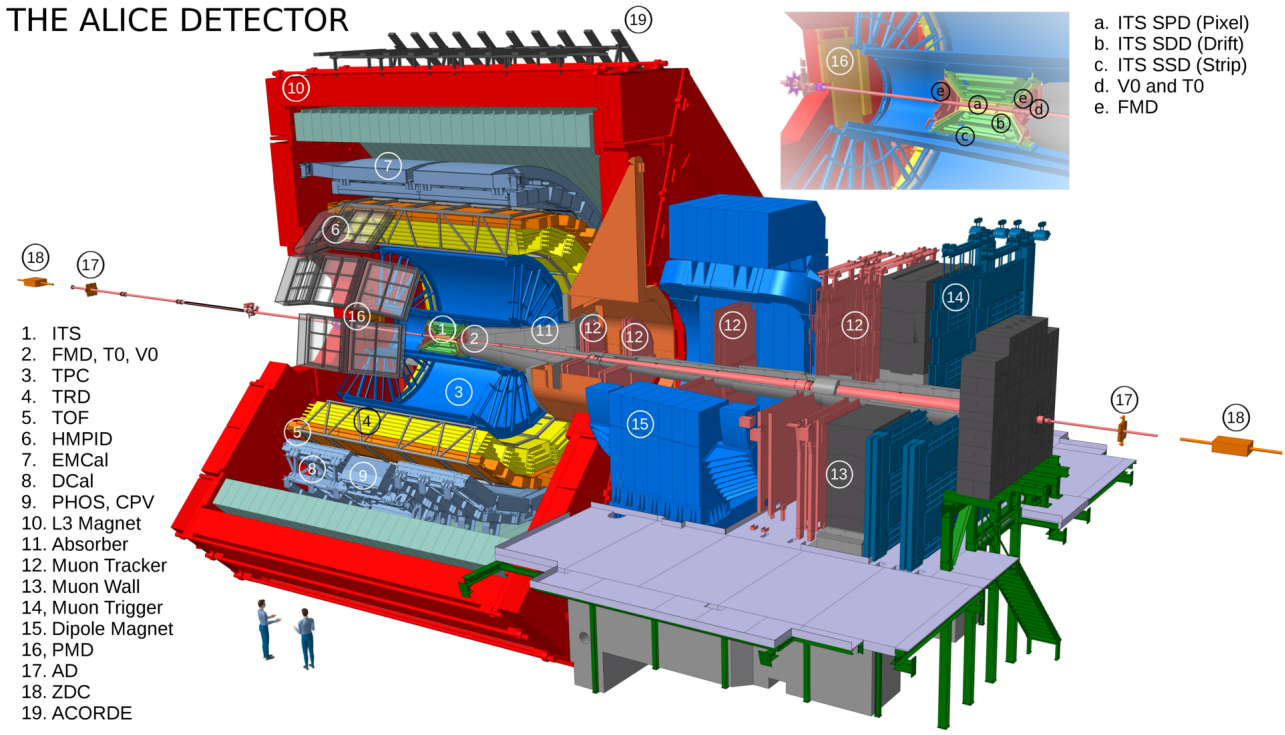

Figure 2.1: Schematic view of the ALICE detector system

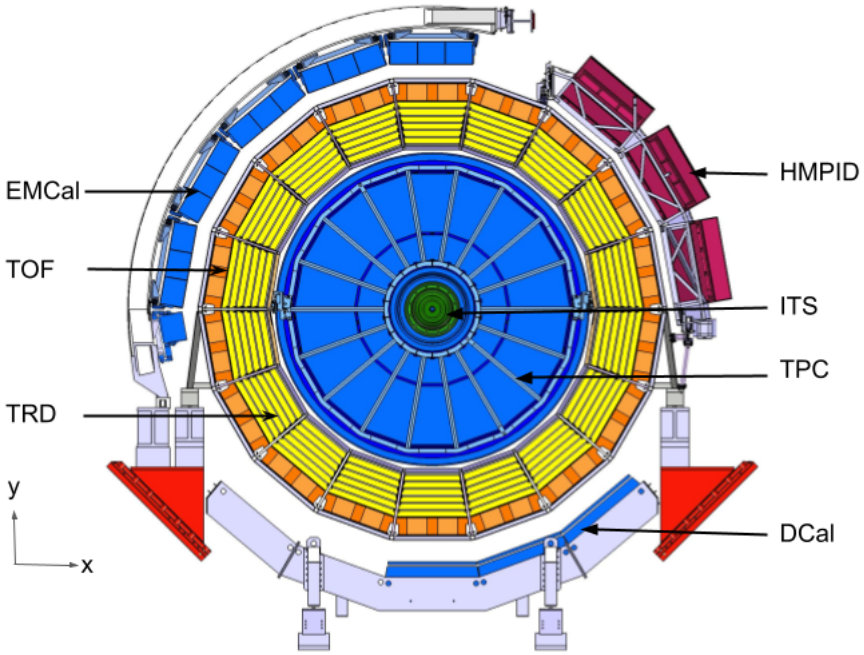

Figure 2.2: Cross sectional view of the ALICE detector system

extensive study of the electrons, hadrons, photons and muons produced in such collisions up to the highest multiplicities anticipated in the collisions. The ALICE is designed to handle

extreme charged particle multiplicity densities ($\mathrm{d}N_{\mathrm{ch}}/\mathrm{d}\eta$) at mid-rapidity in central Pb-Pb collisions. It is optimized for $\mathrm{d}N_{\mathrm{ch}}/\mathrm{d}\eta = 4000$, and is tested up to $\mathrm{d}N_{\mathrm{ch}}/\mathrm{d}\eta = 8000$. One of the key abilities of ALICE is its capability of tracking and identifying charged particles over four magnitudes in particle transverse momentum (10^{-2} - 10^{2} GeV/c) which allows for extensive studies of topics from soft physics to jets and high-p_{T} particle production.

The overall dimensions of the ALICE detector are $16\times16\times26$ m^3 with a total weight of $\approx$ 10000 tons. ALICE consists of a central barrel detector system, which measures electrons, hadrons, and photons, and a forward muon spectrometer. The central part is installed in a large solenoid magnet reused from the L3 experiment at LEP and covers a maximum pseudorapidity region of $|\eta| < 1$ over the full azimuth. A schematic diagram of the ALICE detector is shown in figure 2.1. A cross sectional view of the detector system in the xy plane, where z is the beam direction [77], is shown in figure 2.2 for visualization of the azimuthal coverage of the detectors of the central barrel detector system. The following detectors are a part of the central barrel detector system, enumerated in the order from inside to out. Their dimensions, η, ϕ coverage and main working purpose have been summarized in table 2.1.

1. Inner Tracking System (ITS)

2. Time-Projection Chamber (TPC)

3. Transition Radiation Detector (TRD)

4. Time-Of-Flight (TOF)

5. High-Momentum Particle Identification Detector (HMPID)

6. Electro-Magnetic calorimeters: Electromagnetic + Dijet Calorimeter (EMCAL + DCAL) and Photon Spectrometer (PHOS)

7. ALICE COsmic Ray DEtector (ACORDE)

Table 2.1: Summary of the central barrel detector acceptances in η, ϕ and their main working principles. The azimuthal angle ϕ increases counter-clockwise from x ($\phi = 0$) to y ($\phi = \pi/2$) with the observer standing at positive z direction [77]. 'r' is the radial distance of the detectors from the beam line.

Central Barrel Detectors		η	ϕ	r (cm)	Main Purpose
ITS	Layer 1,2 SPD	± 2, ± 1.4	360°	3.9 , 7.6	tracking, vertexing, triggering
	Layer 3,4 SDD	± 0.9, ± 0.9		15 , 23.9	tracking using dE/dx
	Layer 5,6 SSD	± 0.97, ± 0.97		38 , 43	tracking using dE/dx
TPC		± 0.9	360°	85 (inner) 250 (outer)	tracking, PID, momentum measurement
TRD		± 0.84	360°	290 (inner) 368 (outer)	electron identification using their specific energy loss and transition radiation
TOF		± 0.9	360°	378	PID in intermediate momentum
HMPID		± 0.6	1.2° – 58.8°	500	high momentum PID through detection of Cherenkov radiation
EM Calorimeters	EMCal	± 0.7	80° – 187°	460	triggering, electron and photon identification
	DCal	±0.22 to ± 0.7	260° – 327°		
	PHOS	± 0.12	220° – 320°		low and high momentum photon and π^0 measurement
ACORDE		± 1.3	- 60° – 60°	850	trigger on cosmic rays

Tracking in the central barrel is performed using the ITS and TPC. The TRD can also be used for tracking thereby improving the p_{T} resolution at high momentum. The ITS also provides for high-multiplicity triggering and secondary vertex reconstruction. Particle IDentification (PID) is achieved with TPC, TOF, TRD, HMPID, EMCal (DCal) detectors. The TPC along with tracking and PID also allows for the determination of the momentum of charged particles. An array of scintillators (ACORDE), positioned on top of the L3 magnet, is used to trigger on cosmic rays. Since the ITS, TPC, TOF, EMCal (DCal) detectors have mainly been used for obtaining the results in this thesis, detailed information

on these detectors have been discussed in sections 2.2.1, 2.2.2, 2.2.3, 2.2.4 respectively, of this chapter.

The forward muon arm (2° - 9°) was primarily designed to measure the production of heavy-quark resonances (J/ψ, ψ' etc.) with a mass resolution sufficient to separate all states. It consists of several detectors, located at small angles for global event characterization and triggering. The forward muon arm is also equipped with a complex arrangement of absorbers, a large dipole magnet along with the detectors. The forward detectors including the Muon spectrometer have been listed below.

1. Muon Spectrometer (MUON) : Several tracking planes and triggering chambers
2. Zero Degree Calorimeter (ZDC)
3. Photon Multiplicity Detector (PMD)
4. Forward Multiplicity Detector (FMD)
5. Time Zero Detector (T0)
6. VZERO Detector (V0)

   Details on the V0 detector are presented in section 2.2.5.

The η coverage, distance from the vertex, main purpose and detection techniques of the detectors of the forward arm are summarized in table 2.2.

2.2.1 Inner Tracking System (ITS)

The Inner Tracking System (ITS) [78, 79] is one of the main detectors of the ALICE central barrel detector system. The ITS is used to determine the primary vertex with a resolution better than 100 μm and to reconstruct the secondary vertices from decays of D and B mesons, and hyperons. It is used as a stand-alone detector for tracking and identification of very low momentum particles ($p_{\mathrm{T}} < 200$ MeV). The ITS also helps to reconstruct the

Table 2.2: Summary of the forward arm and their main working principles

Forward Detectors		η	Position from vertex (m)	Detection principal	Main Purpose
ZDC	ZN	$3.62 < \eta < 5.03$	$\pm$ 116	neutron calorimeter	measure and trigger on the impact parameter of the collision
	ZP	$1.7 < \eta < 3.68$	$\pm$ 116	proton calorimeter	
	ZEM	$-3.4 < \eta < -1.7$	7.27	EM calorimeter	
PMD		$2.3 < \eta < 3.7$	3.64	calorimeter	multiplicity and spatial distribution of photons
FMD	disc 1	$3.62 < \eta < 5.03$	3.2	silicon semiconductor detectors	provides multiplicity information
	disc 2	$1.7 < \eta < 3.68$	0.83 (inner) 0.75 (outer)		
	disc 3	$-3.4 < \eta < -1.7$	-0.63 (inner) -0.75 (outer)		
V0	V0A	$2.8 < \eta < 5.1$	3.4	scintillator counters	min. bias trigger, multiplicity and luminosity
	V0C	$-1.7 < \eta < -3.7$	-0.9		
T0	T0A	$4.61 < \eta < 4.92$	3.75	cherenkov counters	provide signal for start time (t_0) for TOF detector
	T0C	$-3.28 < \eta < -2.97$	-0.7		
MUON Spectrometer					
Tracking Station 1		$-2.5 > \eta > -4.0$	-5.36	cathode pad chambers with gas mixture 80% Ar /20% $C0_2$	μ detection for quarkonia, c,b $\rightarrow \mu$, low mass vector meson studies
Tracking Station 2			-6.86		
Tracking Station 3			-9.83		
Tracking Station 4			-12.92		
Tracking Station 5			-14.22		
Trigger Chamber 1		$-2.5 > \eta > -4.0$	-16.12	Resistive Plate Chamber	
Trigger Chamber 2			-17.12		

particles that traverse through the dead channels of the TPC and to improve the momentum and angle resolution of the particles which are reconstructed through the TPC.

The ITS is the inner-most layer of the central barrel with radius between 3.9 to 43 cm. It surrounds the beam pipe coaxially. It consists of two layers of the following cylindrical silicon

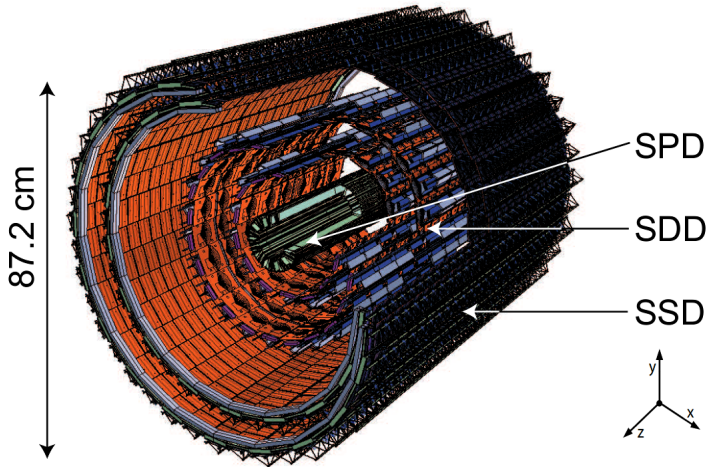

Figure 2.3: Layout of the Inner Tracking System (ITS) detector [78]

detectors (six layers in total): silicon pixel (SPD), silicon drift (SDD) and silicon strip (SSD) detectors [80]. A layout of the ITS detector is shown in figure 2.3. The four outer layers (drift and strip) have analogue read-out and hence can be used for particle identification (PID) in the non-relativistic regime. Silicon detectors generally work through detection of energy lost by particles while traversing through the detector. The two first layers of the ITS (SPD) consist of two dimensional sensor matrices of silicon diodes of thickness $\sim$ 200 μm. The sensor matrices include 256 $\times$ 160 pixels/cells with each pixel measuring 50 μm (rϕ) $\times$ 425 μm (z). The spatial resolution of the SPD along the rϕ plane and z direction is 12 μm and 100 μm, respectively. When a charged particle traverses through a pixel, a digital signal is read out of that pixel. Energy deposition information is not retained like the drift and strip detectors. Due to the extreme fine segmentation of the SPD, the SPD can operate in a region with track density as high as 50 tracks/cm^2 making it suitable for high multiplicity measurements. The SPD can be used for triggering high multiplicity events.

2.2.2 Time Projection Chamber (TPC)

The Time Projection Chamber (TPC) [81] is the main tracking detector in ALICE. In conjunction with other detectors, the TPC is used for identification of charged particles, charged particle momentum measurement with a good two-track separation and vertex

determination.

The ALICE TPC is a cylindrical chamber of volume ~ 90 m^3 placed coaxially with the beam axis and next to the ITS radially. Its length is ≈ 5 m and, its inner and outer radii are ≈ 0.85 m and ≈ 2.5 m respectively. It covers a pseudorapidity range of $|\eta| < 0.9$ over the full azimuth. A schematic diagram of the TPC is shown in figure 2.4.

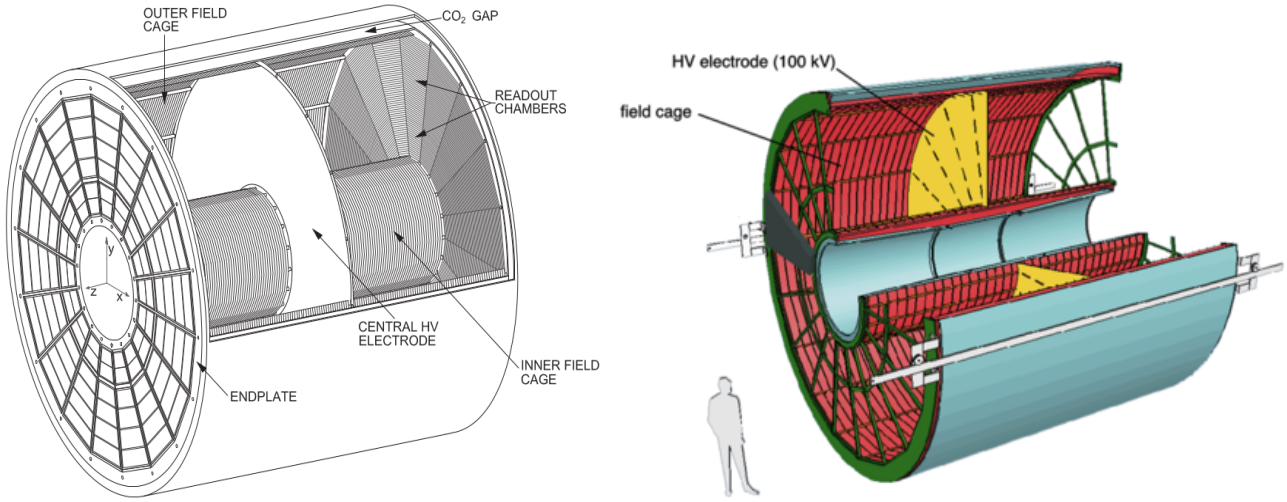

Figure 2.4: Schematic diagram of the Time Projection Chamber (TPC) detector

TPC is a gaseous detector which operates in the proportional region. The large cylindrical field cage of the TPC is divided into two parts using a high voltage electrode ($\sim$ 30 μm thick), which acts as a cathode. It generates drift field in the two volumes. At both ends of the TPC, multiwire proportional chamber (MWPC) based readout chambers are mounted in 18 trapezoidal sectors. The MWPCs have been replaced by Gas Electron Multiplier (GEM) system to match the TPC readout rate for the increased luminosity of the Run-3 data taking compared to that of Run-2 and Run-1. The TPC is filled with a gas mixture of $\sim 90\%$ noble and $\sim 10\%$ quencher gas, e.g. Ne-CO_2-N_2 (85.7%-9.5%-4.8%), which allows for low diffusion, high ion mobility, low multiple scattering and small space-charge effects. Charged particles from collisions passing through the gas, ionizes it. The electrons freed along the ionization tracks drift along the field lines to the end plates. The TPC readout chambers detect the electrons to reconstruct the trajectory of the particles.

The x-y position of the ionization along the track is obtained from the projection of the track on the MWPC pads at the end plates. The z coordinate is determined from the drift velocity of the electrons ($\sim$ 2.58 cm/μs) and the time of arrival of the electrons on the end plate with respect to the collision time of the beams as obtained from the LHC-clock. A uniform magnetic (0.5 T (nominal) or 0.2 T (low)) field is applied due to which particles follow a helical path and this curvature is used to determine the momentum of the particles (p). The position resolution of the TPC is 1100 - 800 μm in the rϕ plane and 1100 - 1250 μm in the z direction. Low momentum tracks (100 MeV/c - 1 GeV/c) are reconstructed using the TPC with a momentum resolution better than 2%. The momentum resolution for electrons of momentum $\sim$ 4 GeV/c is $\sim$ 2%. The TPC, along with other tracking detectors (ITS and TRD), can perform track reconstruction with a momentum resolution reaching $\sim$ 10% for tracks with momentum up to 100 GeV/c.

For identification of charged particles, TPC relies on the measurement of specific energy loss (dE/dx) in a detector gas as a function of the momentum (p). The Bethe-Bloch equation describes the average energy loss of charged particles when travelling through matter. It is given for heavy charged particles in the following equation 2.1.

$$-\frac{\mathrm{d}E}{\mathrm{d}x} = \frac{4\pi e^4}{m_0}\frac{z^2}{v^2}NZ\left\{ln\Big(\frac{2m_0v^2\gamma^2}{I}\Big) - \beta^2 - \delta^2 - \frac{2C}{Z}\right\} \tag{2.1}$$

where,

z = Charge of primary particle

v = Velocity of charged particle

N = Number density of absorber material

Z = Atomic Number of absorber material

I = Mean excitation potential

m_0 = Rest mass of electron

β = v/c, c = Velocity of light

$\gamma = \frac{1}{\sqrt{1-\beta^2}}$

δ = Density Correction factor

C = Shell Correction factor

Electrons and positrons, due to their small masses, follow a modified Bethe-Bloch equation, where the energy loss is mostly dominated by bremsstrahlung [82]. The resolution of the $\mathrm{d}E/\mathrm{d}x$ measurement in pp collisions is around 5.5%. The energy deposited per unit length ($\mathrm{d}E/\mathrm{d}x$) as function for momentum (p) for identified charged particles as measured by the ALICE TPC is shown in figure 2.5. The $\mathrm{d}E/\mathrm{d}x$ bands for different charged hadrons are mostly distinguishable. However, for $p < 1$ GeV/c the kaon, proton and pion/muon bands cross the electron band. At these regions the hadrons can be misidentified as electrons, which increases the contamination in the electron sample. In addition, the merging of the $\mathrm{d}E/\mathrm{d}x$ lines of electrons, muons, pions, and other hadrons limits the particle identification at high momentum ($p \gtrsim 10$ GeV/c). Hence, the TPC alone cannot be used for particle identification with high purity. Detectors with particle identification capabilities, EMCal and TOF, have been used along with the TPC for identification of electrons in this analysis, as it extends over a large momentum region.

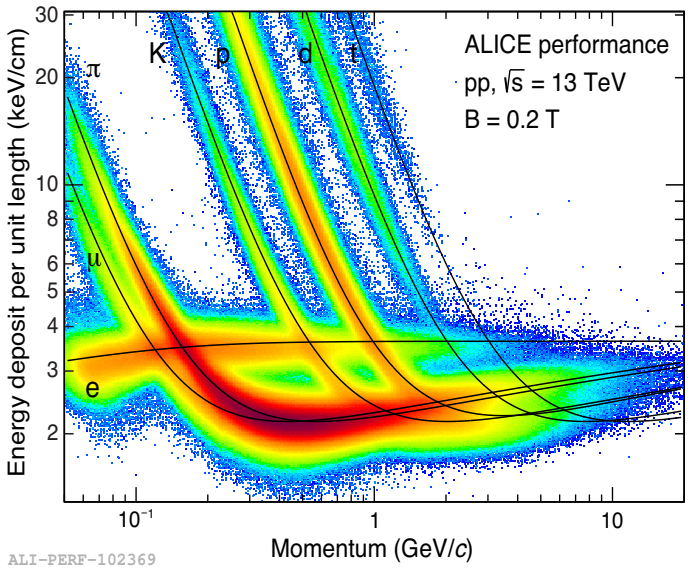

Figure 2.5: Energy deposited per unit length versus momentum measured with the ALICE TPC

2.2.3 Time-Of-Flight (TOF)

The Time-Of-Flight (TOF) detector [83, 84] is extensively used for particle identification (PID) in the low and intermediate momentum range. The TOF, coupled with the ITS and TPC, can distinguish light and heavy particles of same momentum with the help of the difference in their time of flight. The ALICE TOF detector is a gas detector which uses Mutligap Resistive Plate Chamber (MRPC) as its basic detecting element. It is placed at a radial distance of 3.7 m from the beam axis and has a pseudorapidity coverage of $|\eta| < 1$ in full azimuth.

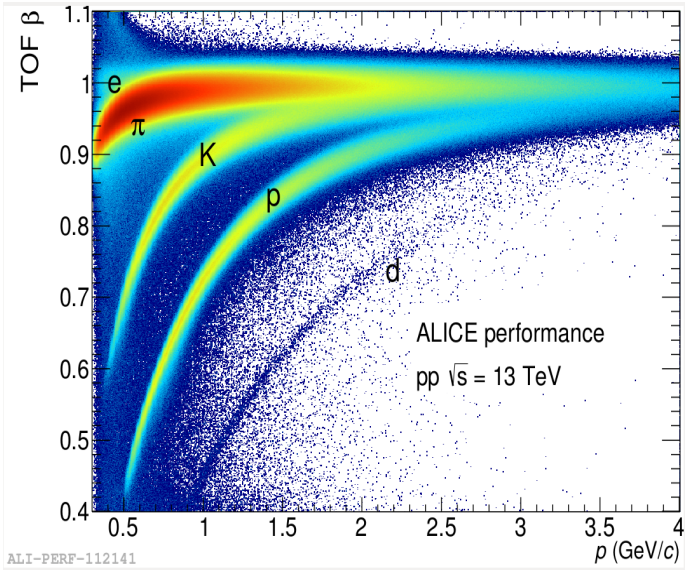

Figure 2.6: TOF β vs momentum performance plot measured in ALICE

The time of flight (t) is defined as the time taken by a particle to travel a certain distance, in this case, from the interaction point to the TOF detector (L). The start time reference (t_0) is provided by the T0 detector, which sits on the opposite sides of the interaction point. The global time resolution of the ALICE TOF is $\sim$ 80 ps. The particle is identified from its mass, which is calculated from the information of the time of flight and the momentum of particle obtained from the TPC (p), using the following equation.

$$m = p\sqrt{\frac{t^2}{L^2} - 1} \tag{2.2}$$

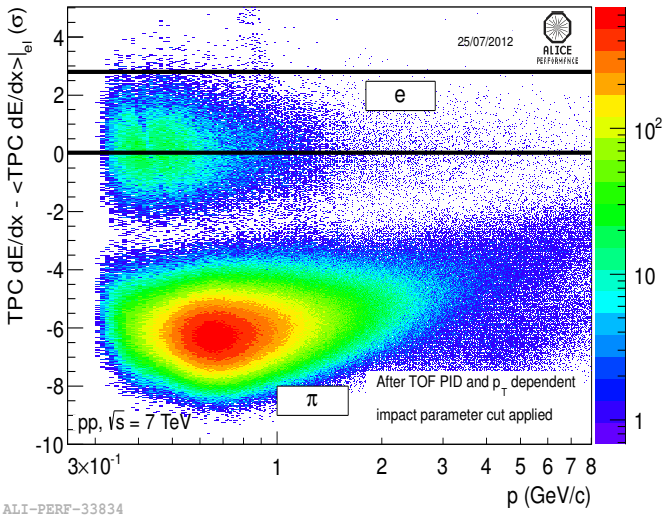

Figure 2.7: TPC signal vs. momentum for tracks passing the TOF PID selection. An example of a selection criteria for electrons is shown as solid black line

The mass resolution obtained from this expression has the following components:

$$\left(\frac{\delta m}{m}\right)_p \propto \frac{\delta p}{p}; \qquad \left(\frac{\delta m}{m}\right)_{\mathrm{L}} \propto \left(\frac{p}{m}\right)^2 \frac{\delta \mathrm{L}}{\mathrm{L}}; \qquad \left(\frac{\delta m}{m}\right)_{\mathrm{t}} \propto \left(\frac{p}{m}\right)^2 \frac{\delta \mathrm{t}}{\mathrm{t}} \tag{2.3}$$

The TOF β is defined as the ratio of the velocity of a particle ($v = \mathrm{L/t}$) with respect to that of light. Figure 2.6 shows the separation of the electrons and various hadrons in the TOF β vs momentum performance plot, measured by ALICE. TOF provides excellent particle identification for electrons at very low momenta ($p_{\mathrm{T}} < 700$ GeV/c) where the electron/pion (e/π) separation is better than 3σ [83]. Pion & kaon (π/K) separation better than 3σ is achieved below ~ 2.5 GeV/c and and kaon & proton (K/p) separation better than 3σ is achieved up to 4 GeV/c. Figure 2.7 shows the energy deposited per unit length ($\mathrm{d}E/\mathrm{d}x$) of charged particles in the TPC as function for momentum (p) after the TOF particle identification selection criteria for electrons were applied. This figure clearly shows a distinct band of electron $\mathrm{d}E/\mathrm{d}x$ with very little contamination from other hadrons compared to that of TPC-alone as shown in figure 2.5 in section 2.2.2. At a relatively high momentum, however, the TOF is not used for particle identification. As seen from the second ($\delta m/m_{\mathrm{L}}$)

and the third ($\delta m/m_{\mathrm{t}}$) components of the equation 2.3, the mass resolution and hence the particle identification capability of the TOF tends to worsen with the square of the particle momentum. At sufficiently high momentum, the mass resolution is driven much more by the errors on the track length measurements and the time of flight than by the error on the momentum determination. Hence, the Electromagnetic Calorimeter (EMCal) is used in the high momentum region for electron identification along with the TPC. The quantitative values of purity and efficiency, along with the selection criteria used in this thesis and the momentum ranges in which the different detector combinations are utilised, are mentioned in chapter 3.

2.2.4 Electromagnetic Calorimeter (EMCal) and Dijet Calorimeter (DCal)

The Electromagnetic Calorimeter (EMCal) [85] and Dijet Calorimeter (DCal) [86] are Pb-scintillator sampling calorimeters with cylindrical geometry stationed adjacent to the ALICE magnet coil at a radial distance of r $\approx$ 4.6 m from the beam line. A sampling calorimeter has alternate layers of absorber material which degrades the particle energy for producing the particle shower and an active material to measure the detectable signal/energy deposited. The EMCal (and DCal) enhances ALICE's capabilities for jet measurements in combination with excellent capabilities to track and identify particles by ALICE. These detectors also allow for an enhanced measurement of high momentum electrons and photons, and triggering on high energy jets.

The EMCal covers $|\eta| < 0.7$ and $\Delta\phi = 107^{\circ}$ ($80^{\circ} < \phi < 187^{\circ}$). The size of EMCal was constraint by the maximum weight which can be supported by the L3 magnet. The DCal was added to the system to extend the ϕ range and is in every way an extension of the EMCal acceptance. The DCal covers $0.22 < |\eta| < 0.7$ and subtends an angle $\Delta\phi = 67^{\circ}$ ($80^{\circ} < \phi < 187^{\circ}$). The η coverage of DCal is not uniform as the space is occupied by the existing PHOS detector. The extension of the scope of the ALICE EMCal system was

specifically designed to expand the acceptance of the EMCal and allow the measurement of hadron-jet and di-jet correlations. A schematic diagram of the EMCal and the DCal arrays are shown in figure 2.8. As the EMCal and DCal are essentially the same detectors and they form the two arms of the electromagnetic calorimeter system, from here on the term 'EMCal' would imply both the EMCal and DCal detectors unless explicitly mentioned otherwise.

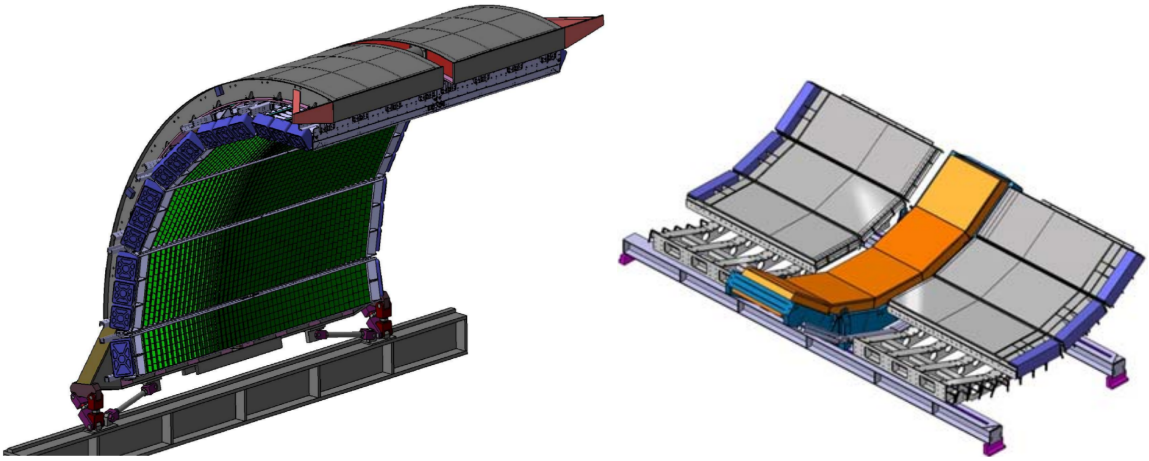

Figure 2.8: Electromagnetic Calorimeter (EMCal) array of super-modules [85] (left) and Dijet Calorimeter (DCAL) super-modules in gray with the PHOS super-modules in orange in the middle (right) [87]

The basic building block of the EMCal (and DCal) is known as a super module and consists of a 2 × 2 towers/cells of 76 alternating layers of 1.44 mm Pb and 77 layers of 1.76 mm polystyrene, injection molded scintillator. The transverse dimension of each tower is ∼ 6.0 ×6.0 cm^2 with acceptance range $\Delta\eta \times \Delta\phi \approx 0.014 \times 0.014$. The EMCal detector system is designed to be a compact detector with sampling fraction 1:22 Pb to scintillator ratio by volume and a detector thickness of 20.1 radiation lengths (20.1X_0, where X_0 = 12.3 mm) and an effective Moliere radius (R_M) of 3.20 cm. Radiation length (X_0) is defined as the mean path traversed by an electron such that energy of the electron is reduced by a factor of 1/e. It is a characteristic of the material traversed. Moliere radius (R_M) is a measure of the transverse dimension of the electromagnetic showers and defined as the radius of a cylinder containing on average 90% of the energy deposition of the shower.

The EMCal measures the energy deposited by particles while traversing through the detector material. Electrons and photons interact primarily through electromagnetic interactions and produce electromagnetic showers while passing through the calorimeter. Electrons loose energy via bremsstrahlung (e + nucleus $\rightarrow$ e + γ + nucleus) while photons are absorbed by pair production (γ + nucleus $\rightarrow$ e^+ + e^- + nucleus). Since, the aim of this thesis is the identification of electrons decayed from heavy-flavour particles, the description of the EMCal in this section is mostly focused on the identification of electrons. Electrons (and photons) tend to deposit all of their energy in the EMCal in the form of clusters through electromagnetic shower since the thickness of the detector is $20.1X_0$. Hence, the total energy deposited by the electrons in the EMCal (E) should be equal to its momentum (p), which is obtained from the TPC, i.e., $E/p \approx 1$. The hadrons, however, do not deposit their entire energy in the EMCal as they interact mainly via the strong nuclear force and the thickness of the towers is about one nuclear interaction length. For hadrons the E/p should be less than 1. Electrons are separated from photons by matching the EMCal clusters to the tracks from TPC as photons do not give signal in the TPC. The energy resolution of calorimeters improves with an increase in the energy of the incident particle. The energy resolution for the ALICE EMCal is lower than 5% for electrons with energy greater than 10 GeV.

As already mentioned in section 2.2.2 and evident from figure 2.5, the hadron dE/dx band from TPC starts to merge with the electrons band as the momentum increases making it difficult to select high purity electrons with $p \gtrsim 6$ GeV/c. Figure 2.9 shows a distribution of E/p from the EMCal vs. TPC $n\sigma_e$, where $n\sigma_e$ is defined as the difference between of the measured signal from the expected calculations for electrons in terms of detector resolution. From the figure, a clear distinction between electron region and other hadrons is observed. Additionally, other discriminating variables of the EMCal clusters such as the shape of the shower can be used to distinguish between electrons and hadrons. Details on the quantitative measure and selection criteria are discussed in chapter 3. In addition to electron (photon) identification, EMCal is also used as high momentum triggers.

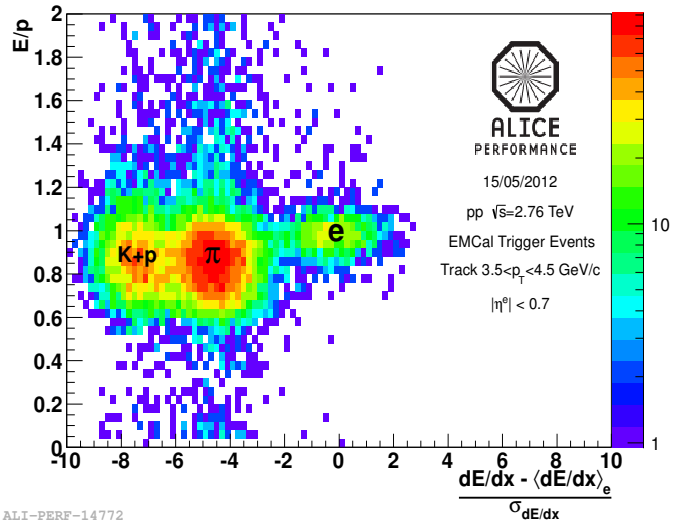

Figure 2.9: E/p vs. TPC nσ_e distribution measured in ALICE. Energy (E) is obtained from the EMCal.

2.2.5 VZERO detectors (V0)

The VZERO (V0) detector [88, 89] is a small angle detector which consists of two arrays of scintillator counters, called V0A and V0C. They are installed on either side of the ALICE interaction point. The V0A is located 3.4 m from the vertex, on the side opposite to the muon spectrometer and V0C is fixed at the front face of the front absorber 0.90 m from the vertex as shown in figure 2.10. V0A and V0C cover the pseudorapidity ranges 2.8 $< \eta <$ 5.1 and -3.7 $< \eta <$ -1.7 respectively.

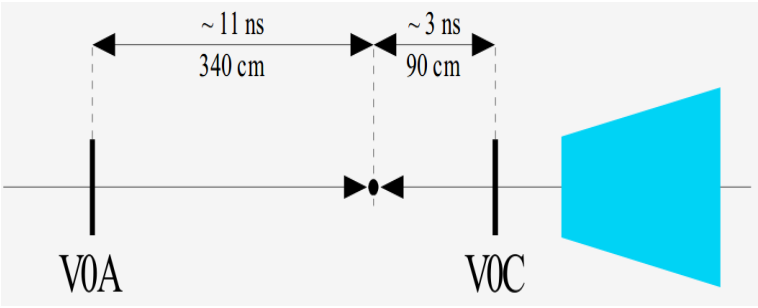

Figure 2.10: Time alignment condition on V0A and V0C [88]

V0 detector provides minimum-bias (MB) triggers for the central barrel detectors in pp and A-A collisions. Apart from the initial beam collisions, interactions due to presence

of matter such as, beam pipe, front absorber results in formation of secondary particles, which will distort physical information expected from primary charged particles. Hence, to identify particles from the beam-beam (BB) collisions minimum-bias trigger is used. The minimum-bias trigger confirms that an event has occurred if hits are detected on each disk (V0A and V0C) at the expected time, i.e., 11 ns after the collision on V0A and 3 ns after the collision on V0C.

The V0 detector also provides centrality and multiplicity measurements based on the energy deposited in the scintillator.

The V0 detector is involved in the measurement of luminosity in pp collisions using the van der Meer scan method [90].

2.3 Off-line Computation in ALICE

The raw data obtained from the detector systems have to be processed before being ready in the form of events for further analysis. In this section the off-line data processing and tools used for analysis have been presented.

2.3.1 ROOT and AliROOT

The base tool for analysis in a large fraction of the high energy physics experimental community, including ALICE, is an analysis framework/software written mainly in C++, known as ROOT [91]. ROOT was developed at CERN which includes functionalities for big data processing and analysis in high-energy physics. ROOT packages allow for data storage and management, and contains a plethora of functions for mathematical and statistical analysis. The AliRoot framework [92] is an extension of ROOT, developed by specifically for ALICE simulation and reconstruction.

2.3.2 Simulation

Simulation of actual data taken from experiments plays a paramount role in the analysis of the high energy collision experiments. Simulated samples are used to correct physics data for detector efficiencies and acceptance limitations. Simulations consist of two parts, the event generator and the transport code. Event generators aim to create events and particles with the same average behaviour as in the real data using the theoretical understanding of the collision dynamics. Different event generators utilize different theories and physics processes for generating events as close to the known real data as possible. Monte carlo techniques are used for the simulations, and hence the simulated data created from the event generators are known as 'Monte Carlo samples' or 'MC sample'. PYTHIA [93, 94] is the most commonly used event generator used by ALICE for simulation of pp events. Other prominent event generators include EPOS [95] and HIJING [96] which are used for simulating both pp and heavy-ion collisions. Outputs from the event generators are then fed to the input of transport models. Transport models such as GEANT [97, 98] simulate the behaviour of detectors. The output from the transport models aim at reproducing as realistically as possible the number and properties of particles that are observed by the detectors systems in the experiment. A simulation can be summarized as a virtual model of experiments done through computers.

2.3.3 ESD and AOD files

The raw data after reconstruction is stored in the so-called Event Summary Data (ESD) files. The ESD files include detailed reconstructed information from all sub-detectors such as trigger information, collision vertex measurements and individual particle track information from several sub-detectors etc. However, the ESD files are inconvenient and impractical for local analysis due to their large size. Hence, Analysis Object Data (AOD) files are created from the ESD files, which store only relevant information for specific analyses. AOD files are used as input for local analysis.

2.3.4 Data reconstruction procedure and tracking

Reconstruction of raw data, to be stored in ESD and AOD files, starts with calibration followed by clusterization separately for each detector. Clusters are group of adjacent cells fired and are used as input for track/tracklet reconstruction for tracking detectors. Clusters from the calorimeter based detectors are also stored in the ESD files. The interaction vertex position is reconstructed using algorithms which utilize correlation between SPD tracklets [99]. Tracklets are formed from adjacent clusters of both layers of the SPD in alignment with the reconstructed primary vertex within a small azimuthal window (order of 0.01 rad) [100]. The preliminary interaction vertex is estimated to be the space point where maximum number of lines from a linear extrapolation of the tracklets converge. The vertex determination efficiency depends on the tracklet multiplicity [99]. Track recognition (finding) and reconstruction is performed in the central barrel of ALICE using the Kalman filter method [101] in three iterations. The first iteration begins from the outer radius of the TPC. A track seed is built from the primary vertex estimated from SPD and pairs of TPC cluster in adjacent pad rows. The track seed is projected inwards towards the inner radius of TPC and is updated at each step with the nearest TPC cluster if it fulfils a proximity cut. A preliminary particle identification based on the $\mathrm{d}E/\mathrm{d}x$ is done at this step. These tracks are known as the "TPC-only tracks". These tracks are then propagated towards the ITS for track finding in the ITS and further extrapolated to the point of closest approach to the preliminary interaction vertex. In the second iteration these tracks from the preliminary vertex are propagated backwards to the outer radius of the TPC using the clusters found in the previous iteration. Particle identification is also updated based on the specific energy loss. These tracks are then prolonged towards to TRD, TOF, HMPID, EMCAL and PHOS, detectors for cluster matching. In the final iteration the tracks are re-fitted inwards using the clusters from the second iteration to their distance of closest approach to the SPD vertex. These are known as the "global tracks". The final interaction vertex is recalculated using the global tracks with a higher precision compared to the preliminary interaction vertex.

2.3.5 Clustering in EMCal

Electrons and photons traversing the Electromagnetic Calorimeter deposit energy in different towers through electromagnetic shower. Due to the tower size, the showers produced cover a group of adjacent towers. These groups of adjacent towers/cells are called 'clusters'. Sets of information related to a cell, e.g., position of the cell, energy deposited etc. is called a digit. Clusters are formed from digits that have energy deposition for same particle using

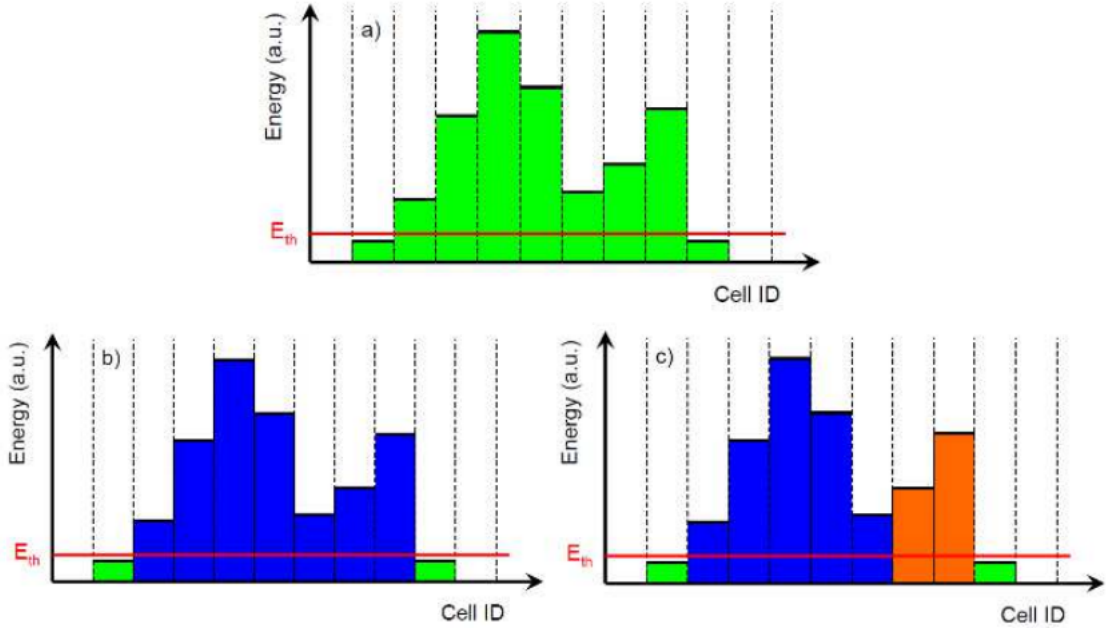

Figure 2.11: Different clusterization algorithms [102]. Boxes represent energy in cells. E_{th} is threshold energy for clusterization. a) Energy in cells before clusterization (marked in green color). b) Result of Clusterizer V1. There is one big cluster made of cells in blue color. Green cells are below threshold and not associated to the cluster. c) Result of Clusterizer V2. There are two clusters made of blue and orange cells. Green cells are below threshold and not associated to any cluster.

any of the available clusterization algorithms. There are currently four types of clusterizers in the EMCal, namely *Clusterizer V1*, *Clusterizer V2*, *Clusterizer 3×3* and *Clusterizer V1 with unfolding*. In this analysis, the *Clusterizer V1* and *Clusterizer V2* have been used and briefly described in this section. The *Clusterizer V1* is the simplest clusterizer algorithm which works by simple aggregation of neighbouring digits/cells until no more cells above a certain energy threshold are left. A set of clusterizer parameters [102] is initialized and

used to select a "working array" of digits. The algorithm starts by finding a the digit in the working array with the maximum energy deposit and it works as the seed digit. For selection, the energy of the digits have to be above the minimum energy threshold (E_{th} = 500 MeV used for this analysis). The neighbouring digits to the seed digits which are above the threshold energy are associated to the cluster. Neighbouring digits are the adjacent digits, which share a common edge with the seed. The digits added to the cluster are removed from the working array to ensure that no two clusters contain the same digit. The algorithm continues to look for neighbours of the digits already added to the cluster. This process continues till no more neighbour digits are present in the working array. Once the cluster is formed and there are still remaining digits in the working array, the clustering algorithm starts again to check for new seeds and its neighbouring digits to form new cluster and the process continues till no seed digits are available in the array. The algorithm of *Clusterizer V2* is similar to *Clusterizer V1*, however, energy of neighbouring digit should be smaller in order to become a neighbour. Figure 2.11 shows the *V1* and *V2* clusterization algorithms. Boxes represent energy in cells and E_{th} is threshold energy for clusterization. The top panel (a) represents the energy in cells before clusterization. Bottom left panel (b) shows result of *Clusterizer V1*. There is one big cluster made of cells in blue colour. Bottom right panel (c) shows result of *Clusterizer V2*. There are two clusters made of blue and orange cells. In both the bottom panels the green cells are below threshold and not associated to any cluster. In the analysis presented in this thesis, the *Clusterizer V2* has been used for obtaining the final results.

Shower Shape of clusters

The lateral shape of showers in the η-ϕ plane of the EMCal is used as an additional parameter to differentiate electrons from neutrons and hadrons. The shower shape is characterized by the squared eigenvalues of the dispersion matrix of the shower shape ellipse, obtained from the energy distribution of the individual detector cells [103]. A toy model of such

a cluster is shown in figure 2.12 [104]. The short and the long axes of the ellipse are known as λ^2_{short} (M20) and λ^2_{long} (M02) respectively. Neutrons hitting the readout electronics of the scintillator in the EMCal produce abnormal high energy signals which tend to be mainly localized in one cell with a few surrounding low energy cells [105]. Hence, a lower threshold of shower shape axis is applied (e.g. $\lambda^2_{\text{long}} > 0.1$) to eliminate contamination due to contributions from neutrons. At high p_{T} ($p_{\text{T}} \gtrsim 10$ GeV/c) the shower shape parameter is also

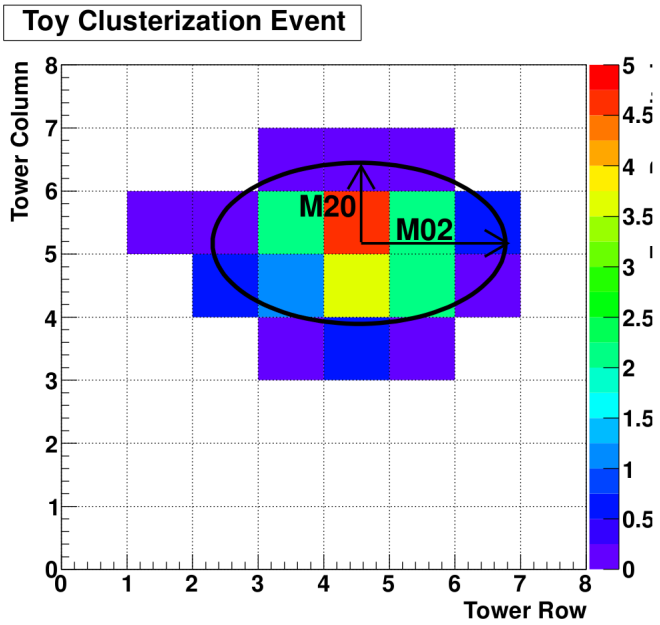

Figure 2.12: A sample of clusterization event. The cluster is fitted with a ellipse and the two axes are labelled M02 and M20. Each square corresponds to a tower/cell [104]

used to reject contribution from hadrons such as neutral pions [105]. Neutral pions decay into pairs of photons which can produce overlapping showers and hence can be reconstructed into a single elongated cluster. A p_{T} dependent higher threshold of the shower shape parameter has been used in the analysis to reduce contributions from such contaminations. The details of the quantitative values are shown in chapter 3. More detailed discussions on the shower shape parameters can be found in [104].

Chapter 3

p_{T}-differential cross section of electrons decayed from heavy-flavour hadrons

In this chapter, the p_{T}-differential cross section of electrons decayed from heavy-flavour hadrons obtained from the analysis of pp collisions at $\sqrt{s} = 13$ TeV, recorded by the ALICE experiment at the LHC, is presented in p_{T} range 0.5 GeV/c to 35 GeV/c. The p_{T}-differential cross section from data has also been compared with perturbative QCD model predictions.

3.1 Introduction and analysis strategy

In ALICE, open heavy-flavour production is investigated with the following complementary approaches, via fully reconstructed hadronic decays, or via the measurement of leptons from leptonic or semi-leptonic heavy-flavour hadron decays. A brief discussion on the decay modes of heavy-flavour hadrons are given in section 1.5.2. In this analysis, the study is done through the semi-leptonic decay channel where the heavy-flavour mesons decay into a

lepton + neutrino + hadron(s) through weak interaction.

$$\mathrm{B, D} \rightarrow \mathrm{e} + \nu_{\mathrm{e}} + \mathrm{X} \qquad \mathrm{BR} \sim 10\%$$

Due to this missing neutrino, the momentum of the parent particles cannot be reconstructed, to identify the heavy-flavour decay electrons. Hence, to select the heavy-flavour decay electrons, the non-heavy-flavour electron background is subtracted from inclusive electrons sample.

The electron identification in low and intermediate p_{T} (0.5 GeV/c < p_{T} < 4 GeV/c), is ensured by the Time Projection Chamber (TPC) and Time-Of-Flight (TOF) detectors and in the high transverse momentum (3 GeV/c < p_{T} < 35 GeV/c) by the TPC and Electromagnetic Calorimeter (EMCal). The Inner Tracking System (ITS) is used for vertex determination and, together with the TPC for tracking in the mid rapidity region. The charged particle identification (PID) in the TPC is based on the specific energy loss measurement (dE/dx) of a particle in the gas detector while the TOF detector uses the time of flight of the charged particle. For the low and intermediate p_{T} range the electron sample is selected within the optimized TOF PID cut $|n\sigma_e^{\mathrm{TOF}}| < 3$ where $n\sigma_e$ is the difference of the measured signal in the detector from the expected value for electrons in terms of units of variance. To remove the hadron contamination from the sample, the TPC nσ (dE/dx - $\langle$dE/d$x\rangle$ in terms of the dE/dx resolution) is evaluated in several momentum slices and the resulting plots are fitted with Gaussian functions for electrons and protons, kaons and a convolution of Landau and exponential function for pions. The electron sample is selected within the TPC PID interval -1 < $n\sigma_e^{\mathrm{TPC}}$ < 3. In the high transverse momentum region, the discriminating variable based on the energy deposited in the EMCal, i.e., the E/p and shower shape parameter ($\lambda^2_{\mathrm{long}}$), have been used along with the TPC PID selection ($n\sigma_e^{\mathrm{TPC}}$) to identify electrons. The optimized values of -1 < $n\sigma_e^{\mathrm{TPC}}$ < 3, 0.85 < E/p < 1.2 and a p_{T}-dependent $\lambda^2_{\mathrm{long}}$ selection criteria have been used for electron selection.

To obtain the yield of electrons from the heavy-flavour decays, the non-heavy-flavour background sources are subtracted from the inclusive electron spectra. The photonic background electrons mainly come from the Dalitz decay of light neutral mesons (π^0 and η) and γ conversions in the detector material. To identify electrons from the photonic sources, opposite signed partners (e^- e^+) are paired in an invariant mass spectrum. While the unlike sign (ULS) pairs give both the correlated signals from actual decay (π^0 and η), γ conversions and uncorrelated combinatorial background, the like sign (LS) pairs are used to estimate and subtract the random combinatorial background.

The non-heavy-flavour contribution is subtracted from the inclusive electron sample and is corrected for tracking, particle identification selection criteria as well as the detector acceptance and efficiency losses using monte-carlo samples. The contributions from W, Z $\rightarrow$ e, which form a significant contamination at sufficiently high p_{T} ($p_{\mathrm{T}} >$ 20 GeV/c) and estimated using PYTHIA + POWHEG simulations, is subtracted from the above yield to obtain the final heavy-flavour hadron decay electron spectra.

3.2 Data sets and number of events

During the raw data collection from the collisions, the data-taking configurations are reset under software control from time to time [106]. When this happens, a new 'run' is started which is identified by a 'run number' and the run number increases at the start of each 'run'. The huge amount of data collected over the years (from 2015 to 2018 for Run-2 data taking at the LHC) are grouped into the so-called 'production cycles' or 'data taking periods'. For each of the data taking periods the list of run numbers (run-list) are taken from [107] with detector requirement SSD, SPD, SDD, V0, TPC, EMC for the TPC–EMCal analysis and SSD, SPD, SDD, V0, TPC, TOF for the TPC–TOF analysis. The following production cycles/periods have been used in this analysis:

2016 (pass1): d, e, g, p, o, i, j, h;

(pass2): l, k ;

2017 (pass1): c, f, h, i, j, k, i, m, o, r ;

2018 (pass1): b, d, e, f, h, l, g, i, m, n, o, p ;

As already mentioned in section 2.3, the raw data obtained from the detector systems are processed such that the data is stored in the form of events in Event Summary Data (ESD) and Analysis Object Data (AOD) files which can be used for further analysis. This processes which include alignment, calibration, simulation, reconstruction etc. are done through few successive reconstruction passes [71]. During the first pass reconstruction, also known as 'pass1', high-precision alignment and calibration data are produced. The feedback obtained from analysis of the data from the first pass, is used to tune the parameters for a second pass processing (pass2). Depending on the limited computing resources available and the large number of jobs required for processing the data, a third reconstruction pass (pass3) may be performed for completing the tuning of the data.

While for the TPC–TOF analysis all of the above production cycles have been used, for the analysis using the TPC–EMCal detectors the only 2016k, 2016l and all cycles from 2018 have been used. The other production cycles from 2016 have not been used as the statistics in the triggered samples are not ample due to which the rejection factor could not be accurately determined. The triggers and calculation of rejection factor has been discussed in section 3.3.2. The cycles from 2017 have also been omitted from the TPC–EMCal analysis as quality assurance checks have shown a deviation of TPC calibration at high p_{T}. Moreover, the 2016k, 2016l and all cycles from 2018 provide adequate statistics for the analysis resulting in a reasonable statistical uncertainty on the results.

General purpose and enhanced monte-carlo (MC) productions have been used for obtaining efficiencies. Enhanced monte-carlo samples are used in the TPC–EMCal analysis as the statistics of electrons decreases with increasing p_{T} in the general purpose MC, similar to that of minimum bias data. In the enhanced monte-carlo samples the number of π^0 and η have been enhanced with respect to the minimum bias sample to increase the statis-

tics of electrons from their decays at high p_{T}. The samples also have charm and beauty enhancement to increase the statistics of electrons from heavy-flavour hadron decays.

The cross section (σ) for pp collisions at $\sqrt{s} = 13$ TeV is 57.8± 2.9 mb [108]. The number of events is defined as $N = \sigma \int \mathcal{L}dt$, where $\int \mathcal{L}dt$ is the integrated luminosity. The number of events selected from the pp collisions for different triggers (minimum bias and EMCal triggers) are listed in table 3.1. The triggers used in this analysis have been discussed in section 3.3.2.

Table 3.1: Number of selected events in pp collisions for different triggers

	TPC–TOF	TPC–EMC		
Trigger	MB	MB	EG2	EG1
Number of events ($\times$ 10^6)	1755	700	48	38

3.3 Heavy-flavour hadron decay electron spectra using TPC–EMCal:

3.3.1 Event selection

The event selection criteria used in this analysis to select relevant events for study has been discussed in this section. Events are selected using different triggers depending on the p_{T} range of analysis. A trigger is used to select relevant and interesting events based on the requirements of the analysis. The collision rate in ALICE is very high and a trigger system is used to select the relevant parts of the incoming data in ALICE containing the physics information of interest which is later stored for analysis.

The minimum bias trigger, as the name suggests, are inelastic events selected with as little bias as possible. In ALICE, the minimum bias trigger selection (kINT7 trigger) requires a hit on both sides of the V0 disks, i.e., both V0A and V0C (V0AND). The minimum bias trigger warrants that the collision has happened. For this analysis, the kINT7 trigger was

used for analysis in the region $p_{\mathrm{T}} \lesssim 6$ GeV/c. For analysis in the high p_{T} region ($p_{\mathrm{T}} \gtrsim 6$ GeV/c), where the statistics in the minimum bias event is not sufficient the EMCal triggers are used. As already mentioned in section 2.2.4 of chapter 2, 'EMCal' would imply both the EMCal and DCal detectors unless explicitly mentioned otherwise. The EMCal triggers are used to select events consisting mostly of high p_{T} particle. A criteria is set on the total amount of energy deposited in the detector as the trigger condition. For this analysis, the EMCal L1 gamma trigger (kEMCEGA) [109] with two trigger thresholds has been used. The lower threshold ($\sim$ 4.5 GeV) is known as the EG2 trigger and the higher threshold ($\sim$ 10 GeV) is known as the EG1 trigger.

A selection criterion on the primary Z vertex position (z_{vtx}) from the centre of the ALICE detector system is applied along the beam direction to ensure uniform reconstruction efficiency of the charged particles. The primary Z vertex range is taken to be $\pm$ 10 cm.

Events were also selected based on the number of contributors to primary vertex. Events with at least two contributors to primary vertex from track (SPD vertex) were used for the analysis. In many cases due to missing tracklets/tracks, vertices have contributors < 1 and the vertex reconstruction fails. Vertices with one contributor have the transverse coordinates of the mean vertex and the Z coordinate determined from the only track/tracklet is available. Hence, a minimum of two contributors has been considered.

Events with pile-up are also removed. Pile-up refers to multiple collisions being recorded as a single event. There are two main categories of pileup: same-brunch-crossing pileup, where more than one collision occurs in the same bunch crossing and out-of bunch pileup, where one or more collisions occur in bunch crossings different from the one which triggered the data acquisition. The in-bunch pile-up events are especially high in high-luminosity experiments. Pile-up events are rejected at the physics selection level if another collision occurs in a given time window before and after the trigger. The SPD vertexer in pp collisions is also used to tag pile-up events based on the multiple reconstructed vertices. An event is tagged as pileup if more than one vertex is present. After finding the first vertex, coined as

the "main" vertex, the tracklets which do not point to this "main" vertex are used to check if there are other vertices from which particles originate. Table 3.2 summarizes the event selection criteria applied in this analysis.

Table 3.2: Event selection criteria

Event selection :	Values :
Trigger	kINT7 (MB), kEMCEGA (EG2 and EG1)
Primary Z vertex range	± 10 cm
Min. no. of contributors to primary vertex	2
Pile-up rejection	Applied

3.3.2 EMCal triggers and trigger rejection factor

Figure 3.1 shows the energy distributions of the EMCal clusters, which are matched with the tracks from TPC, for the MB, EG2, EG1 triggers. With the triggered events, the events which have high cluster energy (and consequently high p_{T}) are enhanced. The triggered events increases the statistics of electrons at high p_{T} compared to the minimum bias events. Hence, the p_{T} differential spectra of particles for these events are normalized with a factor, to make them equivalent to minimum bias, which is known as the trigger rejection factor (R).

The trigger rejection factor (R) is defined according to the formula in equation 3.1.

$$\begin{aligned} R &= \frac{\text{Cluster energy distribution in EMCal triggered events}}{\text{Cluster energy distribution in MB triggered events}} \frac{N^{\mathrm{MB}}_{\mathrm{events}}}{N^{\mathrm{EMC}}_{\mathrm{events}}} \\ &= S.\frac{N^{\mathrm{MB}}_{\mathrm{events}}}{N^{\mathrm{EMC}}_{\mathrm{events}}} \end{aligned} \tag{3.1}$$

where S is the ratio of cluster energy distributions without event normalisation and $N^{\mathrm{MB}}_{\mathrm{events}}$, $N^{\mathrm{EMC}}_{\mathrm{events}}$ are the number of events in minimum bias and EMCal triggered samples respectively. The value S is required for the multiplicity analysis (in chapter 4) and is a constant for all multiplicity bins as shown in section 4.3. The rejection factor (R) is obtained from the

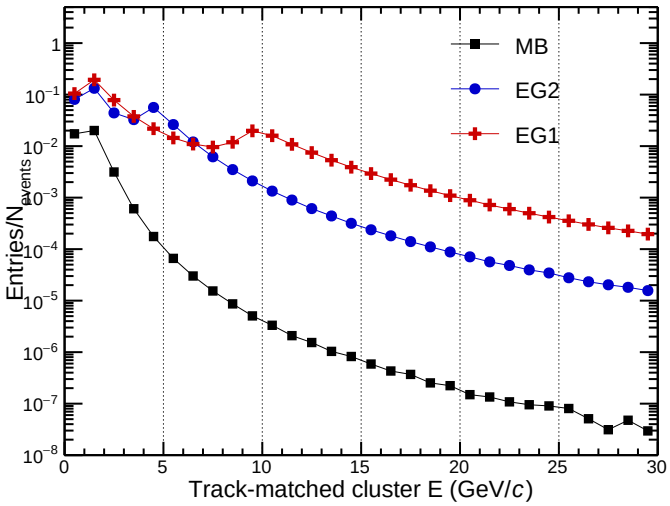

Figure 3.1: Energy distribution of EMCal clusters (which are matched with tracks from TPC) for different triggers (MB, EG2, EG1)

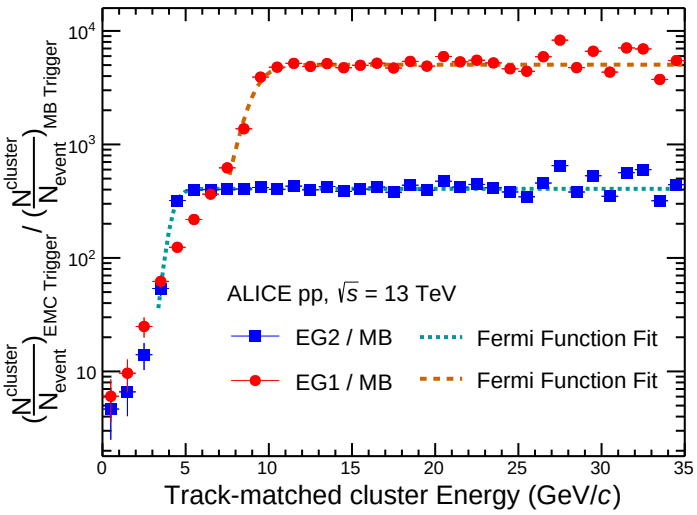

Figure 3.2: Trigger rejection factor for EG2 and EG1 triggers

trigger turn-on curves in figure 3.2 shown for the EG2 and EG1 triggers. The flat shape of the curve shows the stability of trigger performance. The rejection factor is obtained by fitting the turn on curves from trigger threshold up to higher p_{T} where the distribution flattens with a Fermi function [110, 111]. Table 3.3 shows the final value of the trigger rejection factor used in this analysis for the the combined data sets of 2016 and 2018. The

R values have been chosen from the best fit of the function. Systematic uncertainty on the trigger rejection factor, obtained by varying the fit range and fit function, are shown in section 3.5.

	Triggers	
	EG2	EG1
Rejection Factor (R)	406 ± 12	5040 ± 202

Table 3.3: Trigger rejection factors for EG2 and EG1 triggers in pp collisions at $\sqrt{s}$ = 13 TeV

Cross-check between individual periods :

Figure 3.3 shows the trigger turn on curves for the EG2 (left) and the EG1 (right) triggers for the individual run cycles/periods used in this analysis. It can be seen the rejection factor values are similar among the individual periods. There are statistical variations which are attributed to decreased statistics in the MB sample in few periods.

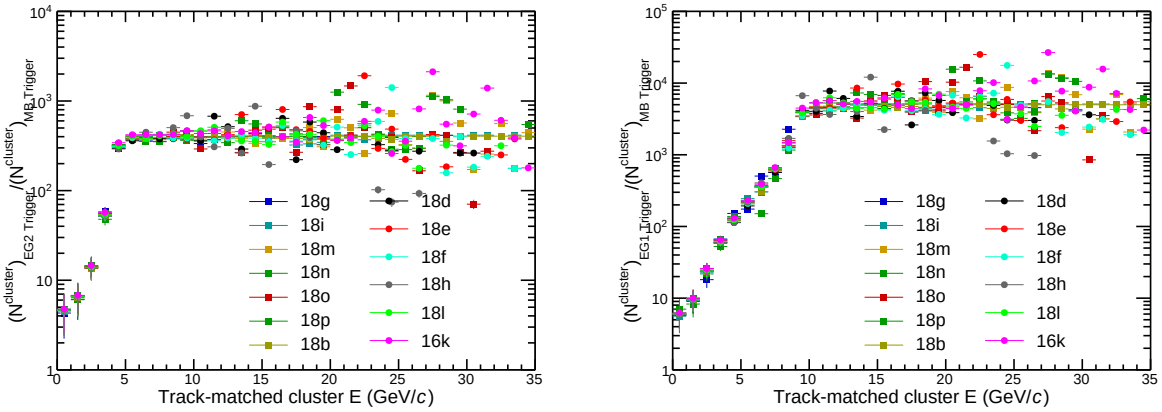

Figure 3.3: Rejection factor plot for individual periods. Left: EG2, Right : EG1

Cross-check with other analysis in ALICE in pp collisions at $\sqrt{s}$ = 13 TeV:

The trigger rejection factor obtained in the study was cross checked with the other analyses in ALICE in pp collisions at $\sqrt{s}$ = 13 TeV to ensure consistency between the different

analysis in ALICE. A comparison of the rejection factor values has been performed with the J/ψ analysis results in pp collisions at $\sqrt{s}$ = 13 TeV [66]. The values of rejection factors are in good agreement between the analyses, within 3%, for both EG2 and EG1 triggers.

3.3.3 Track selection criteria and electron identification

Track selection criteria:

Each track was subjected to a set of track selection criteria, usually known as "cuts", to select a high purity electron samples by rejecting fake and uncorrelated tracks which produce signals in the detector. The following track selection cuts are applied, summarized in table 3.4. Filter bits correspond to a given set of cuts. The filter bit AliAODTrack::kTrkGlobalNoDCA

Table 3.4: Track Selection

Track Cuts :	**Selection Values :**
FilterBit	AliAODTrack::kTrkGlobalNoDCA
$\|\eta\|$	≤ 0.6
No. of TPC CrossedRows	≥ 70
Number of TPC Clusters for dE/dx calculation	≥ 80
Ratio of TPC Crossed Rows (Found/Findable)	≥ 0.8
Number of ITS Clusters	≥ 3
Hits on layers of SPD	kAny
ITS and TPC Refit	Required
DCA$_{xy}$	≤ 1 cm
DCA$_z$	≤ 2 cm
χ^2 /clusters of the momentum fit in the TPC	≤ 4
Kink Candidates	Rejected

is a standard cut set with very loose distance of closest approach selection value. A pseudo-rapidity range of $|\eta| < 0.6$ is applied to ensure a uniform track reconstruction efficiency. A charged particle passing through the TPC deposits energy which creates signal in the pad-rows of the TPC. If the deposited energy exceeds a certain threshold, it is called a cluster. There can be a maximum of 159 clusters per track which is also equal to the number of

pad-rows in a given TPC sector. The pad length of the TPC increases with radial distance. The number of crossed rows which is equivalent to the effective cluster track length is used as a selection criteria of electrons. Number of crossed rows is defined as number of clusters plus number of missing clusters. It can so happen that few findable clusters are missing due charges being deposited below threshold due to baseline shifts etc. Those clusters can be identified by checking the neighboring clusters e.g., if no reconstructed cluster is found on pad-row 'i', however, clusters are found in pad-rows 'i-1' and 'i+1', pad-row 'i' is considered as a missing cluster. A threshold of minimum 70 crossed rows is used for track selection in this analysis. The clusters at the sector edges of the TPC or overlapping tracks are not considered for the $\mathrm{d}E/\mathrm{d}x$ calculation, as the edge effects can distort the $\mathrm{d}E/\mathrm{d}x$ measurement. The average number of clusters per track is higher for electrons on an average than hadrons since the electron tracks are already on their fermi plateau region, in momentum regions where the hadron fermi plateau is not reached yet. Thus, a high number of clusters are required for the reconstruction of the track. A minimum of 80 clusters is required for $\mathrm{d}E/\mathrm{d}x$ calculation for particle identification. It takes into account the limited η-acceptance or dead zones due to chamber boundaries. A minimum cut of 0.8 on the ratio of the number of found TPC cross rows divided by the number of findable clusters is applied. A minimum of 3 ITS clusters is required to ensure rejection of fake tracks especially at the low p_{T} regions. Additionally, at least one hit on any layer of the SPD is required. The final refit of the global track with the kalman filter back to the identified primary vertex is required to pass the ITS and TPC for each track candidate. The number of findable clusters is the number of geometrically possible clusters which can be assigned to a track. Cuts in the distance of closest approach (DCA) in the transverse plane (xy) as well as in the beam direction (z) to the primary vertex for a track is applied to distinguish tracks (form the primary vertex) from the ones coming originating from decays of strange hadrons or interactions with the beam. A cut on the χ^2 per degree of freedom (χ^2/ndf) of the momentum fit in the TPC is applied to each track to suppress contribution of random uncorrelated combination of

clusters in TPC during momentum reconstruction. Tracks which are not consistent with the track model of continuous particle trajectories and show deviations due to emission of bremsstrahlung or due to decays in flight, also known as kink candidates were discarded from the analysis. The TPC dE/dx resolution of kink tracks are poor compared to those of regular tracks.

Track-cluster matching criteria:

As EMCal detects particles which primarily interact through electromagnetic forces, it is used for detection and analysis of electrons as well as photons. To select electrons and distinguish them from photons in the EMCal, the tracks from the TPC are matched to the clusters in EMCal, as photons do not form tracks in TPC. The difference in the ϕ and η of projection of charged particle tracks from the TPC on the EMCal surface and the reconstructed cluster in the EMCal is taken to be smaller than 0.01 for selecting electrons.

Table 3.5: Track-Cluster match cuts

Track-Cluster match :	Selection values :
$\Delta\eta$	≤ 0.01
$\Delta\phi$	≤ 0.01

Electron identification criteria:

The charged particle identification (PID) in the TPC is based on the specific energy loss measurement (dE/dx) of a particle in the gas detector, which has been discussed in details in the section 2.2.2 of chapter 2. The electron sample is selected within the TPC PID cut -1$< n\sigma_e^{\mathrm{TPC}} <$ 3 where nσ is defined as the difference between of the measured signal from the expected calculations in terms of the detector resolution. Hadron samples, used for estimating contamination in the electron sample, are selected within $n\sigma_e^{\mathrm{TPC}} <$ - 3.5. EMCal is used to identify electrons at high p_{T} as merging of the dE/dx bands of electrons, muons,

pions, and other hadrons limits the particle identification at high momentum ($p \gtrsim 6$ GeV/c), as seen in figure 2.5 of chapter 2. E/p, where E is total energy deposited by the electrons in the EMCal and p is the momentum from TPC, is used as the discriminating variable to select electrons from hadrons. An optimized cut of $0.85 < \mathrm{E}/p < 1.2$ is used to select electrons as they are expected to deposit all their energy in the EMCal through electromagnetic interactions. The E/p distributions are shown in figure 3.4. As the momentum range

Table 3.6: Particle identification cuts for hadron and electron selection

	Electron selection values:	Hadron selection values:
TPC nσ	-1 < nσ_e^{TPC} < 3	nσ_e^{TPC} < -3.5
E/p	0.85 <E/p < 1.2	Varied between range E/p < 0.7
Shower shape	$0.02 < \mathrm{M}_{02} < 0.9$ ($p_{\mathrm{T}} < 12$ GeV/c)	same as
(σ^2_{long} or M_{02})	$0.02 < \mathrm{M}_{02} < 0.7$ ($12 < p_{\mathrm{T}} \leq 20$ GeV/c)	electron
	$0.02 < \mathrm{M}_{02} < 0.5$ ($p_{\mathrm{T}} \geq 20$ GeV/c)	

increases, the E/p peak of the hadrons tends to move towards the electron E/p. The separation of the electrons from hadrons using only the $n\sigma_e^{\mathrm{TPC}}$ and E/p selection criteria becomes more critical. Hence, the shower shape parameter (λ_{long}, M02), an additional property from EMCal cluster, has been used to improve the signal/background and to select higher electron purity sample. A lower threshold of $\lambda_{\mathrm{long}} > 0.02$ has been used to remove contributions from neutron hitting the detector readouts. A higher p_{T}-dependent selection criteria of $\lambda^2_{\mathrm{long}} < 0.9, 0.7, 0.5$ for $p_{\mathrm{T}} <$ 12 GeV/c, 12 GeV/c < p_{T} < 20 GeV/c and $p_{\mathrm{T}} >$ 20 GeV/c respectively has been applied to reduce contamination from neutral pion and other hadron decays. Details on the EMCal and shower shape parameters have been discussed in sections 2.2.4 and 2.3.5 respectively. The electron identification cuts for particle identification using TPC and EMCal are shown in table 3.6.

3.3.4 Inclusive electron selection using the E/p distribution

The left panels of the figure 3.4 show the E/p distributions of electron and hadron candidates in various p_{T} ranges. The E/p distribution of the raw counts of electron candidates obtained

after applying the $n\sigma_e^{\mathrm{TPC}}$ and σ^2_{long} selection for electron identification as mentioned in table 3.6 (represented by the red curve) has contribution from hadron contamination, which is clearly evident in the region E/p < 0.7 and is especially dominant in the high p_{T} intervals. To remove the contamination of hadrons in the electron sample, the E/p distributions of hadrons, selected using $n\sigma_e^{\mathrm{TPC}}$ < -3.5, is scaled to that of the electrons (represented by the gray curve). The right panels of the figure 3.4 shows the ratio of the hadron E/p distribution to the electron candidate E/p distribution. The scaling factor is chosen in a region within E/p < 0.7 from the ratio plots where the it is almost flat, indicating that the contribution in that region is almost fully due to hadrons. The scaled E/p distribution representing the hadron contamination (gray curve) is statistically subtracted from the electron candidate (red curve) to obtain the pure electron sample (represented in blue in the left panels of figure 3.4). The inclusive electron spectra is obtained after taking the integral of the contamination subtracted electron E/p distribution within 0.85 < E/p < 1.2 for each p_{T} interval.

3.3.5 Background non-heavy-flavour electrons selection (Photonic electrons)

The following data driven statistical method is used to identify and subtract the non heavy-flavour decay electrons from the inclusive sample of electrons to obtain the heavy-flavour decay electron spectra. The sources of background non-heavy-flavour decay electrons are listed below. The majority and the most dominant source of the background electrons (> 90 % especially at low and mid p_{T}) are the:

- **Photonic electrons,** which comes from:
  - decay of light neutral mesons such as π^0 ($\mathrm{m}_{\pi^0} \sim 140$ MeV/c^2) , η ($\mathrm{m}_{\eta} \sim 548$ MeV/c^2)
    - Dalitz decay : e.g., $\pi^0 \rightarrow e^- e^+ \gamma$,
    - 2 γ decay of π^0: e.g., $\pi^0 \rightarrow \gamma\gamma$

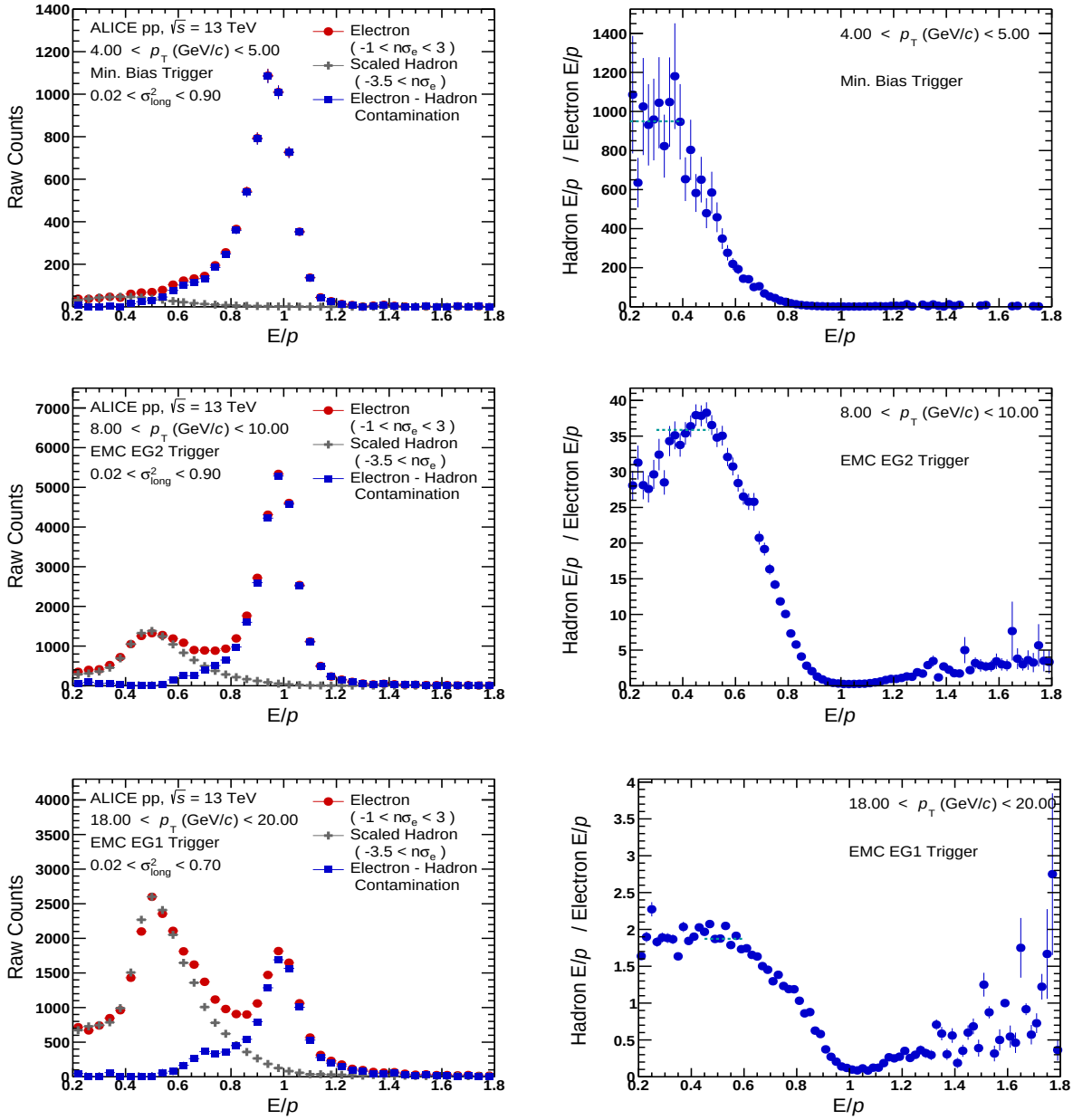

(a) E/p distribution (b) Ratio of hadron and electron E/p distribution

Figure 3.4: The E/p distributions and ratio for scaling hadron E/p for different p_{T} bins

• γ conversions : Most γ from π^0 convert into the detector material, as well as from prompt virtual and real photons from thermal and hard scattering processes : $\gamma \rightarrow e^- e^+$

For π^0 the branching ratio for the 3-body dalitz decay into $e^-e^+\gamma$ and the decay in to 2 γ together is $\sim 99.996\%$ [39]. The electrons from these sources are called **photonic electrons** as a photon (real or virtual) is involved in the production of the electron. The photonic electrons are estimated using a data-driven method, photonic electron tagging method, which is described in this section.

Rest of the sources of non-heavy-flavour decay electrons are :

- Di-electron decays of light vector mesons : ρ, ϕ, ω. [total spin 1 and odd parity]
  This has a negligible contribution [112]. Although they contribute to the background through dalitz and/or di-electron decay channels and conversion of photons, none of the contributions are of any practical importance compared to the π or η meson.

- Di-electron decays of quarkonia (J/ψ, Υ) [113] has a negligible contribution to the background.

- Electrons from weak decays of $\mathrm{K}^{0/\pm}$: The relative contribution from K_{e3} decays to the electron background is negligible [30, 114].
  $\mathrm{K}^0 \to \pi^{\pm}e^{\mp}\nu_e^{(-)}$ $\quad$ $\mathrm{K}^{\pm} \to \pi^0 e^{\pm}\nu_e^{(-)} \to$ called $\mathrm{K}^{\pm}_{e3}$

- **Electrons from of $\mathrm{W}^{\pm}$ and Z bosons**: e.g., $\mathrm{W}^- \to e^-\bar{\nu_e}$
  The contribution of electrons from these decays has non-negligible effect at high p_{T} ($p_{\mathrm{T}} > 20$ GeV/c). This contribution has been calculated in section 3.3.8.

- Partonic hard scattering processes such as the Drell-Yan process

The photonic electron tagging method is used to estimate and subtract the photonic electrons from the inclusive sample. The photonic electrons are always created in pairs of an electron (e^-) and a positron (e^+). To identify electrons from the photonic sources, all opposite signed partners ($\mathrm{e}^-\mathrm{e}^+$) from the inclusive electron sample are paired in an invariant mass (m_{ee}) spectrum, as shown in figure 3.5. This unlike sign paired spectrum (ULS, $\mathrm{e}^-\mathrm{e}^+$)

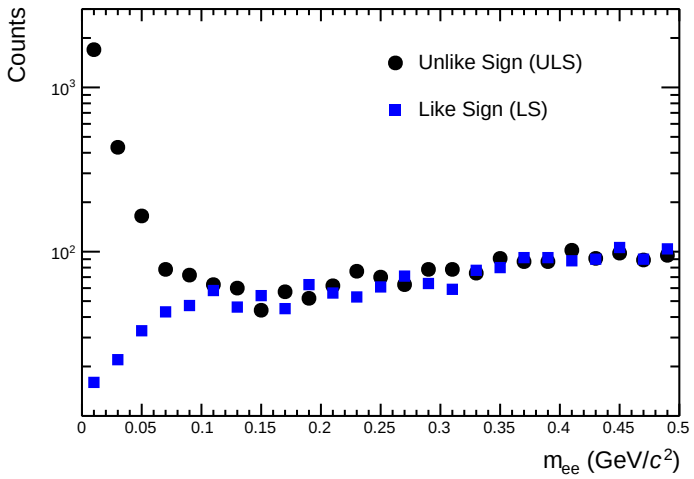

Figure 3.5: Invariant mass spectra from unlike and like sign data

consists of correlated pairs of e^- and e^+ from actual photonic decay and random uncorrelated pairs (represented in black in figure 3.5). To separate and subtract the random combinatorial background, like signs (LS, e^-e^- and e^+e^+) are paired in the invariant mass spectrum (represented by the blue plot in figure 3.5) since the actual decays particles into e^-e^- and e^+e^+ is highly suppressed in nature. The raw photonic electrons are given by :

$$N^{raw}_{photonic} = N_{\mathrm{ULS}} - N_{\mathrm{LS}}$$

where N_{ULS} andN_{LS} are the number of unlike-sign and like-sign pairs selected respectively. The invariant mass spectrum of both the ULS and LS pairs is a continuum. Since the invariant mass of a photon is zero ($m_0^2|_\gamma = E^2 - |p|^2 = 0$), the spectrum shows a peak as it approach towards zero. The invariant mass of the e^-e^+ pair is always less than or equal to the mass of the mother hadron. The ULS and LS pairs are selected within invariant mass, $m_{ee} < 0.14$ GeV/c^2 ($\sim m_{\pi_0}$). To select the pair candidate (associated track) for each track from the inclusive sample of electrons, certain track selection cuts are applied, which is summarized in table 3.7. To maximize the probability of finding the associated partner tracks, these track selection cuts are less stringent than the primary track selection cuts shown in table 3.4.

Table 3.7: Associated track selection criteria and values

Track cuts :	Selection values :
FilterBit	AliAODTrack::kTrkTPCOnly
Number of TPC Clusters	≥ 60
Number of TPC Clusters for PID	≥ 60
ITS and TPC Refit	Required
DCA_{xy}	≤ 1 cm
DCA_{z}	≤ 2 cm
χ^2 /clusters of the momentum fit in the TPC	≤ 4
TPC nσ	$\pm 3.5\sigma$
p_{T} range	0.1 GeV/c
$\lvert\eta\rvert$	≤ 0.9

3.3.6 Tagging efficiency

All photonic decays do not get identified in the data as there can be photonic pairs where respective partner may be outside detector acceptance, did not pass necessary thresholds, or was not selected during the track reconstruction. Hence, the raw number of photonic electrons is corrected with the tagging efficiency (ϵ_{tag}), where ϵ_{tag} is the efficiency of tagging the photonic electrons and is obtained from monte-carlo (MC) sample. The tagging efficiency is defined as the ratio of the true number of photonic pairs from the same mother ($\mathrm{N}^{\mathrm{true,pairs}}_{\mathrm{found}}$) which have passed the associated track selection cut and the total number of electrons (positrons) from photonic origins ($\mathrm{N}^{\mathrm{photonic}}_{\mathrm{total}}$), both obtained from MC sample.

$$\epsilon_{tag} = \frac{N^{\mathrm{true,pairs}}_{\text{found from same mother}}}{N^{\mathrm{photonic}}_{\mathrm{total}}}$$

In order to consider only the electrons coming from the real primary π^0, η and γ the contributions from π^0, η and γ coming from feed-down of light meson and from charm and beauty contribution are rejected. The following sources of photonic electrons have been considered:

$\eta \to e, \quad \eta \to \pi^0 \to e, \quad \eta \to \gamma \to e, \quad \eta \to \pi^0 \to \gamma \to e, \quad \pi^0 \to e, \quad \pi^0 \to \gamma \to e$

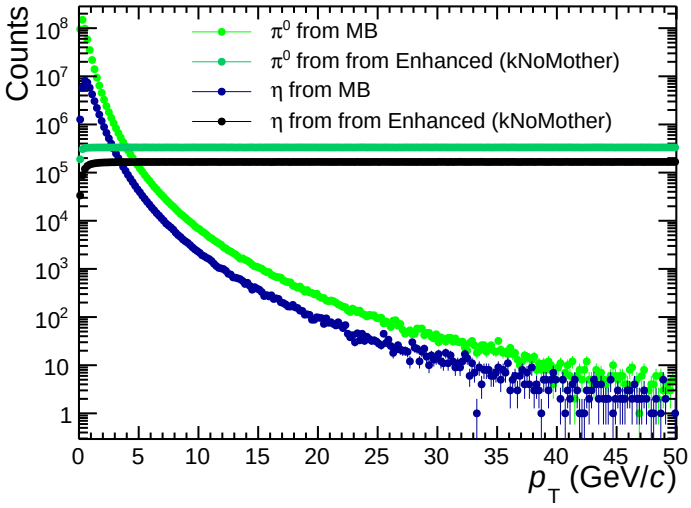

Figure 3.6: p_{T} distribution of π^0 and η from minimum bias events and embedded events

An enhanced MC sample is used for the calculation of the efficiencies at the high p_{T} ranges

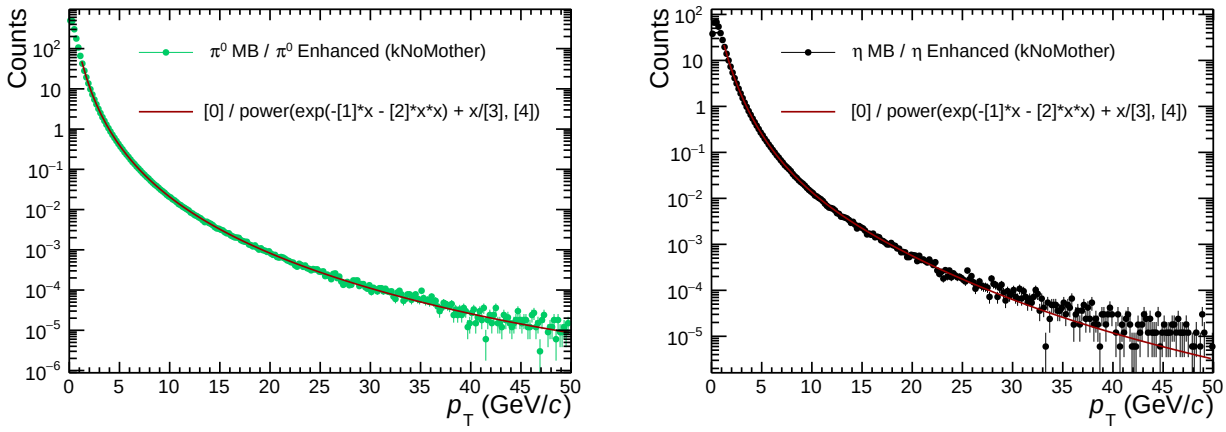

Figure 3.7: Weights for π^0 and η

to reduce the statistical uncertainty which arises from using general purpose MC at such high p_{T}. Figure 3.6 shows the p_{T} distributions of π^0 and η from monte-carlo (PYTHIA event generator) in minimum bias process as well as with the enhanced part where extra π^0 and η have been embedded. In a general purpose MC cycle particle productions are simulated according to the minimum bias process, similar to those of minimum bias collisions in data. Hence as the p_{T} increases the number of particles steeply decreases. In an enhanced MC, the number of π^0 and η are enhanced with respect to the minimum bias process such

that the number of π^0 (η) remains constant with increasing p_{T}, as shown in figure 3.6. For calculating the tagging efficiency, the enhancement of π^0 and η has been taken into consideration. Weights are calculated from the ratio of the π^0 and η obtained from the MB process with respect to that from the embedded (enhanced) samples. Figure 3.7 shows ratio

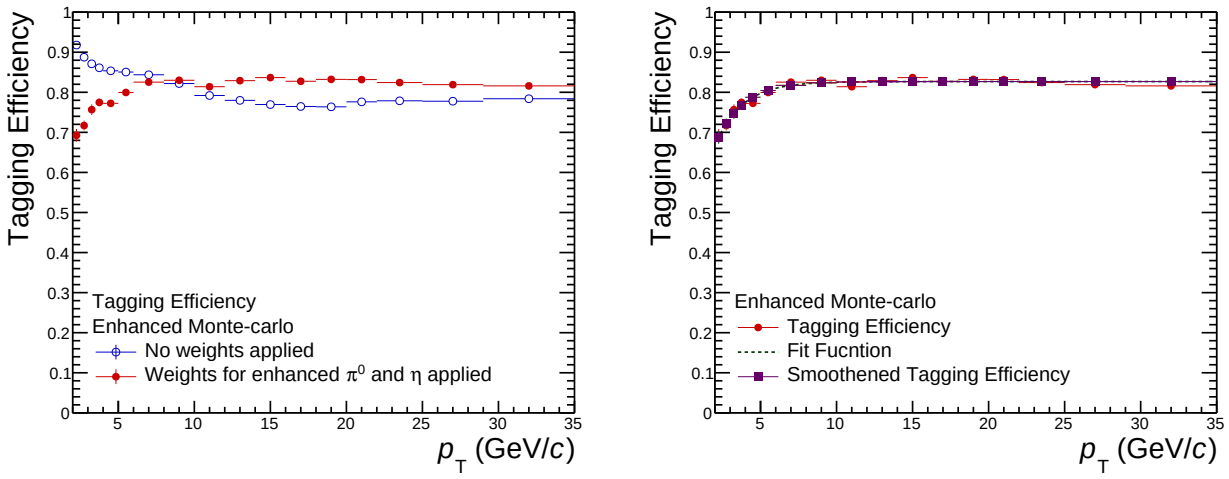

Figure 3.8: Tagging efficiency for photonic electrons

of minimum bias spectra with respect to that of the enhanced spectra for π^0 (left) and and η (right). The ratio plots are fitted with a Hagedron function which gives the weight at a particular p_{T}. When calculating the tagging efficiency, these weights are applied to the spectra of the enhanced sample of electrons coming from decays of π^0 and η to remove any bias arising from their enhancement. The tagging efficiency before and after the weighting procedure is shown in the left panel of figure 3.8. The tagging efficiency is smoothened using a Fermi function [110, 111] to even out any fluctuations due to statistical variations, as shown in the right panel of figure 3.8.

3.3.7 Reconstruction efficiency

The heavy-flavour hadron decay electron spectrum from data has been corrected for track & particle identification selection criteria, and detector inefficiencies and acceptances using the reconstruction efficiency. The heavy-flavour hadron decay electron reconstruction efficiency

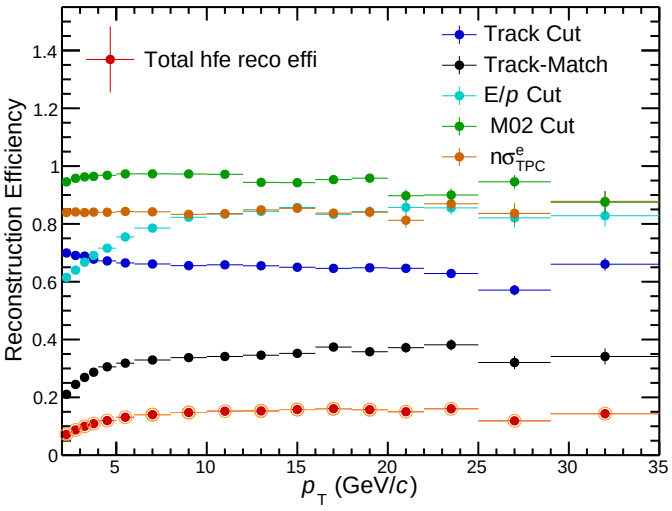

Figure 3.9: The total reconstruction efficiency for the heavy-flavour hadron decay electrons from MC

($\epsilon_{\mathrm{reco}}^{\mathrm{c,b\to e}}$) is the ratio of the heavy-flavour hadron decay electrons after passing through all the geometric, track and particle identification cuts to the generated heavy-flavour hadron decay electron counts both obtained from monte-carlo sample within the same rapidity acceptance. $\epsilon_{\mathrm{reco}}^{\mathrm{c,b\to e}}$ consists of the contributions from track selection cuts ($\epsilon_{\mathrm{track-cuts}}$), track-cluster matching cut ($\epsilon_{\mathrm{track-cluster-match}}$) and electron identification cuts ($\epsilon_{n\sigma_e^{\mathrm{TPC}}}$, ϵ_{M02}, $\epsilon_{\mathrm{E/p}}$) from TPC and EMCal, as shown in equation 3.2.

$$\epsilon_{\mathrm{reco}}^{\mathrm{c,b\to e}} = \epsilon_{\mathrm{track-cuts}} \times \epsilon_{\mathrm{track-cluster-match}} \times \epsilon_{n\sigma_e^{\mathrm{TPC}}} \times \epsilon_{\mathrm{M02}} \times \epsilon_{\mathrm{E/p}} \tag{3.2}$$

Figure 3.9 shows the total reconstruction efficiency for electrons from heavy-flavour hadron decays (represented in red), along with the individual contributions from the track and particle identification selection criteria. The efficiencies of electron identification selection criteria, specifically the efficiency for the shower shape parameter cut ($\epsilon_{\mathrm{M02}}^{\mathrm{data}}$) and for the $n\sigma_e^{\mathrm{TPC}}$ cut ($\epsilon_{n\sigma_e^{\mathrm{TPC}}}^{\mathrm{data}}$), have also been calculated from data using the methods discussed below. The efficiencies obtained from data have been compared with those obtained from monte-carlo and a slight difference has been observed. Although, the total reconstruction efficiency

is usually calculated from the monte-carlo samples, due to the small mismatch between the contributions from data and MC for the shower shape and TPC nσ cuts, the efficiencies for these electron identification cuts have been used from data. It is not feasible to calculate the efficiency of the E/p cut from the data at higher p_{T} ($p_{\mathrm{T}} \gtrsim 6$ GeV/c) and has been discussed in this section below. The total data-driven reconstruction efficiency is described by equation 3.3.

$$\epsilon_{\mathrm{reco}}^{\mathrm{c,b\to e}}|_{\mathrm{data-driven}} = \epsilon_{\mathrm{track-cuts}} \times \epsilon_{\mathrm{track-cluster-match}} \times \epsilon_{n\sigma_e^{\mathrm{TPC}}}^{\mathrm{data}} \times \epsilon_{\mathrm{M02}}^{\mathrm{data}} \times \epsilon_{\mathrm{E}/p} \tag{3.3}$$

Data-driven E/p cut efficiency ($\epsilon_{\mathrm{E}/p}^{\mathrm{data}}$)

The efficiency of the E/p selection criteria for electrons in data ($\epsilon_{\mathrm{E/p}}^{\mathrm{data}}$) is obtained from the projection of the TPC nσ distribution in several p_{T} intervals, before and after the E/p cut, as shown in the left and the right panels of figure 3.10 respectively. The projection of the TPC $n\sigma_e$ distribution, in each p_{T} interval, is fitted with a combination of three gaussian functions and a landau×exponential function, to parametrize the contributions from protons, kaons, electrons and pions respectively. A detailed discussion on the fit functions and the procedure are discussed in section 3.4.3. The E/p efficiency is defined as the ratio of the total number of electron candidates selected after the E/p cut with respect to the total number of electron candidates present in the sample before the selection has been applied. The total electron candidates is obtained from the integral of the gaussian function which is used to parametrize the electron contribution, from the projection of the TPC $n\sigma_e$ distribution.

$$\epsilon_{\mathrm{E/p}}^{\mathrm{data}} = \frac{\text{Integral of } e^{-}\text{gaussian from TPC n}\sigma \text{ distribution with E/p cut}}{\text{Integral of } e^{-}\text{gaussian from TPC n}\sigma \text{ distribution without E/p cut}}$$

A comparison of the E/p cut efficiency obtained from data and MC has been shown in figure 3.11 on the left panel, along with their ratios on the right panel. The efficiency from data cannot be calculated beyond $p_{\mathrm{T}} \gtrsim 6$ GeV/c by using this data driven method when the TPC nσ bands for electrons and hadron starts to merge with increasing p_{T} ranges and the fit

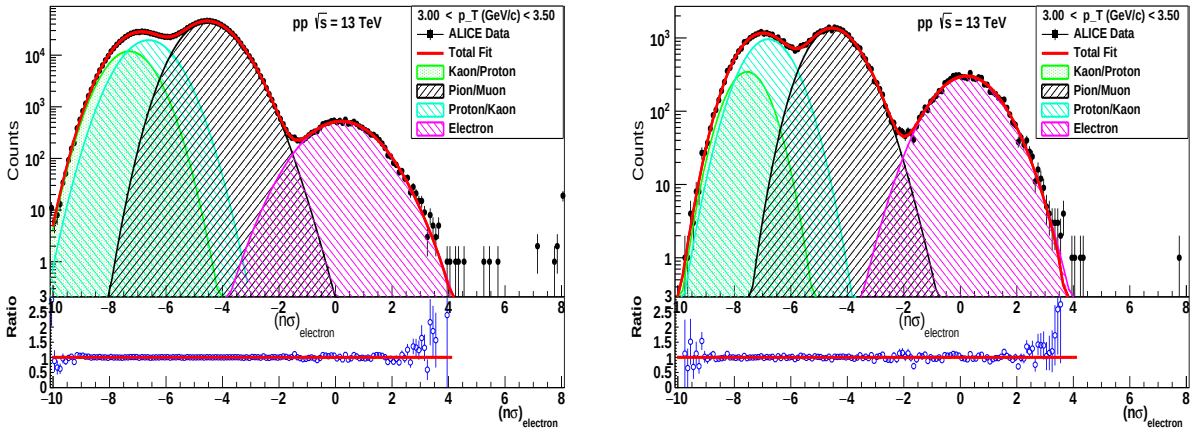

(a) Before E/p cut

(b) After applying E/p cut

Figure 3.10: Projection of TPC $n\sigma_e$ distribution in a particular p_{T} range

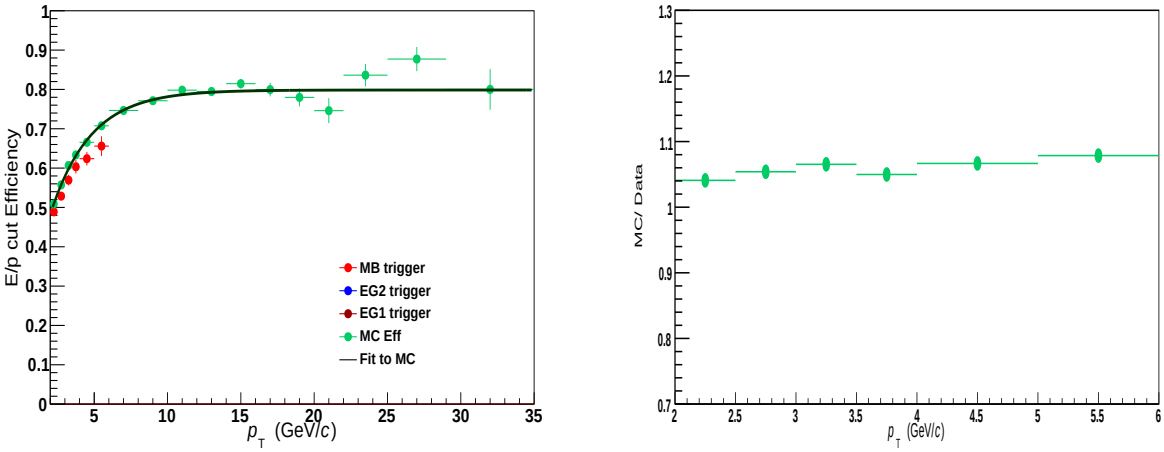

(a) E/p efficiency obtained from data and MC

(b) Ratio of MC and data

Figure 3.11: E/p cut efficiency

tends to breakdown. Hence, the $\epsilon_{\mathrm{E/p}}$ is taken from MC to calculate the total reconstruction efficiency. The $\epsilon_{\mathrm{E/p}}$ from monte-carlo has been fitted with a Fermi function to even out variations due to statistical fluctuations specially at the highest p_{T} intervals.

Data-driven TPC $n\sigma_e$ cut efficiency ($\epsilon^{\mathrm{data}}_{\mathrm{n}\sigma_{\mathrm{e}}^{\mathrm{TPC}}}$)

The data driven TPC $n\sigma_e$ cut efficiency is obtained from the projection of the TPC $n\sigma_e$ distribution after applying the E/p cut, as shown in figure 3.10(b), by calculating the ratio

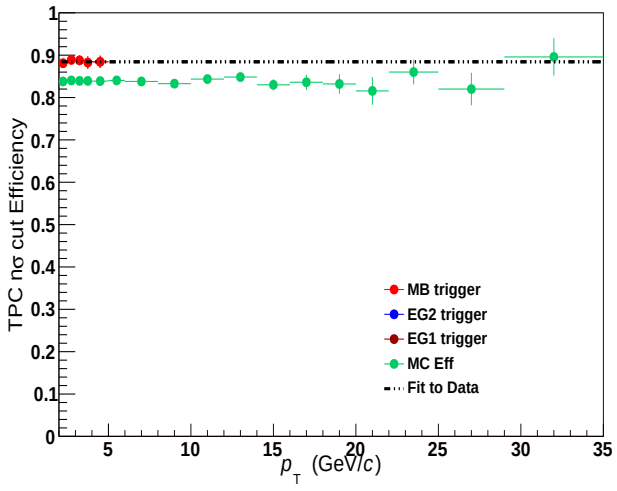

Figure 3.12: TPC $n\sigma_e$ cut efficiency obtained from data and MC

of the integral of electrons within selection criteria -1 $< n\sigma_e^{\mathrm{TPC}} <$ 3 with respect to the total electrons present before the cut $n\sigma_e$ cut, which is obtained from the total integral of the gaussian function used to parametrize the electron contribution.

$$\epsilon^{\mathrm{data}}_{\mathrm{n}\sigma^{\mathrm{TPC}}_{\mathrm{e}}} = \frac{\text{Integral of } e^{-}\text{gaussian from TPC n}\sigma \text{ within} -1 < n\sigma < 3}{\text{Integral of } e^{-}\text{gaussian from TPC n}\sigma \text{ over entire range of n}\sigma}$$

Figure 3.12 shows the E/p cut efficiency obtained using the data driven method and from MC and they differ by $\sim 2\%$ in the entire measured p_{T} range. As mentioned earlier in this section, using this method, the $\epsilon^{\mathrm{data}}_{\mathrm{n}\sigma^{\mathrm{TPC}}_{\mathrm{e}}}$ cannot be calculated beyond $p_{\mathrm{T}} \gtrsim 6$ GeV/c. The TPC $n\sigma_e$ efficiency is ideally expected to be same at all p_{T} and hence the $\epsilon^{\mathrm{data}}_{\mathrm{n}\sigma^{\mathrm{TPC}}_{\mathrm{e}}}$ curve is fitted with a linear function to obtain the efficiency in entire p_{T} range required for the analysis.

Data-driven shower shape cut efficiency ($\epsilon^{\mathrm{data}}_{\mathrm{M02}}$)

The shower shape cut efficiency is obtained from the E/p distributions using the following equation:

$$\epsilon^{\mathrm{data}}_{\mathrm{M02}} = \frac{e^{-}\text{counts from the E/p distribution after M02 , E/p , TPCn}\sigma \text{ cuts}}{e^{-}\text{counts from the E/p distribution after E/p , TPCn}\sigma \text{ cuts}}$$

The shower shape cut efficiencies obtained from the data-driven method and MC are shown

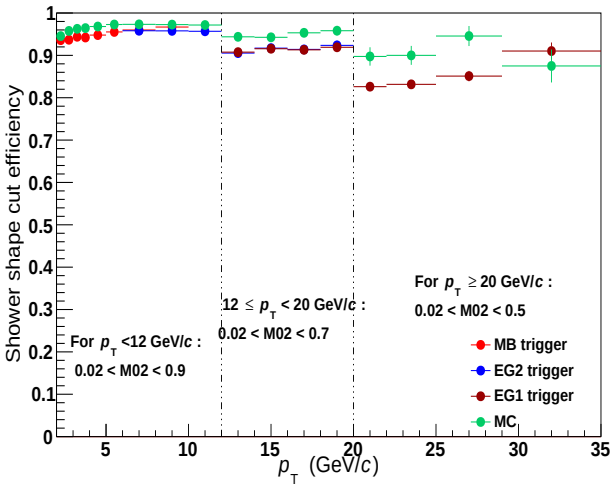

Figure 3.13: Shower shape cut efficiency obtained from data and MC

in figure 3.13.

Data-driven reconstruction efficiency ($\epsilon_{\mathrm{reco}}^{\mathrm{c,b\to e}}|_{\mathrm{data-driven}}$)

The total data-driven reconstruction efficiency for heavy-flavour hadron decay electrons ($\epsilon_{\mathrm{reco}}^{\mathrm{c,b\to e}}|_{\mathrm{data-driven}}$) obtained using equation 3.3 is used to correct the background subtracted inclusive electron spectra from data. Figure 3.14 shows the reconstruction efficiencies obtained from the data-driven method (in red) and from MC only (in green) on the left panel and their ratio on the right panel. They are in agreement within $\sim 3\%$ in the entire p_{T} range.

3.3.8 Other background electron removal : W, Z $\to$ e

Electrons from decays of W and Z bosons form a significant background to the heavy-flavour hadron decayed electrons at high p_{T} ($p_{\mathrm{T}} >$ 20 GeV/c). Details of the sources of background non-heavy-flavour hadron decay electrons are listed in section 3.3.5. The W, Z $\to$ e spectra is calculated using PYTHIA + POWHEG simulation. The generation of W and Z is performed using POWHEG [115] as the event generator. POWHEG implements next-to-leading-order

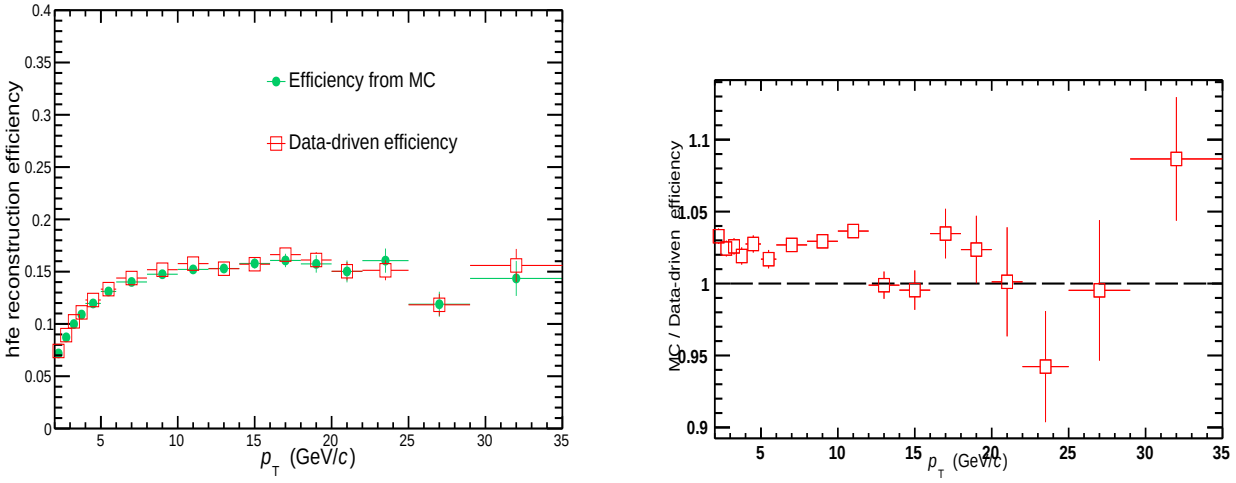

(a) Data-driven method and MC only

(b) Ratio of MC and data-driven reconstruction efficiency

Figure 3.14: Total reconstruction efficiency for heavy-flavour hadron decay electrons

(NLO) calculations and generates hard events for various processes where heavy quarks, Higgs and electroweak bosons are involved. However, since POWHEG is only a hard event generator, it is interfaced with PYTHIA [93], which is a shower Monte-Carlo program, for subsequent showering processes. Figure 3.15 shows the spectra of electrons from W and Z boson decays in the left panel and the relative contribution of electrons from Z boson with respect to that from W boson (average of W^- and W^+) on the right panel. The ratio is shown in the range $20 < p_{\mathrm{T}}$ (GeV/c) <40, which is the region of interest (non-negligible contribution) for this analysis. The relative contribution of Z boson decay is found to be $\sim$ 15% - 25%. It is also observed from the figure that the contribution of electrons (positrons) from W^- decays is more than the contribution from W^+ decays in the mid rapidity region. The asymmetry in the yields of W^+ and W^- bosons has been discussed in [116, 117]. Z boson decay electrons dominate over W decay electrons for $p_{\mathrm{T}} < 10$ GeV/c. For consistency check, a comparison of these results has been done with that of W, Z $\rightarrow$ μ results from the c,b $\rightarrow$ μ analysis at forward rapidity in pp collisions at $\sqrt{s} = 5$ TeV. Similar results have been observed in the c,b $\rightarrow$ μ analysis.

Figure 3.16 shows the ratio of the W, Z $\rightarrow$ e spectra with the central value of the FONLL

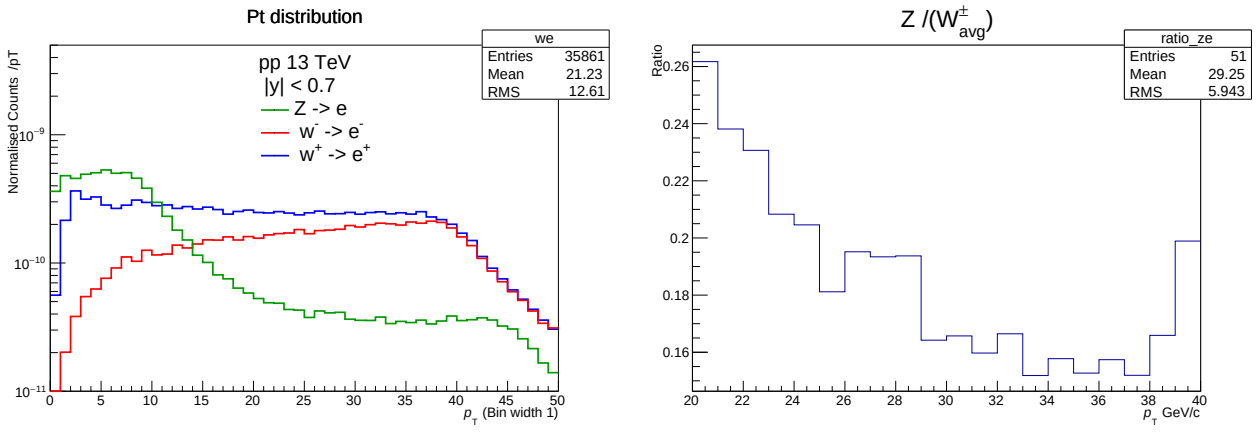

Figure 3.15: Left: Spectra of $W^- \rightarrow e^-$, $W^+ \rightarrow e^+$ and $Z^0 \rightarrow e^{\pm}/2$, Right : Relative contribution of Z with respect to W (average of W^- and W^+)

predictions for c, b $\rightarrow$ e. The values for this analysis are similar to the values from hf$\rightarrow \mu$ [i.e., (WZ$\rightarrow \mu$) / FONLL (hf$\rightarrow \mu$)] analysis.

- The contribution of Z decay electrons is negligible over almost the whole p_{T} range and is $\sim$ 5% at $p_{\mathrm{T}} = 35$ GeV/c.

- The fraction of W-decay electrons is negligible for $p_{\mathrm{T}} < 15$ GeV/c and is $\sim$ 12% at $p_{\mathrm{T}} = 25$ - 30 GeV/c, $\sim$ 34% at $p_{\mathrm{T}} = 30$ - 35 GeV/c.

- The total contribution of W and Z decay electrons is negligible for $p_{\mathrm{T}} < 15$ GeV/c and is $\sim$ 14% at $p_{\mathrm{T}} = 25$ - 30 GeV/c, $\sim$ 40% at $p_{\mathrm{T}} = 29$ - 35 GeV/c.

Systemtics

The systematic uncertainty of contribution of electrons from W and Z decays was estimated by varying of parton distribution function from CT10nlo (standard) to CTEQ6l in the POWHEG event generator, as shown in figure 3.17. The resulting variation was found to be negligible.

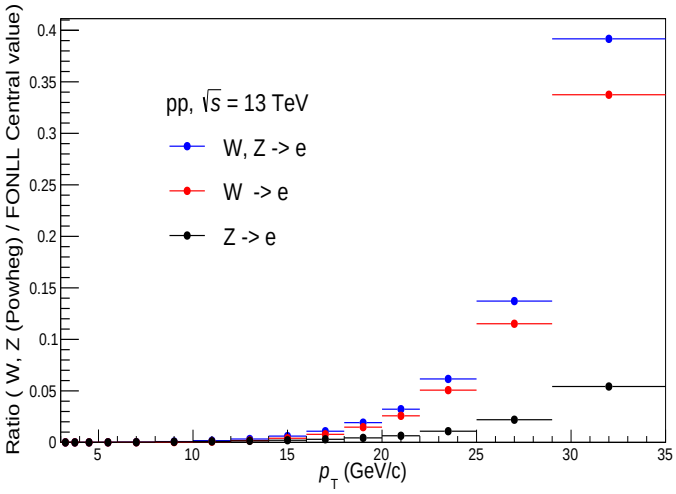

Figure 3.16: Ratio of the W, Z → e spectra with respect to the FONLL predictions of c,b → e

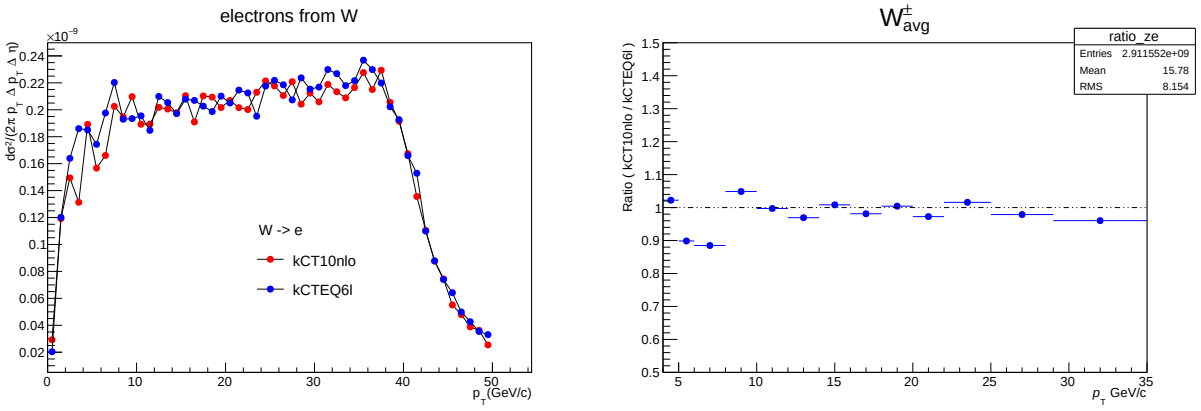

Figure 3.17: Contribution of electrons from W and Z decays by varying of parton distribution function from CT10nlo (standard) to CTEQ6l (left) and their ratio (right)

3.3.9 Spectra of electrons from decays of heavy-flavour hadrons from the TPC–EMCal analysis

The spectra of electrons from heavy-flavour hadron decays was obtained by following the steps mentioned below. The tagging efficiency corrected photonic electron spectra was subtracted from the inclusive electron spectra, which was then corrected for the reconstruction efficiency. This was then subtracted by the W, Z → e contribution to obtain the final spectra. The spectra obtained from different analyses and data periods were compared as

a cross check and to ensure consistency amongst each other as is discussed in this section below.

Consistency check between EMCal and DCal for EMCal + DCal results

Analyses separating the EMCal and DCal detectors (of the EMCal detector system) were performed. The spectra of electrons from heavy-flavour hadron decays obtained from the two separate analyses are cross-checked with the combined result from EMCal + DCal. The left panel of figure 3.18 shows the comparison of spectra obtained from EMCal + DCal

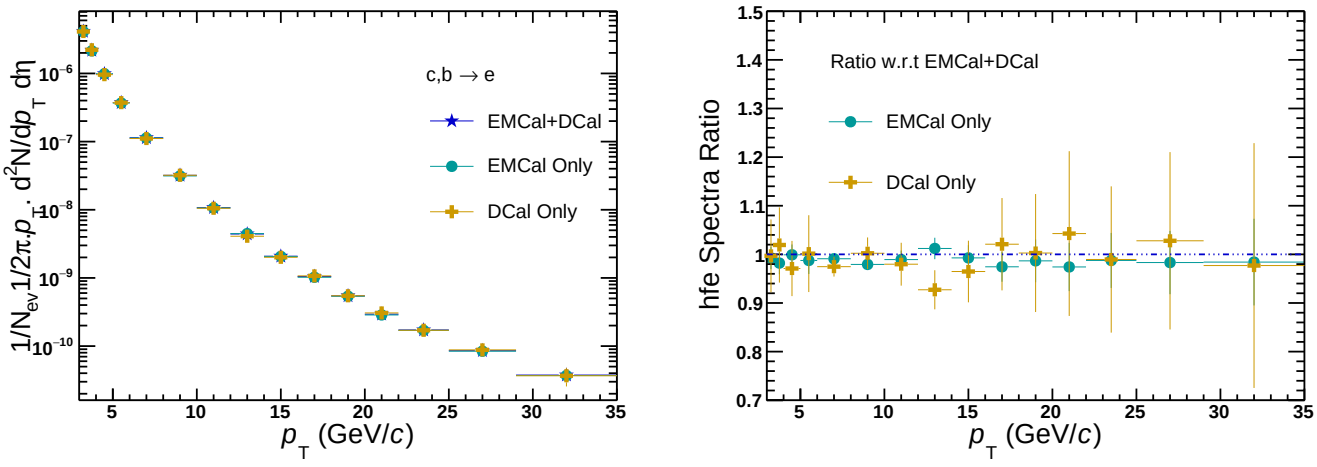

Figure 3.18: Heavy-flavour hadron decay electron spectra obtained from EMCal only, DCal only and EMCal + DCal analyses (left) and the ratio of the spectra obtained from EMCal only, DCal only analyses with respect to the EMCal + DCal result (right)

analysis along with EMCal only and DCal only analyses. The right panel shows the ratio of the spectra with respect to EMCal + DCal results. The results from the three analyses (EMCal + DCal, EMCal only and DCal only) are in good agreement with each other. For obtaining the final spectra of electrons from heavy-flavour hadron decay shown in section 3.7 and mentioned further in this thesis as results from the "TPC–EMCal analysis", the results from the EMCal + DCal detector system has been used.

Consistency check between different production cycles used for this analysis

The spectra of electrons from heavy-flavour hadron decay has been obtained from the different production cycles used for this analysis and compared with one another before merging to obtain the final spectra. The left panel of figure 3.19 shows the electron spectra from

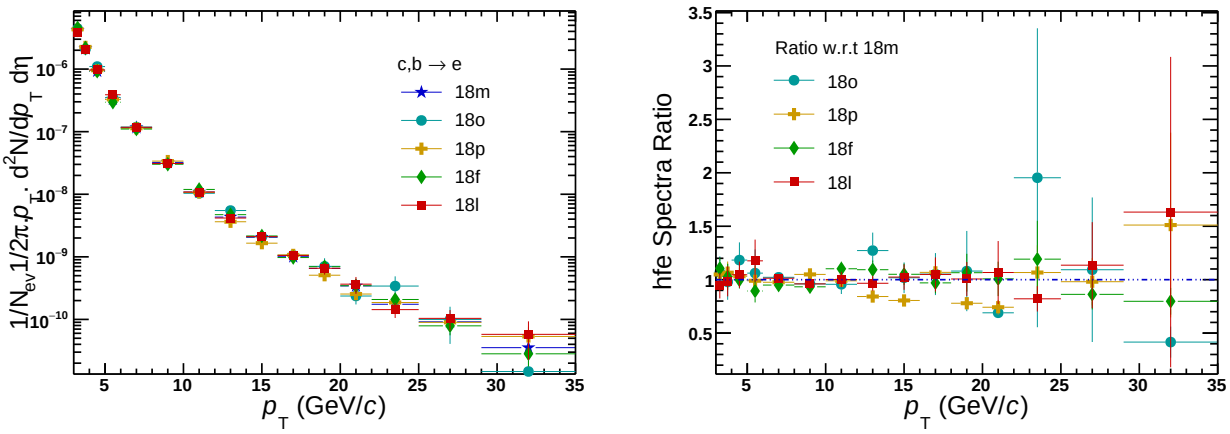

Figure 3.19: Heavy-flavour decayed electron spectra for several production cycles of 2018 (left) and their ratio with respect to 18m (right)

heavy-flavour hadron decays for the different production cycles/periods of 2018 and the right panel shows the ratio of the spectra from various periods of 2018 with respect to the spectra from 2018m period. The 2018m has one of the highest statistics amongst all periods and only those periods with high statistics have been chosen for this comparison. Figure 3.19 shows that the periods are consistent among themselves. The left panel of figure 3.20 shows the comparison of spectra of the electrons from heavy-flavour decays for the 2016k period and for all periods of 2018 after merging. The right panel shows the ratios of the inclusive electron spectra after subtraction of the photonic electron contribution (red), the reconstruction efficiency (black), and the heavy-flavour hadron decay electron spectra (green) for all periods of 2018 after merging with respect to that from the 2016k period. The spectra of electrons from heavy-flavour hadron decay are consistent between the production cycles of 2018 and 2016k period. The spectra from the various periods have been merged using

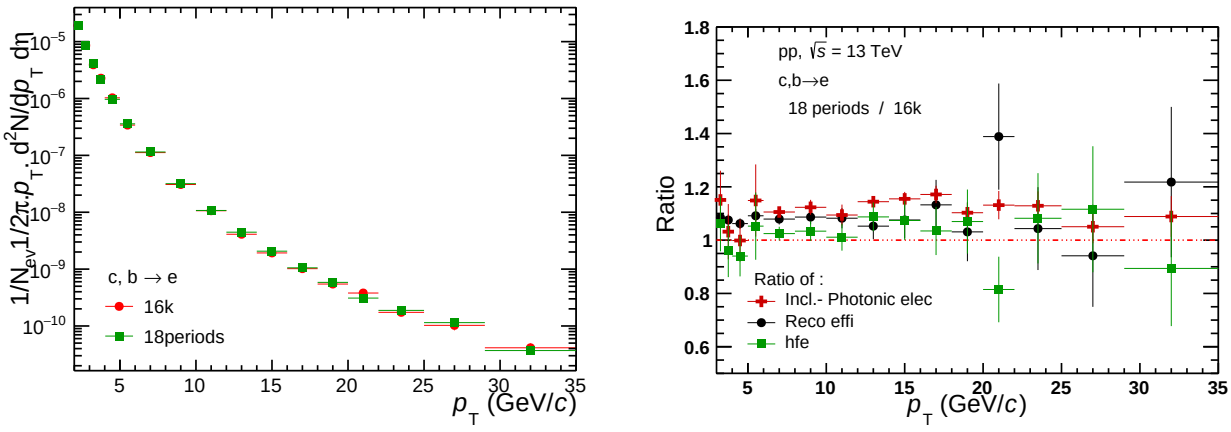

Figure 3.20: Left: Heavy-flavour decayed electron spectra of 16k and 2018 periods merged. Right: Ratio for 2018 periods with respect to 16k period for heavy-flavour decayed electron spectra along with that of the (inclusive - photonic) electron spectra and reconstruction efficiency

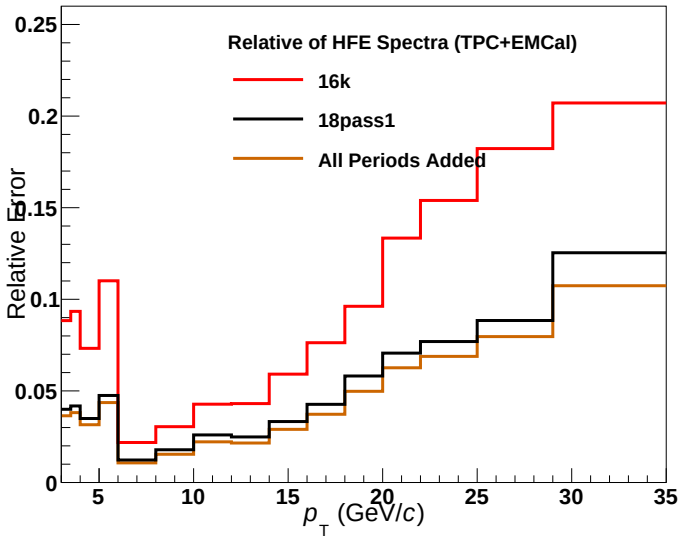

Figure 3.21: Relative error (σ_i^2) of heavy-flavour hadron decay electron spectra for 2018 periods, 16k and the combined spectra

the formula in equation 3.4.

$$\frac{\sum x_i/\sigma_i^2}{\sum 1/\sigma_i^2} \tag{3.4}$$

The statistical error has been calculated using the formula in equation 3.5.

$$\sigma = \sqrt{\frac{1}{\sum 1/\sigma_i^2}} \tag{3.5}$$

where σ_i^2 is the statistical error of individual periods.

The relative errors of the periods are shown in figure 3.21. The relative error of the 16k period is larger due to its lower statistics compared to the merged periods of 2018. The relative error is greater for all periods for $p_{\mathrm{T}} < 6$ GeV/c, since the spectra in this p_{T} range has been calculated from the minimum bias sample. For $p_{\mathrm{T}} >$ 6 GeV/c, the EMCal triggered samples have been used. The EMCal triggered samples have larger statistics of electrons compared to that from the MB sample till a certain p_{T}, and hence the relative error is smaller till that p_{T}. The final spectra of electrons from the heavy-flavour decays and the details of selecting the p_{T} ranges from the different triggered sample have been discussed in section 3.7.

3.4 Heavy-flavour hadron decay electron spectra using TPC–TOF:

3.4.1 Event selection

The following selection criteria given in he table 3.8 have been used to select events for the analysis with TPC–TOF detectors and are similar to those applied in the TPC–EMCal analysis. The details on the selection criteria are discussed in section 3.3.1.

Table 3.8: Event selection criteria

Event cuts :	Values :
Trigger Selection	kINT7
Primary Z vertex range	± 10 cm
Min. no. of contributors to primary vertex	2
Pile-up rejection	Applied

3.4.2 Selection criteria for tracks and electron identification

The track selection criteria applied for the TPC–TOF analysis are summarized in table 3.9. Track selection parameters are same for the TPC–EMCal and TPC–TOF analysis. Detailed explanations for the track cut parameters are given in section 3.3.3. In the TPC–TOF analysis, however, tracks are selected within rapidity $|\eta| \leq 0.8$ due to greater acceptance of TPC and TOF than that of the EMCal detector. For track selection, a stricter cut on the SPD hit layer is applied, to reduce background from the photonic sources which are relatively high in the low p_{T} region. The signal/background ratio increases from $\sim 3\%$ at $p_{\mathrm{T}} = 0.5$ GeV/c to ~ 12 % at $p_{\mathrm{T}} = 35$ GeV/c.

The electron identification cuts from TPC and TOF are shown in table 3.10. The particle identification (PID) with TPC and TOF detectors are discussed in sections 2.2.2 and 2.2.3 respectively of chapter 2. Figure 2.7 shows the TPC $n\sigma_e$ vs. p distribution after TOF selection criteria, where the nσ_e (in terms of detector resolution) is defined as the difference

Table 3.9: Track selection criteria

Track cuts :	Selection values :
FilterBit	AliAODTrack::kTrkGlobalNoDCA
No. of TPC CrossedRows	≥ 70
Number of TPC Clusters for dE/dx calculation	≥ 80
Ratio of TPC CrossedRows (Found/Findable)	≥ 0.8
Number of ITS Clusters	≥ 3
ITS and TPC Refit	Required
Hits on layers of SPD	kBoth
DCA$_{xy}$	≤ 1 cm
DCA$_z$	≤ 2 cm
χ^2 /clusters of the momentum fit in the TPC	≤ 4
$\lvert\eta\rvert$	≤ 0.8
Kink Candidates	Rejected

between the measured signal in the detector and the expected value for electrons. Electrons are selected with ± 3 σ from the TOF signal (i.e., TOF β vs. p distribution as shown in figure 2.6). After applying the TOF PID cut a large number of kaons, protons and deuterons are rejected up to $\sim$ 4 GeV/c, while the electron band has almost no changes. This can be observed from figure 2.7. To reduce the contamination from pions/muons an asymmetric TPC PID selection criterion of -1 $< n\sigma_e^{\mathrm{TPC}} <$ 3 has been applied. Table 3.10 lists the electron identification parameters and values for electron selection.

Table 3.10: Particle identification parameters and values for electron selection

	Electron selection values :
TPC nσ	-1 $< n\sigma_e^{\mathrm{TPC}} <$ 3
TOF nσ	$\mid n\sigma_e^{\mathrm{TOF}} \mid <$ 3

3.4.3 Inclusive electron selection and determination of hadron contamination

To estimate the contamination of hadron in the sample of electrons selected using the TPC and TOF PID selection criteria, a projection of the the TPC nσ vs. p distribution after TOF cut, is taken on the nσ axis and is fitted in several momentum slices. Figure 3.22 shows the projection of the TPC nσ vs. p distribution for 1.0 GeV/c $< p <$ 1.1 GeV/c (left) and 3.5 GeV/c $< p <$ 4.0 GeV/c (right). The mean value of the dE/dx distribution at a fixed momentum is gaussian in general, with standard deviation σ, which is determined by the detector properties and the quality of a reconstructed track. The residual contamination to the electron sample is given by the contribution of misidentified charged particles. The projection of the TPC nσ distribution is fitted with a combination of three gaussian functions and a landau $\times$ exponential function, to parametrize the contributions from protons, kaons, electrons and pions respectively, as shown in the left panel of figure 3.22. Above a certain p ($p \gtrsim 2.5$ GeV/c) since the kaon and proton dE/dx bands tend to merge, only one gaussian function has been used to parameterize their combined contribution (right panel of figure 3.22). The pion tail is better fitted with a landau $\times$ exponential function instead of a gaussian. The energy lost by a particle traveling through a medium deviates from the mean value due to statistical fluctuations in the number of collisions suffered and amount of energy lost in each collision. For a thick absorber, the energy loss distributions becomes a gaussian. However, for thin absorbers, such as the TPC, the incident particles do not suffer enough collisions for the central limit theorem to hold true. In addition, at higher energies the incident particle can transfer a large one-shot energy which can knock out electrons from the absorber (δ electrons). Due to these large single energy transfers in a thin absorber, the energy loss distribution is skewed. The distorted gaussian distribution with a high energy loss tail can be described by a Landau function multiplied with an exponential function. The dominant contribution to contamination comes from the tail of the pions above 1 GeV/c, which is fitted with a landau $\times$ exponential. The electron energy loss is primarily

due to radiative process, hence is fitted with a gaussian distribution. A more detailed discussion on the energy loss electrons and pions can be found in [82]. The contamination

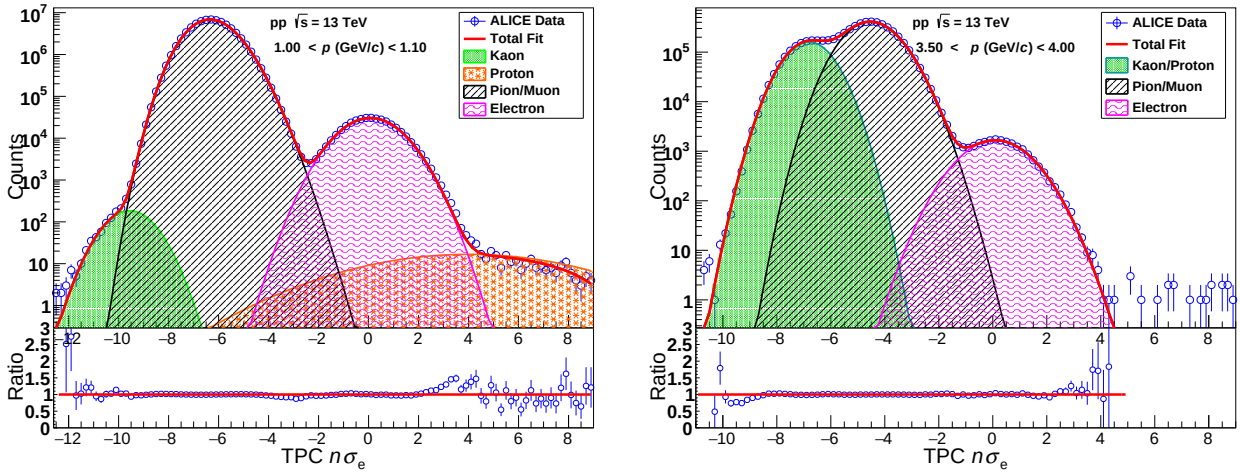

Figure 3.22: Projection of the TPC $n\sigma_e$ vs. p distribution in $1.0 < p$ (GeV/c) < 1.1 (left) and $3.5 < p$ (GeV/c) < 4.0 (right)

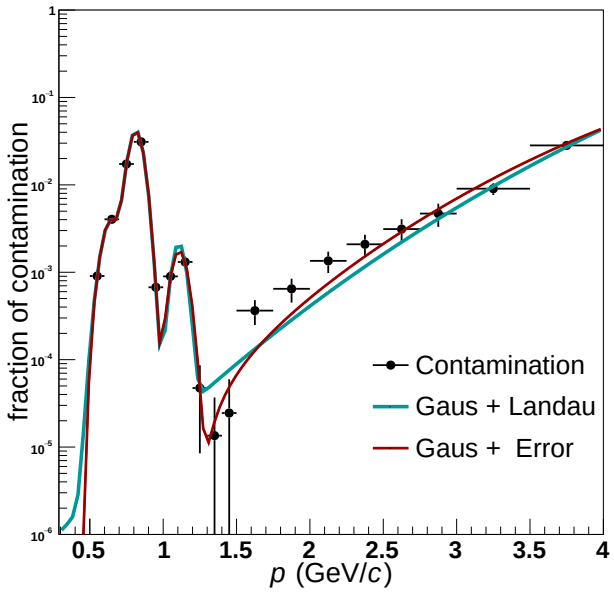

Figure 3.23: Hadron contamination in the electron sample as a function of momentum, fitted with a Landau and an Error function

from misidentified hadrons in the electron sample is calculated for each momentum interval as the ratio of the pions, kaon, proton counts taken together within -1 $< n\sigma_e^{\mathrm{TPC}} <$ 3 with

respect to the total counts within -1 < $n\sigma_e^{\mathrm{TPC}}$ < 3 as shown in equation 3.6.

$$\text{Hadron contamination (h)} = \frac{\text{Integral of kaons, protons, pions in } -1 < n\sigma_e^{\mathrm{TPC}} < 3}{\text{Total integral within } -1 < \mathrm{n}\sigma_{\mathrm{e}}^{\mathrm{TPC}} < 3} \tag{3.6}$$

The hadron contamination vs p is fitted with Landau and Error functions, as shown in figure 3.23. From the fit functions the hadron contamination at a particular momentum can be determined. For this analysis, the Error function has been used for determination of hadron contamination. The Landau function has been used for systematic studies. Figure

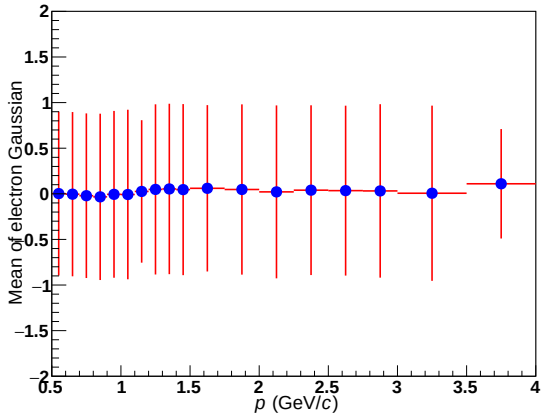

Figure 3.24: Mean of the gaussian which used to fit electron contribution. The error bars signify the σ of the gaussian curve.

3.24 shows that the mean of the gaussian used to fit the electron contribution in the $n\sigma_e^{\mathrm{TPC}}$ distribution is at 0. The error bars signify the σ of the gaussian curve, which is around 1.

The Bethe-Bloch formula, shown in equation 2.1, describes the energy loss as a function of the momentum (p) and not in terms of the transverse momentum (p_{T}). Hence, a p spectrum of inclusive electrons has been obtained from selecting electron candidates within the TPC–TOF PID criteria in the several momentum slices. Figure 3.23 provides the value of the hadron contamination for a particular momentum (p). This value can be treated as the probability of a track with the particular momentum to be hadron. To extract the p_{T} spectra of inclusive electrons, for each track with momentum p and transverse momentum p_{T}, the hadron contamination value at the particular p is assigned as the "weight" for the cor-

responding p_{T} of the track. The hadron contamination information is obtained in terms of p_{T} and is statistically subtracted from raw spectrum of electrons + hadrons to get inclusive electron spectrum. The transverse momentum (p_{T}) spectrum of the inclusive electrons is shown in figure 3.25.

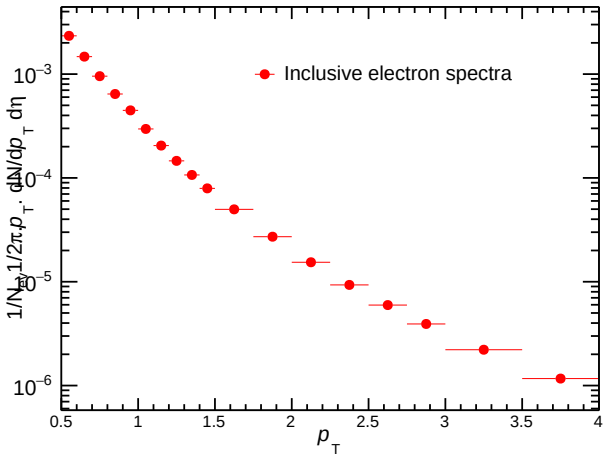

Figure 3.25: p_{T} spectrum of inclusive electrons from TPC–TOF analysis.

3.4.4 Background non-heavy-flavour electrons selection (Photonic electrons)

Details on the background sources and the method and criteria of removal are similar to that in the TPC–EMCal analysis and is mentioned in section 3.3.5. The selection criteria for associated tracks for the TPC–TOF analysis are mentioned in table 3.11.

3.4.5 Tagging efficiency

Unlike the TPC–EMCal analysis, a minimum bias (general purpose) sample has been used to calculate the tagging efficiency for the TPC–TOF analysis. As evident from the figure 3.6 the statistics in the minimum bias sample is higher in the low p_{T} region compared to that in the enhanced sample. Hence, using a minimum bias (general purpose) MC sample

Table 3.11: Associated track selection criteria

Track cuts :	Selection values :
FilterBit	AliAODTrack::kTrkTPCOnly
Number of TPC Clusters	≥ 60
Number of TPC Clusters for PID	≥ 60
ITS and TPC Refit	Required
DCA_{xy}	≤ 1 cm
DCA_{z}	≤ 2 cm
χ^2 /clusters of the momentum fit in the TPC	≤ 4
TPC nσ	$\pm 3.5\sigma$
p_{T} range	0.1 GeV/c
$\lvert\eta\rvert$	≤ 0.9

significantly reduces statistical error. As already mentioned in section 3.3.6 the tagging efficiency is defined as the ratio of the true number of photonic pairs from the same mother ($\mathrm{N}_{\mathrm{found}}^{\mathrm{true,pairs}}$) which have passed the associated track selection cut to the total number of electrons (positrons) from photonic origins ($\mathrm{N}_{\mathrm{total}}^{\mathrm{photonic}}$), both obtained from the MC sample. However, if the shape of the p_{T} spectra of photonic sources i.e., π^0 and η from data do not match with that from monte-carlo, the tagging efficiency is not correctly calculated. The π^0 spectra were estimated as the average of the spectra of π^+ and π^- spectra [118] and the η spectra were estimated using m_{T} scaling as explained in [119]. Figure 3.26 shows the comparison of the p_{T} spectra of π^0 and η obtained from data [118,119] and from monte-carlo. Figure 3.27 shows the ratio of π^0 and η spectra obtained from data to that obtained from MC. The p_{T} distributions of π^0 and η from MC were re-weighted with the ratio to match the measured shapes. Figure 3.28 shows the ratio of the tagging efficiency with and without the re-weighting procedure on the left. With increasing p_{T} the difference in the tagging efficiencies with and without re-weighting decrease. This observation is also corroborated in the ratio plot in figure 3.27 where the ratio is ~ 1, for $p_{\mathrm{T}} \gtrsim 2$ GeV/c. The tagging efficiency after the re-weighting procedure has been fitted with a Fermi function to smoothen out statistical fluctuations, as shown the right panel of the figure 3.28.

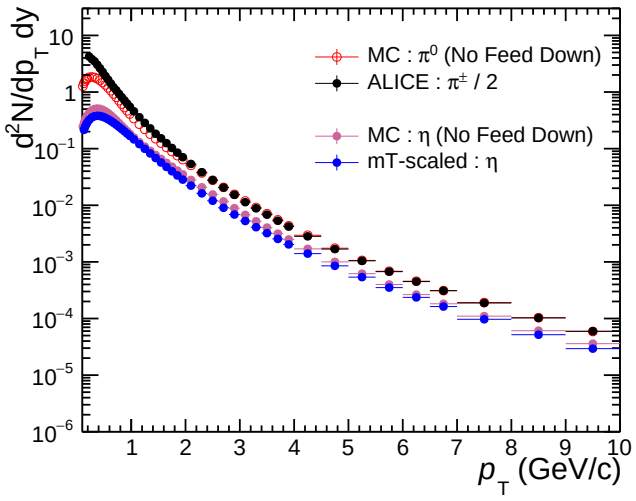

Figure 3.26: p_{T} spectra of π^0 and η obtained from data [118, 119] and from monte-carlo

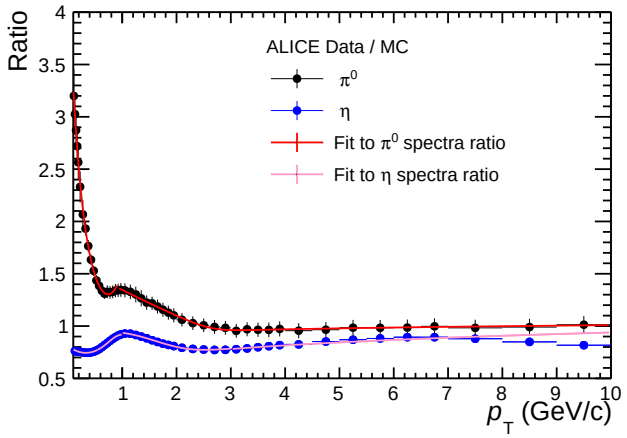

Figure 3.27: Ratio of p_{T}-spectra of π^0 and η obtained from data and Monte-Carlo

3.4.6 Reconstruction efficiency

The spectra of electrons from heavy-flavour decays from data is corrected by the reconstruction efficiency ($\epsilon_{\mathrm{reco}}^{\mathrm{c,b\to e}}$). The reconstruction efficiency is the ratio of the heavy-flavour hadron decay electrons after passing through all the geometric and particle identification (PID) cuts to the generated heavy-flavour hadron decay electron counts both within the same rapidity acceptance.

$$\epsilon_{\mathrm{reco}}^{\mathrm{c,b\to e}} = \frac{\text{Heavy-flavour decay electrons after passing through track + PID cuts}}{\text{Generated heavy-flavour decay electrons from MC}}$$

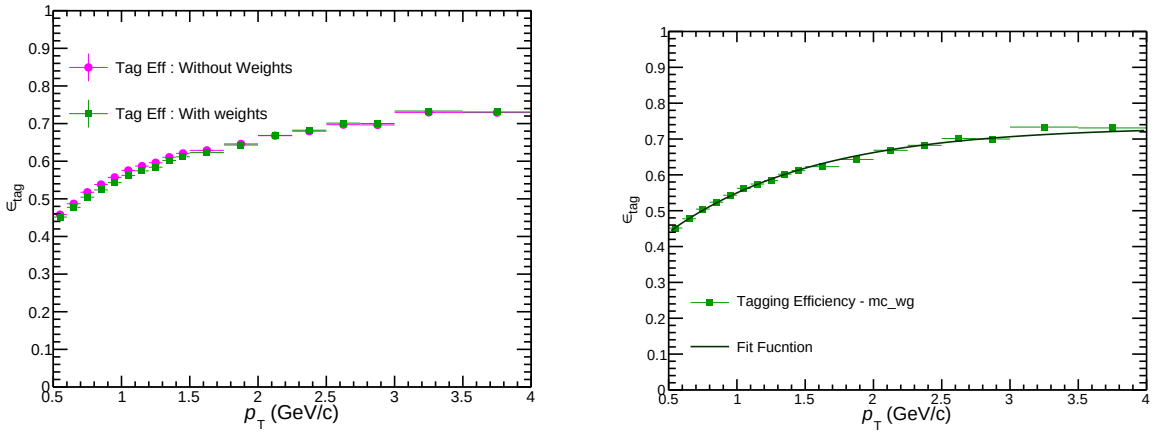

Figure 3.28: Tagging efficiency obtained from the TPC–TOF analysis

$\epsilon_{\mathrm{reco}}^{\mathrm{c,b}\to\mathrm{e}}$ consists of the contribution from track cuts and electron identification cuts from TPC and TOF. The total reconstruction efficiency, along with the separate contributions from track and electron identification cuts, calculated from the monte-carlo sample are shown in figure 3.29.

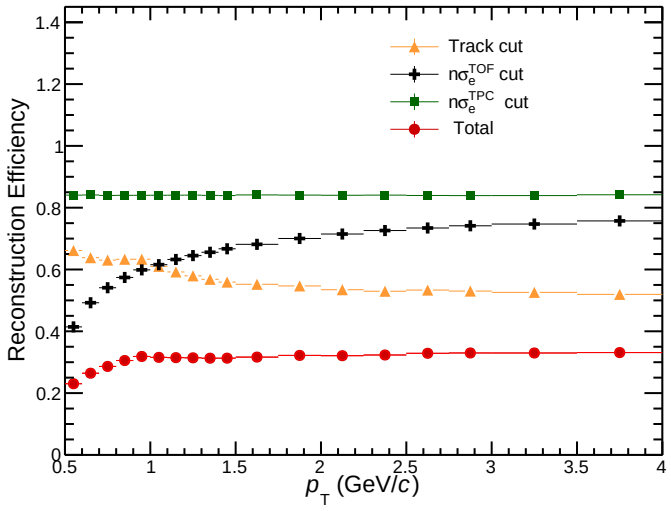

Figure 3.29: Reconstruction efficiency of electrons from heavy-flavour decay electrons obtained from MC for TPC–TOF analysis

Data-driven TPC nσ cut efficiency ($\epsilon^{\mathrm{data}}_{\mathrm{n}\sigma^{\mathrm{TPC}}_{\mathrm{e}}}$)

The efficiency of selection of the electron sample from data is obtained from figure 3.22. It is defined as the ratio between the integral of TPC (-1 < nσ_{e} <3) PID cuts for electrons, and the total amount of electrons within the gaussian fit curve shown in the figure.

$$\epsilon^{\mathrm{data}}_{\mathrm{n}\sigma^{\mathrm{TPC}}_{\mathrm{e}}} = \frac{\text{Integral of } e^{-}\text{gaussian from TPC n}\sigma \text{ within} -1 < n\sigma < 3}{\text{Integral of } e^{-}\text{gaussian from TPC n}\sigma \text{ over entire range of n}\sigma} \tag{3.7}$$

Figure 3.30 shows a comparison of the efficiency of selection of the electron sample from data and MC sample. The mean efficiency from data is $\sim$ 84 % while for MC is $\sim$ 86 %. Similar to the TPC–EMCal analysis, a data-driven reconstruction efficiency is used in the

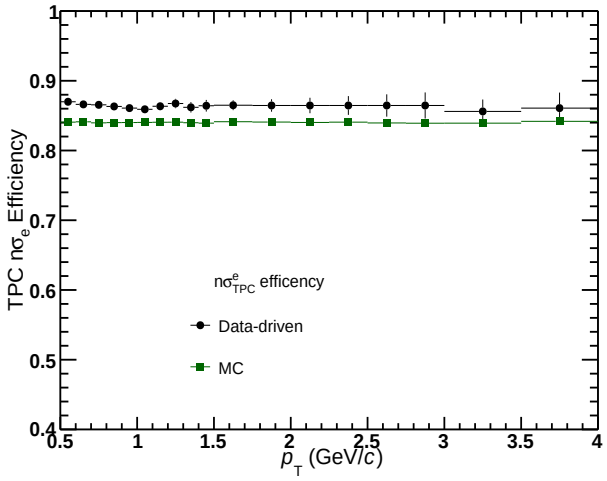

Figure 3.30: TPC $n\sigma_e$ cut efficiency obtained from data and MC

TPC–TOF analysis and $\epsilon^{\mathrm{data}}_{\mathrm{n}\sigma^{\mathrm{TPC}}_{\mathrm{e}}}$ is used for the calculating total reconstruction efficiency.

Data-driven reconstruction efficiency ($\epsilon^{\mathrm{c,b}\to\mathrm{e}}_{\mathrm{reco}}|_{\mathrm{data-driven}}$)

The total data-driven reconstruction efficiency for heavy-flavour hadron decay electrons ($\epsilon^{\mathrm{c,b}\to\mathrm{e}}_{\mathrm{reco}}|_{\mathrm{data-driven}}$) for the TPC–TOF analysis is obtained using the following equation 3.8.

$$\epsilon^{\mathrm{c,b}\to\mathrm{e}}_{\mathrm{reco}}|_{\mathrm{data-driven}} = \epsilon_{\mathrm{track-cuts}} \times \epsilon_{\mathrm{n}\sigma^{\mathrm{TOF}}_{\mathrm{e}}} \times \epsilon^{\mathrm{data}}_{\mathrm{n}\sigma^{\mathrm{TPC}}_{\mathrm{e}}} \tag{3.8}$$

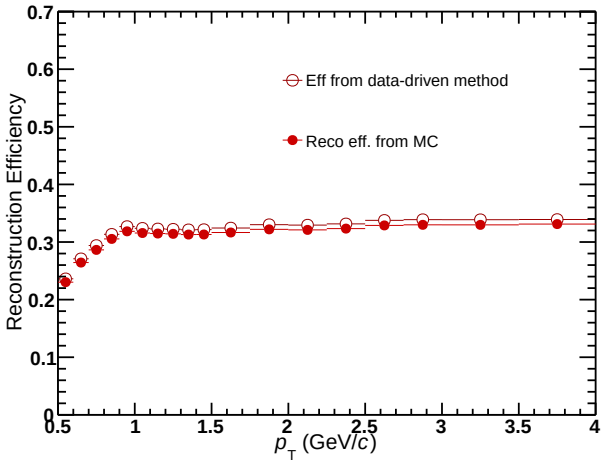

Figure 3.31: Total reconstruction efficiency for electrons from heavy-flavour hadron decays

Figure 3.31 shows the reconstruction efficiency for electrons from heavy-flavour hadron decays from the data-driven method and from the MC. They are consistent within $\sim 2\%$. An

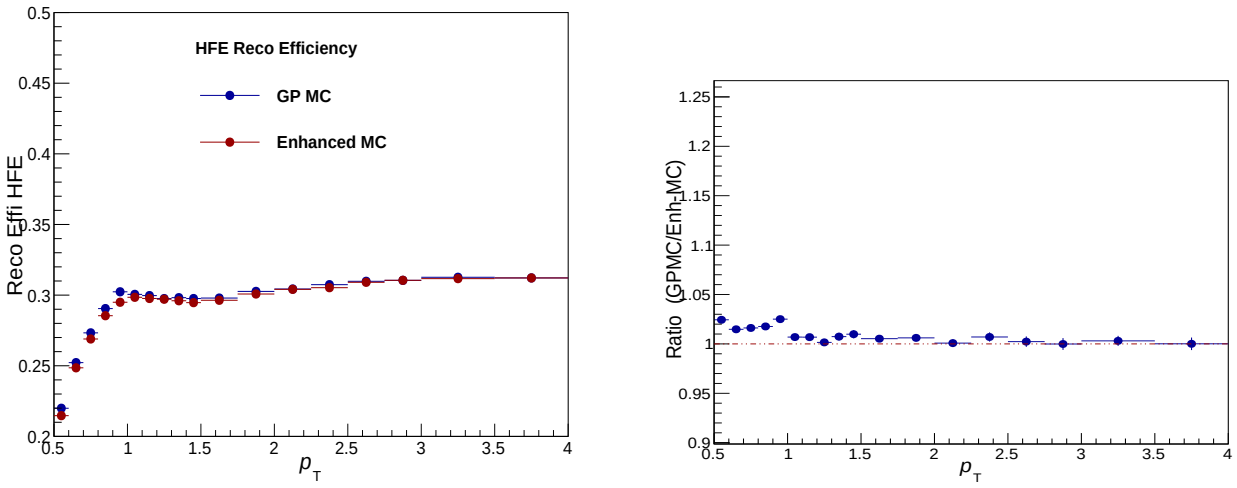

(a) Reconstruction efficiency from GP and enhanced MC sample

(b) Ratio of efficiencies from GP MC to enhanced MC sample

Figure 3.32: Total reconstruction efficiency for electrons from heavy-flavour hadron decays

enhanced MC sample has been used to obtain the contributions from track cuts and TOF PID cut. The data-driven total reconstruction efficiency for heavy-flavour decay electrons obtained from the general purpose MC sample has been compared with that from the enhanced MC sample as shown in the left panel of figure 3.31. Their ratio is shown on the

right panel of the figure and they are found to be consistent with each other, with a small variation ($\sim 2\%$) at low p_{T}.

3.4.7 Spectra of electrons from decays of heavy-flavour hadrons from the TPC–TOF analysis

The final spectra of electrons from heavy-flavour hadron decays from the TPC–TOF analysis was obtained by the following steps. The inclusive electron yield was subtracted by the tagging efficiency corrected photonic yield. This yield was then corrected by data-driven reconstruction efficiency to obtain the heavy-flavour hadron decay electron cross section. To ensure consistency between the results from different production cycles/periods, the heavy-flavour hadron decay electron cross sections obtained from each year were compared as discussed below.

Consistency check between different run periods/cycles used for this analysis

Figure 3.33 shows the ratio of the heavy-flavour hadron decay electron spectra for ALICE data periods of different years of Run-2 (2016, 2017, 2018) with respect to 2016k period. The ratio varies around unity within statistical uncertainty implying that the spectra from the different periods are consistent. The spectra is merged using formula 3.4 and the statistical error has been calculated using the formula 3.5 as shown in section 3.3.9. The relative errors from the spectra of the various years are shown in figure 3.34.

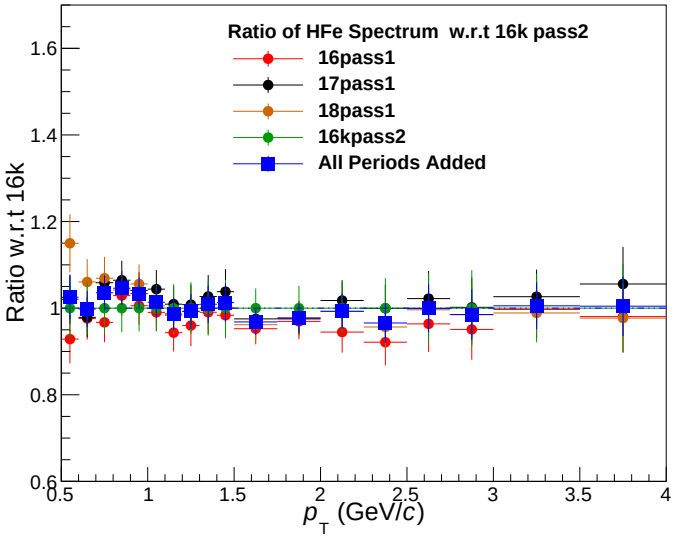

Figure 3.33: Ratio of heavy-flavour decay electron spectra of different periods with respect to 2016k

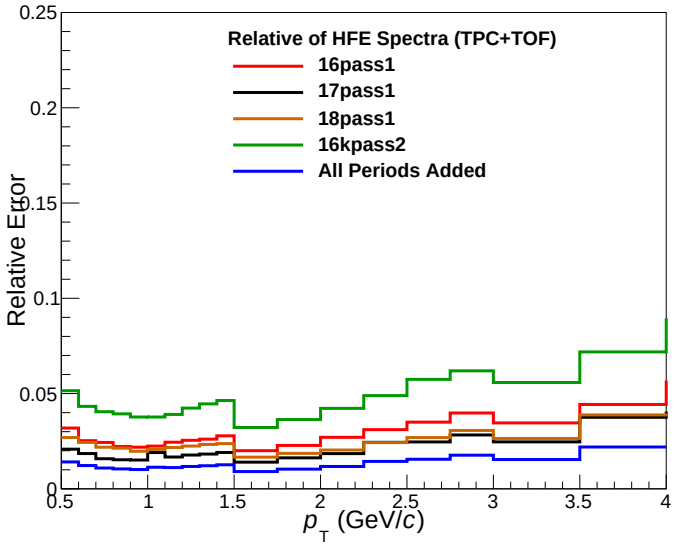

Figure 3.34: Relative error of heavy-flavor electron spectra for different periods

3.5 Systematic uncertainty for TPC–EMCal analysis

The following sources of systematic uncertainty mentioned in table 3.12 were considered for the TPC–EMCal analysis. To remove the contribution of statistical fluctuations in the

Table 3.12: Sources of systematics variations of heavy-flavour decay electron spectra for TPC–EMCal analysis

Sources of systematics		Standard Value	Variations
Rejection factor	EG2 trigger	406	Changing the fit function
	EG1 trigger	5040	and fit range
Track cuts	TPC Crossed Rows	70	60,80
	TPC clusters for PID	80	70,90
	ITS clusters	3	2,4
Electron identification cuts	E/p cut	0.85 (lower cut)	0.9, 0.8, 0.75
		1.2 (upper cut)	1.15, 1.25
	M02 cut	0.9 ($p_{\mathrm{T}} < 12$ GeV/c)	0.8, 1.0
		0.7 ($p_{\mathrm{T}} > 12$ GeV/c)	0.6, 0.8
	TPC $n\sigma_e$	(-1,3)	(-0.75,3), (-1,3.5), (-1.5,3)
Photonic electron selection cuts	Pair invariant mass	0.14 (GeV/c^2)	0.10, 0.16 (GeV/c^2)
	Min. associated p_{T}	0.10 (GeV/c)	0, 0.2 (GeV/c)
Hits on SPD layers		Any layer (kAny)	Both layers (kBoth)
Variation of hadron scaling range on E/p distribution for determination of hadron contamination		0.5 < E/p < 0.6 ($p_{\mathrm{T}} > 18$ GeV/c)	Variation in E/p scaling range

systematic uncertainty calculations a Barlow check [120] was performed. If $n_{\mathrm{Barlow}} < 2$, the contribution is excluded where

$$n_{\mathrm{Barlow}} = \frac{\mathrm{Yield}_{\mathrm{Var}} - \mathrm{Yield}_{\mathrm{Std}}}{\sqrt{\sigma^2_{\mathrm{Var}} - \sigma^2_{\mathrm{Std}}}}$$

σ signifies the statistical error. Subscripts "Std" and "Var" imply contributions from standard cut and cut variations, respectively. The sources which do not pass the Barlow criteria contribute to the systematic uncertainty. They are tabulated in table 3.13. The correlated uncertainty are summed linearly in p_{T}, while the uncorrelated uncertainty are summed in quadrature. Details of the uncertainty calculations are discussed in the following subsections.

Table 3.13: Cut variations used for systematic uncertainty calculations (that did not pass the Barlow criteria)

	Standard Value	Variations
ITS clusters	3	2,4
E/p cut	0.85 (lower cut)	0.9, 0.8, 0.75
	1.2 (upper cut)	1.15, 1.25
M02 cut	0.9 ($p_{\mathrm{T}} < 12$ GeV/c)	0.8, 1.0
	0.7 ($p_{\mathrm{T}} > 12$ GeV/c)	0.6, 0.8
TPC $n\sigma_e$	(-1,3)	(-0.75,3), (-1,3.5), (-1.5,3)
Pair Invariant Mass (GeV/c^2)	0.14	0.16
Min Associated p_{T} (GeV/c)	0.10	0.2
Hits on SPD layers	Any layer (kAny)	Both layers (kBoth)
Variation of fit function and range for rejection factor of triggered data		
Variation of hadron scaling range on E/p distribution for determination of hadron contamination		

3.5.1 Track cut variation

The ratio of the yields of electrons from heavy-flavour hadron decays from the variations of minimum ITS cluster cut with respect to the standard cut is shown in figure 3.35(a). To obtain the spectra of electrons from heavy-flavour hadron decays, the yield of electrons (inclusive - photonic sample) from the data is corrected for detector inefficiencies, acceptances and particle identification selection criteria using the reconstruction efficiency. The ratios of the yields of (inclusive - photonic) electrons and the reconstruction efficiencies, due to

variations with respect to the standard cuts are also shown separately. The ratio of yields

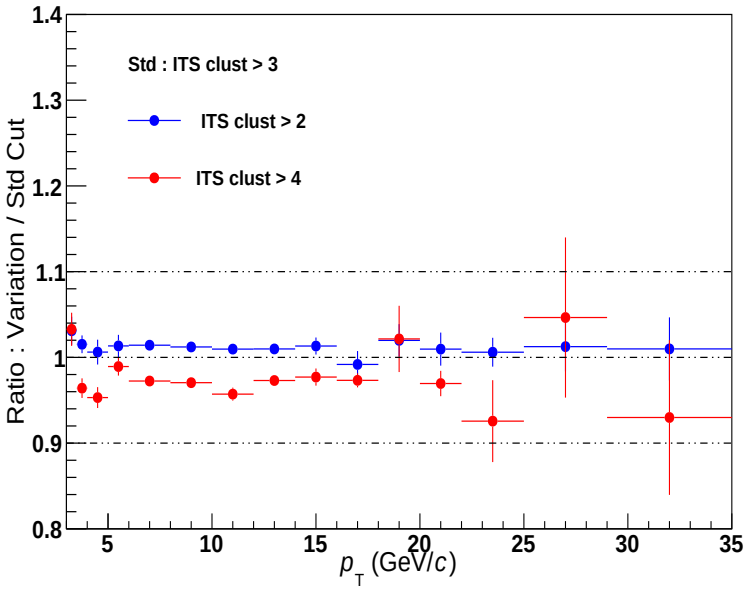

(a) Ratio of yield of electrons from heavy-flavour hadron decays from different track cut variations (ITS cluster cut)

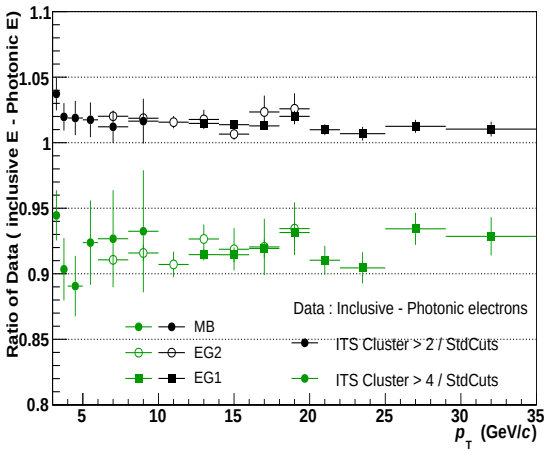

(b) Data : Inclusive - photonic electrons

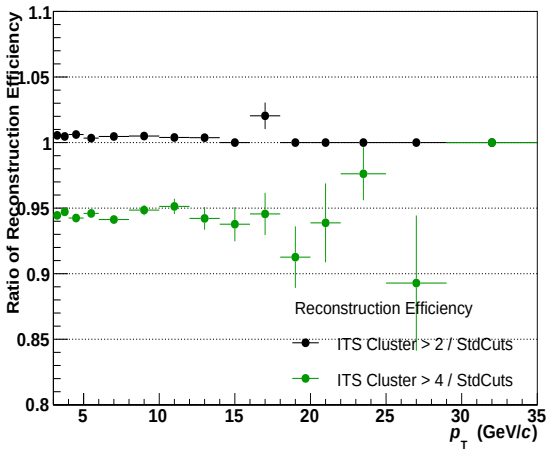

(c) Reconstruction efficiency

Figure 3.35: Ratio of yields and efficiencies for ITS cluster cut (track cut) variation

of (inclusive - photonic) electrons obtained from data, due to ITS variations with respect to the standard cut, is shown in figure 3.35(b) while the ratio of reconstruction efficiencies is shown in figure 3.35(c). The difference in yield from data with respect to standard cut (minimum ITS clusters = 3) for ITS cluster > 4 is $\sim$ 8 %, while the difference of recon-

struction efficiency is only $\sim 5\%$. Hence, the difference in the total heavy-flavour hadron decay electron yield for ITS cluster > 4 is $\sim 3\%$ ($0.92/0.95 \sim 0.97$) as seen in figure 3.35(a) and for ITS cluster > 2 is $\sim 1\%$.

3.5.2 Electron identification cut variation

The systematic uncertainty on the yield of electrons from heavy-flavour hadron decays arising from the variations for electron identification cuts with respect to the standard cuts are discussed in this section.

Figure 3.36(a) shows the ratio of the yields of electrons from heavy-flavour hadron decay from the different E/p cut variations. The ratio of (inclusive - photonic) electron yield from data and of reconstruction efficiencies for variations in the E/p cut with respect to the standard cut are shown separately in figures 3.36(b) and 3.36(c) respectively, for the largest variations ($0.75 <$ E/p < 1.2 and $0.9 <$ E/p < 1.2). The total uncertainty in the yield of electrons from heavy-flavour hadron decays arises due to the difference in the electron yields from data and the difference in the reconstruction efficiencies (from monte-carlo) as shown in the figures 3.36(b) and 3.36(c). The difference in the ratios between data and MC may arise due to the difference in the shapes of E/p distribution in data and MC, which is especially more pronounced at the higher p_{T} intervals.

Figure 3.37(a) shows the ratio of yields of electrons from heavy-flavour hadron decays for the different M02 cut variations. A systematic value of 1% is observed. The ratios of variations in the (inclusive - photonic) electron yield obtained from data and of reconstruction efficiency obtained from MC are similar, as seen from the bottom panels of figure 3.37.

Figure 3.38(a) shows the ratios of yields of electrons from heavy-flavour hadron decays for the different the TPC $n\sigma_e$ cut variations with respect to the standard cut. The ratios of the (inclusive - photonic) electron yield from data and of reconstruction efficiency from MC due to the different TPC $n\sigma_e$ cut variations are shown separately in figures 3.38(b) and

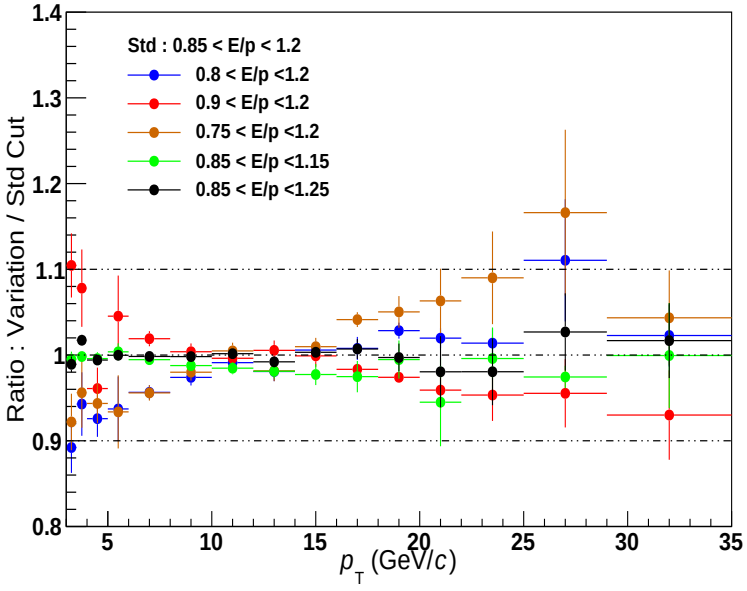

(a) Ratio of yields of electrons from heavy-flavour hadron decay from different E/p cut variations

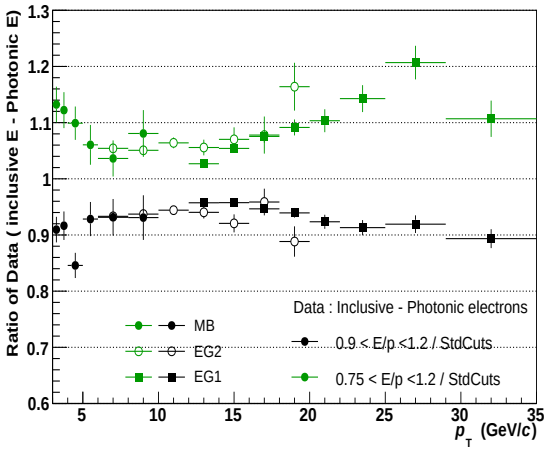

(b) Data : Inclusive - photonic electron

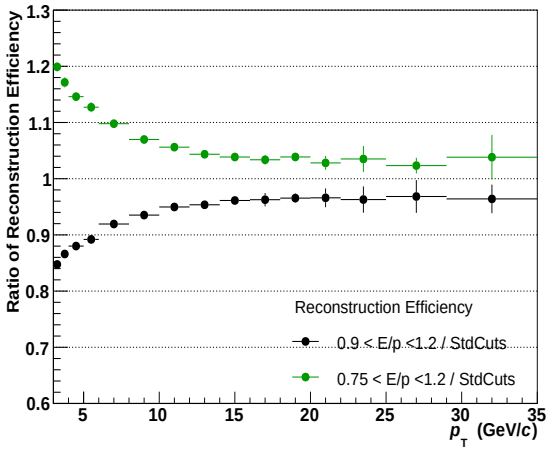

(c) Rconstruction efficiency

Figure 3.36: Ratio of yields and efficiencies for E/p cut (electron identification cut) variation

3.38(c) respectively.

These sources of electron identification cuts are correlated and the values of systematic uncertainty are obtained by summing the variation linearly. The value assigned for the electron identification cut variation are listed in table 3.14.

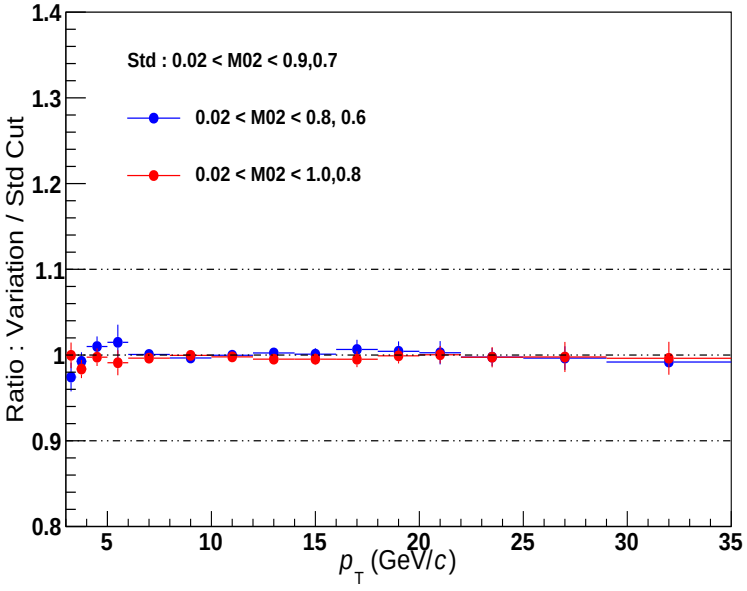

(a) Ratio of yields of electrons from heavy-flavour hadron decay from different M02 cut variations

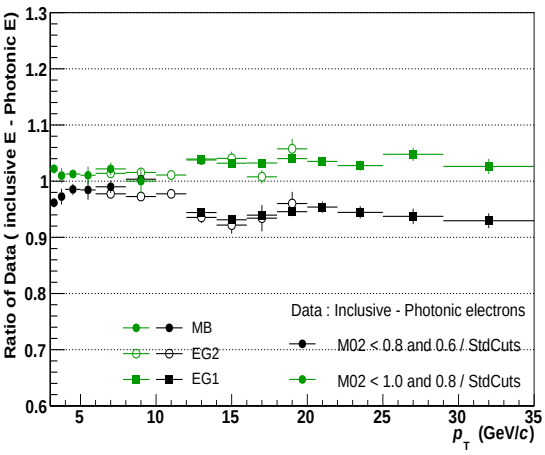

(b) Data : Inclusive - Photonic electron

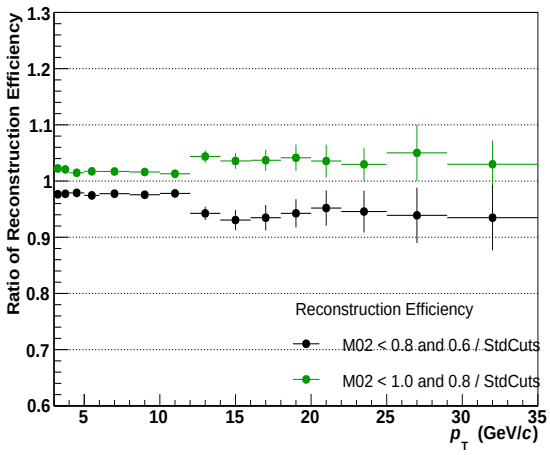

(c) Reconstruction Efficiency

Figure 3.37: Ratio of yields and efficiencies for M02 cut (electron identification cut) variation

3.5.3 Photonic electron selection cut variation

The systematics uncertainty on the yields of electrons from heavy-flavour hadron decay due to the photonic cut variations is negligible as seen from figure 3.39. The ratios of the yields of the photonic electrons (from data) and the ratios of tagging efficiency (from monte-carlo) due to the variation in the photonic electron cuts with respect to standard cuts are similar,

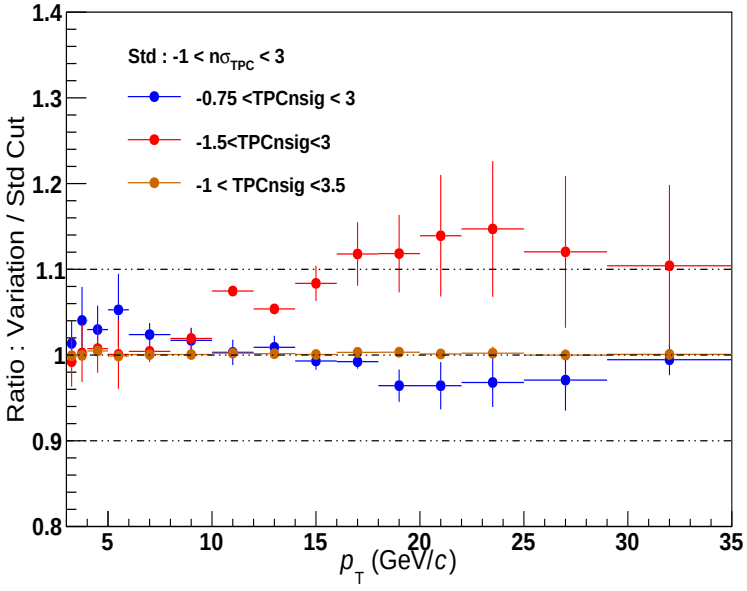

(a) Ratio of yields of electrons from heavy-flavour hadron decay from different TPC nσ_{e} cut variations

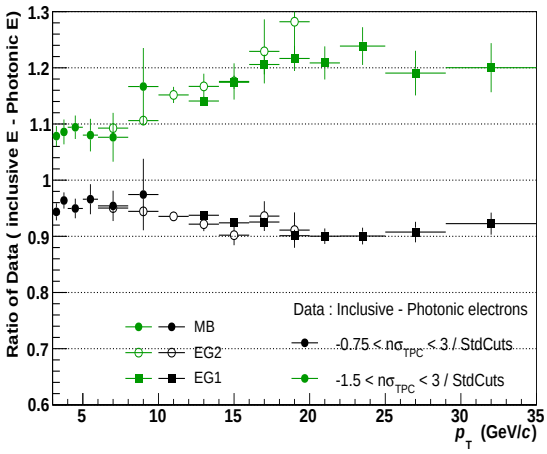

(b) Data : Inclusive - photonic electron

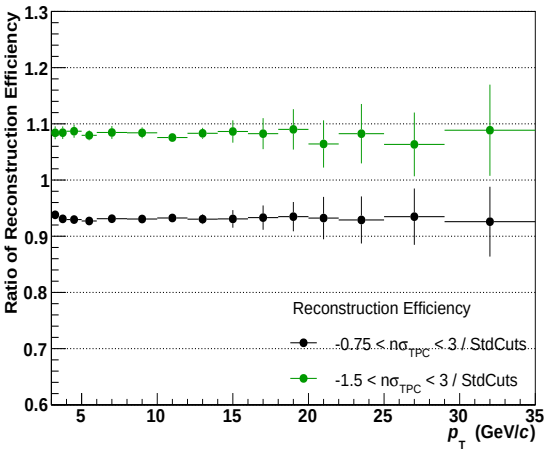

(c) Reconstruction efficiency

Figure 3.38: Ratio of yields and efficiencies for TPC nσ_e cut (electron identification cut) variation

as shown in figures 3.40(a) and 3.40(b) respectively. Hence, the ratio for the yields of electrons from heavy-flavour hadron decays is ~ 1 for all p_{T} ranges.

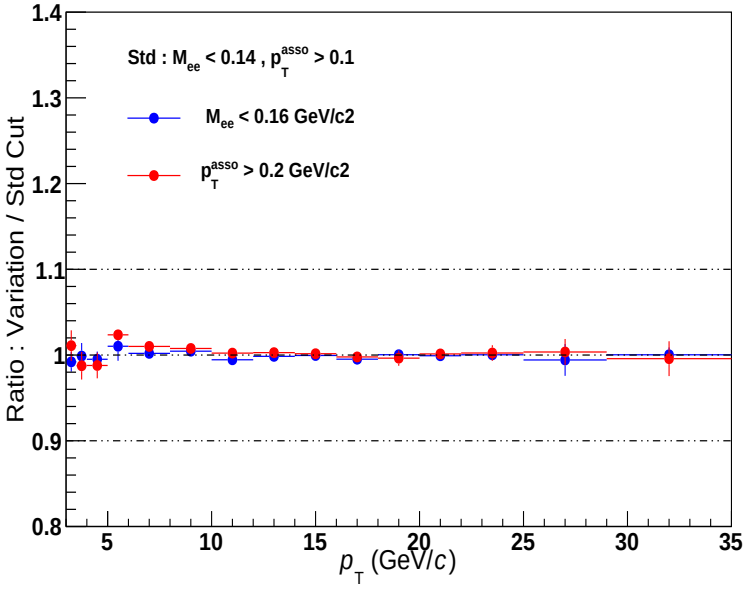

Figure 3.39: Ratio of yields of electrons from heavy-flavour hadron decay from the different photonic electron cut variations

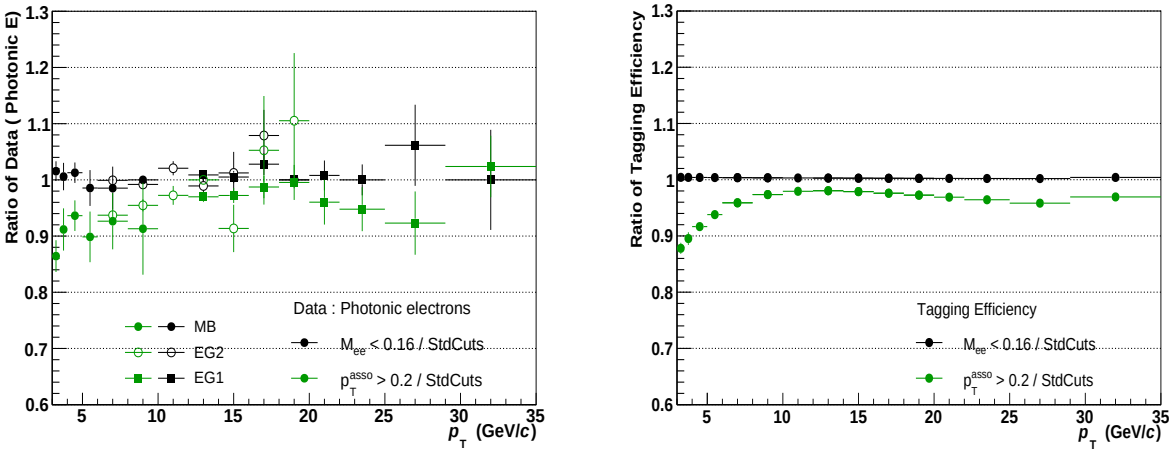

(a) Ratio of yields of photonic electrons (from data) (b) Ratio of tagging efficiencies (from monte-carlo)

Figure 3.40: Ratio of yields of photonic electrons and tagging efficiency from different variation in photonic electron selection cuts

3.5.4 SPD hit variation

The ratio the yield electrons from heavy-flavour hadron decays for SPD hits variation is shown in figure 3.41. The systematics uncertainty of $\sim 5\%$ is applied for $p_{\mathrm{T}} < 10$ GeV/c and

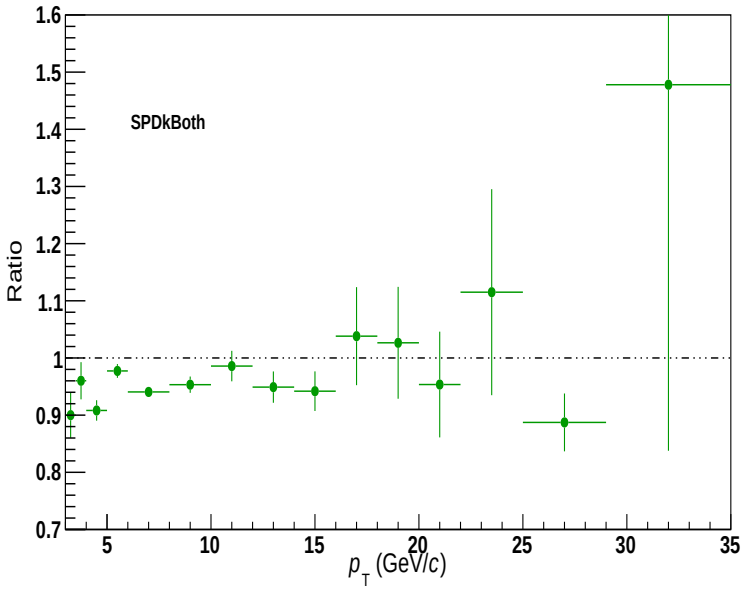

Figure 3.41: Ratio of yields of electrons from heavy-flavour hadron decay from different SPD hits variations

is negligible for $p_{\mathrm{T}} > 10$ GeV/c. The ratios of yields of (inclusive - photonic) electron obtained from data and the ratio of reconstruction efficiency from MC are shown in figures 3.42(a) and 3.42(b) respectively.

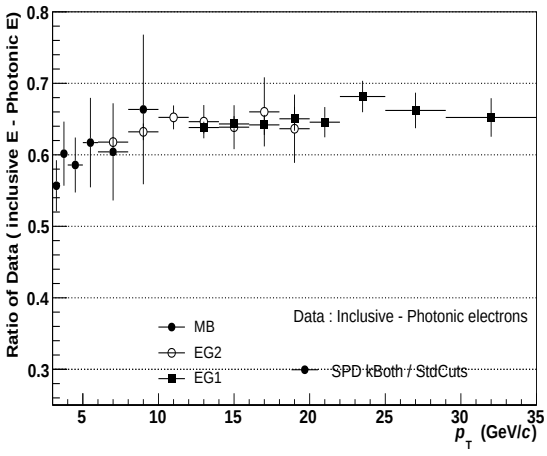

(a) Data : Inclusive - photonic electron

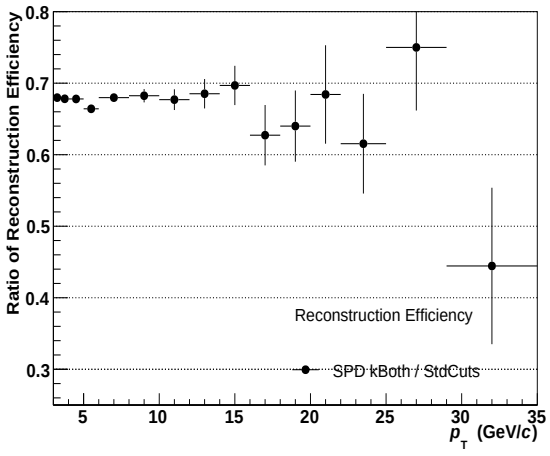

(b) Ratio of reconstruction efficiency

Figure 3.42: Ratio of yields and efficiencies for for SPD hits variations

3.5.5 Hadron contamination from E/p scaling range variation

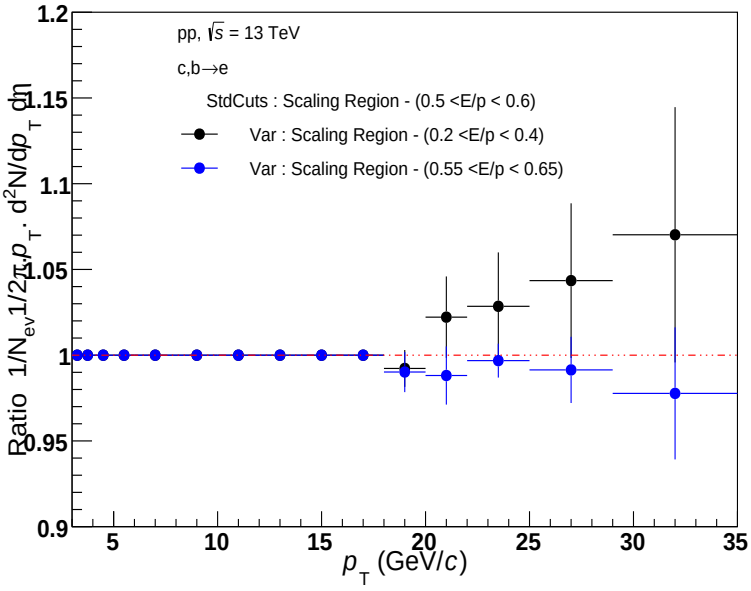

Figure 3.43: Ratio of yields of electrons from heavy-flavour hadron decay arising due to different E/p scaling range variation

The estimation of inclusive electron yield from the E/p distribution and the subsequent calculation of hadron contamination has been discussed in details in section 3.3.4. The systematic uncertainty arising due to variations in the hadronic contamination is calculated by varying the E/p scaling range to obtain the inclusive electron spectra. Figure 3.43 shows the ratios of yields of the electrons from heavy-flavour hadron decays due to variations in the E/p scaling range. The following systematics uncertainty values are applied:

Negligible for $p_{\mathrm{T}} <$ 18 GeV/c

$\sim$ 3% for 18 $< p_{\mathrm{T}} <$ 29 GeV/c

$\sim$ 7% for 29 $< p_{\mathrm{T}} <$ 35 GeV/c

3.5.6 Total systematics uncertainty

The total systematics uncertainty (σ_{total}) on the yield of electrons from heavy-flavour hadron decays is calculated in quadrature from the uncertainties obtained from the various sources mentioned above, using the formula in equation 3.9.

$$\sigma^2_{\mathrm{total}} = \sigma^2_{\mathrm{Track-Cut}} + \sigma^2_{\mathrm{eID-Cut}} + \sigma^2_{\mathrm{Photonic}} + \sigma^2_{\mathrm{RF}} + \sigma^2_{\mathrm{SPD-hits}} + \sigma^2_{\mathrm{Had-Cont}} + \sigma^2_{\mathrm{ITS-TPC}} \tag{3.9}$$

where,

$\sigma_{\mathrm{Track-Cut}}$ is the systematic uncertainty value obtained from variations of track cuts (minimum no. of ITS cluster cuts),

$\sigma_{\mathrm{eID-Cut}}$ is the systematic uncertainty value obtained from variations of electron identification cuts (E/p, M02, TPC $n\sigma_e$ cuts),

$\sigma_{\mathrm{Photonic}}$ is the systematic uncertainty value obtained from variations of photonic electron selection cuts (invariant mass cut, minimum associated p_{T} cut),

σ_{RF} is the systematic uncertainty value obtained from changing the fit function from a Fermi function to a linear function and varying fit range to obtain the trigger rejection factor from the turn on curve,

$\sigma_{\mathrm{SPD-hits}}$ is the systematic uncertainty value obtained from variations of the requirement of hits on minimum layers of SPD,

$\sigma_{\mathrm{Had-Cont}}$ is the systematic uncertainty value obtained from variations of E/p scaling ranging to obtain the hadron contamination, and

$\sigma_{\mathrm{ITS-TPC}}$ is the systematic uncertainty value of the ITS–TPC matching, which has been obtained from [121]. A 3% values is applied for all p_{T} intervals.

The total systematic uncertainty on the heavy-flavour hadron decay electron spectra in different p_{T} ranges is listed in table 3.14.

Table 3.14: Total systematic uncertainty on the yield of electrons from heavy-flavour hadron decays for the TPC–EMCal analysis. "-" in the columns implies both 'negligible' or 'not applicable'.

p_{T} range (GeV/c)	$\sigma_{\mathrm{Track-Cut}}$	$\sigma_{\mathrm{eID-Cut}}$	$\sigma_{\mathrm{Photonic}}$	$\sigma_{\mathrm{SPD-hits}}$	σ_{RF}	$\sigma_{\mathrm{Had-Cont}}$	$\sigma_{\mathrm{ITS-TPC}}$	Total (σ_{total})
3 - 4	3 %	10 %	-	5 %	-	-	3 %	12 %
4 - 8	3 %	6 %	-	5 %	-	-	3 %	9 %
8 - 10	3 %	2 %	-	5 %	-	-	3 %	7%
10 - 16	3 %	6 %	-	5 %	-	-	3 %	9%
16 - 20	3 %	12 %	-	-	2 %	1 %	3 %	13%
20 - 29	3 %	12 %	-	-	2 %	3 %	3 %	13%
29 - 35	3 %	12 %	-	-	2 %	7 %	3 %	15%

3.6 Systematic uncertainty for TPC–TOF analysis

The sources of systematic uncertainty mentioned in table 3.15 were considered for the TPC–TOF analysis. The ratio of the yields of electrons from heavy-flavour hadron decays obtained

Table 3.15: Variations used for systematics

	Standard Value	Variations
Track selection criteria :		
TPC clusters	> 100	120, 110, 90, 80
TPC clusters for PID	> 80	100, 90, 70, 80
DCA(r,z) (cm)	(1,2)	(0.5,1), (2,3), (2.4,3.2)
Min. ITS clusters	3	2,4
Particle identification criteria :		
$n\sigma_e^{\mathrm{TPC}}$	(-1,3)	(-0.5,3), (-1.5,3), (-1,3.5)
$n\sigma_e^{\mathrm{TOF}}$	$\pm$ 3	$\pm$ 2, $\pm$ 2.5, $\pm$ 3.5
Photonic electron selection :		
Pair Invariant Mass (GeV/c^2)	0.14	0.08, 0.12, 0.18
Min Associated p_{T} (GeV/c)	0.10	0.0, 0.12, 0.14
Associated TPC cluster	60	40, 50, 70, 80
Other Cuts :		
η cut	0.8	0.5, 0.6, 0.7
SPD Hits	Both layers (kBoth)	Any layer (kAny)
Hadron Contamination	Error Function	Landau Function
ITS-TPC track matching		
TPC-TOF track matching		

from the cut variations with respect to the yield obtained from the standard value, mentioned in the table, is shown in the following figures below. The ratios of yields due to variation in the track selection criteria are shown in figure 3.44. A difference of $\sim 1\%$ in the yield of electrons from heavy-flavour hadron decays is observed, which arises from the variation in the minimum number of ITS cluster required for track selection. From the variations of

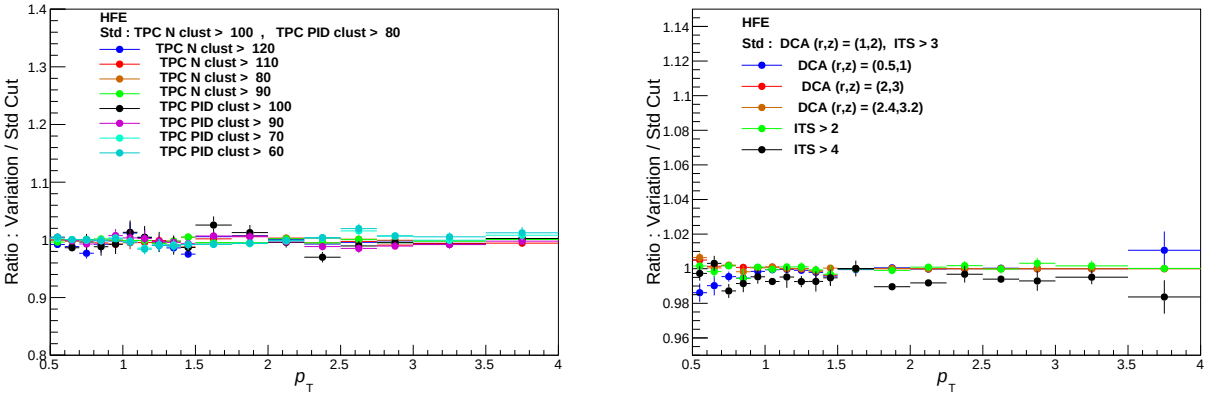

Figure 3.44: Ratio of yields of electrons from heavy-flavour hadron decays from variations of track cuts

the particle identification criteria a $\sim 5\%$ systematics uncertainty on the yields of electrons from heavy-flavour hadron decays is applied for $p_{\mathrm{T}} < 1.0$ GeV/c, as seen from figure 3.45.

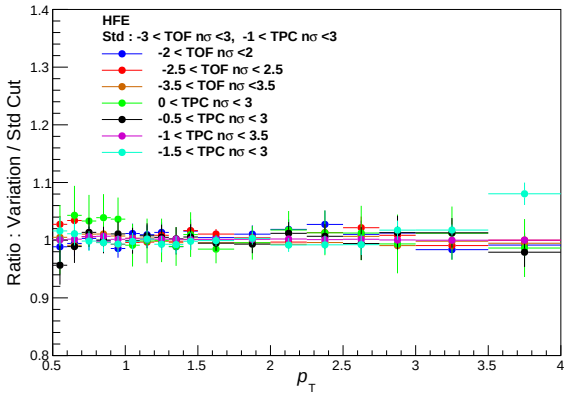

Figure 3.45: Ratio of yields of electrons from heavy-flavour hadron decays from variations of particle identification cut variation

The ratio of the yields of electrons from heavy-flavour hadron decays due to variations of the selection criteria of associated electrons for photonic electron selection is shown in figure 3.46. The following p_{T}-dependent systematic uncertainty is applied on the yields of electrons from heavy-flavour hadron decays: 7% ($0.5 < p_{\mathrm{T}}$ (GeV/c) < 0.7), 3% ($0.7 < p_{\mathrm{T}}$ (GeV/c) < 1.5), 1% ($1.5 < p_{\mathrm{T}}$ (GeV/c) < 4).

Figure 3.47 shows the ratio of the yields of electrons from heavy-flavour hadron decays due to the variations in the η selection window. A negligible systematics has been applied

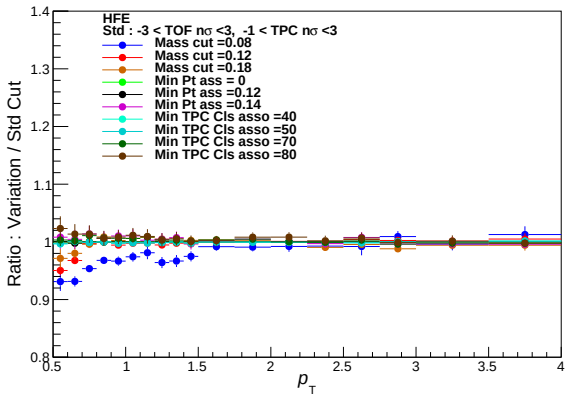

Figure 3.46: Ratio of yields of electrons from heavy-flavour hadron decays from variations of photonic electron selection

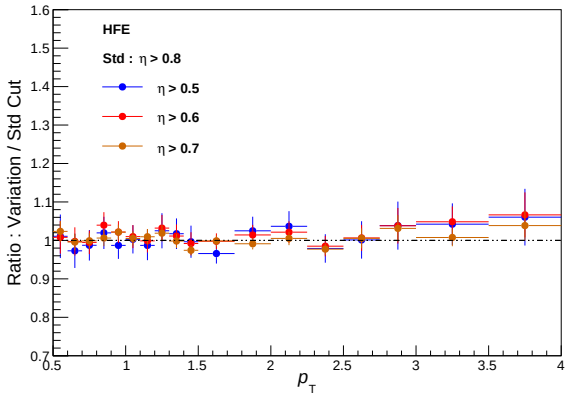

Figure 3.47: Ratio of yields of electrons from heavy-flavour hadron decays from variations of η cut variation

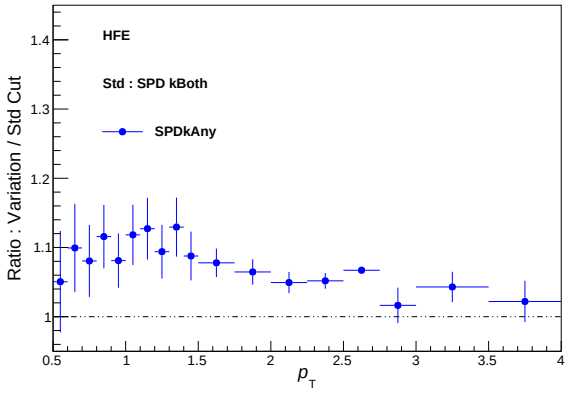

Figure 3.48: Ratio of yields of electrons from heavy-flavour hadron decays from variations in the requirement of minimum number of SPD hits

for this analysis as the variations are within statistical error.

In figure 3.48, the ratio of the heavy-flavour hadron decay electron yield due to SPD hit variation is shown. A systematic value of 10% for $p_{\mathrm{T}} < 1.5$ GeV/c and 3% for $p_{\mathrm{T}} > 1.5$ GeV/c has been considered.

The systematic uncertainty values due to the ITS–TPC matching and TPC–TOF matching has been obtained from [121]. A 3% uncertainty is applied in all p_{T} ranges for ITS–TPC matching. A systematics uncertainty of 2% is assigned for the entire p_{T} range for TPC–TOF matching.

A 2% systematic uncertainty value is obtained from varying the function used to estimate the hadron contamination. Figure 3.23 shows the fit to hadron contamination using Landau and Error functions. The Landau function has been considered for estimating the systematic uncertainty value.

The total systematics uncertainty (σ_{total}) on the yield of electrons from heavy-flavour hadron decays in the TPC–TOF analysis is calculated in quadrature from the sources mentioned above using the following equation 3.10.

$$\begin{aligned}\sigma^2_{\mathrm{total}} =& \sigma^2_{\mathrm{Track}} + \sigma^2_{\mathrm{PID}} + \sigma^2_{\mathrm{Photonic}} + \sigma^2_{\eta-\mathrm{cut}} + \\ & \sigma^2_{\mathrm{SPD-hits}} + \sigma^2_{\mathrm{Had-Cont}} + \sigma^2_{\mathrm{ITS-TPC}} + \sigma^2_{\mathrm{TPC-TOF}}\end{aligned} \tag{3.10}$$

where,

σ_{Track} is the systematic uncertainty value obtained from variations of track cut,

σ_{PID} is the systematic uncertainty value obtained from variations of electron identification cuts,

$\sigma_{\mathrm{Photonic}}$ is the systematic uncertainty value obtained from variations of photonic electron selection cuts,

$\sigma_{\mathrm{SPD-hits}}$ is the systematic uncertainty value obtained from variations of the requirement of hits on minimum layers of SPD,

$\sigma_{\mathrm{Had-Cont}}$ is the systematic uncertainty value obtained from variations of fit functions, i.e.,

Error and Landau functions,

$\sigma_{\eta-\mathrm{cut}}$ is the systematic uncertainty value due to variation in η gap, which is considered to be negligible in the entire p_{T} range,

$\sigma_{\mathrm{ITS-TPC}}$ is the systematic uncertainty value of the ITS-TPC matching, and

$\sigma_{\mathrm{TPC-TOF}}$ is the systematic uncertainty value of the TPC-TOF matching.

The total systematic uncertainty on the yield of electrons from heavy-flavour hadron decays for the TPC–TOF analysis in the different p_{T} ranges considered in the analysis is listed in table 3.16.

Table 3.16: Total systematic uncertainty on the yield of electrons from heavy-flavour hadron decays for the TPC–TOF analysis. "-" in the columns implies both 'negligible' or 'not applicable'.

p_{T} interval (GeV/c)	σ_{Track}	σ_{PID}	$\sigma_{\mathrm{Photonic}}$	$\sigma_{\mathrm{SPD-hits}}$	$\sigma_{\mathrm{Had-Cont}}$	$\sigma_{\mathrm{ITS-TPC}}$	$\sigma_{\mathrm{TPC-TOF}}$	Total (σ_{total})
0.5 - 0.7	1 %	5 %	7 %	10 %	-	3 %	2 %	14 %
0.7 - 1.0	1 %	5 %	3 %	10 %	-	3 %	2 %	12 %
1.0 - 1.5	1 %	5 %	1 %	10 %	-	3 %	2 %	12 %
1.5 - 4.0	1 %	-	-	3 %	2 %	3 %	2 %	5 %

3.7 RESULT: p_{T}-differential cross section of electrons from heavy-flavour hadron decays

The p_{T}-differential cross section of electrons from decays of heavy-flavour hadrons at mid rapidity is calculated using the following formula in equation 3.11.

$$\frac{\mathrm{d}^2\sigma}{\mathrm{d}p_{\mathrm{T}}\mathrm{d}y} = \frac{1}{2}\frac{1}{\Delta y \Delta p_{\mathrm{T}}}\frac{N_{\mathrm{raw}}}{\epsilon_{\mathrm{reco}}^{\mathrm{c,b\to e}}}\frac{1}{\int \mathcal{L}\mathrm{d}t} \tag{3.11}$$

where $\int \mathcal{L}\mathrm{d}t$ is the integrated luminosity, and Δy and Δp_{T} are the width of the rapidity and p_{T} intervals, respectively. N_{raw} is the raw number of electrons from heavy-flavour hadron decays which is obtained after subtracting the tagging efficiency corrected photonic electron yield from the inclusive electron sample. The N_{raw} is then corrected for the losses in signal with the reconstruction efficiency ($\epsilon_{\mathrm{reco}}^{\mathrm{c,b\to e}}|_{\mathrm{data-driven}}$). To account for the contributions of both electrons and positrons, the spectra is scaled by a factor of two.

In this thesis, the p_{T}-differential production cross section of electrons from the semi leptonic decays of heavy-flavour hadrons in pp collisions at $\sqrt{s} = 13$ TeV is measured in the transverse momentum region 0.5 GeV/c < p_{T} < 35 GeV/c, using the data collected with the nominal magnetic field (B) of 0.5 T. This measurement has been compared with cross section of electrons from heavy-flavour hadron decays obtained from the low magnetic field (B = 0.2 T) data [122]. The low magnetic field measurements are available in transverse momentum range 0.2 GeV/c < p_{T} < 4 GeV/c. For publication of the p_{T}-differential cross section of electrons from heavy-flavour hadron decays, the cross sections from both the low and nominal magnetic field measurements have been used. This helps to extend the cross section to wide p_{T} range, from low (0.2 GeV/c) to high (35 GeV/c) transverse momentum.

Figure 3.49 presents the comparison of the cross section of electrons decayed from

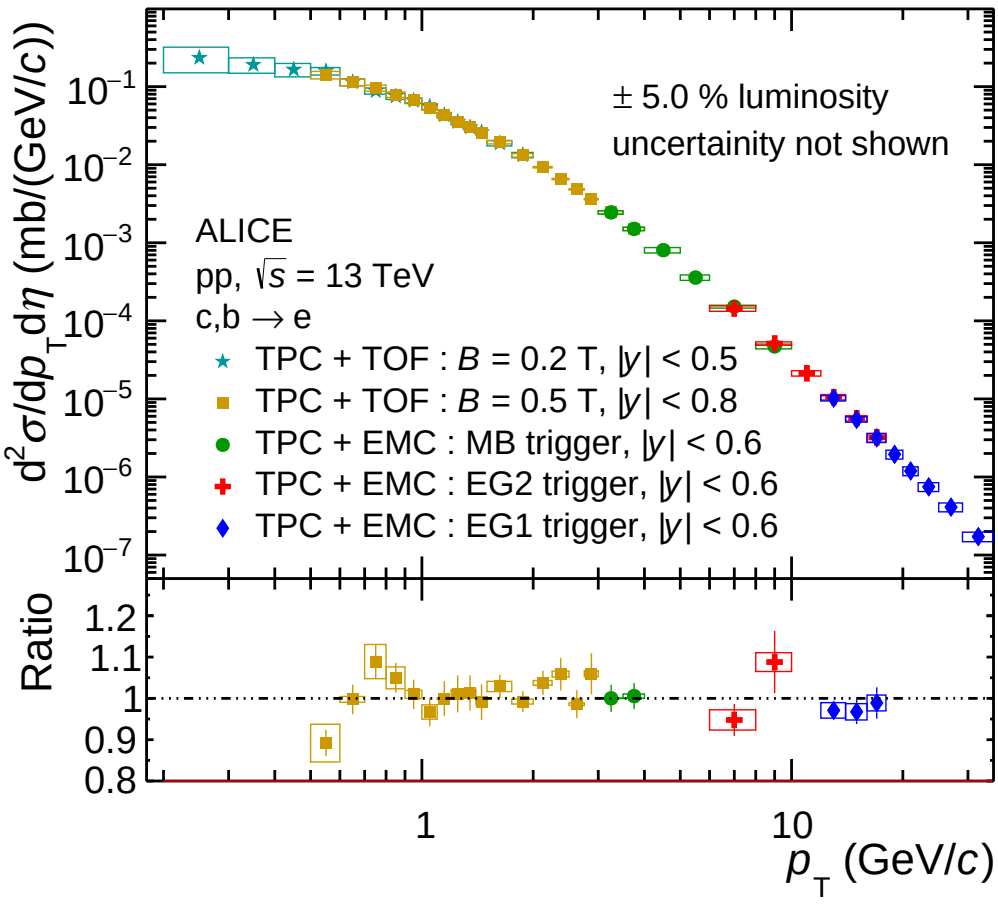

Figure 3.49: The p_{T}-differential cross section of electrons from heavy-flavour hadron decays in pp collisions at $\sqrt{s} = 13$ TeV from different measurements

heavy-flavour hadrons measured from different analyses. A comparison of the cross sections from two different data sets collected with different magnetic fields (0.2 T low B and 0.5 T nominal B) in the overlapping p_{T} interval of 0.5 - 4.0 GeV/c and comparison of the cross sections obtained from nominal magnetic field data sets using the TPC–TOF and the TPC–EMCal detectors are shown. Using the TPC–TOF detectors, the cross section has been obtained in p_{T} intervals 0.4 - 5 GeV/c. The cross sections, using the TPC–EMCal detectors with MB, EG2, EG1 triggers, have been obtained in p_{T} intervals 3.0 - 10.0 GeV/c, 6.0 - 16.0 GeV/c, 12.0 - 35.0 GeV/c respectively. A comparison of the overlapping intervals are shown in the figure. The cross sections of the electrons decayed from heavy-flavour hadrons are consistent and in good agreement with each other within the uncertainties.

The final spectra of the electrons decayed from heavy-flavour hadrons is shown in figure 3.50. The cross sections are selected from the low magnetic field ($B = 0.2$ T) TPC–TOF analysis within $0.2 < p_{\mathrm{T}}$ (GeV/c) < 0.5, nominal magnetic field ($B = 0.5$ T) TPC–TOF analysis within $0.5 < p_{\mathrm{T}}$ (GeV/c) < 4, TPC–EMCal analysis within $4.0 < p_{\mathrm{T}}$ (GeV/c) < 6.0, $6.0 < p_{\mathrm{T}}$ (GeV/c) < 12.0 and $12.0 < p_{\mathrm{T}}$ (GeV/c) < 35.0 for MB, EG2 and EG1 triggered analyses respectively. The aforementioned p_{T} intervals have been chosen such that the statistical and systematic uncertainties are minimized.

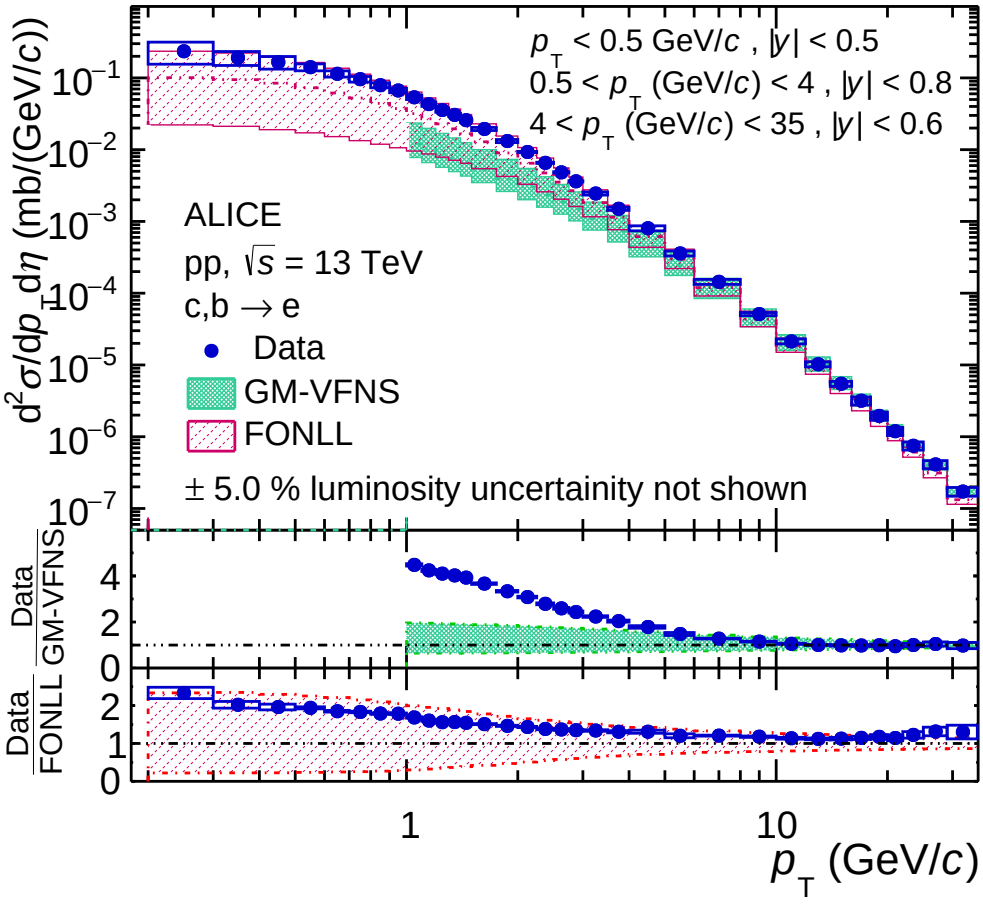

Figure 3.50: The p_{T}-differential cross section of electrons from heavy-flavour hadron decays in pp collisions at $\sqrt{s} = 13$ TeV compared with FONLL and GM-VFNS predictions

The p_{T}-differential cross section of the electrons decayed from heavy-flavour hadrons is compared with the Fixed-Order-Next-to-Leading-Log (FONLL) [123] and General-Mass-Variable-Flavour-Number-Scheme (GM-VFNS) [124, 125] perturbative QCD calculation, as

also shown in the figure 3.50. The FONLL calculations describe the measurements within the statistical and systematic uncertainties and the data points are found to be close to the upper edge of the theoretical prediction up to $p_{\mathrm{T}} < 5$ GeV/c, as also observed in pp collisions at $\sqrt{s} = 2.76$, 5.02 and 7 TeV [30, 112, 114, 126]. The GM-VFNS model largely under predicts the data in low and mid p_{T}, while data the lies within the uncertainty in the high p_{T} range ($p_{\mathrm{T}} > 10$ GeV/c). Similar observation was made for the non prompt D meson measurements [127].

Chapter 4

Multiplicity dependent study of electrons decayed from heavy-flavour hadrons

The measurement of the self normalized yield of electrons decayed from heavy-flavour hadrons as a function of the nominalized charged particle density in pp collisions at $\sqrt{s}$ = 13 TeV has been presented in this chapter. Comparison of the self normalised yields of electrons decayed from the heavy-flavour hadrons with the normalised yields of other species of particles such as, D-mesons, J/ψ, strange and charged particles and with the PYTHIA model predictions have also been presented.

4.1 Analysis Strategy

The self-normalized yield of electrons from the heavy-flavour hadron decays is obtained by dividing the yield of the heavy-flavour decay electrons in different multiplicity intervals by the average yield calculated in minimum-bias events. The self-normalized yield of electrons from the heavy-flavour hadron decays is plotted as function of the self-normalized charged particle density to study the dependence of production of the electrons from decays of

heavy-flavour hadrons on the charged particle multiplicity. The measurement of the p_{T}-differential cross section (multiplicity integrated yield) of electrons from heavy-flavour decays are discussed in details in chapter 3. The multiplicity dependent p_{T}-differential yield is obtained using the same methodology discussed in chapter 3. In the following section (section 4.2), the multiplicity measurement has been presented.

4.2 Multiplicity Measurement

For this analysis, the multiplicity is calculated in the mid rapidity region using the tracklet information from the Silicon Pixel Detector (SPD) of the Inner Tracking System (ITS) within $|\eta| < 1.0$ (N_{tr}). A tracklet is reconstructed by joining clusters of both the SPD layers which point back to the primary vertex. Due to the high granularity of the SPD, it can measure high density of particles. The total number of charged particles in an event (multiplicity, N_{ch}) is obtained from the N_{tr} with corrections applied using monte-carlo simulations.

4.2.1 Multiplicity estimation from SPD tracklets (N_{tr})

Figure 4.1 shows the distribution of the number of SPD tracklets at mid rapidity, $|\eta|$ <1.0 (N_{tr}) as a function of Z vertex (z_{vtx}). The non-uniform distribution of the observed raw N_{tr} as a function of the z_{vtx}, as seen in the left panel of figure 4.1, is due to :

- Inhomogeneous acceptance and dead modules of SPD
- Changes in the number of active modules in the SPD during each data taking period

To obtain the true SPD tracklets ($N_{\mathrm{tr}}^{\mathrm{corr}}$), the SPD efficiency is equalized along the Z vertex for each event. The right panel of figure 4.1 shows the distribution of the number of SPD tracklets as a function of Z vertex after the correction has been applied. The average profile of the number of tracklets as a function of z_{vtx} is also overlaid in both the panels of the figure. Figure 4.2 shows the average profile of SPD tracklets (N_{tr}) vs. z_{vtx} before the correction has been applied for the various data taking periods used in this analysis.

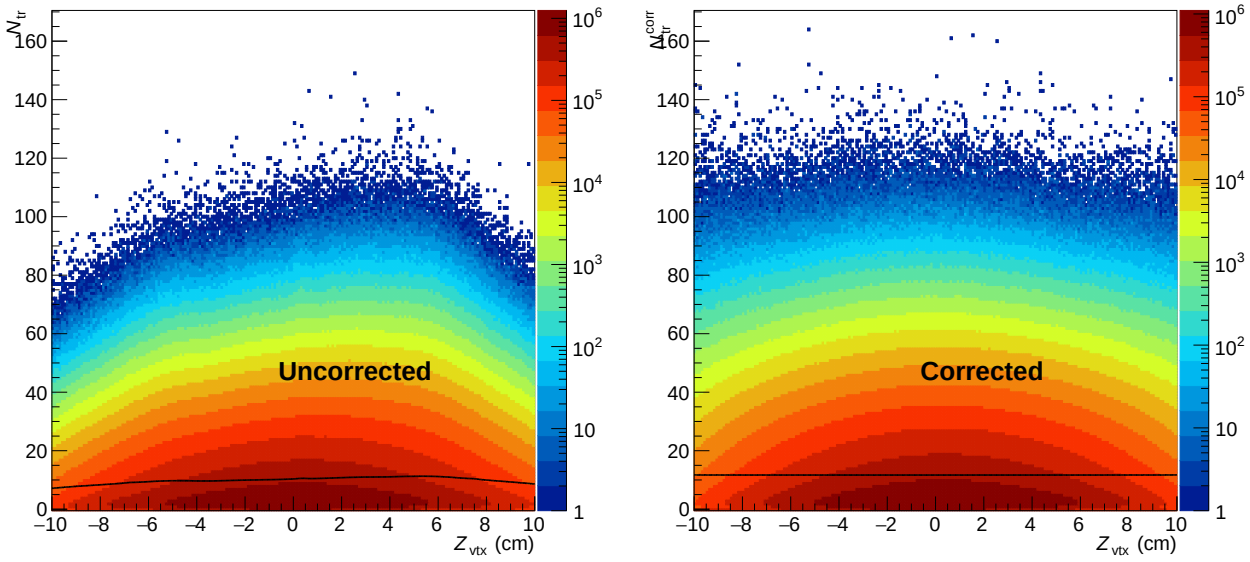

Figure 4.1: SPD tracklets ($|\eta| < 1.0$) vs. Z vertex distribution. Left panel shows the uncorrected distribution and the right panel shows the distribution after the correction is applied

For applying the equalization of SPD efficiency, the $N_{\rm tr}$ vs. $z_{\rm vtx}$ distribution is scaled with respect to a reference value of $N_{\rm tr}$ at a particular Z vertex. The reference point is taken as the highest value from the profile i.e., $\langle N_{\rm ref}\rangle \sim 11.7$ at $z_{\rm vtx} \approx 5.5$ cm. The corrected tracklet ($N_{\rm tr}^{\rm corr}$) is obtained by adding the missing tracklets (ΔN) due to the acceptance and dead modules of SPD as mentioned above, to the raw number of tracklets obtained in each event. Taking the maximum as reference, ΔN is the difference of the average number of tracklets for an event with respect to the reference.

$$\Delta N = N_{\rm tr}\frac{\langle N_{\rm ref}\rangle - \langle N_{\rm tr}(z)\rangle}{\langle N_{\rm tr}(z)\rangle}$$

where, $N_{\rm tr}$ is the number of SPD tracklets for each event and $\langle N_{\rm tr}(z)\rangle$ is the average number of tracklets at a particular Z vertex, which is obtained from the profile vs. Z vertex distribution shown in figure 4.3. A Poisson distribution is used to smear the number of missing tracklets, as previously discussed in details in [128]. The number of corrected tracklets is

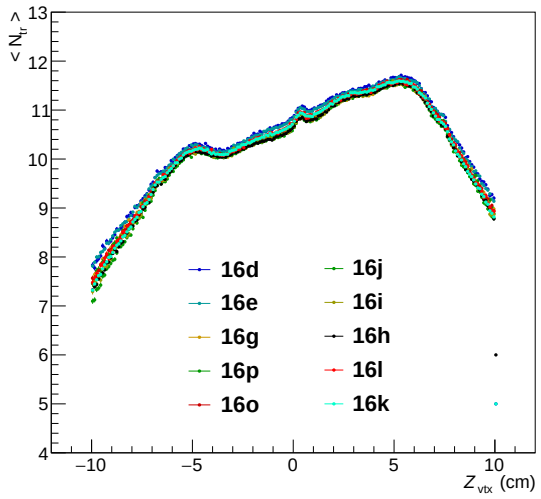

(a) 2016 periods

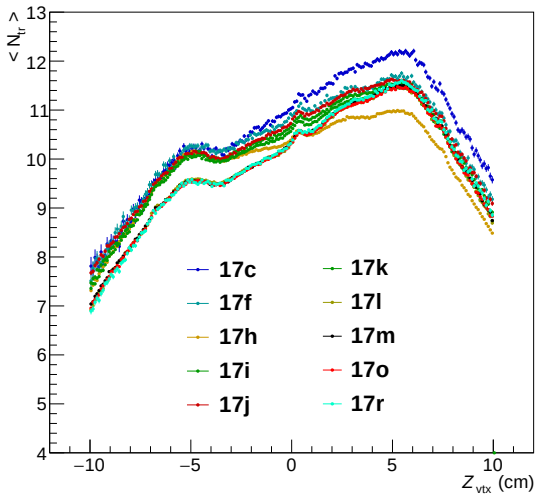

(b) 2017 periods

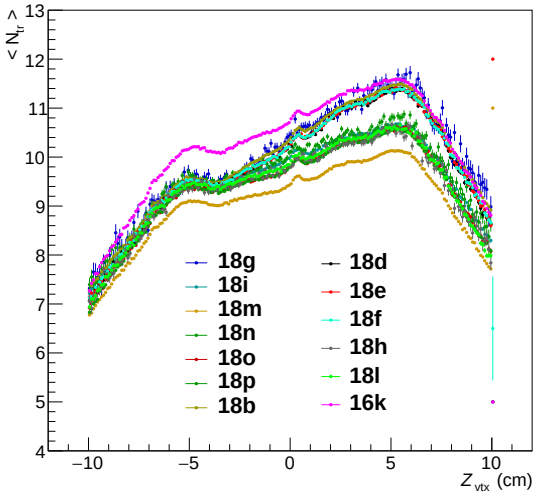

(c) 2018 periods

Figure 4.2: The 1 dimensional profiles of the uncorrected SPD tracklets (N_{tr}) as a function of z_{vtx} for different data taking periods

obtained using the formula in equation 4.1.

$$\begin{aligned} N_{\mathrm{tr}}^{\mathrm{corr}} &= N_{\mathrm{tr}} + \Delta N \\ &= N_{\mathrm{tr}} + \mathrm{Poisson}\Big(N_{\mathrm{tr}} . \Big(\frac{\langle N_{\mathrm{ref}} \rangle}{\langle N_{\mathrm{tr}}(z) \rangle} - 1\Big)\Big) \end{aligned} \tag{4.1}$$

The profile of the corrected number of SPD tracklets ($N_{\rm tr}^{\rm corr}$) as a function of $z_{\rm vtx}$ is shown in figure 4.3 for data (left) and general purpose MC (right). For comparison, the uncorrected tracklet distribution ($N_{\rm tr}$) has also been shown in the figures. The profile for the corrected SPD tracklet ($|\eta| < 1.0$), $N_{\rm tr}^{\rm corr}$ vs. $z_{\rm vtx}$ is flat and uniform for all periods.

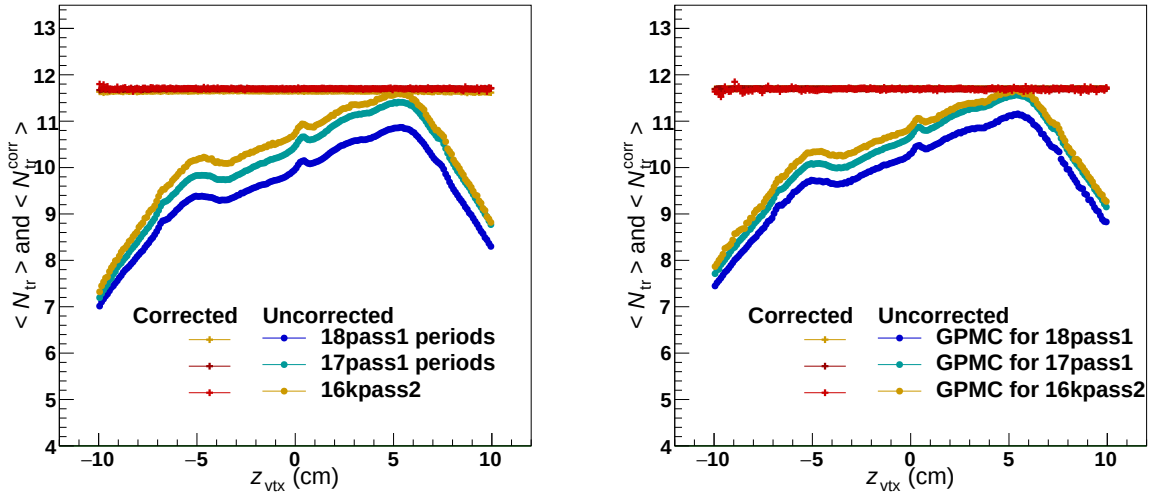

Figure 4.3: The 1-dimensional $N_{\rm tr}$ vs. $z_{\rm vtx}$ profiles before and after the correction for both data (left) and their corresponding MC (right)

4.2.2 Conversion of $N_{\rm tr}^{\rm corr}$ to $N_{\rm ch}$

The correction performed through equation 4.1 equalizes the SPD acceptance along the Z vertex, however it does does not account for the global efficiency loss of SPD. The corrected number of tracklets $N_{\rm tr}^{\rm corr}$, obtained is not the true charged particle multiplicity of the event ($N_{\rm ch}$), which is estimated from the general purpose monte-carlo samples anchored to the data taking samples.

The distributions of the number of corrected tracklets ($N_{\rm tr}^{\rm corr}$) from data and MC are shown in the left panel of figure 4.4. A difference between the distributions is observed towards higher multiplicity values. The ratio of data and MC is shown in the right panel of the figure. This difference in the distribution is corrected by applying weights obtained from the ratio plot. For $N_{\rm tr}< 40$, the weight is taken as the direct ratio of data over MC

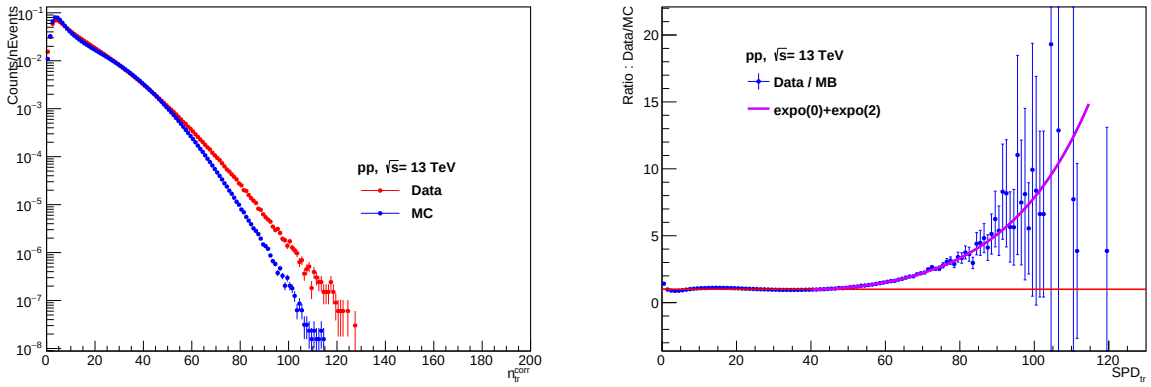

Figure 4.4: The distribution of the number of corrected SPD tracklets ($N_{\rm tr}^{\rm corr}$) for the data and MC (left) and their ratio (right)

at a given $N_{\rm tr}$. For $N_{\rm tr}\geq$ 40, the weight is taken from fitting the ratio plot with a double exponential function. The $N_{\rm tr}^{\rm corr}$ distribution for the data and MC after re-weighting the MC

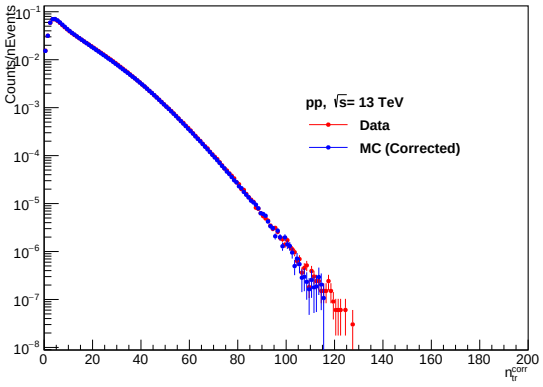

Figure 4.5: The distribution of the corrected number of SPD tracklet distribution ($N_{\rm tr}^{\rm corr}$) for the data and MC after re-weighting the MC distribution to match data

distribution to match data is shown in figure 4.5. The true charged particle multiplicity of the event ($N_{\rm ch}$) and corresponding $\mathrm{d}N_{\rm ch}/\mathrm{d}\eta$ is obtained using a $N_{\rm ch}$ vs. $N_{\rm tr}^{\rm corr}$ distribution as shown in figure 4.6. This accounts for the track-to-particle corrections needed to get the actual charged particle multiplicity. The $N_{\rm ch}$ vs. $N_{\rm tr}^{\rm corr}$ distribution was fitted with an ad hoc polynomial shown in equation 4.2 for obtaining the $N_{\rm ch}$ corresponding to a particular

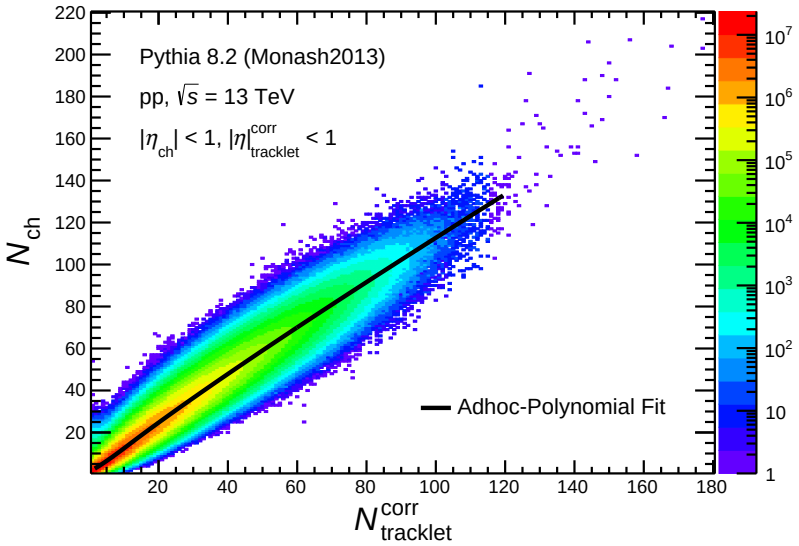

Figure 4.6: $N_{\rm ch}$ vs.$N_{\rm tr}^{\rm corr}$ fitted with an adhoc polynomial

$N_{\rm tr}^{\rm corr}$ intervals.

$$\begin{aligned} f(x) &= ax^c + b; x < x_0 \\ &= a_2 x^{c_2} + b_2; x > x_0 \end{aligned} \tag{4.2}$$

where,

$a_2 = \left(\frac{a.c}{c_2}\right) x_0^{c-c_2}$ and $b_2 = \left(\frac{a - a.c}{c_2}\right) x_0^c$ + b

a, b, c , c_2, x_0 are fit parameters.

The $\langle N_{ch} \rangle$ corresponding to $N_{\rm tr}^{\rm corr}$ bins is calculated as :

$$\langle N_{ch} \rangle = \frac{\sum_i^{n_{bins}} n_i \, . f(N_{corr}^{tr})}{\sum_i^{n_{bins}} n_i} \tag{4.3}$$

where, n_i = Number of events in i-th $N_{\rm tr}^{\rm corr}$ bin taken from data

n_{bins} = Number of bins in the $N_{\rm tr}^{\rm corr}$ interval

The table 4.1 shows the corrected SPD tracklet ($N_{\rm tr}^{\rm corr}$) intervals considered in this analysis and the corresponding charged particle multiplicity ($N_{\rm ch}$). The $N_{\rm ch}$ value was also obtained using a linear fit function, which is discussed later in section 4.2.6, and is used for systematics

study of the charged particle multiplicity estimation.

Table 4.1: Multiplicity intervals in terms of $N_{\rm tr}^{\rm corr}$and the corresponding $N_{\rm ch}$ values

$N_{\rm tr}^{\rm corr}$ Intervals	$\langle N_{\rm ch} \rangle$
1-200	14.57
1-14	7.28
15-24	22.10
25-34	33.89
35-44	45.28
45-54	56.42
55-64	67.37
65-200	81.99

4.2.3 Corrections to the multiplicity values:

The following sources of efficiency were considered, to correct for the loss of events due to the event selection criteria, which affects the multiplicity distribution.

- $\varepsilon_{\rm INEL>0}$: Minimum bias (kINT7) trigger efficiency for INEL > 0 events
- $\varepsilon_{\rm vtx-range}$: Efficiency for vertex range cuts
- $\varepsilon_{\rm pu}$: Pile up rejection

The total efficiency is:

$$\varepsilon_{\rm total} = \varepsilon_{\rm INEL>0} \times \varepsilon_{\rm vtx-range} \times \varepsilon_{\rm pu} \tag{4.4}$$

Figure 4.7 shows the $\varepsilon_{\rm INEL>0}$ (left) and $\varepsilon_{\rm vtx-range}$ (right) in multiplicity intervals and multiplicity integrated case.

The INEL > 0 events is defined as an event class containing at least one physical primary charged-particle within $-1.0 < \eta < 1.0$. The INEL > 0 trigger efficiency ($\varepsilon_{\rm INEL>0}$) is the

ratio of events with and without the INT7 trigger. While the physical selection cuts (PS) were applied, no event cuts has been applied in both the numerator and denominator.

$$\varepsilon_{\mathrm{INEL>0}} = \frac{\text{No. of events with kINT7 (PS + No event cuts)}}{\text{No. of events with out kINT7 (PS + No event cuts)}} \tag{4.5}$$

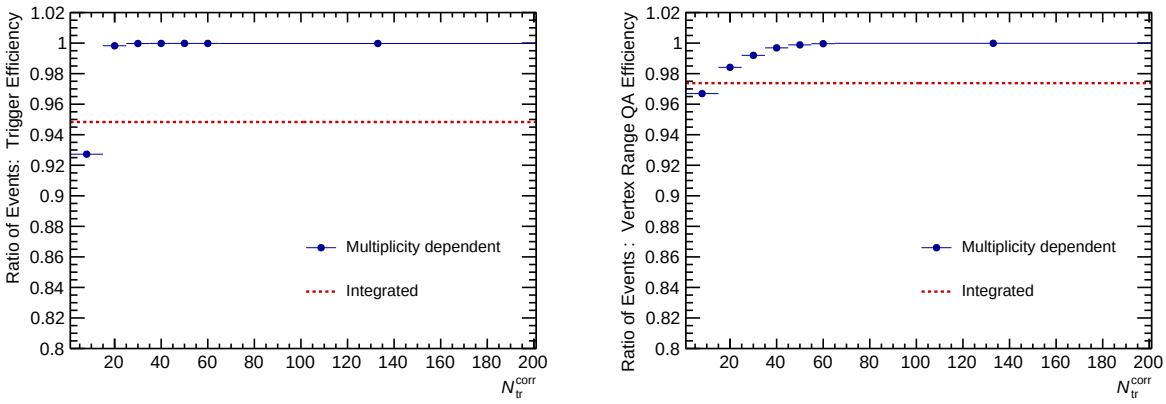

Figure 4.7: Left : INEL > 0 trigger efficiency, Right : Vertex cut efficiency

The integrated INEL > 0 trigger efficiency is $\varepsilon^{\mathrm{integ}}_{\mathrm{INEL>0}} \simeq 0.95$. The multiplicity dependent INEL > 0 trigger efficiencies are $\varepsilon^{\mathrm{i=1}}_{\mathrm{INEL>0}} \simeq 0.93$ and $\varepsilon^{\mathrm{i\geq 2}}_{\mathrm{INEL>0}} \sim 1$. The values obtained in the analysis are consistent to ones obtained for multiplicity dependent J/ψ analysis in pp collisions at $\sqrt{s} = 13$ TeV [66] for the minimum bias INEL > 0 trigger.

The vertex cut efficiency is defined as :

$$\varepsilon_{\mathrm{vtx-range}} = \frac{\text{No. of events with vertex range + QA cut (PS + kINT7)}}{\text{No. of events w/o vertex range and QA cut (PS + kINT7)}} \tag{4.6}$$

The integrated vertex efficiency is $\varepsilon^{\mathrm{integ}}_{\mathrm{INEL>0}} \simeq 0.97$. A multiplicity dependent vertex trigger efficiencies is observed.

The pile up efficiency $\varepsilon_{\mathrm{pu}} \sim 1$ for integrated and multiplicity bins which is also confirmed in [66].

The total efficiency obtained from the product these contributions is shown in figure 4.8. The integrated total efficiency is $\varepsilon^{\mathrm{integ}}_{\mathrm{total}} \simeq 0.93$. The first multiplicity bin has the efficiency of $\simeq 0.90$.

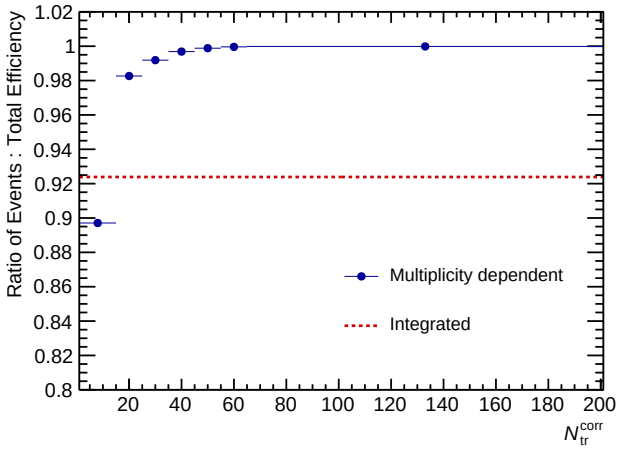

Figure 4.8: Total integrated efficiency and in corresponding $N_{\mathrm{tr}}^{\mathrm{corr}}$ intervals to correct the $\langle N_{\mathrm{ch}} \rangle$

4.2.4 $\langle \mathrm{d}N_{\mathrm{ch}}/\mathrm{d}\eta \rangle$ in pp collisions at $\sqrt{s} = 13$ TeV and comparison with the published results

The average pseudorapidity density ($\langle \mathrm{d}N_{\mathrm{ch}}/\mathrm{d}\eta \rangle$) for pp collisions at $\sqrt{s} = 13$ TeV within $|\eta| < 1.0$ measured from this analysis is:

$$\begin{aligned} \mathrm{d}N_{\mathrm{ch}}/\mathrm{d}\eta &= \epsilon_{\mathrm{trig}} \times \epsilon_{\mathrm{vtx-range}} \times \mathrm{d}N_{\mathrm{ch}}^{\mathrm{effi-uncorr}}/\mathrm{d}\eta \\ &= \epsilon_{\mathrm{trig}} \times \epsilon_{\mathrm{vtx-range}} \times 7.29 \\ &= 6.77 \end{aligned}$$

This value is in good agreement (within $\sim 3\%$) with the previous published ALICE measurements [129, 130] in pp collisions at $\sqrt{s} = 13$ TeV.

4.2.5 Self-normalised charged particle density in pp collisions at $\sqrt{s} = 13$ TeV

The following values of the self-normalised charged particle density are used for this analysis.

Table 4.2: Multiplicity intervals in terms of $N_{\rm tr}^{\rm corr}$ and the corresponding $\mathrm{d}N_{\rm ch}/\mathrm{d}\eta/\langle \mathrm{d}N_{\rm ch}/\mathrm{d}\eta\rangle$ values

$N_{\rm tr}^{\rm corr}$ Intervals	$\mathrm{d}N_{\rm ch}/\mathrm{d}\eta$ / $\langle \mathrm{d}N_{\rm ch}/\mathrm{d}\eta\rangle$
1-14	0.48
15-24	1.63
25-34	2.50
35-44	3.34
45-54	4.16
55-64	4.97
65-200	6.05

4.2.6 Uncertainty on the multiplicity axis

The following sources of uncertainty was considered for $\mathrm{d}N_{\rm ch}/\mathrm{d}\eta$ calculation:

1. Difference in $\mathrm{d}N_{\rm ch}/\mathrm{d}\eta$ value obtained from fitting the $N_{\rm ch}$ vs. $N_{\rm tr}^{\rm corr}$ distribution with functions other adhoc polynomial fit as shown in section 4.2.2.

2. Uncertainty due to residual Z_{vtx} dependence after tracklet correction

The $N_{\rm ch}$ vs. $N_{\rm tr}^{\rm corr}$ distribution was fitted with a polynomial of first order, in the total $N_{\rm tr}^{\rm corr}$ vs. $N_{\rm ch}$ distribution and in several multiplicity intervals, as shown in figure 4.9. A linear function (polynomial of first order) is used, f(x) = α x, where α=$N_{\rm ch}/N_{\rm tr}^{\rm corr}$ gives the SPD tracklet-to-particle correction factor. Using the linear pol1 function the $\mathrm{d}N_{\rm ch}/\mathrm{d}\eta$ / $\langle \mathrm{d}N_{ch}/\mathrm{d}\eta\rangle$ (x-axis) is calculated in following method:

For multiplicity interval 'i' : $\left.\frac{dN_{ch}}{d\eta}\right|_{i} = \frac{\langle N_{tr}^{corr}\rangle_i.\alpha_i}{\Delta\eta}$

For integrated multiplicity : $\left\langle \frac{dN_{ch}}{d\eta} \right\rangle = \frac{\langle N_{tr}^{corr}\rangle.\langle\alpha\rangle}{\Delta\eta}$

Self normalized x-axis values : $\frac{\mathrm{d}N_{ch}/\mathrm{d}\eta}{\langle \mathrm{d}N_{ch}/\mathrm{d}\eta\rangle} = \frac{\langle N_{tr}^{corr}\rangle_i.\alpha_i}{\langle N_{tr}^{corr}\rangle.\langle\alpha\rangle}$

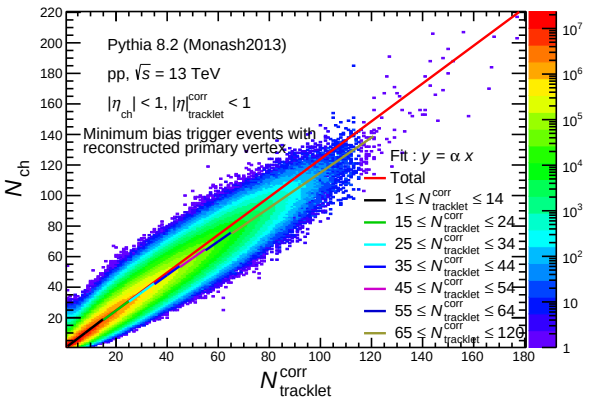

Figure 4.9: $\langle N_{ch} \rangle$ vs. $\langle N_{tr}^{corr} \rangle$ distribution along with the linear fit for the total distribution and in multiplicity bins

Table 4.3: Multiplicity bins in terms of $N_{\rm tr}^{\rm corr}$ and the corresponding $\mathrm{d}N_{\rm ch}/\mathrm{d}\eta$ values

SPD n_{tr}^{corr} Intervals	Mean $N_{\rm tr}^{\rm corr}$ Value	$N_{\rm tr}^{\rm corr}/\langle N_{\rm tr}^{\rm corr} \rangle$	α	$\mathrm{d}N_{\rm ch}/\mathrm{d}\eta$ / $\langle \mathrm{d}N_{\rm ch}/\mathrm{d}\eta \rangle$
0-200	13.046		1.174	
0-14	7.004	0.536	1.206	0.551
15-24	18.731	1.435	1.188	1.453
25-34	28.656	2.196	1.176	2.200
35-44	38.542	2.954	1.160	2.920
45-54	48.432	3.712	1.146	3.623
55-64	58.339	4.471	1.133	4.315
65-200	71.346	5.468	1.118	5.210

The $\mathrm{d}N_{\rm ch}/\mathrm{d}\eta$ / $\langle \mathrm{d}N_{ch}/\mathrm{d}\eta \rangle$ values corresponding to $N_{\rm tr}^{\rm corr}$ intervals and the corresponding α values obtained from this method is tabulated in table 4.3.

Ratio of the $\langle N_{\rm ch} \rangle$ values obtained from the fit of adhoc polynomial to those obtained from linear fit was shown in figure 4.10. There are differences in the two methods especially in the low multiplicity bins while the integrated and high multiplicity values seem to match. A maximum difference of $\sim$ 10% is seem. A similar value ($\sim$ 11%) was observed in the J/ψ study in pp collisions at 13 TeV [66]. As the overall systematic value is small, a 1% systematic value is assigned.

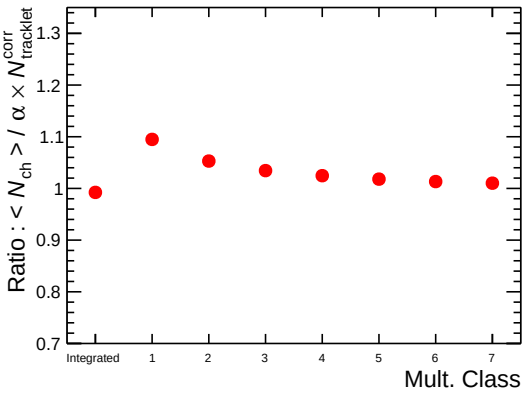

Figure 4.10: Ratio of $\langle N_{\rm ch} \rangle$ obtained from adhoc polynomial fit and linear pol1 function for the total distribution and in multiplicity bins

A deviation of linearity (α value) in the $N_{\rm ch}$ vs. $N_{\rm tr}^{\rm corr}$ correlation can be observed from figure 4.9. The multiplicity dependent values α_i value and from the global fit is plotted in figure 4.11. Global fit was also performed using $N_{\rm ch} = \alpha\ N_{\rm tr}^{\rm corr} + \epsilon$, where ϵ is a small value. The ratio to α from this fit to the global α value from table 4.3 is also plotted in figure 4.11 (in red). These fit variations also add a difference in the $\mathrm{d}N_{\rm ch}/\mathrm{d}\eta$ value. The largest

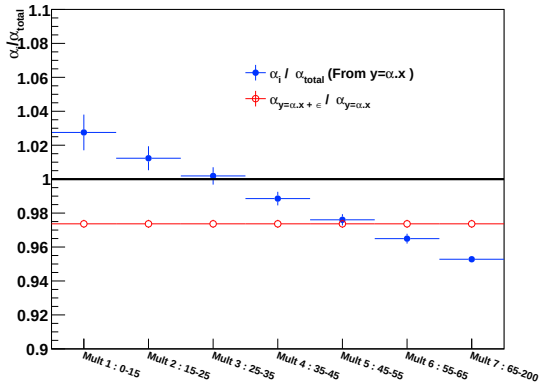

Figure 4.11: Ratio of α due to deviation of linearity.

effect comes from the highest multiplicity bin, which accounts for less than 5 % uncertainty ($\sigma_{lin} \sim 5\%$).

To estimate the uncertainty due to residual z_{vtx} dependence after tracklet correction, the $N_{\rm ch}$ vs. $N_{\rm tr}^{\rm corr}$ distribution is divided in several z_{vtx} intervals and fitted with linear function, as shown in figure 4.12. Figure 4.13 shows the uncertainty due to residual Z_{vtx} dependence

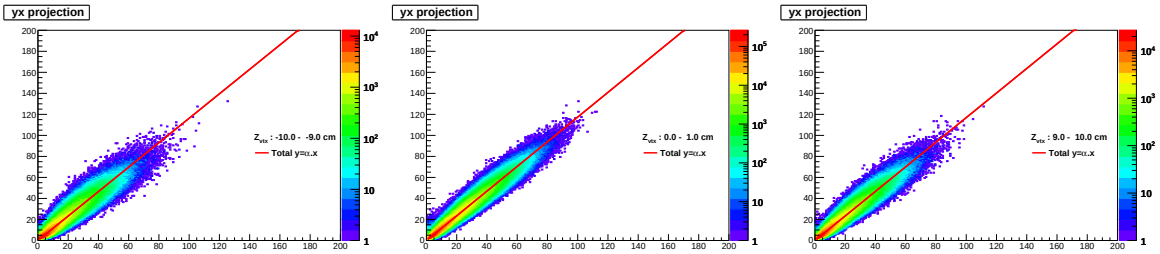

Figure 4.12: Fit of $N_{\rm ch}$vs $N_{\rm tr}^{\rm corr}$plots in z_{vtx} bins (selected bins shown)

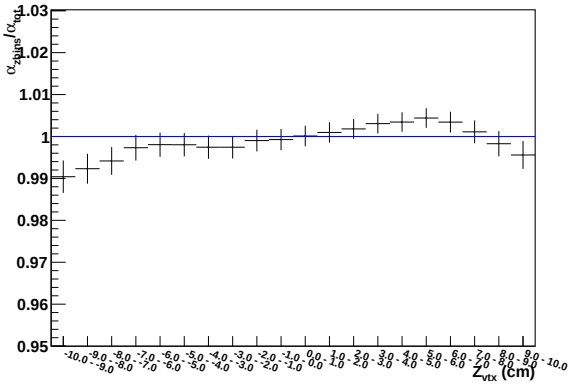

Figure 4.13: Ratio of α due to residual z_{vtx} dependence after tracklet correction

after tracklet correction and it is within 1 % ($\sigma_{zvtx} = 1\%$). The total uncertainty (σ_{x-axis}) on $\mathrm{d}N_{\rm ch}/\mathrm{d}\eta$ / $\langle \mathrm{d}N_{ch}/\mathrm{d}\eta \rangle$ is calculated as the square root of the uncertainties from all the sources added in quadrature.

$$\sigma_{x-axis} = 5\%$$

4.3 Multiplicity dependent analysis using TPC–EMCal

4.3.1 Rejection Factor

The trigger rejection factor (R) has been discussed in details in section 3.3.2. The rejection factor is defined as

$$R^i = \mathrm{S} \ \frac{N_{events}^{MB,i}}{N_{events}^{EMC,i}}$$

where i denotes multiplicity classes and :

$$\mathrm{S} = \frac{\text{Cluster energy distribution in EMCal triggered events}}{\text{Cluster energy distribution in MB triggered events}}$$

S is expected to be constant for all multiplicity intervals. The multiplicity dependence of

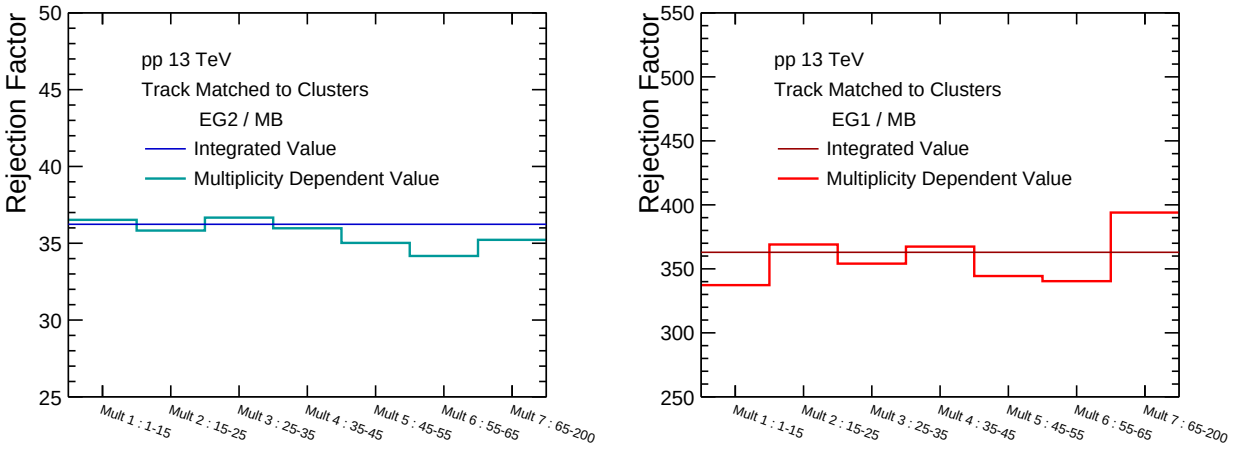

(a) RF for EG2 trigger

(b) RF for EG1 trigger

Figure 4.14: Multiplicity dependence check for the rejection factor values for both the EMCal triggers, EG2 (left) and EG1 (right)

S are plotted in figure 4.14 for both the triggers used in this analysis. Since S is a proxy for the rejection factor R and is used only in this section as a multiplicity dependence check, S is also called the rejection factor. From figure 4.14 no systematic variation is seen in the multiplicity dependent values of S. The rejection factors are considered to be independent of multiplicity for both EG2 and EG1 triggers.

4.3.2 Tagging efficiency and reconstruction efficiency

The tagging efficiency and the reconstruction efficiencies of electrons from heavy-flavour hadron decays, calculated in the multiplicity intervals chosen in this analysis, are plotted in figure 4.15, along with the multiplicity integrated values (shown in dashed lines). Both the tagging efficiency and the reconstruction efficiencies are independent of multiplicity within the statistical uncertainty.

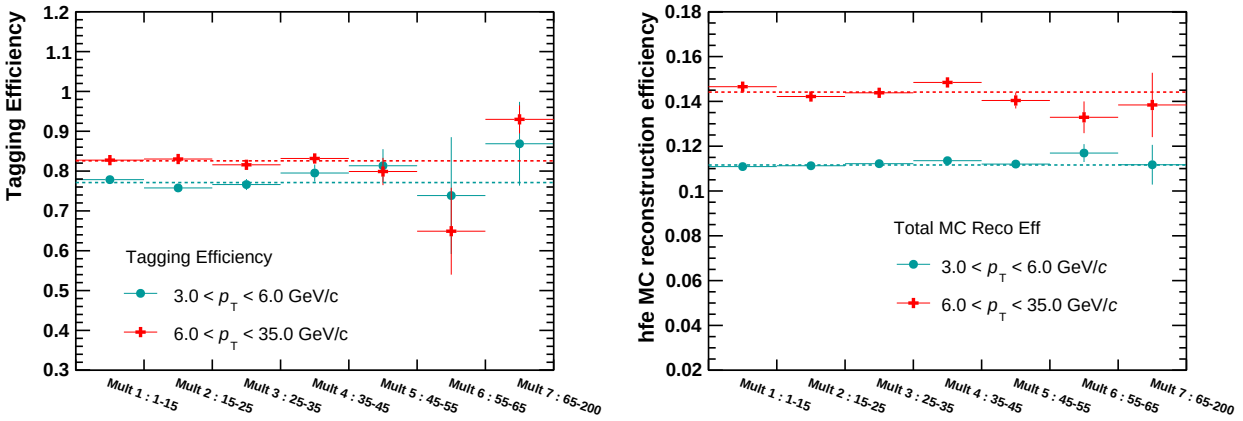

(a) Tagging efficiency

(b) Reconstruction efficiency of electrons from heavy-flavour hadron decays

Figure 4.15: Multiplicity dependence checks on efficiencies

4.3.3 Self-normalised yields of electrons from heavy-flavour hadron decays from the TPC–EMCal analysis

The self-normalized yield of electrons from decays of heavy-flavour hadrons is calculated according to the formula in equation 4.7.

$$\frac{\mathrm{d}^2N/\mathrm{d}p_\mathrm{T}\mathrm{d}\eta}{\langle \mathrm{d}^2N/\mathrm{d}p_\mathrm{T}\mathrm{d}\eta\rangle} = \frac{N^i_\mathrm{counts}/(\epsilon^i \times n^i_\mathrm{events})}{(N^\mathrm{MB}_\mathrm{counts})/(\epsilon^\mathrm{MB} \times n^\mathrm{MB}_\mathrm{events})} \tag{4.7}$$

N_{counts} = Yield of electrons from heavy-flavour hadron decays;

n_{events} = Number of events in the corresponding multiplicity interval;

ϵ = Reconstruction efficiency for electrons from decays of heavy-flavour hadrons,

'i' denotes multiplicity intervals.

Before obtaining the final self-normalised yield, as shown in figure 4.22, the yields were obtained separately from the merged data periods of 2018 and 2016k. Two representative p_{T} intervals have been chosen for this comparison. From the figure 4.16, it is seen that the periods are consistent between each other. The self-normalised yields from 2018 and 2016k were merged according to the formula in equation 3.4 and the statistical error has been calculated using the formula in equation 3.5. The final merged result of the self-normalised yields of electrons from heavy-flavour hadron decays from the TPC–EMCal analysis has also been plotted in the figure 4.16. The dashed line the figure is linear function with a slope of unity and is shown for better visualization of the increasing trend of the self-normalised yields.

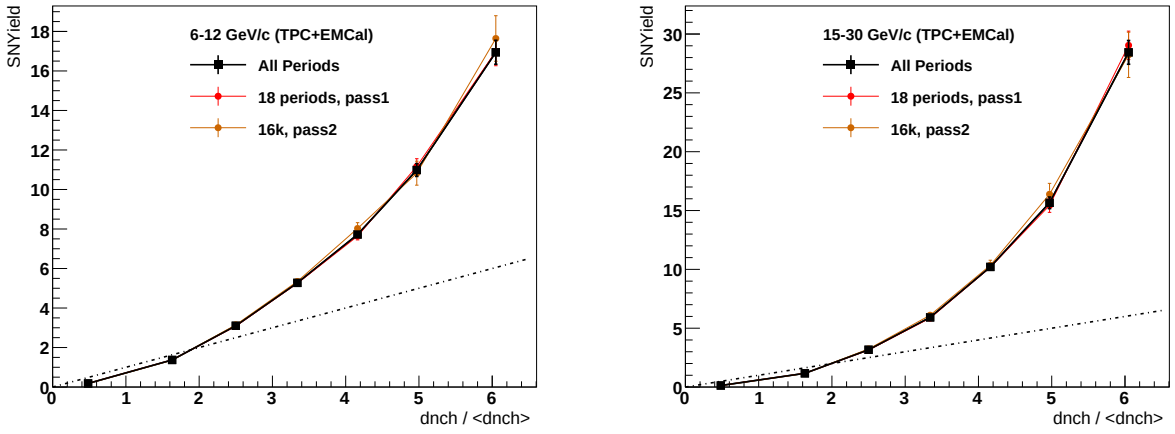

(a) $6 < p_{\mathrm{T}} < 12$ GeV/c (b) $15 < p_{\mathrm{T}} < 30$ GeV/c

Figure 4.16: Self-normalised yields of electrons from heavy-flavour hadron decays from the TPC–EMCal analysis. The dashed line the figure is linear function with a slope of unity.

4.4 Multiplicity dependent analysis using TPC–TOF

4.4.1 Tagging efficiency and reconstruction efficiency

A dependence on multiplicity of the tagging efficiency and the reconstruction efficiency of electrons from heavy-flavour hadron decays used in the TPC–TOF analysis, can be observed from figure 4.17. Dashed lines in the figure are the multiplicity integrated values. A multiplicity dependent tagging efficiency and reconstruction efficiency has been used for calculation of the self-normalised yields of electrons from decays of heavy-flavour hadrons in the TPC–TOF analysis.

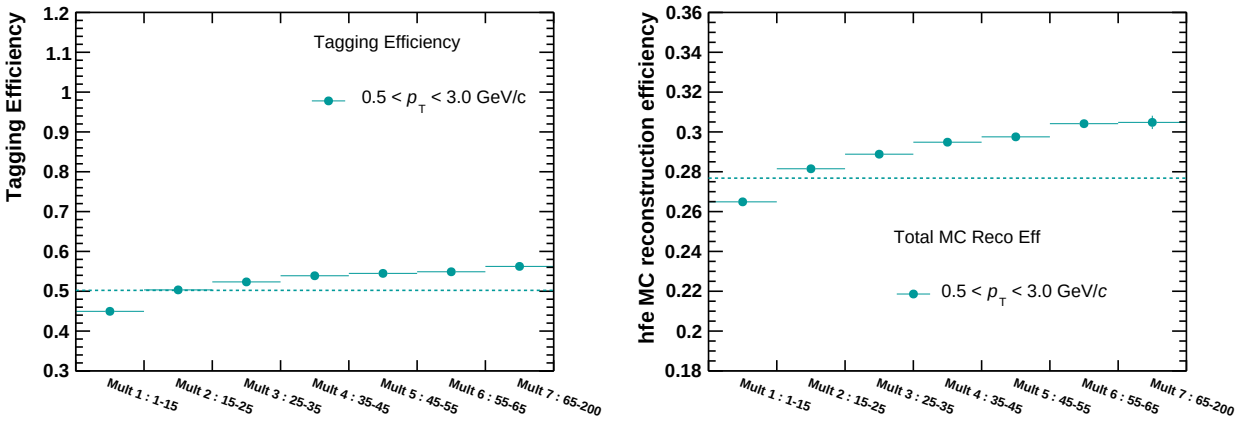

(a) Tagging efficiency

(b) Reconstruction efficiency of electrons from heavy-flavour hadron decays

Figure 4.17: Multiplicity dependence of efficiencies

4.4.2 Self-normalised yield of heavy-flavour hadron decay electron from TPC–TOF analysis

Similar to the TPC–EMCal analysis as shown in section 4.3, consistency of the self-normalised yields of electrons from decays of heavy-flavour hadrons between different periods used for this analysis is shown in figure 4.18. The self-normalised yields have been calculated according to the equation 4.7. As seen from the figure, the self-normalised yields obtained from

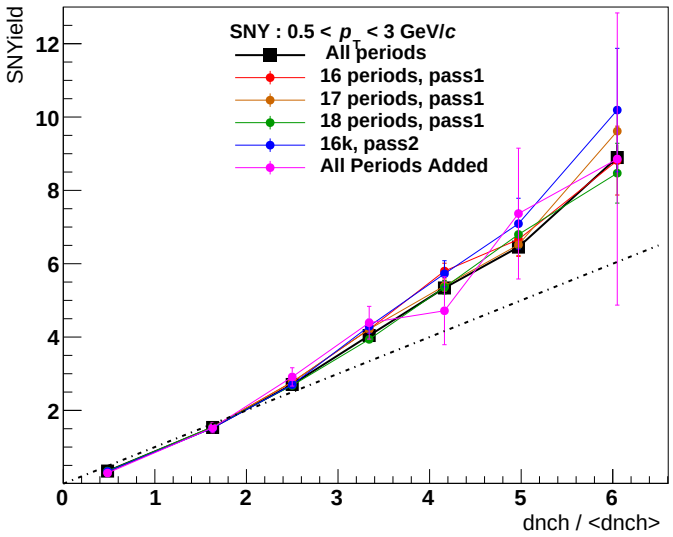

Figure 4.18: Self-normalised yields of electrons from heavy-flavour hadron decays from the TPC–TOF analysis. The dashed line the figure is linear function with a slope of unity.

different periods of 2016, 2017 and 2018 are consistent within the statistical uncertainty. The self-normalised yields from all the periods have been merged according to the formula in equation 3.4 and the statistical error has been calculated using the formula in equation 3.5. The final merged result of the self-normalised yields of electrons from heavy-flavour hadron decays from the TPC–TOF analysis has also been plotted in the figure. The dashed line the figure is linear function with a slope of unity and is shown for better visualization of the increasing trend of the self-normalised yields.

4.5 Systematic uncertainty for self-normalized yield of electrons decayed from heavy-flavour hadron

The sources of systematics considered are the same as those chosen in sections 3.5 and 3.6. Since the self-normalized yield is a ratio of spectra, contributions from many sources cancel out. Only the sources which have relevant contribution to the final systematic value is shown in this section. The systematics for all p_{T} intervals have been calculated separately. Same strategy for calculation of the uncertainty has been considered for all the p_{T} intervals.

In this section, uncertainty calculations are shown for the p_{T} interval $6 < p_{\mathrm{T}} < 12$ GeV/c to demonstrate the process of obtaining the systematic uncertainty value.

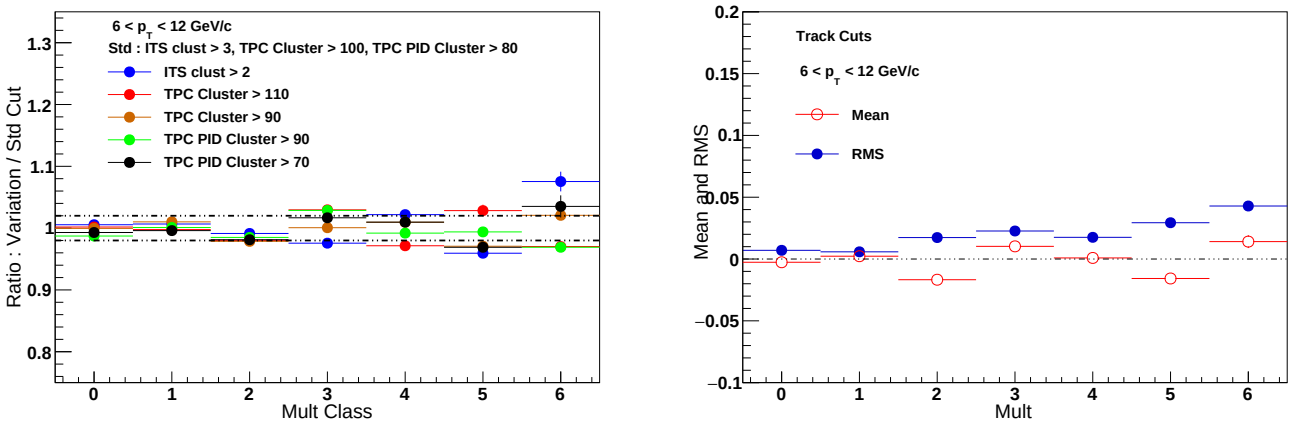

Figure 4.19: Track cut variation: Ratio of self-normalised yields with variations with respect to standard cuts (left) and their mean and RMS (right) for $6 < p_{\mathrm{T}} < 12$ GeV/c

Figures 4.19, 4.20, 4.21 show the ratio of the self-normalised yields obtained from cut variations with respect to that with the standard cuts (left) and their mean and RMS (right) for $6 < p_{\mathrm{T}} < 12$ GeV/c, for track cut, electron identification cut and photonic track selection cut variations respectively.

The uncertainty values are obtained from the square-root of the mean of the variation with respect to the standard cut (RMS). For track cut variation a $\sim 2\%$ systematic value (σ_{Track}) is assigned for all multiplicity and p_{T} bins. For electron identification cut, a $\sim$

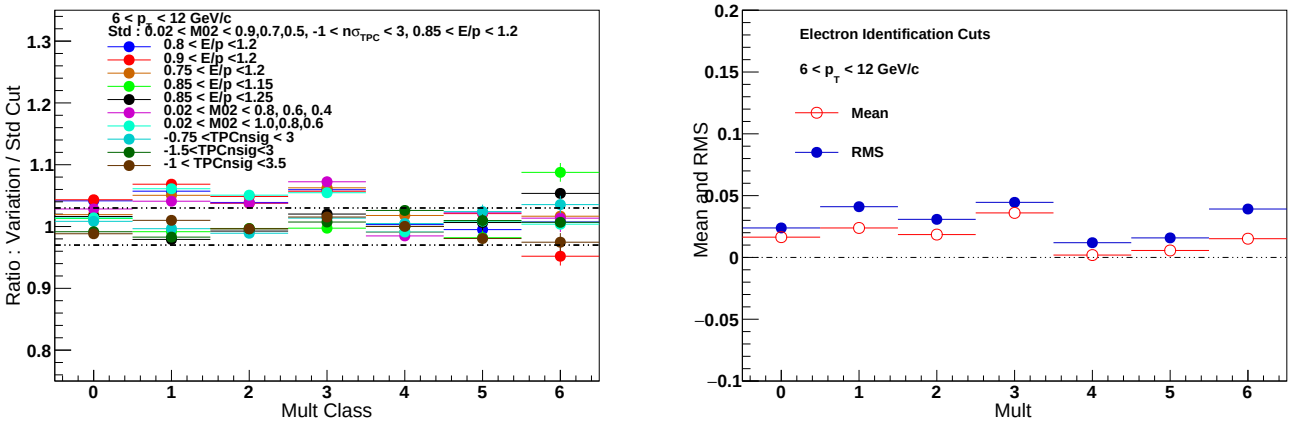

Figure 4.20: Electron identification cut variation: Ratio of self-normalised yields with variations with respect to standard cuts (left) and their mean and RMS (right) for $6 < p_{\mathrm{T}} < 12$ GeV/c

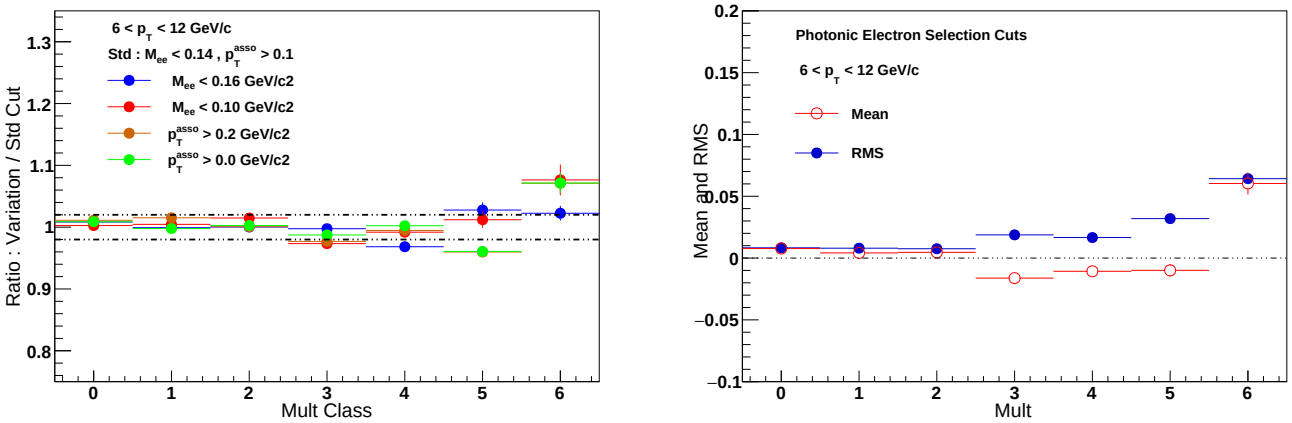

Figure 4.21: Photonic track selection cut variation: Ratio of self-normalised yields with variations with respect to standard cuts (left) and their mean and RMS (right) for $6 < p_{\mathrm{T}} < 12$ GeV/c

3% systematic value (σ_{eID}) is assigned for all multiplicity and p_{T} intervals. For photonic track selection cut, a $\sim$ 2% systematic value ($\sigma_{\mathrm{Photonic}}$) is assigned for all multiplicity and p_{T} intervals. For SPD hits, a multiplicity and p_{T} dependent systematic value ($\sigma_{\mathrm{SPD-hits}}$) is assigned as shown in table 4.4.

4.5.1 Total Systematics

Total systematic uncertainty value is calculated as :

$$\sigma_{\text{total}} = \sqrt{\sigma^2_{\text{Track}} + \sigma^2_{\text{eID}} + \sigma^2_{\text{Photonic}} + \sigma^2_{\text{SPD-hits}}}$$

Table 4.4 shows the total systematic uncertainty on the self-normalized yield of electrons from heavy-flavour decays in few representative multiplicity intervals and p_{T} intervals amongst all the intervals considered in this analysis.

Table 4.4: Systematic uncertainty on self-normalised yield of electrons from heavy-flavour hadron decays in pp collisions at $\sqrt{s} = 13$ TeV

		p_{T} interval (GeV/c)		
Observable	Multiplicity	0.5-6 GeV/c	6-12 GeV/c	15-30 GeV/c
Track Selection	I	negligible	2%	2%
	III	negligible	2%	2%
	V	negligible	2%	2%
Electron Identification	I	1%	3%	3%
	III	1%	3%	3%
	V	1%	3%	3%
Photonic Electron	I	1%	1%	2%
	III	1%	2%	2%
	V	1%	2%	2%
SPD Hits	I	10%	6%	14%
	III	3%	6%	6%
	V	4%	6%	6%

4.6 RESULT : Multiplicity dependent self-normalised yield of electrons decayed from heavy-flavour hadrons

The self-normalized yields of electrons decayed from heavy-flavour hadrons are calculated according to equation 4.7. The trigger and vertex finding efficiencies are close to unity

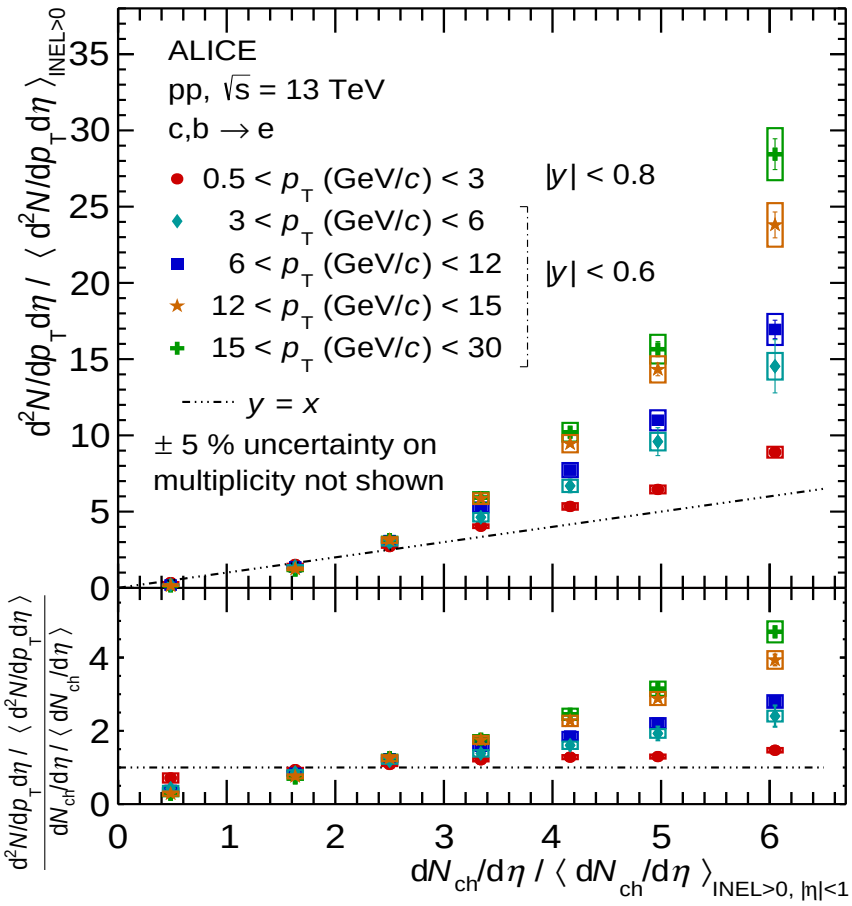

Figure 4.22: Self-normalised yield of electrons decayed from heavy-flavour hadrons as a function of normalised charged-particle pseudorapidity density at mid rapidity in different p_{T} intervals

for all multiplicity intervals except for the lowest multiplicity range as shown in section 4.2. The lowest multiplicity range has been corrected with the trigger and vertex finding efficiencies. Figure 4.22 shows the self-normalized yields of electrons decayed from heavy-flavour hadrons ($\mathrm{d}^2N/\mathrm{d}p_{\mathrm{T}}\mathrm{d}\eta/\ \langle \mathrm{d}^2N/\mathrm{d}p_{\mathrm{T}}\mathrm{d}\eta \rangle$) as a function of normalised charged-particle

pseudorapidity density ($\mathrm{d}N_{\mathrm{ch}}/\mathrm{d}\eta$/ $\langle \mathrm{d}N_{\mathrm{ch}}/\mathrm{d}\eta \rangle$) at mid rapidity ($|\eta| < 1.0$) in five p_{T} intervals from $0.5 < p_{\mathrm{T}} < 30$ GeV/c on the top panel. The dashed line shown in the figure for better visualization is a linear function with a slope of unity. The bottom panel of the figure shows the ratio of the self-normalized yield of electrons from heavy-flavour hadron decays to the self-normalised charged-particle pseudorapidity density (double ratio) as a function of the self-normalised charged-particle pseudorapidity density. The normalised yield has a faster than linear increasing trend with respect to normalised charged-particle density and higher p_{T} ranges show a tendency of steeper increase. The increase in yield is approximately a factor of ~ 9 for the lowest measured p_{T} ($0.5 < p_{\mathrm{T}} < 3$ GeV/c) and a factor of ~ 28 for the highest measured p_{T} ($15 < p_{\mathrm{T}} < 30$ GeV/c) for multiplicities of 6 times the average multiplicity. Figure 4.23 shows the ratio of the normalised yield in different p_{T} intervals

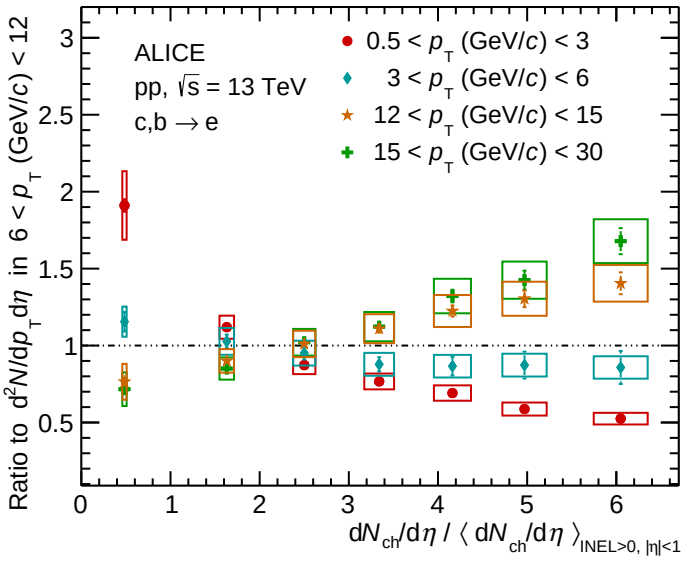

Figure 4.23: Ratio of the normalised yields electrons of heavy-flavour hadron decays in different p_{T} intervals with respect to that of the $6 < p_{\mathrm{T}} < 12$ GeV/c

with respect to that of the $6 < p_{\mathrm{T}} < 12$ GeV/c. The yield of electrons from heavy-flavour hadron decays in the lower p_{T} ranges is higher in low multiplicity events, while it reduces in higher multiplicity events. At higher p_{T} intervals the yield has an opposite trend. The contribution of beauty hadron decay to the yield increases with and dominates over charm

hadron decays for $p_{\mathrm{T}} > 6$ GeV/c. The increase of the slope of the normalized yield and the p_{T} trend is also influenced by the momentum dependence of jet fragmentation which contributes to the measured multiplicity at mid rapidity, also known as auto-correlation effect. Several experimental measurements in ALICE which have used the V0 detector at forward rapidity as a multiplicity estimator instead of SPD tracklets at mid rapidity, with an aim to largely remove a possible auto-correlation bias, have observed significantly faster than linear growth with the normalized multiplicity [65, 66].

4.6.1 Comparison with model predictions: PYTHIA8

The self-normalised yield of electrons from heavy-flavour decays in different p_{T} intervals have been compared with predictions from PYTHIA 8.2 Monash [94] and colour reconnection Mode 2 [131] tune calculations, as shown in the left and right panels of figure 4.24 respectively. Multiple parton interaction (MPI) and colour reconnection (CR) mechanisms are implemented in the PYTHIA, which helps reproduce the charged-particle multiplicity distribution measured at LHC [132, 133]. The Monash tune is the currently used as the

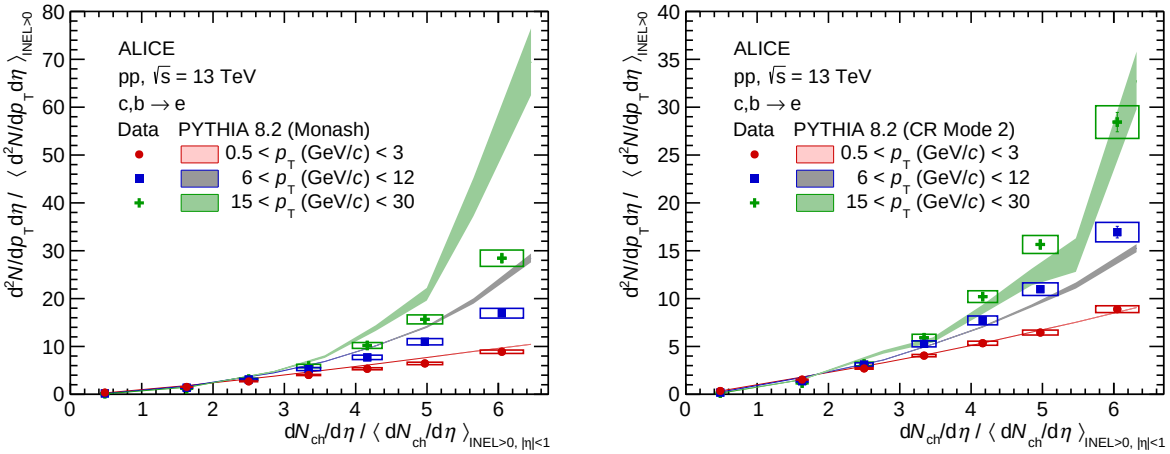

Figure 4.24: Comparison of self-normalised yield of electrons from heavy-flavour decays computed in for different p_{T} intervals with PYTHIA 8.2 Monash [94] (left) and Mode 2 [131] (right) tune calculations

default PYTHIA tune. Recently, several new models for colour reconnection has been in-

cluded in the new tunes of PYTHIA. The default Monash tune uses CR Mode 0, where coloured partons from MPI with certain transverse momentum p_{T} undergo reconnection in such a way that the total string length is minimized. PYTHIA with CR Mode 2 is an improved tune including string formation beyond the leading-colour approximation. In this tune, reconnections are performed in the same way as in the default, however the difference being that only gluons are considered for reconnection, which can affect colour flow from the hard interaction compared to the default model [133].

From figure 4.24, it can be observed that the PYTHIA 8.2 Monash tune describes the overall trend in data, however slope is overestimated at high p_{T}. PYTHIA 8.2 with CR Mode 2 is to reproduces the slope at all p_{T} intervals fairly well. PYTHIA 8.2 CR Mode 2 describes the normalised yield better than that by the Monash tune.

4.6.2 Comparison of self-normalised yields of heavy-flavour hadron decay electrons with those of other particles

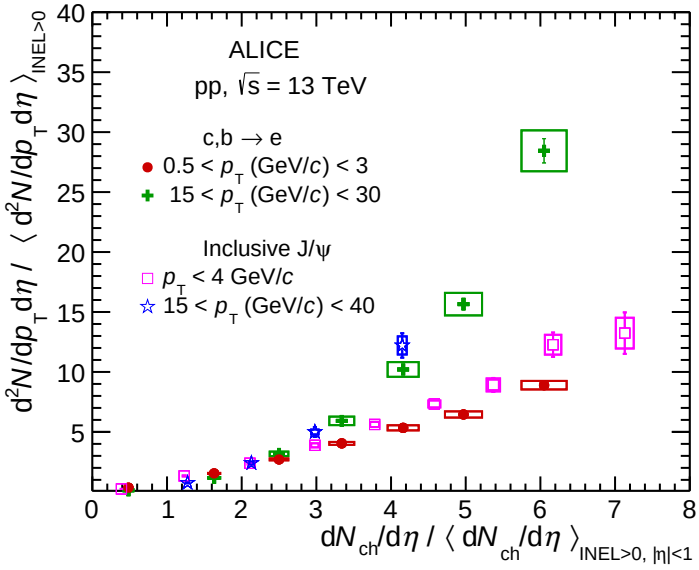

Figure 4.25: Self-normalised yields of electrons from heavy-flavour hadron decays compared with that of J/ψ [66]

The self-normalised yield of electrons from heavy-flavour hadron decays is compared with

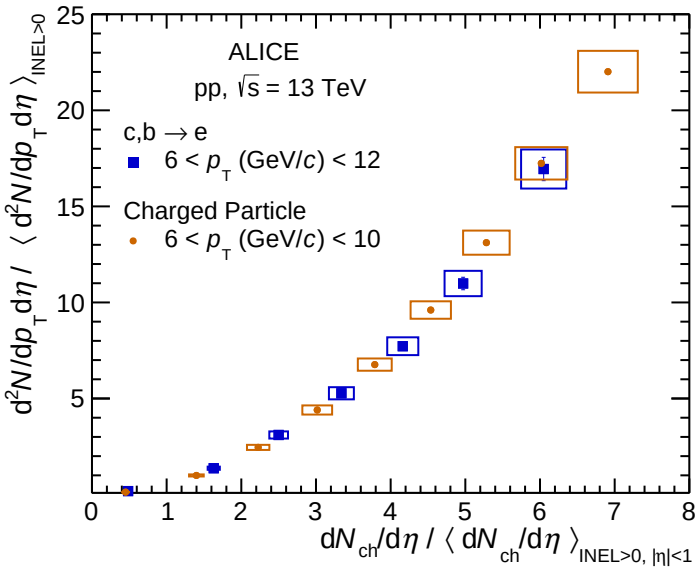

Figure 4.26: Self-normalised yields of electrons from heavy-flavour hadron decays compared with that of all charged particles [67]

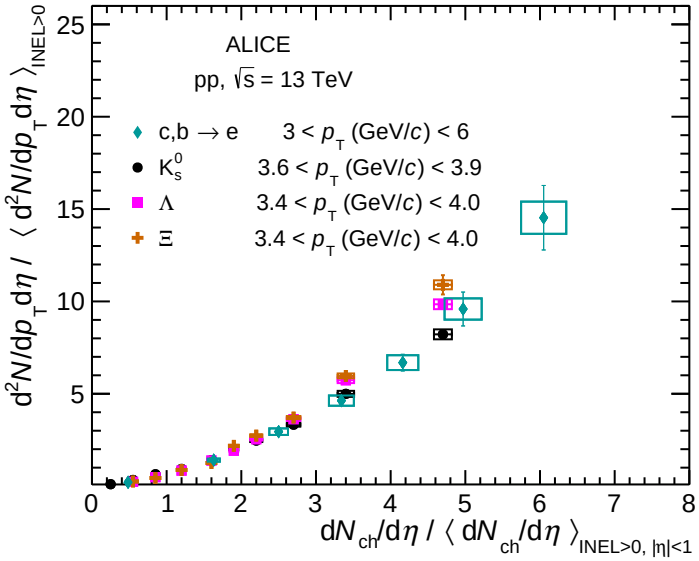

Figure 4.27: Self-normalised yields of electrons from heavy-flavour hadron decays with that of strange particles (K^0_s, Λ, Ξ). Self-normalised yields of K^0_s, Λ and Ξ recalculated from [134]

the normalised yield of other particles measured by the ALICE Collaboration - J/ψ [66], all charged particles [67], strange particles (K^0_s, Λ, Ξ) in pp collisions at $\sqrt{s} = 13$ TeV and with D-mesons [65] in pp collisions at $\sqrt{s} = 7$ TeV, as shown in figures 4.25, 4.26, 4.27, 4.28 respectively. The multiplicity dependent spectra for K^0_s, Λ and Ξ are available from

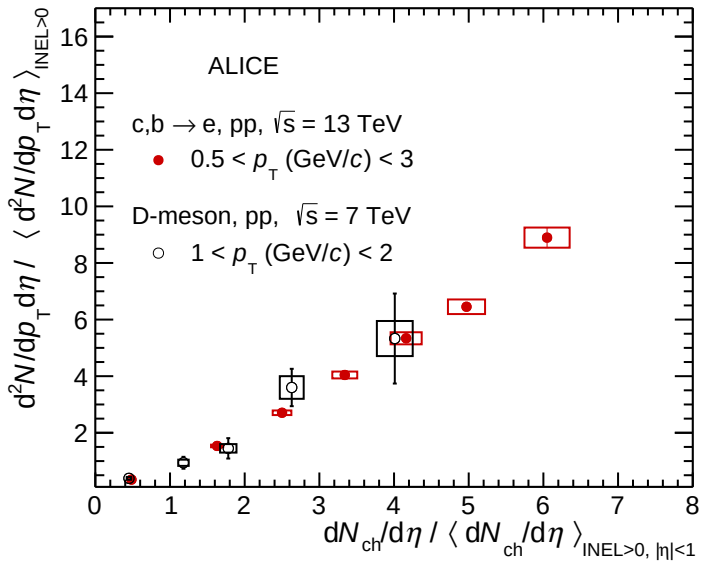

Figure 4.28: Self-normalised yields of electrons from heavy-flavour hadron decays with that of D-mesons [65]

ALICE measurements [134], although not in terms of their self-normalised yields. The self-normalised yields for these strange particles have been calculated from their multiplicity dependent spectra and has been explained in details in section 4.7. The p_{T} intervals of heavy-flavour hadron electrons were selected such that the meant-$p_{\mathrm{T}}$is comparable to that of the p_{T} ranges of the particles chosen for comparison. The slope of the increase of the normalised yields of electrons from heavy-flavour hadron decays as a function of normalised multiplicity in mid rapidity is similar to that measured particles similar p_{T} ranges. This observation has promoted for a more in-depth study of the comparison of the multiplicity dependent normalised yields of various particles, which has been discussed in details in the next section 4.7.

4.7 Comparison of self-normalised yields of electrons from heavy-flavour hadron decays with the self-normalised yields of other particles in common p_{T} ranges

Previous ALICE measurements of self-normalized yields as a function of the self-normalized multiplicity for J/ψ [66] & charged particles [67] in pp collisions at $\sqrt{s}$ = 13 TeV and J/ψ [59] & D-mesons [65] in pp collisions at $\sqrt{s}$ = 7 TeV have shown a faster than linear increase. Comparison of the self-normalized yields of various particles with that of heavy-flavour decay electrons in similar p_{T} ranges has shown a similar increase in slope. The goal of the study in this section is to check whether the increase of the slope for self-normalized yields as a function of the normalized multiplicity is similar for different species of particles and if it could point towards a universal trend amongst various particles.

The double ratio of the self-normalized yields for heavy-flavour hadron decay electrons in different p_{T} intervals (bottom panel of figure 4.22) have been fitted with various functions (power law, linear, quadratic), as shown in figure 4.29. The double ratio in the low p_{T} interval tends to saturate while that in the high p_{T} interval shows no sign of saturation. The linear function shown in figure 4.29(b) fits the data fairly well and is off only in the highest p_{T} and multiplicity point. From the linear fit function it can be inferred that in the measured p_{T} range, the yield increases approximately with the square of the multiplicity with a coefficient which increases with p_{T}. A linear function is also the most simple and hence is used for further studies. The double ratios for different particles have been fitted with a linear function in various p_{T} intervals. The coefficient of slope of the linear fit is plotted against the $\langle p_{\mathrm{T}} \rangle$ of the p_{T} interval.

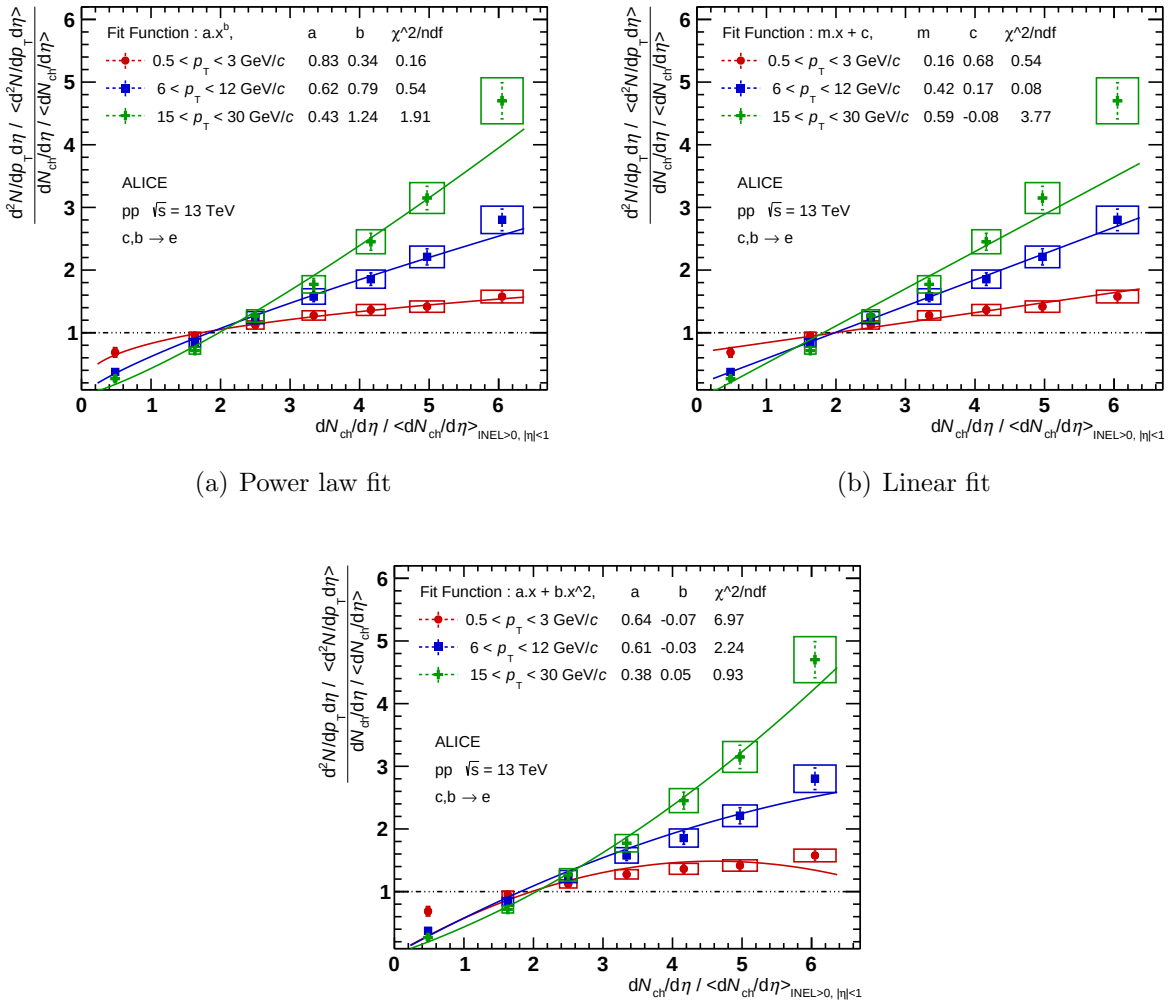

(a) Power law fit

(b) Linear fit

(c) Quadratic fit

Figure 4.29: Different fit functions to the double ratios of electrons from heavy-flavour hadron decays

4.7.1 $\langle p_{\mathrm{T}} \rangle$ from the p_{T}-differential cross section for different particles

Figure 4.30 shows the p_{T}-differential cross sections of identified charged particles (kaons, pions, protons), strange particles ($\mathrm{K}^0_{\mathrm{s}}$, Λ, Ξ), all charged particles and heavy-flavour particles (electrons from heavy-flavour hadron decay, J/ψ, D-meson). These p_{T}-differential cross sections have been fitted with a Tsallis function [135], as shown in equation 4.8, to calculate

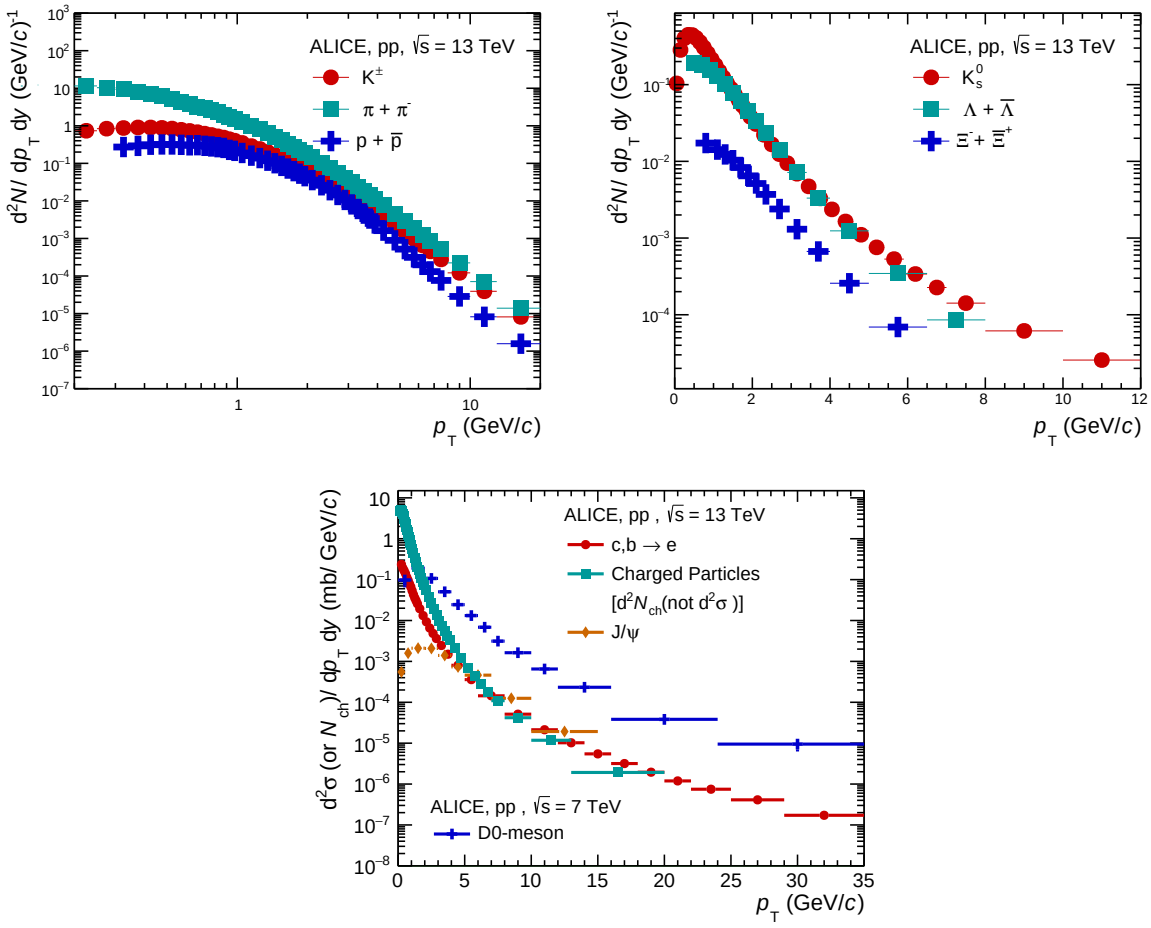

Figure 4.30: p_{T}-differential cross section of identified charged particles (kaons, pions, protons), all charged particles, strange particles ($\mathrm{K}^0_{\mathrm{s}}$, Λ, Ξ), heavy-flavour particles (electrons from heavy-flavour hadron decay, J/ψ, D0-meson)

the $\langle p_{\mathrm{T}} \rangle$ from a given p_{T} range.

$$E\frac{d^3\sigma}{d^3p} = \frac{\sigma_{pp}}{2\pi}\frac{\mathrm{d}N}{\mathrm{d}y}\frac{p_{\mathrm{T}}(n-1)(n-2)}{n\mathrm{T}[n\mathrm{T}+m(n-2)]}\left(1+\frac{\sqrt{m^2+p_{\mathrm{T}}^2}-m^2}{n\mathrm{T}}\right)^{-n} \tag{4.8}$$

where, n, $\dfrac{\mathrm{d}N}{\mathrm{d}y}$, T are the fit parameters. m is the mass of the particle, σ_{pp} is the proton-proton inelastic cross section and p_{T} is the transverse momentum of the particle. The Tsallis fit have been presented in figure 4.31 for D0-meson on the left panel and heavy-flavour decay electron spectra on the right panel. The $\langle p_{\mathrm{T}} \rangle^{\mathrm{D0}}$ of the entire p_{T} range obtained for D0-meson from this measurements is 2.13 GeV/c which is in good agreement with published result

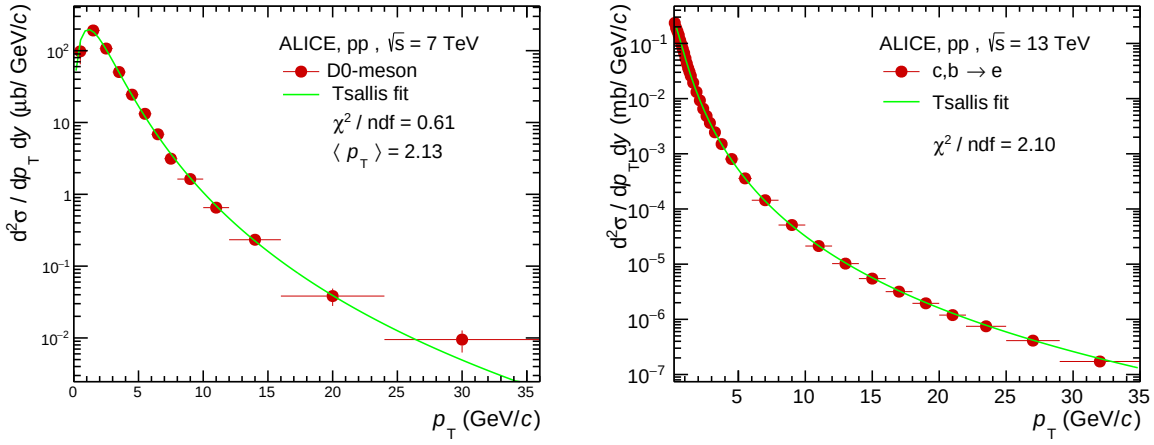

Figure 4.31: p_{T}-differential cross section of D0-meson (left) and heavy-flavour hadron decay electron (right) fitted with a Tsallis function [135]

$\langle p_{\mathrm{T}} \rangle^{\mathrm{D0}}_{\mathrm{published}} = 2.19 \pm 0.06$ (stat) $\pm$ 0.04 (syst) GeV/c [136].

4.7.2 Available multiplicity dependent data and the self normalized yields in ALICE

Multiplicity dependent measurements where SPD tracklets have been used as multiplicity estimator at mid rapidity are available in ALICE for the following particles: heavy-flavour hadron decay electrons from this thesis, all charged particles [67], J/ψ [66], strange particles ($\mathrm{K}^0_{\mathrm{s}}$, Λ, Ξ) [134] in pp collisions at $\sqrt{s}$ = 13 TeV and D-mesons [65] in pp collisions at $\sqrt{s}$ = 7 TeV. Measurements in ALICE where multiplicity is measured using V0 estimator at forward rapidity are available for the following particles: J/ψ [66], strange particles ($\mathrm{K}^0_{\mathrm{s}}$, Λ, Ξ) [134] and identified charged particles (kaons, pions, protons) [137] in pp collisions at $\sqrt{s}$ = 13 TeV. For both SPD and V0 estimators, the $\mathrm{d}N_{\mathrm{ch}}/\mathrm{d}\eta$ has been provided in mid rapidity.

The multiplicity dependent measurements of the strange and identified charged particles are published as p_{T}-differential cross sections in several multiplicity classes. Measurements presented as self-normalized yields are available for heavy-flavour hadron decay electrons,

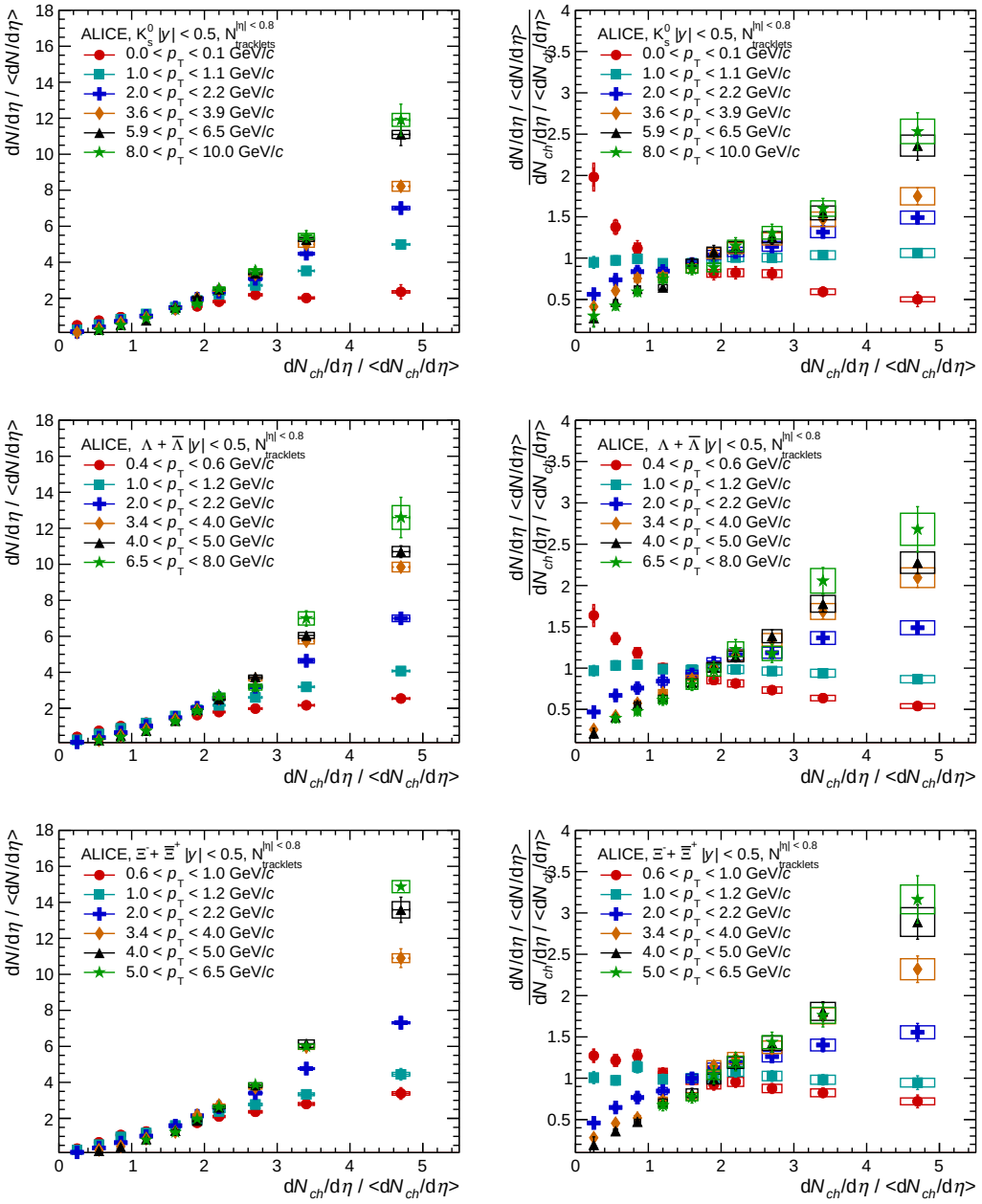

Figure 4.32: Left : Self-normalised yield plots for K^0_s, Λ, Ξ, Right: Double ratio of self-normalised yield for K^0_s, Λ, Ξ

all charged particles, D-mesons and J/ψ. Since, the self-normalized yields of strange and identified charged particles are not available directly, they are calculated from the available multiplicity dependent p_{T}-differential cross sections. From the p_{T}-differential cross sections in different multiplicity classes (N^{i}) and their ratios (R^{i}) with respect to the minimum bias spectra (N^{MB}), which are available for strange and identified charged particles, the

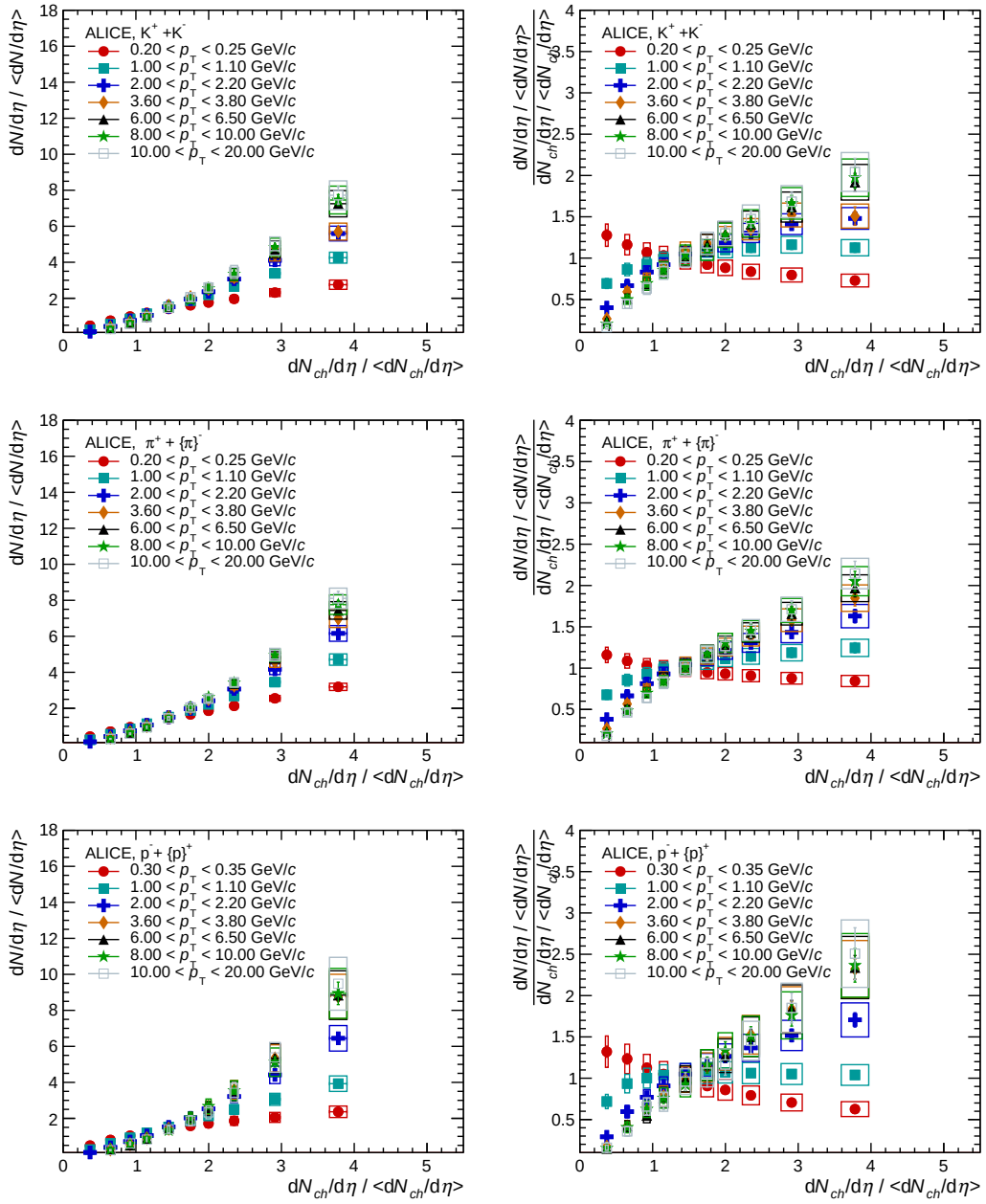

Figure 4.33: Left : Self-normalised yield plots for identified charged particle ($K^{\pm}$, $\pi^{\pm}$, $p^{\pm}$), Right: Double ratios of self-normalised yield for $K^{\pm}$, $\pi^{\pm}$, $p^{\pm}$

normalized yield is calculated in the following way.

- Ratios of the multiplicity dependent spectra of particles with respect to the minimum bias spectra are available from the published measurements i.e., $R^i = N^i / N^{MB}$ vs. p_T

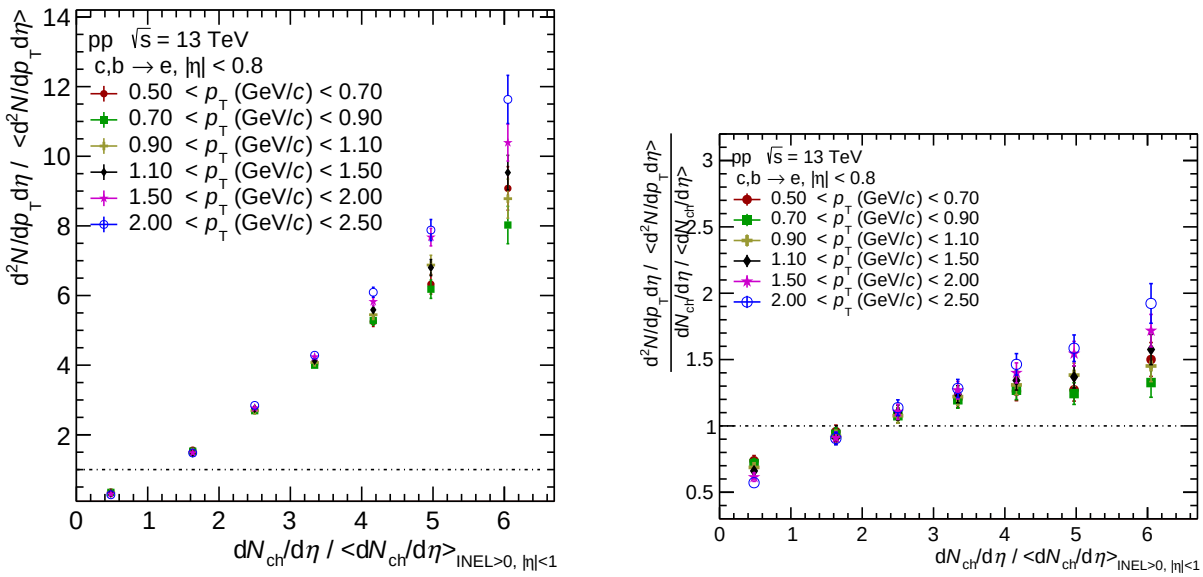

Figure 4.34: Left : Self-normalised yield plots for heavy-flavour hadron decay electron in low p_{T} bins, Right: Plots of double ratios of the self-normalised yields

- The minimum bias p_{T}-differential cross section, N^{MB}, is calculated by dividing the multiplicity dependent cross section with their corresponding ratio (N^{i} /R^{i}). It is required to calculate $\langle p_{\mathrm{T}} \rangle$ as shown in subsection 4.7.1.

- The self-normalised multiplicity values ($\mathrm{d}N_{\mathrm{ch}}/\mathrm{d}\eta$/ $\langle \mathrm{d}N_{\mathrm{ch}}/\mathrm{d}\eta \rangle$) at mid rapidity are obtained from the $\mathrm{d}N_{\mathrm{ch}}/\mathrm{d}\eta$ and $\langle \mathrm{d}N_{\mathrm{ch}}/\mathrm{d}\eta \rangle$ values provided in the publication in the corresponding multiplicity classes.

- The self-normalised yield of a particle is the ratio of yield in multiplicity intervals to the yield from minimum bias event (N^{i} / N^{MB}). Hence, normalised yield of the particle was obtained from ratio and plotted against the normalized multiplicity ($\mathrm{d}N_{\mathrm{ch}}/\mathrm{d}\eta$/ $\langle \mathrm{d}N_{\mathrm{ch}}/\mathrm{d}\eta \rangle$), in several p_{T} intervals .

The self-normalised yield graphs and their double ratio plots for strange particles ($\mathrm{K}^0_{\mathrm{s}}$, Λ, Ξ) are shown in the left and right panels figure 4.32 respectively. The self-normalized yield plots and their double ratio plots for identified charged particle ($\mathrm{K}^{\pm}$, $\pi^{\pm}$, $\mathrm{p}^{\pm}$) are shown in the left and right panels figure 4.33 respectively.

The self-normalized yield for heavy-flavour hadron decay electrons have been calculated in several p_{T} intervals at the low p_{T} range from 0.5 GeV/c to 2.5 GeV/c, as shown in figure 4.34. Comparing the self-normalized yields of heavy-flavour hadron decay electron for $p_{\mathrm{T}} \lesssim 2$ GeV/c with those of strange and light particles (in figures 4.32 and 4.33) it is observed that the normalized yield trend for these electrons is different from those of strange and light particles at low p_{T}. For $p_{\mathrm{T}} \gtrsim 2$ GeV/c a similar trend in the double ratios of self-normalized yields is observed between heavy- and light-flavour particles. This trend can be attributed to the different production mechanisms at different momentum ranges for light-flavour particles. While heavy-flavour particles are produced from hard scattering at all p_{T} ranges and light-flavour particles are only produced from hard scattering after a certain p_{T} scale (~ 2 GeV/c). Light-flavour particles are produced from soft processes and underlying events at low p_{T}.

4.7.3 Linear fit to the double ratio of the self normalized yields of various particles

Figure 4.35 shows the double ratios of th self normalized yields for strange hadrons divided in SPD tracklet percentile classes and fitted with a linear function. Figure 4.36 shows the double ratios of self normalized yields for strange hadrons divided in V0 percentile classes and fitted with a linear function. Figure 4.37 shows the double ratios of self normalized yields for identified charged particle divided in V0 percentile classes and fitted with a linear function. For strange and identified charged hadrons the slope of the double ratio remains almost constant with all p_{T} ranges for $p_{\mathrm{T}} \gtrsim 3$ especially for protons. The $\mathrm{d}N_{\mathrm{ch}}/\mathrm{d}\eta$ is provided in mid-rapidity for both SPD and V0 multiplicity estimators. Figure 4.38 shows the linear fit to the double ratios of self normalized yields of heavy-flavour hadron decay electrons, all charged particles, D-meson, J/ψ at mid rapidity.

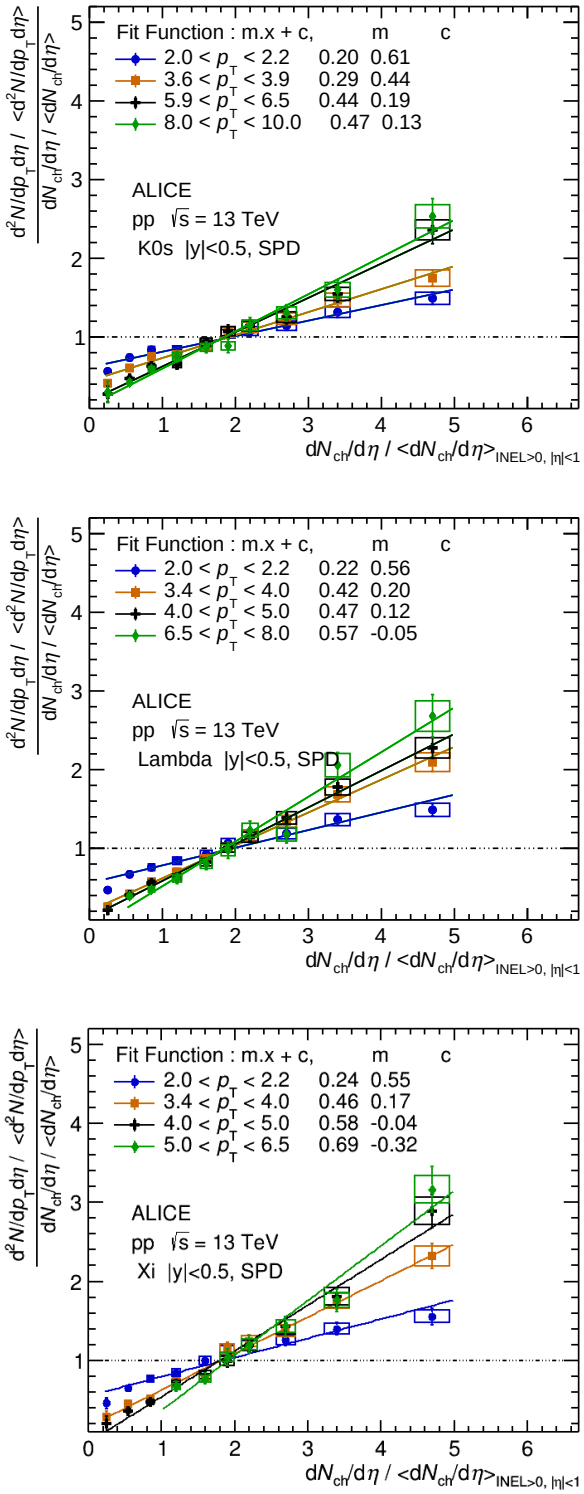

Figure 4.35: Linear fit to strange particle double ratio measured in SPD tracklet at mid rapidity

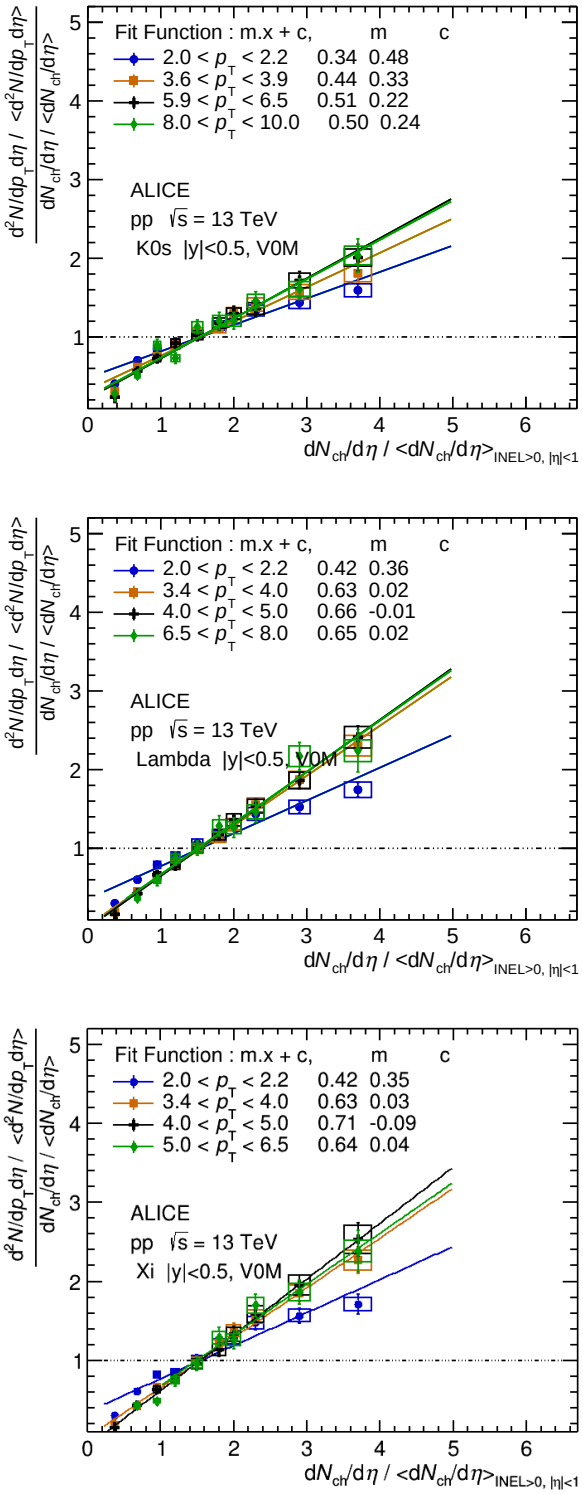

Figure 4.36: Linear fit to strange particle double ratio measured in V0 estimator in forward rapidity

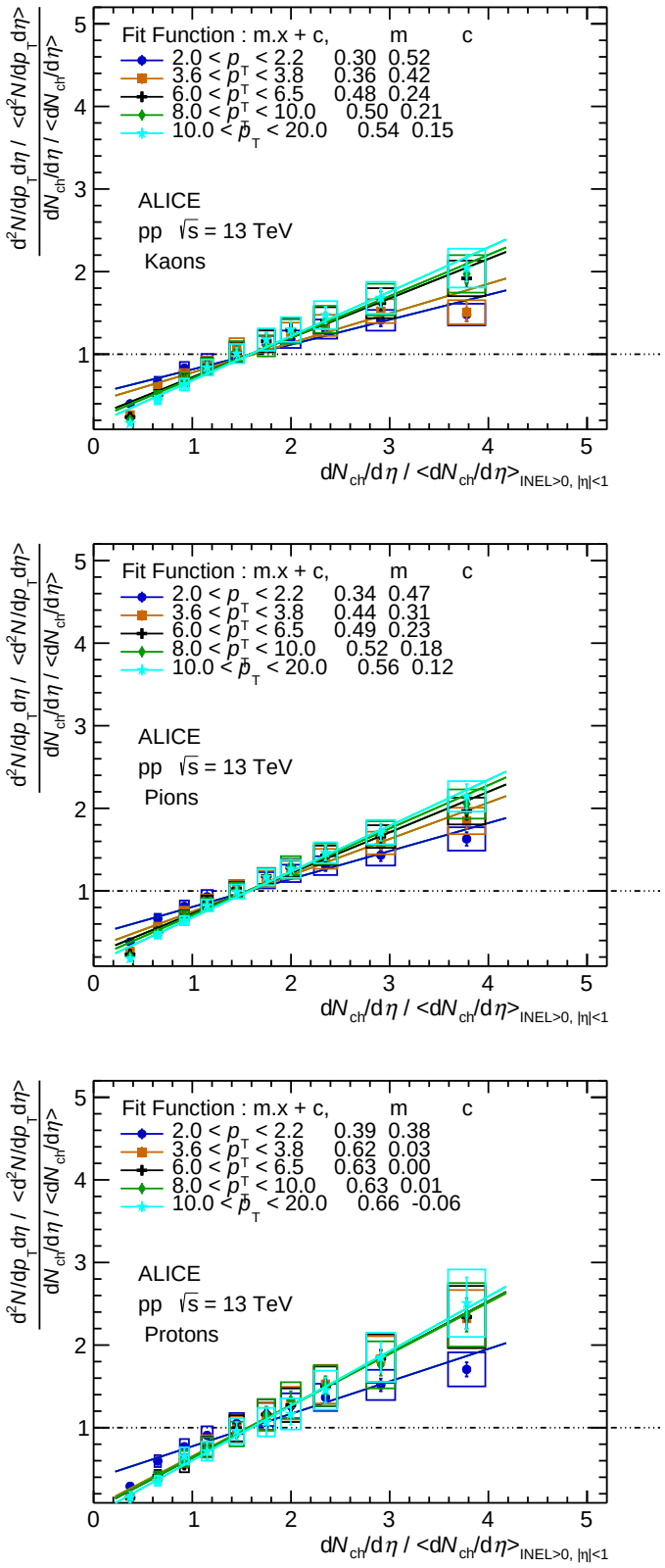

Figure 4.37: Linear fit to identified charged particle double ratio measured in V0 estimator in forward rapidity

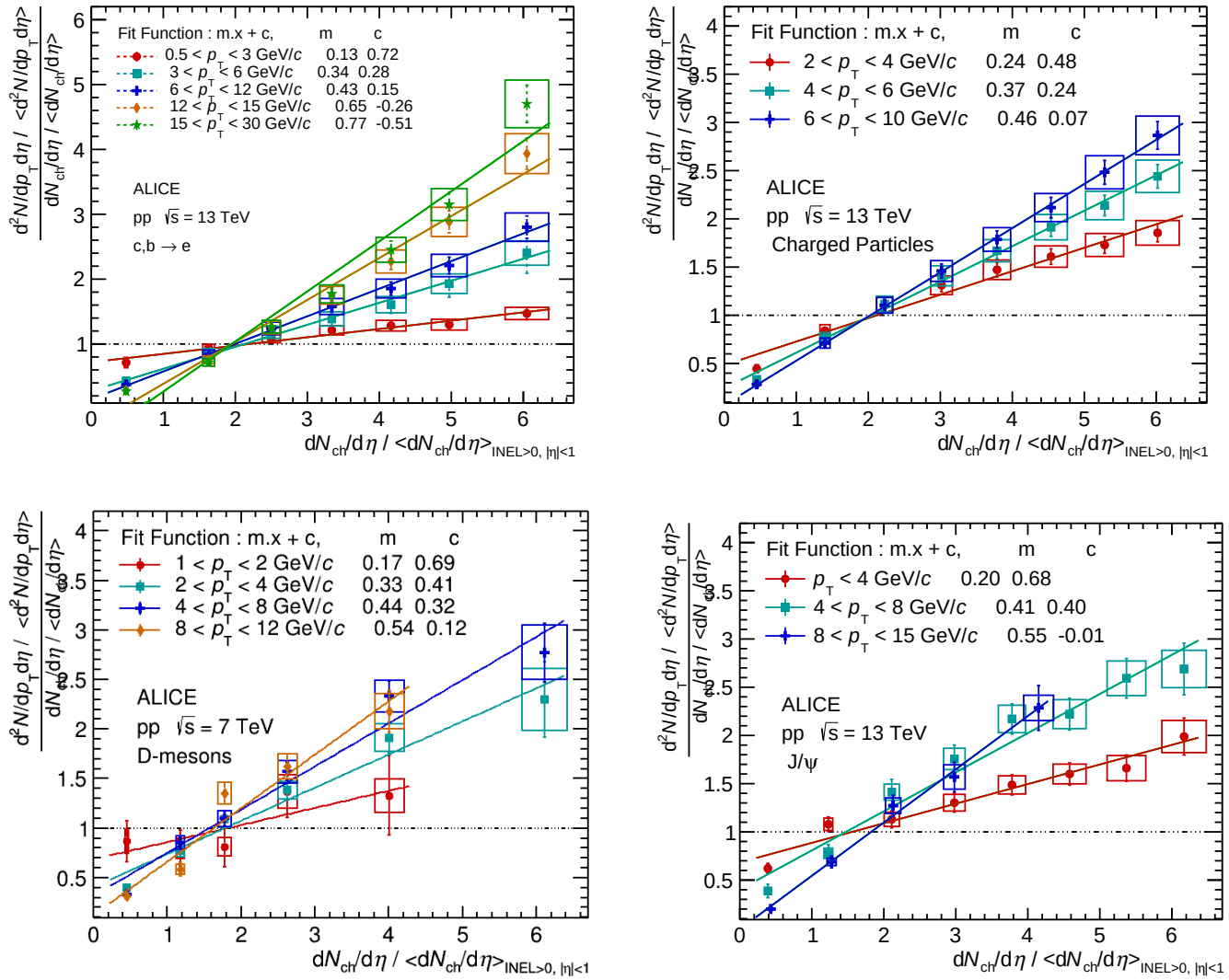

Figure 4.38: Linear fit to heavy-flavour hadron decay electrons, charged particles, D-meson, J/ψ double ratio measured with SPD tracklet at mid rapidity

4.7.4 Mean p_{T} vs. slope of linear fit in different multiplicity selection scenarios

Mean p_{T} vs. slope of linear fit for different particles have been shown in the following figures. The following scenarios of multiplicity selections are there:

- Figure 4.39, left panel, shows the $\langle p_{\mathrm{T}} \rangle$ vs. slope of linear fit for events divided in SPD tracklet intervals/classes. The corresponding $\mathrm{d}N_{\mathrm{ch}}/\mathrm{d}\eta$ has been provided in mid rapidity.

- Figure 4.39, right panel, shows the $\langle p_{\mathrm{T}} \rangle$ vs. slope of linear fit for events divided inV0 estimator percentile classes. The corresponding $\mathrm{d}N_{\mathrm{ch}}/\mathrm{d}\eta$ has been provided at mid rapidity.

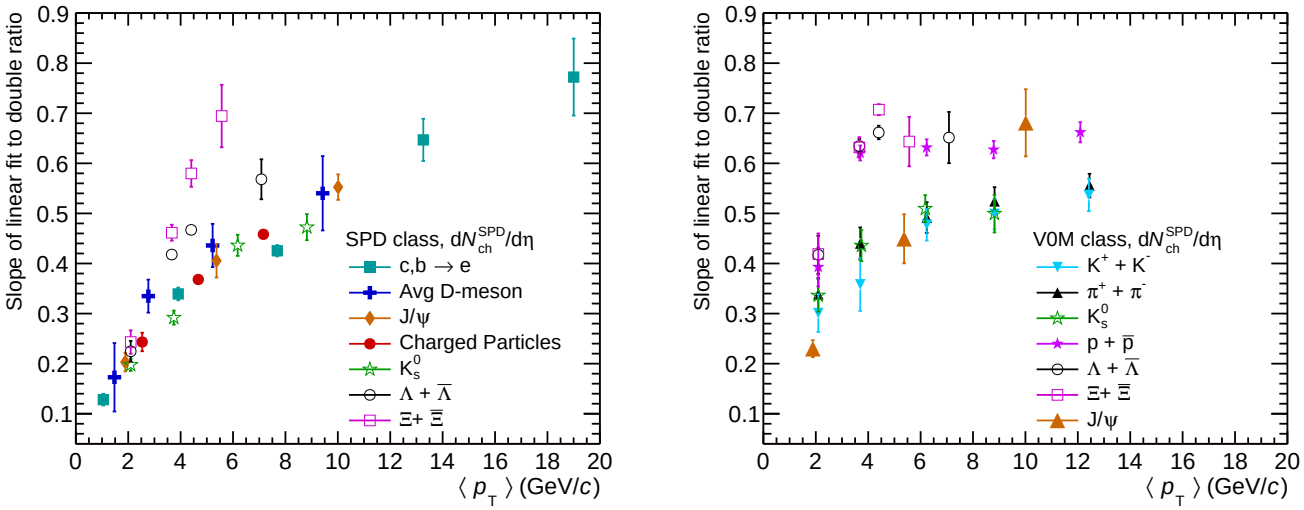

Figure 4.39: $\langle p_{\mathrm{T}} \rangle$ vs. slope of linear fit. Left : Events divided in SPD tracklet intervals, Right : Events divided in V0M tracklet intervals

The baryons and mesons from the figure 4.39 has been separately shown in the different panels of figure 4.40. A meson vs. baryon trend has been observed for both SDP tracklet and V0 estimator. For the SPD tracklet estimator, no saturation with increasing $\langle p_{\mathrm{T}} \rangle$ is seen for meson. Mesons, i.e., heavy-flavour hadron decay electrons, D-mesons, J/ψ, $\mathrm{K}^0_{\mathrm{s}}$ and

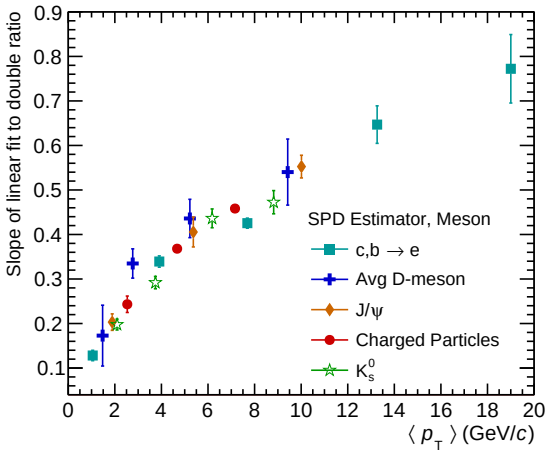

(a) SPD tracklet estimator, Mesons

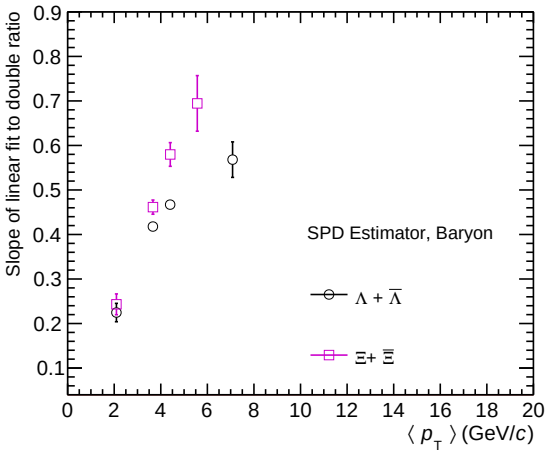

(b) SPD tracklet estimator, Baryons

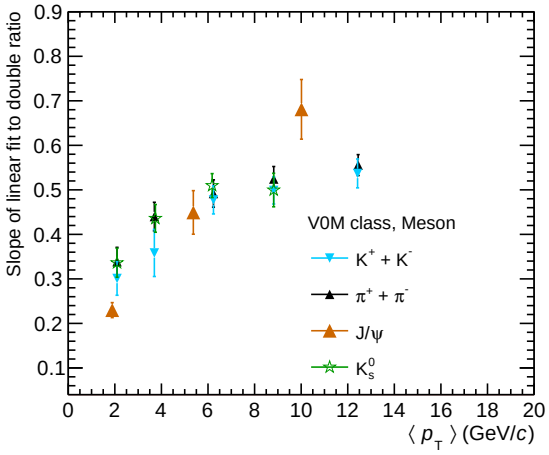

(c) V0M estimator, Mesons

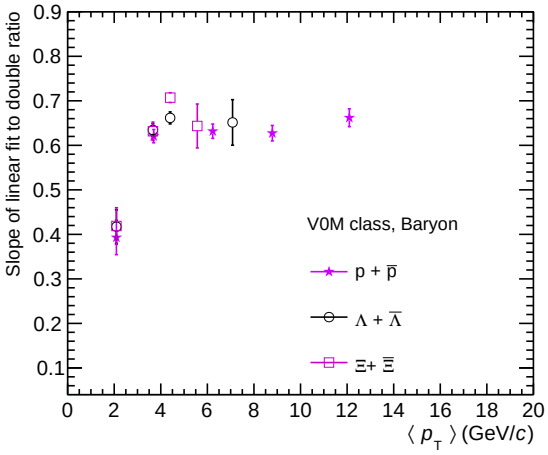

(d) V0M estimator, Baryons

Figure 4.40: $\langle p_{\mathrm{T}} \rangle$ vs. slope of linear fit

charged particles which is mostly π, tend to follow a similar trend. Baryons (Ξ and Λ) follows a different trend. For the V0M estimator, the baryon trend saturates at $p_{\mathrm{T}} \gtrsim 4$ GeV/c. For mesons saturation tends to be achieved except for J/ψ, where the last point at the highest p_{T} seems to have a higher slope.

Chapter 5

Estimation of initial state structures in high energy heavy-ion collisions using Principal Component Analysis (PCA)

In this chapter, a formalism to implement the spatial clusters at the partonic level in the string melting version of the AMPT model for PbPb collisions at $\sqrt{s_{\rm NN}} = 200$ GeV has been presented. These clusters are then propagated through the AMPT hadronization scheme. The Principal Component Analysis (PCA) has been used on the η, ϕ and $p_{\rm T}$ distributions of the produced charged particles and the eigenvalues have been compared before and after the implementation of the clustering.

5.1 Introduction

In heavy-ion collisions at ultra-relativistic energies at Relativistic Heavy Ion Collider(RHIC) and Large Hadron Collider (LHC), corresponding to a medium of high temperature, a state

of strongly interacting medium is formed in which partons are de-confined from the incoming hadrons. A range of observables that are measured to characterize the properties of the medium include thermodynamic properties like temperature, entropy, collective properties given by flow parameters, gluon density of the medium measured by jet-quenching among others. It is a usual practice that the experimental observables are theoretically evaluated by folding the space-time evolution of the colliding medium for finding the sensitivity to the different stages of the evolution [12, 13]. The prominent stages that are modelled include initial state of the collision, formation of the medium, evolution and cooling of the medium, hadronization, rescatterings, chemical and kinetic freeze-out and finally the free streaming of particles. In the initial stage of the collision, when nucleons overlap, the geometry of the collision zone plays a crucial role in deciding the final state observables [138]. It has been observed that the final state collectivity parameters commonly known as flow parameters are correlated with the initial state geometry or corresponding fluctuations. These initial state geometry parameters like various orders of eccentricities from coordinate space (ϵ_n) leave their imprints on the azimuthal distributions of the momentum of the produced particles. The decomposition of the azimuthal distributions have been represented by parameters of various orders like v_1, v_2 etc. as obtained by the Fourier decomposition of the azimuthal distributions with respect to the reaction plane angle [139,140]. The degree of conversion of the initial spatial asymmetry to the final state momentum asymmetry is represented by the correlation between the eccentricities to the flow parameters. For studying such an effect, one needs to evaluate the event by event eccentricities and hadronic flow parameters. It is however important to investigate in detail the effect of these initial state geometry parameters or their fluctuations to the distributions of the final-state observables like pseudo-rapidity or transverse momentum distributions of the produced particles. In literature, a range of models describing high energy heavy-ion collisions have been discussed that include specific structures of the initial state geometry due to nucleonic overlap or formation of new structures at the partonic or hadronic levels in the form of clusters. Prominent examples include

models like Parton cascade Model (PCM) [141], Color Glass Condensate (CGC) [23], Zhang parton cascade (ZPC) [142] among others. It is a usual practice to implement different initial state scenarios before evolution of the medium using ideal or viscous hydrodynamics and a conclusion is made about the suitable description of the initial state that matches the data best. Efforts are also made to study the sensitivity to the fluctuations in the initial state using various methods like sensitivity to the final state observables [143–145].

In the present study, a clustering algorithm on partons formed by the AMPT model [146] in Pb–Pb collisions at RHIC energy has been implemented. The clustering algorithm has been motivated by the formation of spatial domains consisting of thermal partons. These partons are then processed via the hadronization scheme in AMPT string-melting version which is based on the recombination mechanism. The final state particles are then studied in detail.

In literature, distributions of the produced particles are analysed using various decomposition methods like Fourier analysis applied on the azimuthal distributions in order to extract the flow parameters. Recently, Principal Component Analysis (PCA) is being used extensively primarily to study various orders of flow variables and their correlation with the initial geometry parameters and their fluctuations [68]. There are two main approaches applied in the field of high energy heavy-ion collisions for the PCA decomposition. The first one is the decomposition of the covariance of the azimuthal distributions as weighted with a Fourier series and then making connection of the PCA components with the flow parameters [69]. Another approach is to decompose the inclusive distributions using PCA and connect the components with the physical observables like flow parameters in case of decomposition of the azimuthal distributions. Now-a-days PCA is being used extensively in the automated machine learning procedure for finding structures in object spaces. The features primarily detected using PCA are then analysed in details using sophisticated cluster finding algorithm to obtain the features in detail. In this study, the later approach i.e. decomposing the inclusive distributions and study the components has been adopted. The initial clustering

might introduce features in η, ϕ, p_{T} space like flow coefficients in azimuthal distribution. As the eigenvalues are sensitive to these features, one can choose a region of eigenvalues that will select the events considered.

The AMPT model and the PCA procedure as have been applied in the study has been discussed in sections 5.2 and 5.3 respectively. The procedure of implementation of clustering, results and the summary are discussed in sections 5.4, 5.5 and 5.6 respectively.

5.2 AMPT

A Multi-Phase Transport (AMPT) [146] is a Monte Carlo partonic transport model being used widely for simulating NN,NA and AA collisions at high energy. The model implements all major stages of the collision starting from the initial state through the partonic scattering followed by hadronization and hadronic rescattering. The initial stage of the collision has been implemented by HIJING [96] through Monte-Carlo Glauber model calculations in NA and AA collisions. In the initial state of the collisions, either partonic strings and minijets are taken together from HIJING or all strings are melted into partons. There are two versions of AMPT, in the default version, only the minijets are transported using the Zhang's Partonic Cascade (ZPC) and in the string melting version, all melted partons go through ZPC for scattering. The scattering is governed by a parameter to be tuned to match the particle spectra. The hadronization is implemented in two modes known as hadronic mode and partonic mode. In hadronic mode, minijets, after scattering are recombined with the strings and then get fragmented using Lund's string fragmentation model. On the other hand, in the partonic mode, all the partons combine to form hadrons (mesons or baryons) based on the spatial distance, spin structures and the invariant mass of the quarks (quark-antiquark in case of mesons and 3 quarks in case of baryons). The hadrons formed by any of these two mechanisms then undergo scattering among themselves and then scattered hadrons reach the detector. AMPT has been used extensively in high energy heavy-ion collisions and has

been able to explain most of the observables like spectra, flow among others. One extremely prominent finding of the model is the ability to explain the number of constituent quark (NCQ) scaling of elliptic flow parameter v_2 at RHIC. The NCQ scaling refers to the scaling behaviour observed when the v_2 and p_{T} of different identified hadrons are divided by the number of constituent quark (n_q). The v_2/n_q vs. p_{T}/n_q for identified hadrons follow a universal curve suggesting the dominance of quark degrees of freedom at the early stages of collisions. In this study, only the partonic version of the model involving partons at the initial stage and in hadronization has been used. At the initial stage, a separate partonic clustering has been implemented as discussed in section 5.4.

5.3 Principal Component Analysis (PCA)

The principal component analysis (PCA) is a technique for **dimensionality reduction** that enables us to identify correlations and patterns among different features in a data set, so that it can be transformed into a data set of significantly lower dimensions without the loss of any important information. High dimension data are extremely complex to process which increases the computation time and make data processing and analysis more convoluted. This is known as the "curse of dimensionality" in the field of Machine Learning. Hence, the aim is to remove inconsistencies and redundant data and only keep data significant for output. PCA helps to identify correlation between different features in the data set and decomposes the correlated distributions in various components known as **principal components** that reflect the independent variables characterizing the features of the distributions. **Principal components (PC)** are new set of variables that are obtained from the initial set of variables such that they compress and posses most of the useful information that are scattered among the initial variables. If there are N-dimensions, then we have N principal components. The principal comments are formulated such that the first principal component (PC1) stores maximum possible information, the second component(PC2) is the

second most significant variable and so on. After rearranging the principal components in descending order, the first few components are the most important information.

The principal component analysis achieves dimension reduction by using correlated matrix

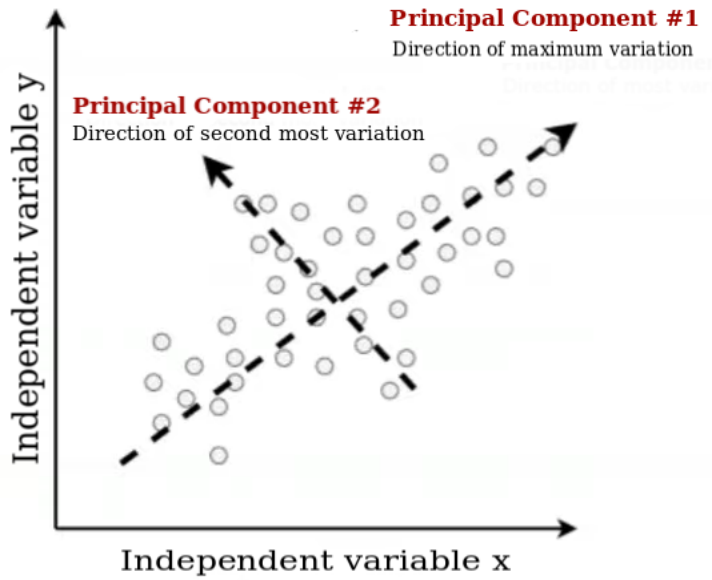

Figure 5.1: Schematic of the principal components analysis (PCA)

with the eigenvalues representing the variance. A covariance matrix expresses a correlation between the different variables in the data set. The covariance value denotes how codependent two variables are. Negative covariance indicates that the variables are indirectly proportional to each other, while positive covariance indicates a direct proportionality. Eigenvectors and eigenvalues are the mathematical constructs that must be computed from the covariance matrix in order to determine the principal components of the data set. Eigenvectors are used to identify where in the data, i.e., in which direction/variable, there is maximum variance with the eigenvalues representing the variance. Mathematically, a covariance matrix (N x m) can be decomposed as

$$M = X\Sigma Z = VZ \tag{5.1}$$

where X, Z are orthogonal matrices of N x N and m x m dimensions respectively, Σ is a diagonal matrix of N x m dimensions with diagonal elements arranged in strict decreasing order. These elements carry physical meaning. The distribution of a variable in an event can be expressed as

$$f = \sum_{j=1}^{m} x_j^{(i)} \sigma_j z_j = \sum_{j=1}^{(i)} v_j^{(i)} z_j \tag{5.2}$$

where z_j is an orthogonal vector such that $Z_i^T x Z_j = \delta_{ij}$, σ_j are the diagonal elements of matrix Σ, index i represents the event number (1,2....N) and m is the number of bins of input variable. $v_j^{(i)}$ is the corresponding coefficient of z_j for ith events. The first principal component (PC1) is in the direction of the eigenvector associated with the highest eigenvalue and so on. More variance in data implies more information and hence is more significant. The eigenvalues σ_j, and hence the PCs, are arranged in decreasing order and only a top few values are enough to describe the distribution, say up to k, then the equation can be rewritten above as below,

$$f = \sum_{j=1}^{k} v_j^{(i)} z_j \tag{5.3}$$

here j is called PCA modes describing the fluctuations in the distribution. A schematic of the principal component analysis is shown in figure 5.1.

PCA has been used so-far mostly for analysing the covariance of the azimuthal distributions of the produced particles as weighted by a Fourier series primarily to extract the flow coefficients [147–149]. The PCA components represent flow fluctuations in different orders and non-linear couplings among the flow coefficients. In another approach, however, the inclusive azimuthal distributions are decomposed by PCA and it is found that the eigenvectors of at least up to 4^{th} order are similar to the distributions of the Fourier components. The eigenvectors have been found to be of the shapes similar to that of the Fourier components as has been used in the conventional method of extraction of the flow coefficients. The eigenvalues have been found to correspond to the flow coefficients. If applied at the partonic level, the eigenvalues of PCA correspond to the eccentricities (ϵ_n) of various orders. The

flow coefficients of various orders have been interpreted to be connected to the initial spatial geometry and their fluctuations to be transferred to the momentum-space anisotropy. Flow coefficients (v_n) follow a linear relationship with their corresponding initial state eccentricities (ϵ_n)[150],[69]. In earlier studies using PCA for the azimuthal distributions, event by event v_ns have been extracted and then correlated with ϵ_n. In the present study, event by event distributions for $\eta, \phi, p_{\mathrm{T}}$ have been divided into n-bins separately. The exercise is then undertaken for a large (N) number of events. Such binned distribution per event along with the number of events form a matrix to be diagonalized. The eigenvalues are obtained in a strictly decreasing order.

In the study, η, ϕ and p_{T} distributions of the produced charged particles are decomposed separately for events having the initial geometry with and without inclusion of additional clustering. The main aim of this study is to investigate the behaviour of the eigenvalues with the changes in the initial conditions. It has been argued elsewhere that the eigenvalues of PCA correspond to the fluctuations in various orders [151]. With the modified initial conditions, the fluctuations are expected to change and the PCA eigenvalues should be sensitive to these changes. In conventional approaches, events with high PCA eigenvalues could be extracted and those events could be further investigated using sophisticated cluster-finding method to find the substructures in the set of events. This approach is used in Machine Learning technique quite extensively. The PCA method in its current form uses the covariance among the data to obtain the results, however the approach is not limited to second order cumulant only. A multivariate cumulants study via their principal components had been first proposed by [152], analogous to the usual principal components of a covariance matrix. This cumulant method of principal component analysis has been used in various fields of research such as mathematics, economics and computer science.

5.4 Implementation of clustering

In the literature, there is a series of models which have implemented the initial states of the high energy heavy-ion collisions, a few prominent models that include different initial conditions include NUXUS [153] , EPOS [154], MC-KLEIN [155], IP-Glasma [156] among others. In the present work, clusters have been implemented at the partonic level which is basically inspired by the discussions on formation of spatial domains at the partonic level. Starting with the partons from the AMPT string melting version, the implementation of the clustering in the following way. A parton, selected as a seed at random, is taken as the center of a cluster. All partons whose inter-parton distance with respect to the seed parton lie within a certain cluster radius (parameter R) are assigned as members of that cluster. The cluster is then formed by bringing the partons closer to the center by reducing

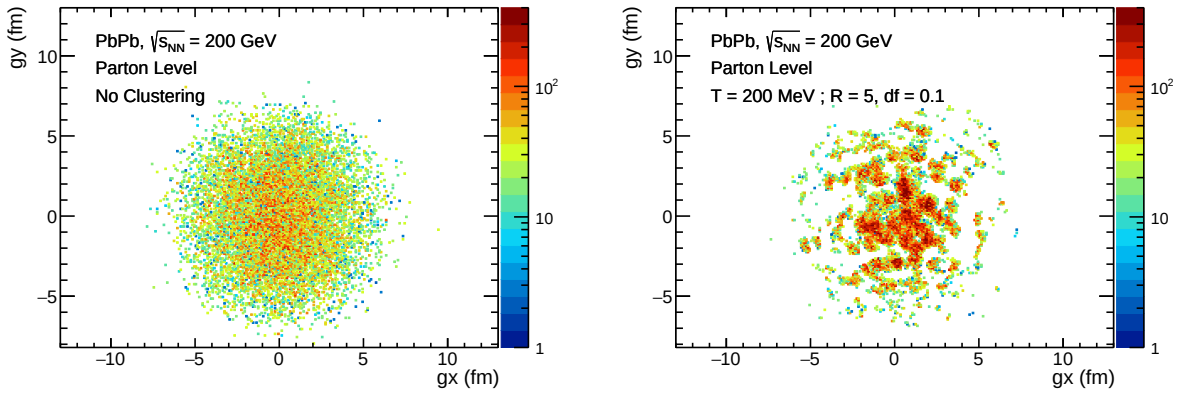

Figure 5.2: X-Y distribution of the partons before (left) and after (right) clustering

the radial distances of the partons by a certain factor (parameter df). Once the formation of one cluster is completed, another unassigned parton is taken as a seed and the process continues till all partons are exhausted.

The next step is to implement a momentum distribution of the members of the partonic cluster. Motivated by the thermally distributed partons, the cluster partons have been

assigned momenta as per the following distribution,

$$f(p_{\mathrm{T}}) = e^{-p_{\mathrm{T}}/\mathrm{T}} \tag{5.4}$$

where, T is a parameter with an analogy to the temperature of the cluster. In this study, T values have been used as 200 MeV/c and 400 MeV/c. The figure 5.2 shows the X-Y distribution of the partons on the transverse plane before (top) and after (bottom) clustering. The clustering parameters for the plot are R = 5 fm df = 0.1, T = 200 MeV/c. As seen in the figure, while before clustering (left), the position distributions of the partons are uniform, clear domain structures are seen in the figure 5.2 (right) which could be said to correspond to the partonic domains in the position space. Please note that with these parameters, the clusters correspond to maximum radii of 0.5 fm (R×df). The figure 5.3 shows the η, ϕ and p_{T} distributions of the initial partons before and after the clustering with two different temperature parameters and different spatial cluster parameters. Three cases of clustering has been considered in the figure which are as follows. The legends where only T values (200 MeV or 400 MeV) are mentioned, are cases where the parton momentum has been distributed according to equation (5.4) and no position clustering has been implemented. Legends where both T and R, df values are mentioned are the ones where both position clustering has been implemented and parton momentum has been assigned according to equation (5.4), and finally the ones with only R, df values and no temperature values are cases where only position clustering has been applied and momentum has not been changed. The η, ϕ and p_{T} distributions obtained after applying the aforementioned changes have been compared with the case where no changes in position and momentum has been made. The η distribution of partons changes from a uniform to a peaking shape at $\eta = 0$ which represents the formation of the clusters. The η distributions for similar temperature parameter overlap e.g., the no-clustering and only position clustering overlap as the momentum has not been changed, while the two curves with T = 200 MeV overlap. For better visibility of the plots

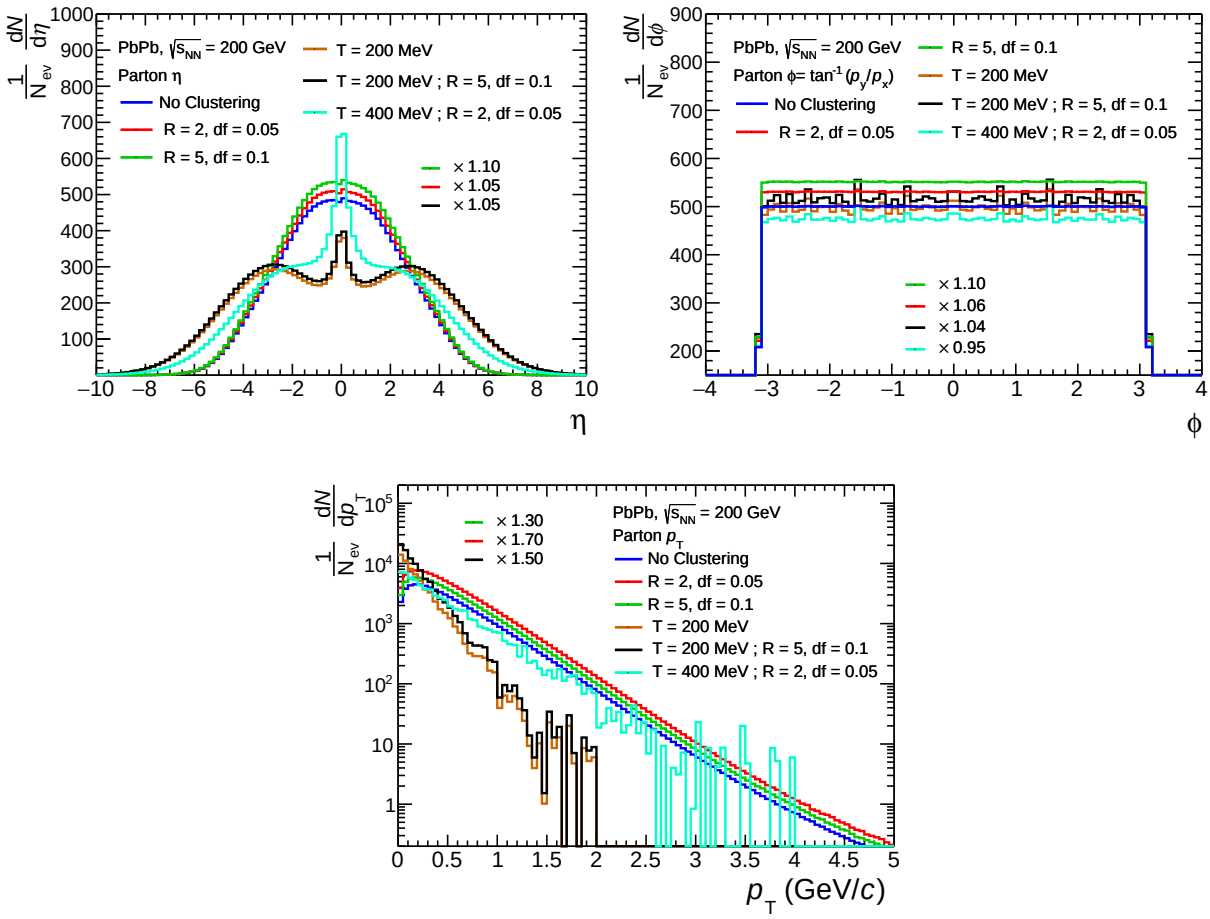

Figure 5.3: η, ϕ and p_{T} distributions of the partons before and after clustering for minimum bias Pb–Pb collisions at $\sqrt{s_{\mathrm{NN}}} = 200$ GeV

some of the overlapping curves have been scaled as shown in the legends. The azimuthal distributions are mostly uniform except a few hints of azimuthal asymmetry/structure in the clusters which have undergone momentum modification and as expected, p_{T} distributions depict the modified distribution as per the value of the input T parameter. Similar to the η distributions in the p_{T} distributions, curves with similar temperature and similar transverse momentum distributions overlap. The partons then undergo scattering using ZPC and hadronization as implemented in the partonic version of AMPT i.e., the coalescence of quarks and anti-quarks. The corresponding distributions of the produced charged particles have been shown in the figure 5.4. It is seen that all characteristic structures seen at the partonic level are smoothened out.The azimuthal distributions of the produced particles on

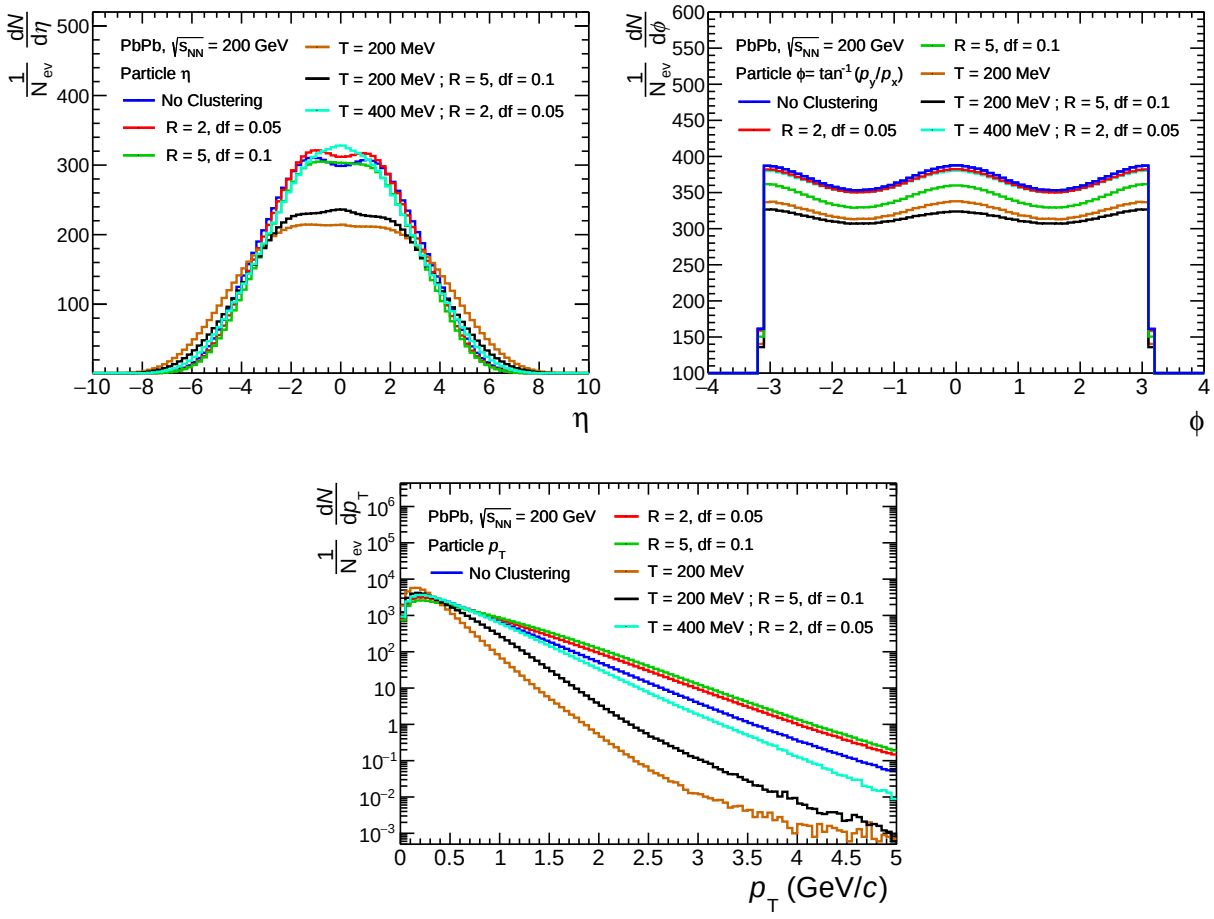

Figure 5.4: η, ϕ and p_{T} distributions of the produced particles before and after clustering for minimum bias Pb–Pb collisions at $\sqrt{s_{\mathrm{NN}}} = 200$ GeV

the other hand show the characteristic asymmetric shape due to elliptic flow. The p_{T} range of the produced particles increases as compared to that of partons due to the production of hadrons consisting of more than one parton.

5.5 Results

In this study, simulation have been performed using AMPT string-melting version for Pb–Pb collisions at $\sqrt{s_{\mathrm{NN}}} = 200$ GeV. $2{\times}10^5$ minimum bias events have been generated to ensured that the statistical error on the event averaged eigenvalues are not significantly large. Only the results from the produced charged particles have been used in this study. As discussed

earlier in section 5.3, each event-wise distribution was divided into 20 bins for the η and p_{T} distributions in the regions of -1 to +1 for η and 0 to 5 GeV/c for p_{T} and 50 bins in the region -π to +π for ϕ . Before discussing the PCA results, the elliptic flow parameter v_2 was first obtained using the event plane method [157] for two cases i.e., with and without clustering. The cluster-parameter have been varied to represent different possibilities. In figure 5.5 and the subsequent figures, two values of the cluster radius parameter (R) have been opted i.e., 2 fm and 5 fm associated with parameter df 0.05 and 0.1 respectively. For cases without any mention of the temperature parameters T, parton momenta remain unmodified compared to that from AMPT. For clusters having thermal partons, the T parameters chosen are 200 MeV/c and 400 MeV/c. It might be mentioned that for partons with no clustering, fitted slope of the p_{T} spectra gives an inverse slope of about 400 MeV/c. The clusters with T = 200 MeV therefore represents significantly softer partons.

The figure 5.5 (left) shows the variation of v_2 with p_{T} for two scenarios. As seen in the figure 5.5 (left), v_2 increases with p_{T} except for T = 200 MeV in which v_2 reduces at higher p_{T}. The ratio of v_2 has been shown in the figure 5.5 (right) taking no-clustering scenario as reference and as discussed earlier, the ratio remains constant at unity thereby insensitive to the clustering except the T = 200 MeV case.

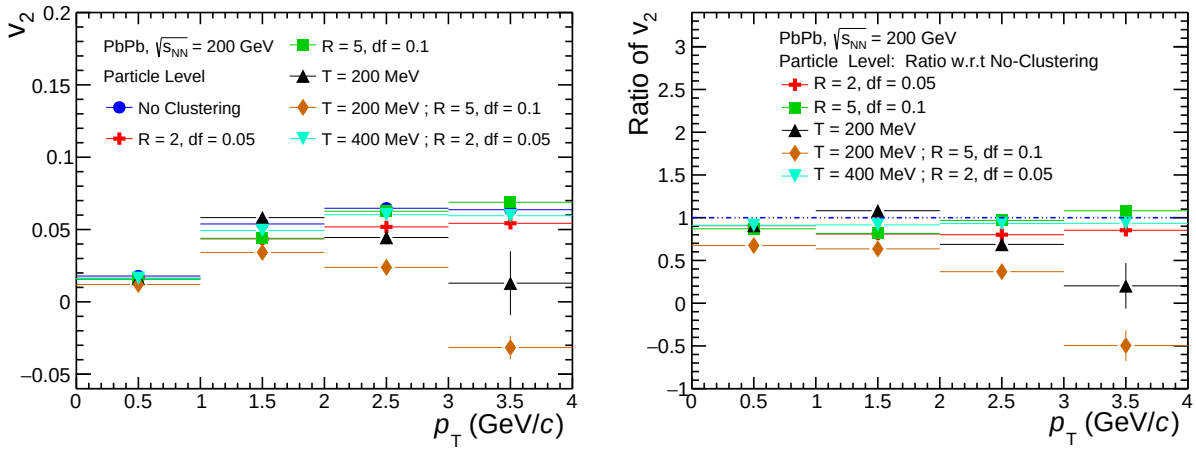

Figure 5.5: p_{T} distributions of v_2 for two scenarios i.e., before and after clustering (left panel) and the ratio of v_2 vs. p_{T} distributions after clustering with respect to the one before (right panel).

As mentioned earlier, the eigenvalues of PCA are related to the eccentricities at the partonic level and various flow components and their fluctuations as obtained from the azimuthal distributions at the particle level. The eigenvalues for different distributions of the charged particles with different cluster parameters have been investigated. The figure 5.6 to figure 5.7 show the distributions of the eigenvalues as obtained for η, ϕ and p_{T} distributions for two different scenarios i.e. with and without clustering. The nodes (α) in the X-axis represents the PCA components. It is clear in all cases that the most prominent eigenvalue is of the first component differing from the next one by varying degree. It can therefore be mentioned that the first eigenvalue, representing the variance of the distribution of the reduced dimension can be used further for investigating the structures in the initial state of the collision zone.

As per the PCA method, eigenvalues are arranged in a decreasing order sometime with a wide difference between the eigenvalue of component and that of the next node. Before discussing PCA results, having a re-look at the figure 5.3 and the figure 5.4 shows the inclusive distributions of partons and of the produced charged particles respectively. It is clearly seen that partonic η and ϕ distributions have structures with more prominent ones for the η distributions presumably due to the inclusion of clustering at the partonic level. However, at the particle level, no such structures are prominently visible. In view of this, it is important to study the PCA-eigenvalues at the particle level with and without clustering.

For the p_{T} distribution, the position clustering lowers the eigenvalues compared to the no-clustering case while the clusters including thermal partons tend to increase the eigenvalues for all nodes. The same pattern is also seen in the η distributions, with exception to the first node ($\alpha = 1$), where for cases involving clustering with R = 5 fm have a higher eigenvalue than the no-clustering scenario. In case of the ϕ distributions, eigenvalues are seen closer in pairs presumably representing the real and imaginary components of the flow parameters [69]. Any detailed investigation towards extraction of flow parameters from these eigenvalues has not been made. It is only pointed out that the eigenvalues differ clearly for

two cases i.e., with and without clustering. It is also observed a clearer effect of the position clustering in case of ϕ as for eigenvalues for R = 5 fm lie considerably higher compared to the no-clustering values. The eigenvalues of the ϕ distributions look more sensitive to the position clustering.

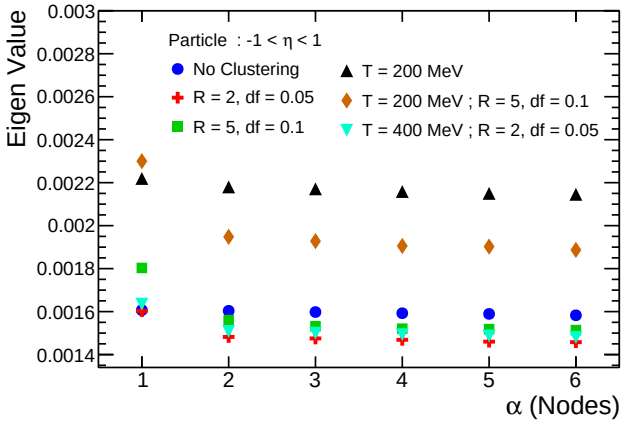

Figure 5.6: Eigenvalues as obtained for η distribution before and after clustering

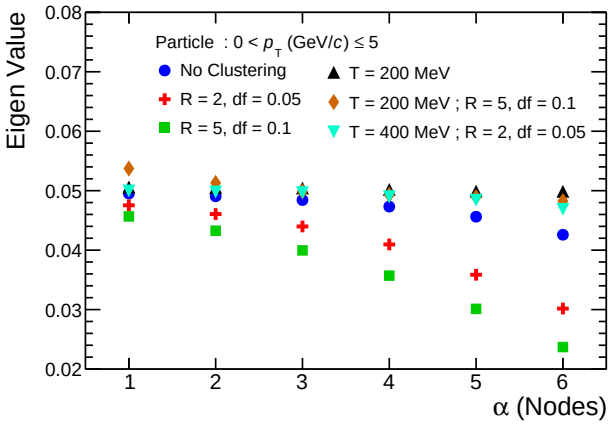

Figure 5.7: Eigenvalues as obtained for p_{T} distribution before and after clustering

Studies for various event centralities have also been performed. The figure 5.9 to figure 5.11 show the variation of the eigenvalues of two different modes (1 and 2) with event centralities. Only taken two cases that showed maximum effect in eigenvalue studies shown earlier have been considered i.e., (i) R = 5 fm, df = 0.1 and no momentum modifications and (ii) T = 200 MeV, R = 5 fm and df = 0.1. It is seen that the eigenvalues of the

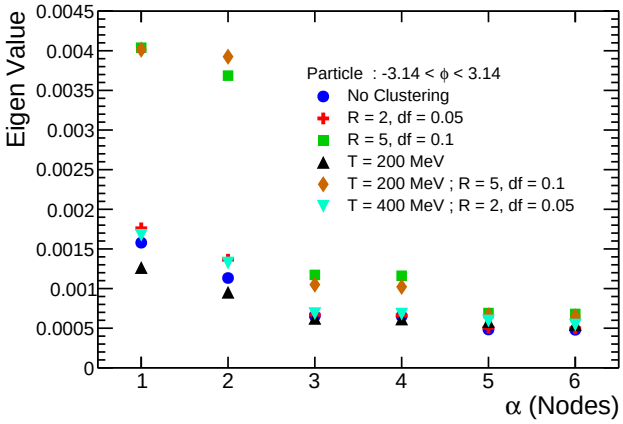

Figure 5.8: Eigenvalues as obtained for ϕ distribution before and after clustering

first component for the ϕ and p_{T} distributions have a decreasing trend for the events where clustering is implemented as compared to the events without clustering.

The observed decreasing trend of the first eigenvalues might be due to higher fluctuations for lower multiplicities in peripheral events. No significant structures are seen for the η distributions of the produced particles in both the cases.

It is also seen that the eigenvalues are considerably lower in case minimum-bias events as shown in the figures 5.6-5.8 discussed earlier. This might be due to dilution of fluctuations for minimum-bias events due to the admixture of events with different multiplicities.

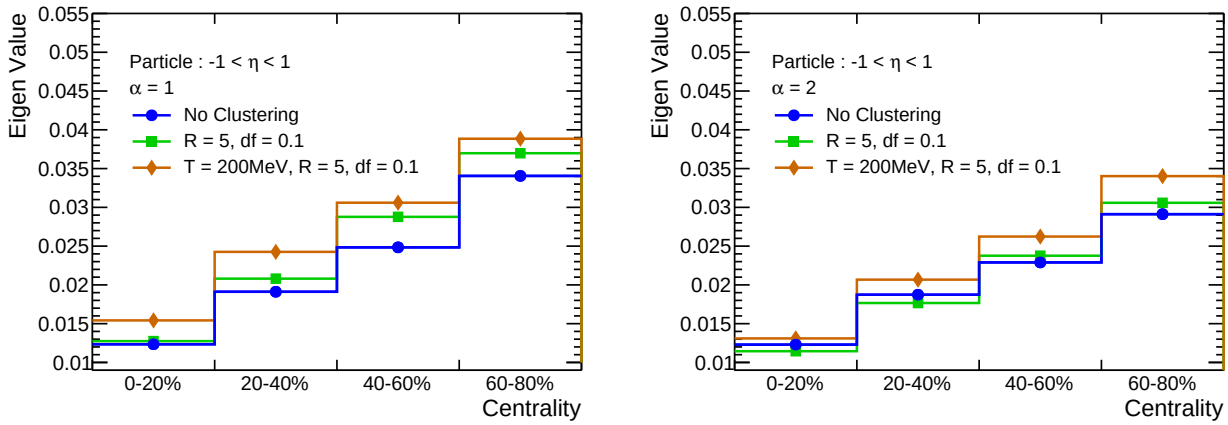

Figure 5.9: Eigenvalues as obtained for η distribution before and after clustering

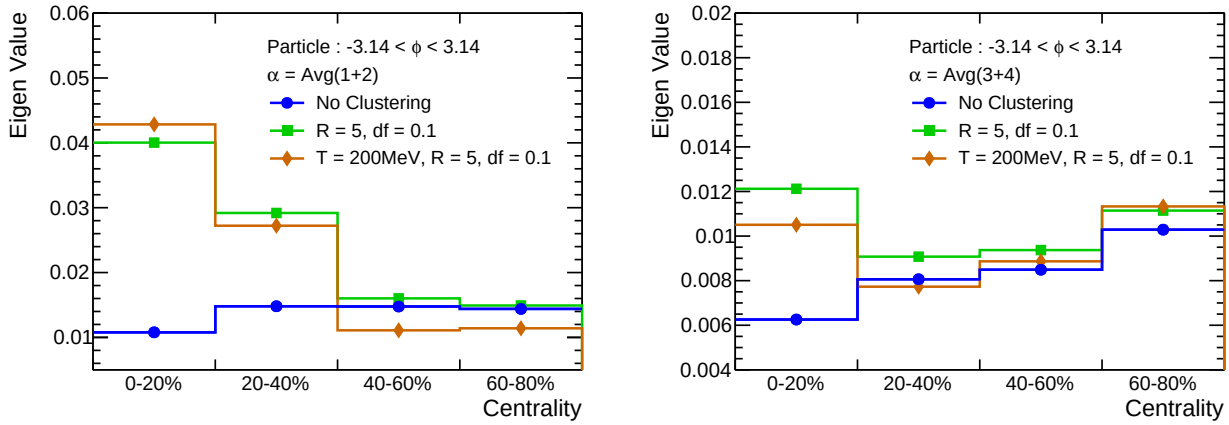

Figure 5.10: Eigenvalues as obtained for ϕ distribution before and after clustering

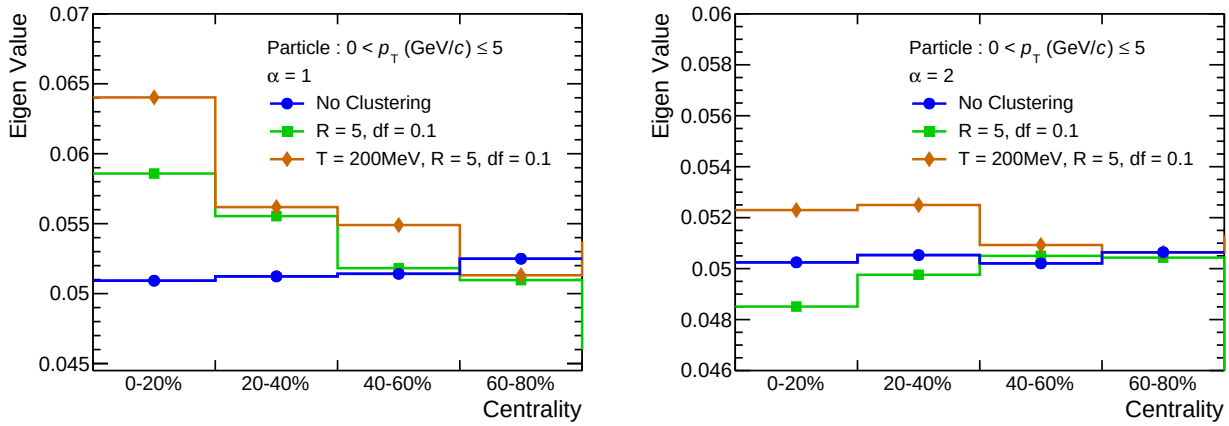

Figure 5.11: Eigenvalues as obtained for p_{T} distribution before and after clustering

5.6 Summary and Conclusions

In an effort to find a method to investigate the initial partonic structure in high energy heavy collisions, the formation of partonic clusters using the partons obtained from the AMPT model of string-melting version has been implemented. The clusters are formed in two steps, first by bringing partons closer in positions to an extent defined by two parameters i.e., the radius of the partonic zone (R) and the scaling factor on the inter-partonic distance. In this work, the following values have been used as R = 2 fm, 5 fm and df = 0.05 and 0.1. Additionally, a thermal distribution to the cluster partons by tuning the temperature parameters has been introduced, two temperature values i.e., T = 200 MeV and T = 400

MeV have been used. The later one is close to the inverse slope of the p_{T} distribution from the AMPT partons. These partons then undergo hadronization by AMPT string-melting hadronization scheme i.e, by coalescence of partons as per their distance, spin and mass. Investigation on the distributions of the produced particles from AMPT in order to find the sensitivity of the particle-level observables to the partonic structures have been made. Even though the structures are reflected in basic distributions of the partons, however, there is no clue of these structures in the inclusive distributions of the produced particles. For this investigation, the Principal Component Analysis (PCA) to analyse the η, ϕ and p_{T} distributions of the produced particles has been used. It may be mentioned that the square-root of the sum of the squares of the paired eigenvalues from the azimuthal distribution of a particular order has been shown to be related to the coefficients of flow up to v_6 [69]. In this work the eigenvalues as the candidate for probing the initial state at different clustering conditions have been taken . For this study, the eigenvalues have been obtained from PCA decomposition of η, ϕ and p_{T} distributions as the observables for various conditions like no clustering, only position clustering, inclusion of thermal partons with T = 200 MeV and 400 MeV. It is found that the first few prominent eigenvalues for all three distributions are sensitive to the inclusion of clustering. For η and p_{T} distributions, two clear groups are seen lying above and below the no-clustering scenario. For T = 200 MeV, all eigenvalues lie above the no-clustering reference. For position clustering, the eigenvalues are grouped below the reference. It is seen that the difference with the no-clustering reference is more for higher values of the R parameter. For the azimuthal distributions, the eigenvalues of which are related to the flow parameters, it appears the the sensitivity is higher towards the position clustering. The centrality dependence of the first two eigenvalues has also been studied. Even though the η-values do not show appreciable sensitivity, for ϕ and p_{T}, they show clearly different trend as compared to the no-clustering reference, which is mostly flat. It can therefore be conclude that the first few eigenvalues are sensitive to the inclusion of domains at the partonic level. The events with domains might be identified on an event

by event basis by discriminating based on the eigenvalues. It is already known that the eigenvalues of the azimuthal distributions represent the flow parameters. In general the PCA eigenvalues represent fluctuations in the distributions of different orders, which are not visible in the inclusive distributions, however, further analysis using the PCA might be performed to extract the physical interpretations of the eigenvalues and eigenvectors from the η and p_{T} distributions.

This study has been published in [158].

Chapter 6

Summary

In this thesis, using the ALICE experimental data, the p_{T}-differential cross section of electrons decayed from open heavy-flavour hadrons in pp collisions at $\sqrt{s} = 13$ TeV has been presented. The cross sections have been measured using two detector combinations for electron identification, namely, the TPC–TOF for the low p_{T} region (0.5 GeV/c < p_{T} < 4 GeV/c) and the TPC –EMCal for the high p_{T} region (3 GeV/c < p_{T} < 35 GeV/c). In the overlapping p_{T} region of 3 GeV/c - 4 GeV/c, the cross sections were found to be consistent. For $p_{\mathrm{T}} <$ 6 GeV/c, the minimum bias trigger has been used to select events and for $p_{\mathrm{T}} >$ 6 GeV/c, EMCal trigger with two different thresholds, namely the EG2 and the EG1 triggers, have been used. All measurements are in good agreement within the uncertainty. The p_{T}-differential cross section of electrons from open heavy-flavour hadron decays has been compared with the Fixed-Order-Next-to-Leading-Log (FONLL) and General-Mass-Variable-Flavour-Number-Scheme (GM-VFNS) perturbative QCD (pQCD) calculations. The FONLL calculation describes the measurements within the statistical and systematic uncertainties and the data is found be close to the upper edge of the theoretical prediction up to $p_{\mathrm{T}} < 5$ GeV/c. The GM-VFNS model largely under predicts the data in low and mid p_{T}, while the data lies within the uncertainty in the higher p_{T} ranges ($p_{\mathrm{T}} > 10$ GeV/c).

The self-normalized yields of electrons decayed from heavy-flavour hadrons ($\mathrm{d}^2N/\mathrm{d}p_{\mathrm{T}}\mathrm{d}\eta/$

$\langle \mathrm{d}^2N/\mathrm{d}p_\mathrm{T}\mathrm{d}\eta \rangle$) as a function of normalised charged-particle pseudorapidity density ($\mathrm{d}N_\mathrm{ch}/\mathrm{d}\eta/\langle \mathrm{d}N_\mathrm{ch}/\mathrm{d}\eta \rangle$) at mid rapidity ($|\eta| < 1.0$) has also been presented in five p_T intervals from 0.5 GeV/c $< p_\mathrm{T} <$ 30 GeV/c. The self-normalised yields in all p_T intervals have a faster than linear increasing trend with respect to normalised charged-particle density and higher p_T ranges show a tendency of steeper increase. The yield increase is approximately a factor of $\sim$ 9 for the lowest measured p_T (0.5 GeV/c $< p_\mathrm{T} <$ 3 GeV/c) and a factor of $\sim$ 28 for the highest measured p_T (15 GeV/c $< p_\mathrm{T} <$ 30 GeV/c) for multiplicities of 6 times the average multiplicity. Comparison of the normalized yields with predictions from the PYTHIA 8.2 Monash tune and the Colour Reconnection (CR) Mode 2 tunes have been presented. PYTHIA 8.2 Monash tune describes the overall trend in data, however the slope is overestimated at the high p_T region. PYTHIA 8.2 with CR Mode 2 reproduces the slope at all p_T intervals fairly well. PYTHIA 8.2 CR Mode 2 describes the normalised yield better than the Monash tune. A comparison of the self normalised yields of electrons from heavy-flavour decays have been done with the self-normalised yields of other heavy- and light-flavour hadrons. To perform an in-depth p_T dependent comparison, the double ratio of the self-normalized yields, in different p_T intervals, have been fitted with a linear function. The $\langle p_\mathrm{T} \rangle$ vs. slope of linear fit of the various particles have been compared. Comparison has been done in two multiplicity selection scenarios, i.e., where events are divided using SPD tracklet multiplicity estimator at mid rapidity and using V0 estimator in forward rapidity. For measurements where multiplicity estimator is SPD tracklet multiplicity no saturation with increasing $\langle p_\mathrm{T} \rangle$ is seen. Mesons, i.e., heavy-flavour hadron decay electrons, D-mesons, J/ψ, K^0_s and charged particles which is mostly π, tend to follow a similar trend. Baryons (Ξ and Λ) follows a different trend. For measurements using V0 multiplicity estimator the baryon trend saturates at $p_\mathrm{T} \gtrsim 4$ GeV/c. A saturating trend in mesons tends to be achieved.

In this thesis, a study on the structures in the initial collision zone and how they effect the final state particles using Pb–Pb collisions from AMPT event generator at $\sqrt{s_\mathrm{NN}} = 200$ GeV using Principal Component Analysis (PCA) method has also been presented. The particle

production mechanisms and initial state and geometry of the system are highly entangled and structures in the initial collision zone is a matter of intense investigation, both from theory and experimental points of views, in high-energy heavy-ion collisions. The main scope of the study in this thesis is to probe the initial conditions by using the method of Principal Component Analysis, is a simple method of unsupervised learning algorithm often used for reducing dimensions and for de-correlating multivariate data. A formalism to implement clusters at the partonic level in the string melting version of the AMPT model for Pb–Pb collisions at $\sqrt{s_{\rm NN}} = 200$ GeV has been presented which are then propagated through the AMPT hadronization scheme. The clusters are formed in two steps, first by bringing partons closer in positions to an extent defined by two parameters i.e., the radius of the partonic zone (R) and the scaling factor on the inter-partonic distance (df). The following values have been used as R = 2 fm, 5 fm and df = 0.05 and 0.1. A thermal distribution to the cluster partons by tuning the temperature parameters has been introduced, using two temperature values i.e., T = 200 MeV and T = 400 MeV. PCA method has been used on η, ϕ and $p_{\rm T}$ distributions of the produced charged particles before and after clustering. Sensitivity of of the PCA eigen values to the introduction of clustering at the partonic level in AMPT has been discussed. It is has been found that the first few prominent eigenvalues are sensitive to the inclusion of clustering for all the three distributions, however different sensitivity of the the eigen values to position and temperature clustering has been found. The centrality dependence of the first two eigenvalues has also been reported [158].

Bibliography

[1] "Press Release: First results from Fermilab's Muon g-2 experiment strengthen evidence of new physics." https://news.fnal.gov/2021/04/first-results-from-fermilabs-muon-g-2-experiment-strengthen-evidence-of-new-physics/.

[2] J. Greensite, *An introduction to the confinement problem*, vol. 821. 2011.

[3] E. Eichten, K. Gottfried, T. Kinoshita, J. B. Kogut, K. D. Lane, and T.-M. Yan, "The Spectrum of Charmonium," *Phys. Rev. Lett.* **34** (1975) 369–372. [Erratum: Phys.Rev.Lett. 36, 1276 (1976)].

[4] L. C. P. Van Hove, "Theoretical prediction of a new state of matter, the "quark-gluon plasma" (also called "quark matter"),". `https://cds.cern.ch/record/183417`.

[5] H. Satz, *Statistical Mechanics of Quarks and Hadrons: Proceedings of an International Symposium Held at the University of Bielefeld, F.R.G., August 24-31, 1980*. North-Holland, 1981. `https://books.google.co.in/books?id=OY8uAAAAIAAJ`.

[6] K. Yagi, T. Hatsuda, and Y. Miake, *Quark-gluon plasma: From big bang to little bang*, vol. 23. 2005.

[7] E. Annala, T. Gorda, A. Kurkela, J. Nättilä, and A. Vuorinen, "Evidence for quark-matter cores in massive neutron stars," *Nature Phys.* **16** no. 9, (2020) 907–910, arXiv:1903.09121 [astro-ph.HE].

[8] J. D. Bjorken, "Highly Relativistic Nucleus-Nucleus Collisions: The Central Rapidity Region," *Phys. Rev. D* **27** (1983) 140–151.

[9] U. W. Heinz and M. Jacob, "Evidence for a new state of matter: An Assessment of the results from the CERN lead beam program," arXiv:nucl-th/0002042.

[10] **BRAHMS** Collaboration, I. Arsene *et al.*, "Quark gluon plasma and color glass condensate at RHIC? The Perspective from the BRAHMS experiment," *Nucl. Phys. A* **757** (2005) 1–27, arXiv:nucl-ex/0410020.

[11] **PHOBOS** Collaboration, B. B. Back *et al.*, "The PHOBOS perspective on discoveries at RHIC," *Nucl. Phys. A* **757** (2005) 28–101, arXiv:nucl-ex/0410022.

[12] **PHENIX** Collaboration, K. Adcox *et al.*, "Formation of dense partonic matter in relativistic nucleus-nucleus collisions at RHIC: Experimental evaluation by the PHENIX collaboration," *Nucl. Phys. A* **757** (2005) 184–283, arXiv:nucl-ex/0410003.

[13] **STAR** Collaboration, J. Adams *et al.*, "Experimental and theoretical challenges in the search for the quark gluon plasma: The STAR Collaboration's critical assessment of the evidence from RHIC collisions," *Nucl. Phys. A* **757** (2005) 102–183, arXiv:nucl-ex/0501009.

[14] **CMS** Collaboration, V. Khachatryan *et al.*, "Observation of Long-Range Near-Side Angular Correlations in Proton-Proton Collisions at the LHC," *JHEP* **09** (2010) 091, arXiv:1009.4122 [hep-ex].

[15] **CMS** Collaboration, V. Khachatryan *et al.*, "Evidence for collectivity in pp collisions at the LHC," *Phys. Lett. B* **765** (2017) 193–220, arXiv:1606.06198 [nucl-ex].

[16] **ALICE** Collaboration, J. Adam *et al.*, "Enhanced production of multi-strange hadrons in high-multiplicity proton-proton collisions," *Nature Phys.* **13** (2017) 535–539, arXiv:1606.07424 [nucl-ex].

[17] P. Bozek, "Elliptic flow in proton-proton collisions at $sqrt(S) = 7$ TeV," *Eur. Phys. J. C* **71** (2011) 1530, arXiv:1010.0405 [hep-ph].

[18] K. Werner, I. Karpenko, and T. Pierog, "The 'Ridge' in Proton-Proton Scattering at 7 TeV," *Phys. Rev. Lett.* **106** (2011) 122004, arXiv:1011.0375 [hep-ph].

[19] E. Shuryak and I. Zahed, "High-multiplicity pp and pA collisions: Hydrodynamics at its edge," *Phys. Rev. C* **88** no. 4, (2013) 044915, arXiv:1301.4470 [hep-ph].

[20] G. Martinez, "Advances in Quark Gluon Plasma," arXiv:1304.1452 [nucl-ex].

[21] M. Strickland, "Anisotropic Hydrodynamics: Three lectures," *Acta Phys. Polon. B* **45** no. 12, (2014) 2355–2394, arXiv:1410.5786 [nucl-th].

[22] E. Iancu and R. Venugopalan, "The Color glass condensate and high-energy scattering in QCD," arXiv:hep-ph/0303204.

[23] F. Gelis, E. Iancu, J. Jalilian-Marian, and R. Venugopalan, "The Color Glass Condensate," *Ann. Rev. Nucl. Part. Sci.* **60** (2010) 463–489, arXiv:1002.0333 [hep-ph].

[24] F. Gelis, T. Lappi, and L. McLerran, "Glittering Glasmas," *Nucl. Phys. A* **828** (2009) 149–160, arXiv:0905.3234 [hep-ph].

[25] **ALICE** Collaboration, L. Vermunt, "Open heavy-flavour production from small to large collision systems with ALICE at the LHC," in *40th International Conference on High Energy Physics*. 11, 2020. arXiv:2011.06291 [nucl-ex].

[26] **ALICE** Collaboration, B. B. Abelev *et al.*, "Transverse momentum dependence of inclusive primary charged-particle production in p-Pb collisions at $\sqrt{s_{\rm NN}} = 5.02$ TeV," *Eur. Phys. J. C* **74** no. 9, (2014) 3054, arXiv:1405.2737 [nucl-ex].

[27] M. H. Thoma and M. Gyulassy, "Quark Damping and Energy Loss in the High Temperature QCD," *Nucl. Phys. B* **351** (1991) 491–506.

[28] I. P. Lokhtin and A. M. Snigirev, "Partonic energy loss in ultrarelativistic heavy ion collisions: Jet suppression versus jet fragmentation softening," *Phys. Lett. B* **567** (2003) 39–45, arXiv:hep-ph/0303121.

[29] R. Baier, Y. L. Dokshitzer, A. H. Mueller, S. Peigne, and D. Schiff, "Radiative energy loss and p(T) broadening of high-energy partons in nuclei," *Nucl. Phys. B* **484** (1997) 265–282, arXiv:hep-ph/9608322.

[30] **ALICE** Collaboration, S. Acharya *et al.*, "Measurement of electrons from semileptonic heavy-flavour hadron decays at midrapidity in pp and Pb-Pb collisions at $\sqrt{s_{\rm NN}} = 5.02$ TeV," *Phys. Lett. B* **804** (2020) 135377, arXiv:1910.09110 [nucl-ex].

[31] **ALICE** Collaboration, K. Aamodt *et al.*, "Harmonic decomposition of two-particle angular correlations in Pb-Pb collisions at $\sqrt{s_{NN}} = 2.76$ TeV," *Phys. Lett. B* **708** (2012) 249–264, arXiv:1109.2501 [nucl-ex].

[32] J. Rafelski and R. Hagedorn, "From hadron gas to quark matter, 2,". http://cds.cern.ch/record/126179.

[33] P. Koch and J. Rafelski, "Time Evolution of Strange Particle Densities in Hot Hadronic Matter," *Nucl. Phys. A* **444** (1985) 678–691.

[34] J. Rafelski, "Strangeness Production in the Quark Gluon Plasma," *Nucl. Phys. A* **418** (1984) 215C–235C.

[35] **ALICE** Collaboration, B. B. Abelev *et al.*, "Multi-strange baryon production at mid-rapidity in Pb-Pb collisions at $\sqrt{s_{NN}} = 2.76$ TeV," *Phys. Lett. B* **728** (2014) 216–227, arXiv:1307.5543 [nucl-ex]. [Erratum: Phys.Lett.B 734, 409–410 (2014)].

[36] **ATLAS** Collaboration, G. Aad *et al.*, "Observation of a new particle in the search for the Standard Model Higgs boson with the ATLAS detector at the LHC," *Phys. Lett. B* **716** (2012) 1–29, arXiv:1207.7214 [hep-ex].

[37] **CMS** Collaboration, S. Chatrchyan *et al.*, "Observation of a New Boson at a Mass of 125 GeV with the CMS Experiment at the LHC," *Phys. Lett. B* **716** (2012) 30–61, arXiv:1207.7235 [hep-ex].

[38] **ALICE** Collaboration, S. Acharya *et al.*, "Investigations of Anisotropic Flow Using Multiparticle Azimuthal Correlations in pp, p-Pb, Xe-Xe, and Pb-Pb Collisions at the LHC," *Phys. Rev. Lett.* **123** no. 14, (2019) 142301, arXiv:1903.01790 [nucl-ex].

[39] **Particle Data Group** Collaboration, P. A. Zyla *et al.*, "Review of Particle Physics," *PTEP* **2020** no. 8, (2020) 083C01.

[40] W. Beenakker, W. L. van Neerven, R. Meng, G. A. Schuler, and J. Smith, "QCD corrections to heavy quark production in hadron hadron collisions," *Nucl. Phys. B* **351** (1991) 507–560.

[41] Y. L. Dokshitzer and D. E. Kharzeev, "Heavy quark colorimetry of QCD matter," *Phys. Lett. B* **519** (2001) 199–206, arXiv:hep-ph/0106202.

[42] **ALICE** Collaboration, S. Acharya *et al.*, "Measurement of D^0, D^+, D^{*+} and D_s^+ production in Pb-Pb collisions at $\sqrt{s_{NN}} = 5.02$ TeV," *JHEP* **10** (2018) 174, arXiv:1804.09083 [nucl-ex].

[43] **ATLAS Collaboration** Collaboration, "Measurement of nuclear modification factor for muons from charm and bottom hadrons in Pb+Pb collisions at 5.02 TeV with the ATLAS detector," tech. rep., CERN, Geneva, May, 2021. http://cds.cern.ch/record/2766615. All figures including auxiliary figures are available at https://atlas.web.cern.ch/Atlas/GROUPS/PHYSICS/CONFNOTES/ATLAS-CONF-2021-020.

[44] J. M. Campbell, J. W. Huston, and W. J. Stirling, "Hard Interactions of Quarks and Gluons: A Primer for LHC Physics," *Rept. Prog. Phys.* **70** (2007) 89, arXiv:hep-ph/0611148.

[45] V. Greco, C. M. Ko, and P. Levai, "Parton coalescence and anti-proton / pion anomaly at RHIC," *Phys. Rev. Lett.* **90** (2003) 202302, arXiv:nucl-th/0301093.

[46] R. J. Fries, B. Muller, C. Nonaka, and S. A. Bass, "Hadronization in heavy ion collisions: Recombination and fragmentation of partons," *Phys. Rev. Lett.* **90** (2003) 202303, arXiv:nucl-th/0301087.

[47] R. C. Hwa and C. B. Yang, "Scaling behavior at high p(T) and the p / pi ratio," *Phys. Rev. C* **67** (2003) 034902, arXiv:nucl-th/0211010.

[48] V. Minissale, F. Scardina, and V. Greco, "Hadrons from coalescence plus fragmentation in AA collisions at energies available at the BNL Relativistic Heavy Ion Collider to the CERN Large Hadron Collider," *Phys. Rev. C* **92** no. 5, (2015) 054904, arXiv:1502.06213 [nucl-th].

[49] V. Greco, "Phase-space coalescence for heavy and light quarks at RHIC," *Eur. Phys. J. ST* **155** (2008) 45–59, arXiv:0710.0486 [nucl-th].

[50] **ALICE** Collaboration, S. Acharya *et al.*, "Λ_c^+ production and baryon-to-meson ratios in pp and p-Pb collisions at $\sqrt{s_{NN}} = 5.02$ TeV at the LHC," arXiv:2011.06078 [nucl-ex].

[51] L. Gladilin, "Fragmentation fractions of c and b quarks into charmed hadrons at LEP," *Eur. Phys. J. C* **75** no. 1, (2015) 19, arXiv:1404.3888 [hep-ex].

[52] V. Minissale, S. Plumari, and V. Greco, "Charm Hadrons in pp collisions at LHC energy within a Coalescence plus Fragmentation approach," arXiv:2012.12001 [hep-ph].

[53] **H1, ZEUS** Collaboration, K. Lipka and Z. experiments, "Recent results from HERA and their impact for LHC," *EPJ Web Conf.* **28** (2012) 02008, arXiv:1201.4486 [hep-ex].

[54] H. J. Lubatti, "Lepton-hadron interactions and nucleon structure,". https://cds.cern.ch/record/134469.

[55] M. Cacciari, M. Greco, and P. Nason, "The P(T) spectrum in heavy flavor hadroproduction," *JHEP* **05** (1998) 007, arXiv:hep-ph/9803400.

[56] C. Peterson, D. Schlatter, I. Schmitt, and P. M. Zerwas, "Scaling Violations in Inclusive e+ e- Annihilation Spectra," *Phys. Rev. D* **27** (1983) 105.

[57] A. V. Karpishkov, M. A. Nefedov, V. A. Saleev, and A. V. Shipilova, "Open charm production in the parton Reggeization approach: Tevatron and the LHC," *Phys. Rev. D* **91** no. 5, (2015) 054009, arXiv:1410.7139 [hep-ph].

[58] R. Sepahvand and S. Dadfar, "NLO corrections to c- and b-quark fragmentation into j/ψ and γ," *Phys. Rev. D* **95** no. 3, (2017) 034012.

[59] **ALICE** Collaboration, B. Abelev *et al.*, "J/ψ Production as a Function of Charged Particle Multiplicity in pp Collisions at $\sqrt{s} = 7$ TeV," *Phys. Lett. B* **712** (2012) 165–175, arXiv:1202.2816 [hep-ex].

[60] T. Sjostrand and M. van Zijl, "A Multiple Interaction Model for the Event Structure in Hadron Collisions," *Phys. Rev. D* **36** (1987) 2019.

[61] P. Bartalini and L. Fano, eds., *Proceedings, 1st International Workshop on Multiple Partonic Interactions at the LHC (MPI08): Perugia, Italy, October 27-31, 2008.* DESY, Hamburg, 2009. arXiv:1003.4220 [hep-ex].

[62] **CDF** Collaboration, D. Acosta *et al.*, "The underlying event in hard interactions at the Tevatron $\bar{p}p$ collider," *Phys. Rev. D* **70** (2004) 072002, arXiv:hep-ex/0404004.

[63] **CMS** Collaboration, V. Khachatryan *et al.*, "First Measurement of the Underlying Event Activity at the LHC with $\sqrt{s} = 0.9$ TeV," *Eur. Phys. J. C* **70** (2010) 555–572, arXiv:1006.2083 [hep-ex].

[64] S. Porteboeuf and R. Granier de Cassagnac, "J/Ψ yield vs. multiplicity in proton-proton collisions at the LHC," *Nucl. Phys. B Proc. Suppl.* **214** (2011) 181–184, arXiv:1012.0719 [hep-ex].

[65] **ALICE** Collaboration, J. Adam *et al.*, "Measurement of charm and beauty production at central rapidity versus charged-particle multiplicity in proton-proton collisions at $\sqrt{s} = 7$ TeV," *JHEP* **09** (2015) 148, arXiv:1505.00664 [nucl-ex].

[66] **ALICE** Collaboration, S. Acharya *et al.*, "Multiplicity dependence of J/ψ production at midrapidity in pp collisions at $\sqrt{s} = 13$ TeV," *Phys. Lett. B* **810** (2020) 135758, arXiv:2005.11123 [nucl-ex].

[67] **ALICE** Collaboration, S. Acharya *et al.*, "Charged-particle production as a function of multiplicity and transverse spherocity in pp collisions at $\sqrt{s} = 5.02$ and 13 TeV," *Eur. Phys. J. C* **79** no. 10, (2019) 857, arXiv:1905.07208 [nucl-ex].

[68] R. S. Bhalerao, J.-Y. Ollitrault, S. Pal, and D. Teaney *Phys. Rev. Lett.* **114** no. 15, (2015) 152301, arXiv:1410.7739 [nucl-th].

[69] Z. Liu, W. Zhao, and H. Song *Eur. Phys. J. C* **79** no. 10, (2019) 870, arXiv:1903.09833 [nucl-th].

[70] "LHC Machine, The CERN large hadron collider: accelerator and experiments," *JINST* **3** (2008) S08001.

[71] **ALICE** Collaboration, K. Aamodt *et al.*, "The ALICE experiment at the CERN LHC," *JINST* **3** (2008) S08002.

[72] **ATLAS** Collaboration, G. Aad *et al.*, "The ATLAS Experiment at the CERN Large Hadron Collider," *JINST* **3** (2008) S08003.

[73] **CMS** Collaboration, S. Chatrchyan *et al.*, "The CMS Experiment at the CERN LHC," *JINST* **3** (2008) S08004.

[74] **LHCb** Collaboration, A. A. Alves, Jr. *et al.*, "The LHCb Detector at the LHC," *JINST* **3** (2008) S08005.

[75] **LHCf** Collaboration, O. Adriani *et al.*, "The LHCf detector at the CERN Large Hadron Collider," *JINST* **3** (2008) S08006.

[76] **TOTEM** Collaboration, G. Anelli *et al.*, "The TOTEM experiment at the CERN Large Hadron Collider," *JINST* **3** (2008) S08007.

[77] L. Betev *et al.*, "Definition of the ALICE coordinate system and basic rules for sub-detector components numbering." http://personalpages.to.infn.it/~tosello/EngMeet/NamingConventions/ALICE-INT-2003-038.pdf.

[78] **ALICE** Collaboration, K. Aamodt *et al.*, "Alignment of the ALICE Inner Tracking System with cosmic-ray tracks," *JINST* **5** (2010) P03003, arXiv:1001.0502 [physics.ins-det].

[79] **ALICE** Collaboration, B. Abelev *et al.*, "Technical Design Report for the Upgrade of the ALICE Inner Tracking System," Tech. Rep. CERN-LHCC-2013-024. ALICE-TDR-017, Nov, 2013. https://cds.cern.ch/record/1625842.

[80] **ALICE** Collaboration, B. B. Abelev *et al.*, "Performance of the ALICE Experiment at the CERN LHC," *Int. J. Mod. Phys. A* **29** (2014) 1430044, arXiv:1402.4476 [nucl-ex].

[81] **ALICE** Collaboration, G. Dellacasa *et al.*, *ALICE time projection chamber: Technical Design Report*. Technical design report. ALICE. CERN, Geneva, 2000. http://cds.cern.ch/record/451098.

[82] W. Leo, *Techniques for Nuclear and Particle Physics Experiments: A How-to Approach*. Springer, 1994. https://books.google.co.in/books?id=W7vHQgAACAAJ.

[83] **ALICE** Collaboration, *ALICE Time-Of-Flight system (TOF): Technical Design Report*. Technical design report. ALICE. CERN, Geneva, 2000. http://cds.cern.ch/record/430132.

[84] **ALICE** Collaboration, P. Cortese, *ALICE Time-Of Flight system (TOF): addendum to the Technical Design Report*. Technical design report. ALICE. CERN, Geneva, 2002. http://cds.cern.ch/record/545834.

[85] **ALICE** Collaboration, T. Cormier *et al.*, "ALICE electromagnetic calorimeter: addendum to the ALICE technical proposal," Tech. Rep. CERN-LHCC-2006-014, CERN, Geneva, Mar, 2006. http://cds.cern.ch/record/932676.

[86] **ALICE** Collaboration, J. Allen *et al.*, "ALICE DCal: An Addendum to the EMCal Technical Design Report Di-Jet and Hadron-Jet correlation measurements in ALICE," Tech. Rep. CERN-LHCC-2010-011. ALICE-TDR-14-add-1, Jun, 2010. https://cds.cern.ch/record/1272952.

[87] **ALICE** Collaboration, A. Fantoni, "The ALICE Electromagnetic Calorimeter: EMCAL," *J. Phys. Conf. Ser.* **293** (2011) 012043.

[88] **ALICE** Collaboration, P. Cortese *et al.*, *ALICE forward detectors: FMD, TO and VO: Technical Design Report*. Technical design report. ALICE. CERN, Geneva, 2004. http://cds.cern.ch/record/781854. Submitted on 10 Sep 2004.

[89] **ALICE** Collaboration, E. Abbas *et al.*, "Performance of the ALICE VZERO system," *JINST* **8** (2013) P10016, arXiv:1306.3130 [nucl-ex].

[90] S. van der Meer, "Calibration of the effective beam height in the ISR," tech. rep., CERN, Geneva, 1968. https://cds.cern.ch/record/296752.

[91] "ROOT webpage." http://root.cern.ch.

[92] "Alice offline webpage." http://aliceinfo.cern.ch/Offline/.

[93] T. Sjostrand, S. Mrenna, and P. Z. Skands, "PYTHIA 6.4 Physics and Manual," *JHEP* **05** (2006) 026, arXiv:hep-ph/0603175.

[94] T. Sjöstrand, S. Ask, J. R. Christiansen, R. Corke, N. Desai, P. Ilten, S. Mrenna, S. Prestel, C. O. Rasmussen, and P. Z. Skands, "An introduction to PYTHIA 8.2," *Comput. Phys. Commun.* **191** (2015) 159–177, arXiv:1410.3012 [hep-ph].

[95] T. Pierog and K. Werner, "EPOS Model and Ultra High Energy Cosmic Rays," *Nucl. Phys. B Proc. Suppl.* **196** (2009) 102–105, arXiv:0905.1198 [hep-ph].

[96] M. Gyulassy and X.-N. Wang, "HIJING 1.0: A Monte Carlo program for parton and particle production in high-energy hadronic and nuclear collisions," *Comput. Phys. Commun.* **83** (1994) 307, arXiv:nucl-th/9502021.

[97] R. Brun, R. Hagelberg, M. Hansroul, and J. C. Lassalle, *Simulation program for particle physics experiments, GEANT: user guide and reference manual*. CERN, Geneva, 1978. https://cds.cern.ch/record/118715.

[98] **GEANT4** Collaboration, S. Agostinelli *et al.*, "GEANT4–a simulation toolkit," *Nucl. Instrum. Meth. A* **506** (2003) 250–303.

[99] E. Bruna, A. Dainese, M. Masera, and F. Prino, "Vertex reconstruction for proton-proton collisions in ALICE,". http://cds.cern.ch/record/1225497.

[100] D. Elia, J. Grosse-Oetringhaus, M. Nicassio, and T. Virgili, "The pixel detector based tracklet reconstruction algorithm in ALICE," tech. rep., CERN, Geneva, Nov, 2009. http://cds.cern.ch/record/1225500.

[101] R. Fruhwirth, "Application of Kalman filtering to track and vertex fitting," *Nucl. Instrum. Meth. A* **262** (1987) 444–450.

[102] "EMCal offline documentation in AliROOT." alisw/AliRoot/EMCAL/doc/EMCALDocumentation.pdf.

[103] T. C. Awes, F. E. Obenshain, F. Plasil, S. Saini, S. P. Sorensen, and G. R. Young, "A Simple method of shower localization and identification in laterally segmented calorimeters," *Nucl. Instrum. Meth. A* **311** (1992) 130–138.

[104] T. R. P.-R. Aronsson, "Cross section of bottom electrons in proton-proton collisions in the ALICE experiment," 2014. http://cds.cern.ch/record/2652553.

[105] **ALICE** Collaboration, S. Acharya *et al.*, "Production of π^0 and η mesons up to high transverse momentum in pp collisions at 2.76 TeV," *Eur. Phys. J. C* **77** no. 5, (2017) 339, arXiv:1702.00917 [hep-ex].

[106] W. Carena *et al.*, "ALICE DAQ and ECS User's Guide,".

[107] https://twiki.cern.ch/twiki/bin/view/ALICE/AliDPGRunLists.

[108] **ALICE Collaboration** Collaboration, "ALICE luminosity determination for pp collisions at $\sqrt{s} = 13$ TeV,". https://cds.cern.ch/record/2160174.

[109] **ALICE EMCal** Collaboration, O. Bourrion, N. Arbor, G. Conesa-Balbastre, C. Furget, R. Guernane, and G. Marcotte, "The ALICE EMCal L1 trigger first year of operation experience," *JINST* **8** (2013) C01013, arXiv:1210.8078 [physics.ins-det].

[110] E. Fermi, "An attempt of a theory of beta radiation. 1.," *Z. Phys.* **88** (1934) 161–177.

[111] F. L. Wilson, "Fermi's Theory of Beta Decay," *Am. J. Phys.* **36** no. 12, (1968) 1150–1160.

[112] **ALICE** Collaboration, B. Abelev *et al.*, "Measurement of electrons from semileptonic heavy-flavour hadron decays in pp collisions at \sqrts = 7 TeV," *Phys. Rev. D* **86** (2012) 112007, arXiv:1205.5423 [hep-ex].

[113] **ALICE** Collaboration, J. Adam *et al.*, "Measurement of electrons from heavy-flavour hadron decays in p-Pb collisions at $\sqrt{s_{\rm NN}} = 5.02$ TeV," *Phys. Lett. B* **754** (2016) 81–93, arXiv:1509.07491 [nucl-ex].

[114] **ALICE** Collaboration, S. Acharya *et al.*, "Measurements of low-p_T electrons from semileptonic heavy-flavour hadron decays at mid-rapidity in pp and Pb-Pb collisions at $\sqrt{s_{\rm NN}} = 2.76$ TeV," *JHEP* **10** (2018) 061, arXiv:1805.04379 [nucl-ex].

[115] S. Alioli, P. Nason, C. Oleari, and E. Re, "A general framework for implementing NLO calculations in shower Monte Carlo programs: the POWHEG BOX," *JHEP* **06** (2010) 043, arXiv:1002.2581 [hep-ph].

[116] **CDF** Collaboration, T. Aaltonen *et al.*, "Direct Measurement of the W Production Charge Asymmetry in $p\bar{p}$ Collisions at $\sqrt{s} = 1.96$ TeV," *Phys. Rev. Lett.* **102** (2009) 181801, arXiv:0901.2169 [hep-ex].

[117] **CMS** Collaboration, S. Chatrchyan *et al.*, "Measurement of the Electron Charge Asymmetry in Inclusive W Production in pp Collisions at $\sqrt{s} = 7$ TeV," *Phys. Rev. Lett.* **109** (2012) 111806, arXiv:1206.2598 [hep-ex].

[118] **ALICE** Collaboration, S. Acharya *et al.*, "Production of light-flavor hadrons in pp collisions at $\sqrt{s} = 7$ and $\sqrt{s} = 13$ TeV," *Eur. Phys. J. C* **81** no. 3, (2021) 256, arXiv:2005.11120 [nucl-ex].

[119] G. Gatoff and C. Y. Wong, "Origin of the soft p(T) spectra," *Phys. Rev. D* **46** (1992) 997–1006.

[120] R. Barlow, "Systematic errors: Facts and fictions," in *Conference on Advanced Statistical Techniques in Particle Physics*. 7, 2002. arXiv:hep-ex/0207026.

[121] "ALICe Twiki page." https://twiki.cern.ch/twiki/bin/viewauth/ALICE/AliDPGtoolsTrackSystematicUncertaintyBookkeping.

[122] "Analaysis Note: Electrons from heavy-flavour hadron decays at mid-rapidity and low transverse momenta in pp collisions at $\sqrt{s} = 13$ TeV with low magnetic field (B = 0.2 T), Sudhir Rode." https://alice-notes.web.cern.ch/node/1019.

[123] M. Cacciari, S. Frixione, N. Houdeau, M. L. Mangano, P. Nason, and G. Ridolfi, "Theoretical predictions for charm and bottom production at the LHC," *JHEP* **10** (2012) 137, arXiv:1205.6344 [hep-ph].

[124] B. A. Kniehl, "Inclusive production of heavy-flavored hadrons at NLO in the GM-VFNS," in *Proceedings, 16th International Workshop on Deep Inelastic Scattering and Related Subjects (DIS 2008): London, UK, April 7-11, 2008*, p. 195. 2008. arXiv:0807.2215 [hep-ph].

[125] B. A. Kniehl, G. Kramer, I. Schienbein, and H. Spiesberger, "Inclusive B-Meson Production at the LHC in the GM-VFN Scheme," *Phys. Rev.* **D84** (2011) 094026, arXiv:1109.2472 [hep-ph].

[126] **ALICE** Collaboration, B. B. Abelev *et al.*, "Measurement of electrons from semileptonic heavy-flavor hadron decays in *pp* collisions at $\sqrt{s} = 2.76$ TeV," *Phys. Rev.* **D91** no. 1, (2015) 012001, arXiv:1405.4117 [nucl-ex].

[127] **ALICE** Collaboration, S. Acharya *et al.*, "Measurement of beauty and charm production in pp collisions at $\sqrt{s} = 5.02$ TeV via non-prompt and prompt D mesons," arXiv:2102.13601 [nucl-ex].

[128] J. Martin Blanco, "Study of $\boldsymbol{J/\psi}$ production dependence with the charged particle multiplicity in p-Pb collisions at $\boldsymbol{\sqrt{s_{\rm NN}}} = 5.02$ TeV and pp collisions at $\boldsymbol{\sqrt{s}} = 8$ TeV with the ALICE experiment at the LHC," Jan, 2016. https://cds.cern.ch/record/2197816. Presented 29 Oct 2015.

[129] **ALICE** Collaboration, J. Adam *et al.*, "Pseudorapidity and transverse-momentum distributions of charged particles in proton–proton collisions at $\sqrt{s} = 13$ TeV," *Phys. Lett. B* **753** (2016) 319–329, arXiv:1509.08734 [nucl-ex].

[130] **ALICE** Collaboration, S. Acharya *et al.*, "Multiplicity dependence of J/ψ production at midrapidity in pp collisions at $\sqrt{s} = 13$ TeV," *Phys. Lett. B* **810** (2020) 135758, arXiv:2005.11123 [nucl-ex].

[131] J. R. Christiansen and P. Z. Skands, "String Formation Beyond Leading Colour," *JHEP* **08** (2015) 003, arXiv:1505.01681 [hep-ph].

[132] **ALICE** Collaboration, J. Adam *et al.*, "Measurement of D-meson production versus multiplicity in p-Pb collisions at $\sqrt{s_{\rm NN}} = 5.02$ TeV," *JHEP* **08** (2016) 078, arXiv:1602.07240 [nucl-ex].

[133] **ATLAS Collaboration** Collaboration, "A study of different colour reconnection settings for Pythia8 generator using underlying event observables," tech. rep., CERN, Geneva, May, 2017. https://cds.cern.ch/record/2262253. All figures including auxiliary figures are available at https://atlas.web.cern.ch/Atlas/GROUPS/PHYSICS/PUBNOTES/ATL-PHYS-PUB-2017-008.

[134] **ALICE** Collaboration, S. Acharya *et al.*, "Multiplicity dependence of (multi-)strange hadron production in proton-proton collisions at $\sqrt{s} = 13$ TeV," *Eur. Phys. J. C* **80** no. 2, (2020) 167, arXiv:1908.01861 [nucl-ex].

[135] C. Tsallis, "Possible Generalization of Boltzmann-Gibbs Statistics," *J. Statist. Phys.* **52** (1988) 479–487.

[136] **ALICE** Collaboration, S. Acharya *et al.*, "Measurement of D-meson production at mid-rapidity in pp collisions at $\sqrt{s} = 7$ TeV," *Eur. Phys. J. C* **77** no. 8, (2017) 550, arXiv:1702.00766 [hep-ex].

[137] **ALICE** Collaboration, S. Acharya *et al.*, "Multiplicity dependence of π, K, and p production in pp collisions at $\sqrt{s} = 13$ TeV," *Eur. Phys. J. C* **80** no. 8, (2020) 693, arXiv:2003.02394 [nucl-ex].

[138] J.-Y. Ollitrault *Phys. Rev. D* **46** (1992) 229–245.

[139] S. Voloshin and Y. Zhang *Z. Phys. C* **70** (1996) 665–672, arXiv:hep-ph/9407282.

[140] U. Heinz and R. Snellings, "Collective flow and viscosity in relativistic heavy-ion collisions," *Ann. Rev. Nucl. Part. Sci.* **63** (2013) 123–151, arXiv:1301.2826 [nucl-th].

[141] B. Muller *Int. J. Mod. Phys. E* **12** (2003) 165–176.

[142] B. Zhang *Comput. Phys. Commun.* **109** (1998) 193–206, arXiv:nucl-th/9709009.

[143] H. Petersen, C. Coleman-Smith, S. A. Bass, and R. Wolpert *J. Phys. G* **38** (2011) 045102, arXiv:1012.4629 [nucl-th].

[144] C. E. Coleman-Smith, H. Petersen, and R. L. Wolpert *J. Phys. G* **40** (2013) 095103, arXiv:1204.5774 [hep-ph].

[145] S. Floerchinger and U. A. Wiedemann *Phys. Rev. C* **88** (2013) 044906, arXiv:1307.7611 [hep-ph].

[146] B. Zhang, C. M. Ko, B.-A. Li, and Z.-w. Lin *Phys. Rev. C* **61** (2000) 067901, arXiv:nucl-th/9907017.

[147] A. Mazeliauskas and D. Teaney *Phys. Rev. C* **91** no. 4, (2015) 044902, arXiv:1501.03138 [nucl-th].

[148] **CMS** Collaboration, A. M. Sirunyan *et al. Phys. Rev. C* **96** no. 6, (2017) 064902, arXiv:1708.07113 [nucl-ex].

[149] P. Bozek *Phys. Rev. C* **97** no. 3, (2018) 034905, arXiv:1711.07773 [nucl-th].

[150] B. Alver and G. Roland *Phys. Rev. C* **81** (2010) 054905, arXiv:1003.0194 [nucl-th]. [Erratum: Phys.Rev.C 82, 039903 (2010)].

[151] I. T. Jolliffe and J. Cadima *Phil.Trans.R.Soc.* (2016) 20150202 : A374.

[152] J. Morton and L.-H. Lim *Principal Cumulant component analysis preprint (2009), http://galton.uchicago.edu/lekheng/work/pcca.pdf* .

[153] H. J. Drescher, M. Hladik, S. Ostapchenko, T. Pierog, and K. Werner *Phys. Rept.* **350** (2001) 93–289, arXiv:hep-ph/0007198.

[154] T. Pierog, I. Karpenko, J. M. Katzy, E. Yatsenko, and K. Werner *Phys. Rev. C* **92** no. 3, (2015) 034906, arXiv:1306.0121 [hep-ph].

[155] H. J. Drescher and Y. Nara *Phys. Rev. C* **75** (2007) 034905, arXiv:nucl-th/0611017.

[156] B. Schenke, P. Tribedy, and R. Venugopalan *Phys. Rev. Lett.* **108** (2012) 252301, arXiv:1202.6646 [nucl-th].

[157] A. M. Poskanzer and S. A. Voloshin *Phys. Rev. C* **58** (1998) 1671–1678, arXiv:nucl-ex/9805001.

[158] S. Acharya and S. Chattopadhyay, "Estimation of initial-state structures in high-energy heavy-ion collisions using principal component analysis," *Phys. Rev. C* **103** no. 3, (2021) 034909, arXiv:2103.12380 [nucl-th].

List of Figures

List of Tables